Charge Carrier Generation Management in Photovoltaics

Charge Carrier Generation Management in Photovoltaics
Ph.D. Thesis, University of Amsterdam, December 2022
Stefan Wil Tabernig

ISBN: 978-94-6421-942-5

Cover design: *AI-generated (https://openai.com/dall-e-2/) visualization derived from the prompts "an array of cylinders in the sun, with electrons running around between them, salvador dali style" and "a storm of small particles blows to the top and separates into blue and red particles". Reuse, copyright and ownership of the generated image is regulated by the terms of use of OpenAI (https://labs.openai.com/policies/terms).*

The work described in this thesis was performed between October 2018 and August 2022 at NWO-institute AMOLF, Science Park 104, 1098XG Amsterdam, the Netherlands and at the School of Photovoltaic and Renewable Energy Engineering, University of New South Wales, Kensington 2052, Australia.

This work is part of the Dutch Research Council (NWO).

A digital version of this thesis is available at:
https://ir.amolf.nl and https://www.lmpv.nl/theses/.

Printed by https://www.proefschriften.nl.

Charge Carrier Generation Management in Photovoltaics

ACADEMISCH PROEFSCHRIFT

ter verkrijging van de graad van doctor
aan de Universiteit van Amsterdam
op gezag van de Rector Magnificus
prof. dr. ir. P.P.C.C. Verbeek
ten overstaan van een door het College voor Promoties ingestelde commissie,
in het openbaar te verdedigen in de Agnietenkapel
op donderdag 08 december 2022, te 10.00 uur

door Stefan Wil Tabernig

geboren te Lienz

Promotiecommissie

Promotores:	prof. dr. A. Polman	Universiteit van Amsterdam
	prof. dr. B. Hoex	University of New South Wales
Copromotor:	dr. E. Alarcón Lladó	AMOLF
Overige leden:	prof. dr. F. Schreck	Universiteit van Amsterdam
	prof. dr. E. C. Garnett	Universiteit van Amsterdam
	prof. dr. W. C. Sinke	Universiteit van Amsterdam
	prof. dr. C. Becker	Helmholtz-Zentrum Berlin
	dr. R. Saive	Universiteit Twente

Faculteit der Natuurwetenschappen, Wiskunde en Informatica

Contents

1

Introduction

Men argue. Nature acts.

Voltaire

1.1. The climate crisis

1.1.1. Planetary boundaries

The climate crisis[1,2] is the most important global problem right now. It threatens the existence of every single living being on earth. It has already started to affect humanity and impacts the less-fortunate disproportionally[3–5]. The ones who share the biggest responsibility for the deteriorating situation have not felt many serious effects yet, but that is coming, and unfortunately, this might be the only thing that can trigger the much-needed change in our approach to this problem. For far too long, we as humanity have suffered from a paradox in our thinking. We have managed to achieve tremendous feats by means of technology. We can use airplanes, cars, and submarines to get to virtually anywhere on earth and spaceships to travel beyond it. We employ satellites and glass fibers to communicate across vast distances. We have extended our lifespans significantly because we have the tools and knowledge to cure injuries and live healthily. And we have enabled a lot of this by using energy sources around us with groundbreaking efficiency, allowing us to power anything we can think of. But even though we are aware of the impressive technological feats that humanity has achieved and how these shaped the world, for far too long we have been too ignorant with respect to the destructive impacts that these technologies can have on our planet, Earth.

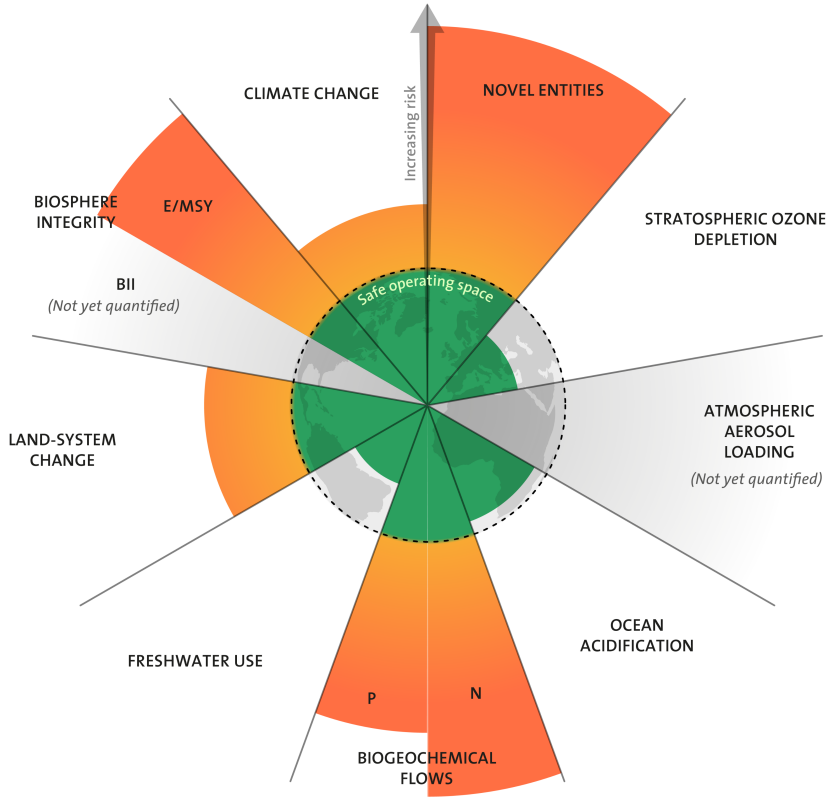

Figure 1.1: Visualization of the nine planetary boundaries, identified by Steffen *et al.*[6], and recently updated by Persson *et al.*[7]. The extent of a segment away from the center represents the degree by which the boundary has been crossed. If parts of the segment are yellow/orange, the issue has become so severe that it is not completely reversible anymore. Note that all main segments have the same width, however, this does not mean they are equally impactful overall. Image Credit: Designed by Azote for Stockholm Resilience Centre, based on analysis in Persson *et al.*[7] 2020 and Steffen *et al.*[6] 2015; CC BY 4.0.

Our negligence in this respect has not only brought us the climate crisis but has led us to cross other "planetary boundaries", which refer to physical and quantifiable limits beyond which serious negative ecological impacts on a global scale are very likely to happen[6–8]. We have already crossed this boundary for climate change, and it is important to note that climate change also impacts all other processes and their planetary boundaries, which is not necessarily true for the others. Figure 1.1 only represents the current danger associated with a process, but not its relative importance compared to the others. If that would be taken into account, the climate change segment would be even more prominent[8] due to the correlation to other processes.

To quantify climate change, the concentration of the most prominent greenhouse gas, CO_2, in the air, is often used as an indicator of the continuously worsening situation[10–14] (Figure 1.2). This is in fact an indirect indicator because greenhouse gases do not heat our planet by themselves. Greenhouse gases strongly scatter infrared radiation

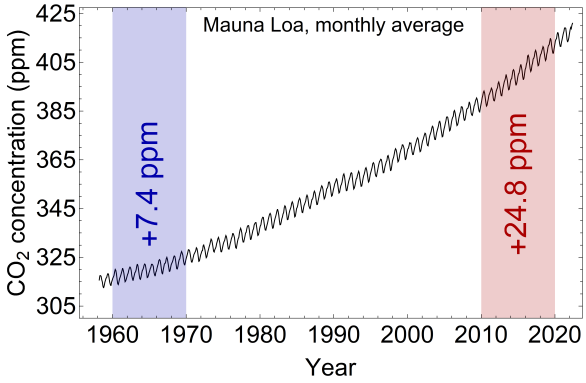

Figure 1.2: Monthly average of atmospheric CO_2 concentration detected at the Mauna Loa Observatory in Hawaii[9], in parts per million (ppm). The dataset ranges from March 1958 to May 2022. The colored ranges mark 10-year intervals for which the absolute increase is given. Within 50 years the accumulation rate of CO_2 in the atmosphere has more than tripled.

that is reflected or emitted from the earth and trap it within the atmosphere[13–16], causing global warming. Burning of fossil fuels for the generation of electricity[17,18], heat[16,19], and other forms of energy[16,20] is the main source of greenhouse gas emission[21], with additional CO_2 arising from certain chemical reactions that are used in industry[21], infrastructure[21] (concrete[22]), as well as miscellaneous sources in the agricultural sector[21,23]. The concentration of CO_2 has risen to a level at which a very optimistic scenario mentioned in the IPCC's 2022-report[24] would lead to a global surface temperature change of +1.4°C in the year 2100, relative to the period 1850-1900. So, the question if we can prevent global warming is not applicable. Instead, we find ourselves with the question of how we can mitigate it.

1.1.2. Renewable energy transition as the answer to the climate crisis

By now, most of the research community has identified and agrees on renewable energy sources[17,25] as the main lever to mitigate the climate crisis. These entail solar (photovoltaics and solar-thermal)[16,26,27], wind[28,29], hydro[30,31], and geothermal power[16,32]. Biomass is sometimes listed as a source of renewable energy source[16,33], which is only true if the used biomass can be replenished as fast as it is consumed[16]. In times of mass deforestation[34], like now, referring to biomass as a renewable energy source is incorrect[35,36], although it is more sustainable than fossil fuels[19]. Nuclear fission power[16,37] is frequently mentioned as well in discussions on the climate crisis, and while it indeed serves as a carbon-free alternative, the risks of radioactive leaks[37], long construction timelines[38], the facts that nuclear fission resources are not renewable[39] and a reliable technology for long-term storage or destruction of radioactive waste has yet to be developed[39], should be reason enough to avoid further integration of this source into our grid. Finally, power from nuclear fusion[40,41] would be a great asset, and might one day be an option, but by that time, the climate dice will have been cast.

Accessing renewable energy sources and converting them at high efficiencies is one

of three crucial steps, with the other ones being transmission and storage of energy. Especially for electricity we find that also the other two aspects are in need of further developments. Our grids have been designed for a system in which a limited number of power sources provide many individual loads with variable amounts of energy. The decentralization of power generation that comes with renewable energies[42] requires a transformation of the energy infrastructure, as we now have many power sources of varying size that can provide energy. This is a significant logistical challenge, and bright ideas such as Suncable[43] and smart grids[44] show what the energy transmission of the future could look like.

Any future grid that is adapted to renewable energy sources will also make use of energy storage, with pumped hydroelectric energy storage[16,45] (PHES), hydrogen fuel[16,46,47], other liquid and gaseous chemical fuels[47–49], and electric batteries[16,18] as the most prominent representatives. PHES, is mostly used in mountainous regions as the required height differences can be found more frequently there[50], but has tremendous potential, and can serve as an efficient mechanical battery in many places in the world[50]. Water-splitting via electricity to obtain H_2 for chemical storage is also promising, already used in heavy vehicles[51], and might utilize the same infrastructure currently being used for fossil gas[52]. Furthermore, H_2 is widely considered as the prime candidate for making many chemical and heat processes within various industries green (e.g. green steel[53]). Other chemical fuels like methane[16,54] (gaseous) or ethanol[16,55] (liquid) have the potential to fill similar roles as H_2. Finally, we are currently experiencing the advent of electrically powered vehicles[56], confirming the significance of electric batteries for the energy transition[57]. Residential batteries[58], as well as large-scale battery storage[59] plants are also on the rise, and can contribute to a more stable grid and electrification of our society.

1.1.3. Photovoltaics as part of the energy transition

Alongside the other renewable energy sources, electrical energy that is directly converted from light, through the photovoltaic effect, has become a key future technology to contribute to the energy transition. To get to this point, solar cells, or photovoltaics (PV), covered a long development path. The photovoltaic effect was first described by Edmond Becquerel in 1839[60] and utilized in a Se cell in 1883[60] (Figure 1.3). In 1954[61], the first practical Si solar cell was fabricated at Bell Labs. These events formed the basis for the growing belief in the promise of “free” energy from a source that will not deplete anytime soon.

Nowadays, the cost of PV electricity is continuously falling[63], and at the same time, we see an increasing penetration of PV in the electricity grid[64]. However, the rise of PV also demonstrates the inflexibility of our current electricity grid with respect to fluctuations and time-varying power output. PV requires storage facilities and technology to advance along with it to exhaust the full potential of PV and other renewable energy sources. There is a broad consensus that PV needs to provide a a major share of future electricity usage[65], and also that the share of electricity within our overall energy consumption has to significantly grow[65]. This is projected to be achieved by electrification of many technologies in our society[66,67] and by producing electrical energy that is so cheap that it becomes financially viable to replace more efficient thermal and chemical processes[67]. The fact that these discussions are seriously held amongst scientists, the

Figure 1.3: The world's first solar cell array (installed 1884), made by Charles Fritts [62], based on his demonstration of the first Se solar cell. Picture taken on a rooftop in New York. Reused from a postcard picture in "Let It Shine: The 6000-Year Story of Solar Energy" [62].

private sector, policy makers, and politicians already underlines that PV will be a key technology to mitigate the climate crisis.

1.1.4. Photovoltaics after the energy transition

Considering the last paragraphs, one might say that the future is bright, research has achieved a tremendous feat, and the fossil fuel reliant industry sectors, guided by politics under public pressure, are slowly getting out of their profit-driven ignorance. Compared to the renewable energy conversion sector, energy storage and transmission are key bottlenecks at the moment. Is the typical timescale of industrialization of new research innovations [68] actually short enough for making additional technological steps to tackle the climate crisis? Or is PV mature enough to shift all scientific efforts towards other fields related to sustainable energy?

These are valid questions to ask, but PV research still has plenty to offer for the energy transition. In fact, some fields are becoming increasingly important, like perovskite research, which is still young, but has already produced its first commercial applications [69,70]. With the growing scale of PV, sustainable PV, which considers aspects as material sourcing [71], fabrication [72], and recycling [73], is also becoming important.

And while the climate crisis is the one big issue of our time, the vision of a society that fully relies on renewable energies will stay relevant and also change after the climate crisis. From an optimist's perspective, a global and large collaborative effort will lead to saturation of the greenhouse gas concentration on earth and hopefully stop global warming. If everything goes according to IRENA's optimistic "Transforming Energy Scenario" [65], 49% of primary energy needs will be served by electricity in 2050, of which 86% will be electricity from renewables. In this scenario, 25% of all electricity comes from PV, which amounts to an installed capacity of 8.5 TW. This will have been achieved for a large part by the means we have right now, likely relying on Si solar cells for the biggest

part, maybe in combination with perovskites. The average module efficiency might lie between 25% and 35%. A significant portion of electricity generation will be done in large-scale PV plants, with modules stacked next to each other, sacrificing vast amounts of landmass. While the prospect of achieving this IRENA scenario sounds very appealing right now, most of us would envision a futuristic society to better use the earth's landmass and to go beyond the numbers mentioned in the scenario.

And exactly this is another important point why current PV research is essential, as it gives us a brighter perspective to fight the climate crisis for after. Commercial solar cell efficiencies of 40%, which are realistic in the long terms[74,75], complete integration of PV in unused surfaces of buildings[76], infrastructure[77], agriculture[78], and water[79], in combination with smart grids and storage could eventually reduce the immediate need for large-scale solar plants[76]. Thus, the challenge after the climate crisis will be to get to a stage where we can decide: We can either reclaim land that has been sacrificed to PV by replacing solar panels with more efficient ones, and by utilization of unused surfaces (building-integrated PV[80], vehicle-integrated PV[81]) as well as improve the integration of PV systems in our environment, to reduce the effective area loss (e.g. Agrivoltaics[78]). Or we can use the high efficiency and low cost for overproduction of energy, which might be used to drive highly inefficient processes, like carbon capture[82,83], because energy has become that cheap.

1.2. Physical principles of photovoltaics

1.2.1. The working principle of solar cells

Are 40% efficient commercial solar panels actually realistic? How much further can photovoltaic record efficiencies grow? The efficiency of solar cells is the result of the charge generation and charge extraction in a solar cell and the key criterion from a practical perspective, although secondary criteria (earth-abundance[84], flexibility[85,86], transparency[87]) are becoming increasingly relevant with respect to integration beyond rooftop and large-scale PV. The upper limit for single junction solar cell efficiencies under 1 sun is given by the detailed balance limit[88,89], which assumes ideal electronic material properties, ideal charge extraction (energy levels, selectivity), and only includes losses that are related to the bandgap of the absorber (thermalization losses for above-bandgap photons, absorption losses for below-bandgap photons, radiative emission) in combination with thermodynamic constraints.

To reach this efficiency limit, it is important to first revisit the governing principles of photovoltaic energy conversion, as well as the practical utilization of the associated energy. Photovoltaic energy conversion relies on the absorption of a photon by an electron in the valence band of a semiconductor[90]. For this to happen, the energy of the photon must be equal to or higher than the energy gap between the valence band and the conduction band in the semiconductor. Upon excitation of an electron from the valence band into the conduction band, it will stay there for an average time(τ_e), that is referred to as the bulk minority charge carrier lifetime of the material, and will be mobile up to a certain degree, described by the mobility (μ_e). At the same time, the excited electron is not spatially bound to an atom in the crystal lattice of the semiconductor, which creates an electron vacancy. This vacancy is filled by other electrons, creating electronic

motion within the valence band as well. This continuous replacement of vacancies by electrons within the valence band can be described by an effectively positively charged mobile hole, with a given lifetime (τ_h) and mobility (μ_h). Thus, the photon frees up an electron and a hole simultaneously. When they recombine, they emit a photon with an energy that corresponds to the difference of their respective energy levels.

In an ideal solar cell absorber, radiative recombination is the only recombination process. This is equivalent to saying that radiative recombination is 100% efficient, as that implies the absence of alternative recombination processes. However, in a solar cell, carriers should always be extracted from the absorber before they have the chance to recombine. With the help of charge-selective extraction layers[91], or electric field gradients[91], the electrons and holes are spatially separated so that they accumulate at opposite poles within the solar cell. This accumulation of the opposite species of charge on each side of the solar cell increases the potential energy within the system.

At equilibrium, the Fermi level describes the potential energy of the electrons and holes. However, in a steady-state, the conduction band and valence band are not in equilibrium. Still, average energies can be found that describe the excited electron and hole populations separately, namely quasi-Fermi-levels (quasi because the system is not actually in equilibrium[91]). A large energy difference between the two quasi-Fermi-levels corresponds to a large difference in potential energy, which corresponds to a large voltage for electric charges. This is similar to the voltage in a charged battery, with the difference that for the solar cell, the charge distribution is continuously replenished by sunlight. Upon contacting the poles of the solar cell within an electrical circuit, the charges flow along this circuit to reach the other end of the cell. This creates a current flow, and if a load is included in the electronic circuit, one can use this flow together with voltage that drops off over the load to power it at a given efficiency.

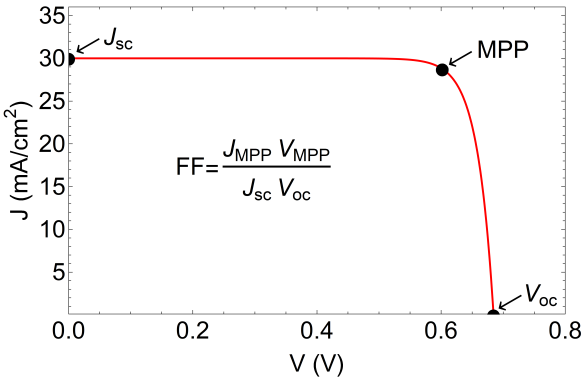

Figure 1.4: Current density (J) - voltage (V) curve of an ideal solar cell under illumination. The three marked points represent the short-circuit current density (J_{sc}), the open-circuit voltage (V_{oc}), and the maximum power point (MPP). The fill factor (FF) is calculated from these points according to equation (1.6).

The efficiency parameter η is the product of the short-circuit current density (J_{sc}), the open-circuit voltage (V_{oc}), and the fill-factor (FF, Figure 1.4), normalized by the incident solar intensity ($I_{AM1.5G}$). It describes the maximum amount of electrical power that can be extracted from a solar cell, relative to $I_{AM1.5G}$.

$$\eta = \frac{J_{sc} V_{oc} FF}{I_{AM1.5G}} \tag{1.1}$$

The intensity of the incident sunlight is wavelength-dependent, and its spectral distribution is derived from the black body spectrum of the sun, at its temperature (5772 K[92]), with various dips in the spectrum that correspond to absorption of light by the gases in our atmosphere. While this spectrum differs throughout the day, year, and location on earth, the scientific community has established reference datasets that serve as a reference for the optimization and evaluation of solar cell performance[93]. The AM1.5G spectrum is one of these and corresponds to a global annual average of direct and diffuse light that has travelled a distance that corresponds to 1.5-times the atmospheric thickness. Integration over this spectrum yields the total power ($P_{AM1.5G}$) that we receive on earth and amounts to $P_{AM1.5G}$=1000.4 W/m^2.

If we want to calculate the maximum obtainable efficiency, assuming an electronically ideal solar cell, we can start by calculating what our obtainable photo-current density (J_γ) is. During photovoltaic conversion of incident photons from the AM1.5G spectrum into electrons, the maximum number of photons that can be converted corresponds to all the photons that are above the bandgap energy of the absorbing semiconductor. Each of these photons can excite one electron-hole pair and upon excitation these rapidly (timescale[94]: 10^{-12}-10^{-11} s) lose energy in the form of heat via thermalization, until they reach the lowest energy level of the conduction band (electrons), or highest energy level of the valence band (holes). From there, they are extracted from the solar cell, and the total amount of extracted charges per second corresponds to the J_{sc}. Equation (1.2) shows the dependence of J_γ on the electron charge (q), the solar photon flux ($\phi_{AM1.5G}$), the photon energy (E), and the bandgap energy (E_{BG}), which can be simplified to a dependence on the number of photons (N_γ) with energy above E_{BG} received within a certain time (t).

$$q \int_{E_{BG}}^{\infty} \phi_{AM1.5G}(E)\, dE = \frac{q N_\gamma(E_{BG})}{t} = J_\gamma(E_{BG}) \tag{1.2}$$

Conceptually, J_γ gives the extracted charges, and at the same time it can be understood as the charge separation rate. However, the reverse process can also happen and is given by the (dark-) recombination current density (J_0). In absence of the sun, with the solar cell at a given temperature (T), and its ambient at the same temperature, the solar cell radiates/emits as much energy as it absorbs, and as there is no net-flow of any quantity, it is in thermal equilibrium. The rate by which it absorbs or emits is the same and we refer to the associated currents as dark currents, which are equal and opposite. Mathematically, J_0 can be expressed as an integral over a black-body emission spectrum that is confined to energies above E_{BG}, as in equation (1.3), with c the speed of light, h Planck's constant, k Boltzmann's constant and V the voltage applied to the cell.

$$J_0(E_{BG}, V) = q \int_{E_{BG}}^{\infty} \frac{E^2}{e^{\frac{E-qV}{kT}} - 1} dE \tag{1.3}$$

The voltage term in equation (1.3) for J_0 only makes sense for the emission of the solar cell for which the applied voltage can be regulated and does not apply for the solar

cell absorption from the ambient. Thus, if we apply a voltage to a solar cell in the dark, we move from equilibrium to a steady-state, for which emission and absorption are not equal anymore. Under forward bias, the emission of the solar cell increases, which corresponds to an increase in recombination current. Under illumination, we will extract an overall current density (J_{ext}) that corresponds to the sum of the solar photo-current density (J_γ), the ambient photo-current density ($J_{0,G}(E_{BG})$), and the voltage-dependent dark recombination current density ($J_{0,R}(E_{BG},V)$).

$$J_{ext}(E_{BG},V) = J_\gamma(E_{BG}) + J_{0,G}(E_{BG},0) - J_{0,R}(E_{BG},V) \tag{1.4}$$

Equation 4 describes the detailed balance limit for solar cells from the perspective of electrical currents, and for a given bandgap, the extracted current as a function of voltage yields a characteristic diode curve shape. By setting the applied voltage to V=0, we obtain J_{ext}=J_γ, which is referred to as the short-circuit current density (J_{sc}). At the point where J_{ext}=0, we find the open-circuit voltage (V_{oc}) of the solar cell. For a band gap that is much larger than the room temperature thermal energy ($E_{BG} >> kT$), equation (1.5) describes the V_{oc} as function of the bandgap.

$$V_{oc}(E_{BG}) = \frac{kT}{q} Log\left(\frac{J_\gamma}{J_0} + 1\right) \tag{1.5}$$

The third important solar cell parameter, the fill factor (FF, equation (1.6)), describes how close the current-voltage product at the maximum-power point of an $I-V$ curve (MPP) comes to the product of the maximum obtainable current (J_{sc}) and voltage (V_{oc}) of the solar cell's $I-V$ curve (Figure 1.4).

$$FF(E_{BG}) = \frac{J_{MPP}V_{MPP}}{J_{sc}V_{oc}} \tag{1.6}$$

Now we have obtained all the parameters that are needed to calculate the efficiency or power that we can obtain from a solar cell (Equation (1.1)). For the case in which the electronic parameters are ideal, and the incident spectrum is fully absorbed above the bandgap, the efficiency is parameterized by only one parameter, E_{BG}. This is the detailed-balance limit[88,89], and it can, in principle, be extended to solar cells with multiple junctions[95], as well as incident spectra at different intensities and shapes[96], and serves as the upper limit to the achievable efficiency.

There is a fair amount of PV device concepts that can circumvent the assumptions of the detailed balance limit and hence could technically go beyond it. However, they have in common that devices with significant efficiency enhancements have not been demonstrated yet. Downconversion[97] can in principle mitigate thermalization losses, by effectively exciting two electrons via one high-energy photon. Upconversion processes[97] bundle the energy of two low-energy photons to excite one electron across the bandgap, and hence minimize subbandgap losses. Another conceptual solar cell is the hot-carrier solar cell[98], which aims to minimize thermalization loss of electrons by extracting them at higher energies, right after excitation. So far, none of these concepts have found commercial applications.

1

1.2.2. How much more can efficiencies improve?

The discrepancy between the described minimum losses and the current record efficiencies is illustrated by Figure 1.5a, where we can find various absorber materials represented by their bandgap and their efficiency trajectory over recent years (2016-2020). This comparison for single-junction solar cells gives an overview of the current challenges within the physics, chemistry, and material science for the individual technology. Figure 1.5b shows the same materials, but with respect to the room for improvement for carrier extraction and carrier generation. The overall trend implies that there is more room for improvement with respect to carrier extraction in comparison to carrier generation. Usually, carrier extraction is addressed by optimizing charge carrier selectivity, band alignment between the layers, reducing surface and interface recombination, and reducing the internal series resistances. Carrier generation cannot easily be improved by working on a specific layer in the solar cell alone but requires consideration of the whole cell architecture.

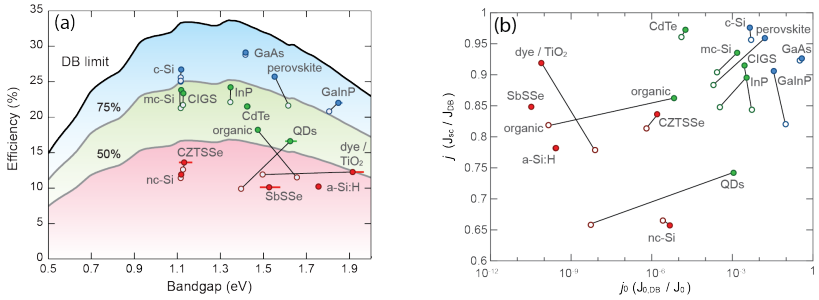

Figure 1.5: (a) The photovoltaic conversion efficiency as a function of the bandgap for various absorber materials. Black lines connect the data points that correspond to the record values in 2016 (open symbols) to the record values in 2022 (colored symbols). The background colors denote efficiency regions below 50% (red), 50%-75% (green), and above 75% (blue), relative to the detailed balance limit. (b) Data for the same records, resolved for the optical (j) and electronic (j_0) performance, relative to the detailed-balance limit. Reused and edited from Ehrler *et al.*[99], and Polman *et al.*[100]

1.3. Light management - nanostructures for PV

Light management for solar cells refers to designing the solar cell architecture in a way that maximizes absorption and carrier generation. The first step for this is to maximize the incoupling of light, so that it can reach the absorber. For this, it needs to pass from air through the encapsulation and top layers towards the absorber layer. Ideally, light travels long enough inside the absorber layer to be completely absorbed. Any light that has passed through the absorber should then be reflected back into it. Incoupling, path length enhancement, and back reflection form the core toolkit used in light management for improvement of solar cells, and are seldom applied independently, but often appear in a combined fashion.

There are, however, additional concepts within light management. An important one is spatial control of the charge generation profile, creating spatially selective light absorption. In this case, electromagnetic field profiles create light concentration hotspots

at desired positions in the cell. Optimizing the location of these hotspots can minimize the losses due to parasitic absorption at lossy interfaces. Creating optical hot spots close to charge selective layers, minimizes extraction losses to electronic interface defects.

For a wide range of applications, such as multijunciton solar cells[95,101], bifacial solar cells[102], semi-transparent solar cells[87], and luminescent solar concentrators[103], spectrally selective transmission and reflection at the front and rear surfaces of PV devices are also interesting. In this case, light within a specific wavelength range is intentionally transmitted through the solar cell, and used for a different function.

Light management can come in various forms, such as micrometer-scale pyramidal texture for improved incoupling of light[104], or a combination of a couple of planar layers of 10s of nanometers for spectral selectivity. With the advent of nanoscience[105], and increasing scalability of nanoscale layers[106–108], nanostructures have found their way into photovoltaics[106?,107]. Light management has profited a lot from nanoscale structures, as the degrees of freedom for light manipulation in nanoscale structures are much more compared to larger structures that rely on geometric optics, owing to physical properties (plasmonic, Fabry-Perót, and Mie-resonances) and processes (diffraction, waveguiding) that often only become accessible at the nanoscale.

The building blocks of light management at the nanoscale are often resonant objects, that are arranged within a consciously chosen pattern. The individual building blocks (nanoparticles) can be optimized via a range of different methods in shape and dimensions so that they interact strongly with light within a specific wavelength range. This strong interaction amounts to scattering and absorption profiles which can be predicted from Maxwell's equations and tuned via the particles' dimensions and optical constants.

By arranging the particles in a periodic pattern, the collective of these scattering processes can be influenced such that constructive interference is achieved for specific angles (diffraction modes), and if done inside or close to a slab of a thin layer, can be trapped very efficiently (waveguide, surface (plasmon/phonon) polariton[109,110] modes).

The optical behavior that emerges from these processes are hotspots that can be generated in the absorber, light that is scattered into wide angles so that its path length through the absorber is enhanced, as well as forward scattering (incoupling) and backscattering (reflection) of light. Furthermore, these processes are strongly wavelength dependent, which allows for wavelength selectivity.

1.4. The importance of absorber-agnosticism in PV

Having discussed the relevance of PV, its prospects, efficiency limits, and light management as an important tool to reach those limits, we can now ask the final question of this introduction, namely, how do we decide which technology is the most promising one, and does this mean we discard the others?

Within the scientific PV community, hardly any material science research group covers the full spectrum of available absorber layers in their research, as these technologies often require very different knowledge as well as infrastructure. The currently most efficient solar cell technologies can be roughly divided in three distinct groups. Many scientist work with Si, which has proven itself as the number one commercial choice time and time again because it is cheap[111] and efficient[74,75]. Others focus on more chemistry-heavy solar cells based on organic[112] and perovskite[113] absorbers, which might be on

the verge of competing with[74,75] or complementing[114] Si. And some researchers advance the highly efficient[74,75] but expensive (concentrator) III-V technologies. In the following, we will see why it is important to keep an open mind with respect to all technologies, independent of their maturity, as all of them can be relevant in their own way, if given sufficient attention (research).

The range of applications and specifics that PV needs to address now, and for what comes after the near future, is just so vast, that it makes sense to ensure the availability of more than one good absorber. Silicon excels when it comes to the accumulated knowledge that exists for it, as well as its maturity. However, Si solar cells are thick, and hence do not qualify as serious candidates for thin film PV, which is much more versatile for applications that require flexible or light-weight solar cells. III-V solar cells are thin-film and efficient, but very expensive. Exactly at this important point, novel PV absorber materials, such as PbS QDs, CZTS, perovskites, and Zn_3P_2 are important to consider as well. While some of them have tunable bandgaps (QDs, perovskites), others have excellent diffusion lengths (Zn_3P_2, perovskites), and again others excel in earth-abundance (Zn_3P_2). Thus, for versatility, it is very important to have access to a range of absorber materials.

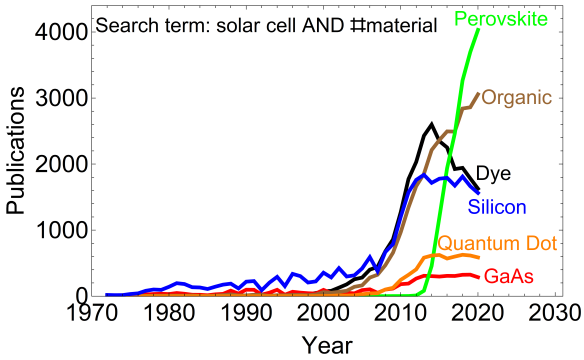

Figure 1.6: Number of publications per year for various materials over the years. Data was obtained from `app.dimensions.ai`, by combining the search term "solar cell" and the material names stated in the figure. The search engine searched through publication titles and abstracts only.

Figure 1.6 shows an interesting aspect about the current state of PV research, especially with respect to the effect of the dominance of perovskites. It describes the annual number of publications over time for selected PV materials. Since the 1970s, Si and GaAs solar cell research experienced slow but continuous growth. Overall, PV research significantly picked up the pace around the year 2000, thanks to organic and dye-sensitized solar cells. Around 2005, Si, GaAs and quantum dot (QD) research started to gain much more interest as well. And, in 2012, perovskites entered the stage, and their monumental rise coincides with the stagnation (Si, GaAs, QDs), decline (dye-sensitized cells), or weakening of the growth (organic cells) of publications on all the other materials.

This suggests that it was not the lack of promise of certain materials that hinders their progress, but it is the advent of a more promising material, perovskite, that has slowed down research on other materials considerably. Note that CdTe, CIGS, CZTS, GaInP, and

InP solar absorber materials show similar trajectories as GaAs and were omitted from Figure 1.6 for simplicity.

1.4.1. Earth-abundance as a fundamental restriction

There is one parameter that deserves special mention and that is the abundance of elements in the earth's crust. While some elements also feature in our oceans and can be obtained from there, the earth's crust is our main source of all elements, and their concentration therein should be regarded as a practical limit to the amount of solar cells that we can make for a given absorber composition.

This aspect has received quite some attention already[115], and often this has focused on calculating the required amount of energy and money to obtain a pure kilogram of a certain element. However, these numbers depend on the method of extraction that is used, and in principle, further research can help improve that. The actual limit is the elemental concentration in the earth's crust.

Figure 1.7 uses the absorption coefficient of various absorbers to evaluate the total absorption as a function of thickness and balances it with extraction losses due to the limited carrier diffusion length. For the absorption of light in the absorber, a perfect backreflector is assumed, which leads to a double pass of the light through the absorber (The exception is the case of the Lambertian limit[116] for Si ($4n^2$), which is also shown). Only imperfect absorption serves as a loss channel for the absorption, reflection and transmission losses are not considered. For the charge extraction, we assume uniform charge distribution after generation, which means that on average, charges only have to travel half of the absorber thickness. Charge drift from electric fields is not considered. In the ideal case, the curve for a material shows a broad peak at a value above 30% efficiency. This means that α and L_D are sufficiently large to enable full charge generation at a thickness for which all charges can be extracted, and GaAs and Si-$4n^2$ represent this case. Silicon, Zn_3P_2 and perovskite peak at very different thicknesses, but show a similar balance of α and L_D. Solar cells based on CZTS and PbS QDs peak at similar thicknesses, and show low achievable efficiencies, due to very short diffusion lengths.

By using the earth-crust abundance of each element of an absorber[123], the bottleneck-element is determined for each cell type and used to relate the efficiency to the resource demand. Finally, we find the relative amount of the bottleneck-elements that is needed to achieve PV generation around the multi-TW-scale (Figure 1.8). For all materials, at 100 TW capacity, the resource usage stays below 0.0001% of its prevalence in the earth's crust. The difference between the most abundant (Si), and the least abundant (GaAs) is a factor 10^4. Assuming similar extraction methods, this number directly correlates to the additional mining effort (size, time, energy, money) that it is needed for GaAs compared to Si. So while we could get to 100 TW with all absorbers, we can do it sustainably by considering earth abundance and low-material-usage. Note that this simple economic analysis focuses on the economic viability of the absorber layer alone, which is the first hurdle. A more extensive analysis would need to also account for other materials used in the solar cell (metal contacts, extraction layers, *etc.*), but this is beyond the scope of this introduction.

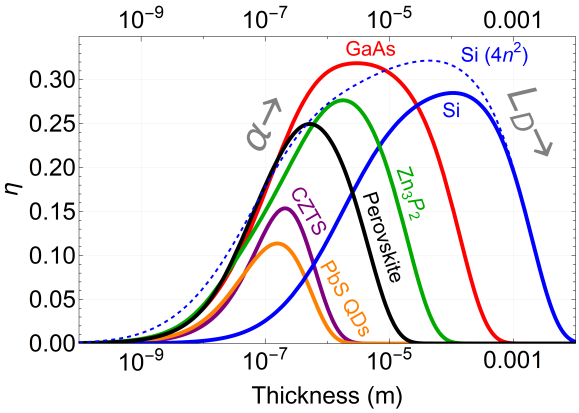

Figure 1.7: Maximum possible PV efficiency for various materials as function of absorber thickness. The Lambertian limit for Si is also shown (blue dashed). Based on the absorption coefficient (α, rise, data from thesis chapters) and the diffusion length (L_D, decline, data from literature [117–122]).

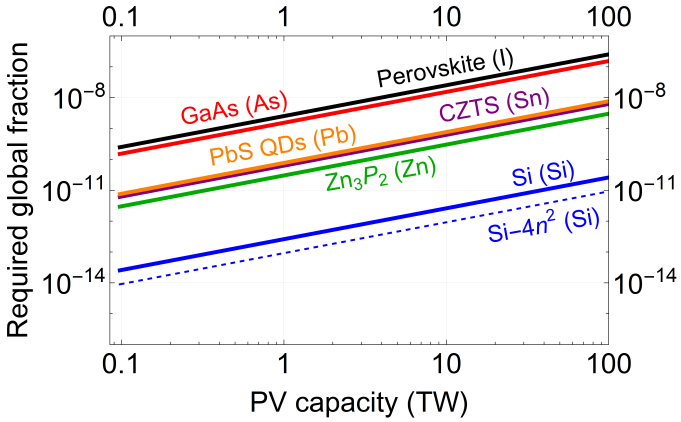

Figure 1.8: Required amount of the bottleneck-element compared to its prevalence in the earth's crust as function of PV capacity that is based on the specific element. The elements in brackets next to the absorber label are the bottleneck-elements for the absorber layer. The curves assume the peak PV efficiency from Figure 1.7.

1.5. Thesis chapters

Increasing the absorption through light management effectively reduces the required thickness for a solar cell. This fits the sustainable approach of PV, as it allows for less material to be used. Throughout this thesis, this sustainable aspect of PV is represented in the approaches that aim to thin the absorber down or by working on earth-abundant absorbers to begin with.

In Chapter 2, we reduce the absorber volume of a PbS quantum dot (QDs) solar absorber to bring carriers closer to their extraction layers and to limit the amount of toxic Pb that the cell contains. This is achieved by nanopatterning of the p-n heterojunction to modify its optical and electronic response. We find that optically resonant QD cylin-

ders can concentrate more light into less absorber volume, and 2.2-times less material is needed to absorb the same amount of light. We also show that this approach can improve charge extraction, which is a major obstacle for PbS QDs (see Figure 1.7).

In Chapter 3, we demonstrate how to minimize reflection losses from metal contacts on a solar cell. We do this by optical cloaking of the metal front contacts. This is especially relevant for concentrator solar cells, where high illumination intensities require large front metal coverage. The optical cloaking can eliminate reflection losses and allows for high front metal coverage at no additional reflection loss. This enables concentrator solar cell setups with concentrations above 1000-suns, which at the same time corresponds to a reduction in absorber material usage by a factor 1000.

In Chapter 4, we shift the focus to thin Si solar cells. These use much less absorber volume, but also absorb weakly, partially due to insufficient incoupling of light. For thick Si solar cells, large (a few micrometers) random pyramids are usually used for ideal incoupling of light. As this is often not possible in thin Si solar cells, we show that a periodic cylindrical nanoscale pattern can be used as an alternative, showing better incoupling than a single layer anti-reflection coating, while not suffering from extra electronic loss (V_{oc}, FF) in comparison. In parallel, we also investigate hyperuniform nanopatterns that strongly scatter light from the Si surface into the bulk. We evaluate the passivation that is necessary for the structure to not just work well optically, but that also allows front-surface recombination currents that are closer to the planar case. The results show that front surface patterning of thin Si solar cells can improve the absorption and might lead to flexible Si solar cells that can compete with other thin-film technologies.

In Chapter 5, we add a perovskite absorber on top of a silicon solar cell and evaluate the maximum efficiency of this tandem geometry via simulations. We then expand the detailed-balance formalism to include spectral splitting at the interface between the perovskite and Si absorbers and determine the cases for which this yields improved efficiencies.

In Chapter 6, we present a novel p-n heterojunction design for a Zn_3P_2-based solar cell. Zn_3P_2 is an earth abundant (Figure 1.8) absorber with high absorption coefficient and diffusion length. We develop a heterojunction architecture , consisting of ITO-TiO_2-Zn_3P_2-Au (front to rear) that can be used to integrate Zn_3P_2 into a simple but efficient solar cell device. Furthermore, we predict an efficiency limit of 20%, that can be increased by additional light management.

In Chapter 7, we look back and summarize the fabrication approaches that have been used throughout the course of this thesis. Furthermore, we highlight our direct imprint approach for ZnO in chapter 2 as an effective and non-invasive fabrication method that could be extended to other solgel layers of any material.

From a practical perspective, the following chapters will demonstrate work that might lead to solar cells with thinner absorber layers (Chapters 2, 4, 5), higher efficiencies (Chapters 3, 5, 6), and emphasizes the potential of novel absorber materials (Chapters 2, 6).

Overall, this thesis introduces novel insights into integrating nanoscale light management with the generation and extraction of charge carriers for improved photovoltaics. We emphasize the importance of spatial control of absorption for the electronic solar cell performance. And we investigate how absorption-enhancing nanostructures influence the electronic integrity of solar cells for a wide range of established as well as novel pho-

tovoltaic technologies.

1.6. Author contributions

S.W. Tabernig wrote the manuscript. Some figures were taken from collaborative work[99] with B. Ehrler, E. Alarcón Lladó, E. Garnett, T. Veeken, S.W.T., and A. Polman.

2

Optically resonant bulk heterojunction PbS quantum dot solar cell

2.1. Abstract

We introduce an optically resonant bulk heterojunction solar cell to study optoelectronic properties of nanostructured p-n junctions. The nanostructures yield strong light-matter interaction, as well as distinct charge-carrier extraction behaviour, which together improve the overall power conversion efficiency. We demonstrate a novel approach using high-resolution substrate conformal soft-imprint lithography technology in combination with state-of-the art ZnO nanoparticles to create a nanohole template in an electron transport layer. The nanoholes are infiltrated with PbS quantum dots (QDs) to form a nanopatterned depleted heterojunction. Optical simulations show the absorption per unit volume in the cylindrical QD absorber layer is enhanced by 19.5% compared to a planar reference. This is achieved for a square array of QD nanopillars of 330 nm height and 320 nm diameter, with a pitch of 500 nm on top of a residual QD layer of 70nm, surrounded by ZnO. Electronic simulations show that the patterning results in a current gain of 3.2 mA/cm^2 and a slight gain in voltage, yielding an efficiency gain of 0.4%. Our simulations further show that the fill factor is highly sensitive to the patterned structure. This is explained by the electric field strength varying strongly across the patterned absorber. We outline a path towards further optimized optically resonant nanopattern geometries with enhanced carrier collection properties. We demonstrate a 0.74 mA/cm^2 current gain for a patterned cell compared to a planar cell in experiments, owing to a much improved infrared response, as predicted by our simulations.

2.2. Introduction

With the continuing rise of photovoltaics (PV) as one of the main pillars of our current and future energy supply system, more and more PV-related applications have appeared and grown into important subfields, such as building-integrated PV[80,124,125], vehicle-integrated PV[126], and PV-integrated electronic devices[127]. While Si solar panels represent the main markets for rooftop solar and large-scale PV plants for the near future, many important high-value markets desire PV materials with higher flexibility. Colloidal PbS quantum dot (QD) based absorbers have emerged as an interesting contender for applications beyond the established large-scale Si PV market. The fact that their bandgap can be tuned across a wide range of the AM1.5G solar spectrum by changing their size[128] makes them an attractive material for various applications beyond traditional PV, such as flexible PV[129], luminescent solar concentrators[103,130], multi-junction PV cells[131,132] and other optoelectronic applications[133]. Furthermore, PbS QD based solar cells can be fabricated by solution processing, which makes them highly relevant for solution deposition methods such as printing via slot-die coating[134] or spray-coating[135], enabling high-speed low-cost manufacturing. Earth-abundance of PbS itself and the recent power conversion efficiency record of 13.8%[136], underline the relevance and promise of PbS QD absorber-based PV.

One major obstacle that has prevented PbS QD solar cells from keeping up the pace with, for example, perovskite PV is the short carrier diffusion length, induced by the nature of PbS QD absorbers. As they are composed of a matrix of closely packed nanocrystals with ligands as spacers[137], charge transport involves a hopping mechanism[137]. The resulting short diffusion length leads to an unsatisfying compromise between optical performance (high short-circuit current - J_{sc}), which requires a thick absorber layer, and electronic performance (high open-circuit voltage - V_{oc}, high fill factor - FF), which is best for thin layers. So far, approaches to increase the diffusion length have involved reduction of QD-QD separation inside the matrix using shorter ligands[138], utilizing stronger electric fields inside the cell via improved device architectures[139,140], reduction of defect densities via better surface passivation[138], and reduction of average carrier-transport layer distances via bulk-heterojunctions[141,142]. Furthermore, improving the absorption of the active layer with front or backside light trapping layers such as backreflectors[143], slightly dented electron transport layers (ETL)[144], bulk-heterojunctions[145,146], patterned ITO substrates[147], and on a larger scale, pyramidal ETL[148] have all been investigated.

With some exceptions[148–150], these optimizations were made mainly considering either charge extraction or charge generation, but not both. Here, we introduce a nanostructured heterojunction geometry that both optimizes charge collection and serves as an optically resonant light absorber at the same time. It comprises a new architecture in which the heterojunction itself is shaped as a resonant optical cavity. We present this new concept by shaping colloidal PbS QD layers as absorber material with local optical resonances and guided (plasmonic) modes.

In the following we will first introduce the concept of an optically resonant p-n junction and then will show how the structure's dimensions are chosen to maximize the absorption per unit volume, using optical simulations. This is followed by an investigation of the electronic performance of the optically optimized structure, using simulations of the carrier diffusion and collection pathways in the nanopatterned cells. We derive a

nanopatterned geometry that shows a strongly enhanced optical absorption spectrum with a heterojunction geometry that strongly enhances carrier collection of charges generated at the bottom of the absorber. We present a novel method using a direct soft imprint process to create the nanopatterned electron conducting ZnO layer. Experimentally measured external quantum efficiency spectra confirm the enhanced light absorption and carrier collection for the new optically resonant heterostructure geometry.

Our results are applicable for a wide range of emergent PV materials, including organics, TiO_2 -dye absorbers, SbSSe, and CZTS, that all suffer from limited carrier diffusion length. Our study indicates that by structuring the p-n junction in three dimensions, the constraints imposed by short diffusion lengths can be weakened, if care is taken with respect to where carriers are generated, as well as how the electric field distribution in the cell is influenced by the nanopattern's geometry. In practice, for each material the optimum nano-patterning process will depend on the deposition method of the absorber and the surrounding n-/p-window or extraction layers.

2.3. Design and fabrication

The design is based on a depleted-heterojunction PbS QD solar cell, which consists of the following layers, from top to bottom (see Figure 2.1a): ITO (front contact), a layer of ZnO nanoparticles (n-type window layer), bulk PbS QDs with PbI_2 ligands (i-type absorber layer), bulk PbS QDs with EDT ligands (p-type layer; EDT: ethanedithiol) and Au (back contact). The "bulk QD layer" is a matrix of closely packed QDs. This layer is then structured into an array of nanocylinders composed of PbS QDs on a residual PbS QD layer, surrounded by ZnO, as illustrated in Figure 2.1a. The front and back contacts as well as the p-type layer form planar layers, meaning the nanopattern is confined to the i-n junction within the solar cell. The residual QD layer consists of a thin p-type QD layer and an i-type QD layer and functions as an electronic barrier between the n-type ZnO layer and the Au contact at the back. The dimensions of the pillars are chosen such that they show strong local optical resonances and guided (plasmonic) modes. In our design the pillars are separated by a fixed distance and arranged in a square lattice. As we will see further on, the nano-geometry creates much shortened carrier collection paths for carriers generated at the back of the cell.

To fabricate the structure shown in Figure 2.1a, we firstly nanopattern holes into a ZnO-NP layer (light-blue) on top of ITO and secondly fill these up with QDs (red). For the patterning, we use substrate conformal soft-imprint lithography (SCIL [107]) which uses a PDMS stamp that contains nanostructures, that are replicated from a nanostructured Si master wafer, to imprint patterns into a liquid solgel. So far, SCIL was used to pattern optically functional silica-like layers. Here, we for the first time use high-resolution SCIL-stamps together with ZnO-NPs, to fabricate a layer that is optically and electronically functional. Figure 2.1b shows such a patterned ZnO layer, consisting of holes of a diameter of 400 nm, arranged in a square lattice with a pitch of 513 nm. The height difference between the residual ZnO layer and the pattern's walls is roughly 100 nm and is fixed by the feature depth in the PDMS stamp. It should be noted that this direct transfer of the nanopattern from the stamp into the ZnO-NP layer represents a straightforward approach and is much less likely to cause undesired degradation of optical or electronic properties of the ZnO layer compared to more conventional patterning schemes that in-

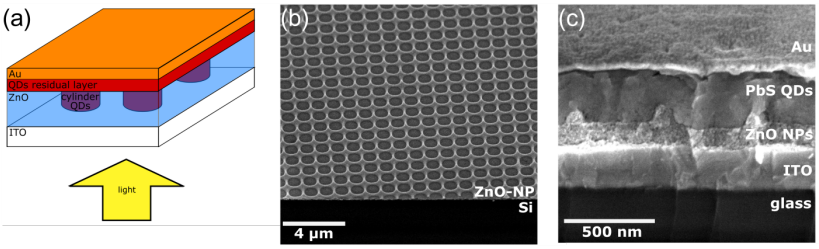

Figure 2.1: (a) Patterned p-i-n for a PbS QD solar cell heterojunction structure. Light is coming from the bottom. ITO and Au serve as front and back contacts, respectively. Bulk PbS QDs act as the p-/i-type layer, and ZnO as the n-type layer, together forming a 3D interface. (b) SEM perspective (45°) of SCIL-patterned ZnO nanoparticle layer on top of a silicon substrate. (c) SEM cross-section image of the patterned cell geometry. Light incident from the bottom. The ZnO holes have been completely infiltrated by PbS QDs and a flat Au layer caps off the geometry.

volve reactive ion etching (RIE) and/or wet-etching. Additionally, the ZnO-NP solution used to fabricate the ETL layer corresponds to the state-of-the-art in the field of QD solar cells [151], which means that no compromise between quality of the ETL layer and compatibility of its precursor solution with SCIL had to be struck. The only parameter tuned for the ZnO-patterning was the spinning duration, to make sure that the layer was still liquid enough to be patterned. High boiling point solvents such as buthanol allow for dilution of the solution and could serve as an additional fabrication parameter if thinner ZnO layers were needed, but this was not necessary in our case.

Next, the holes in the ZnO layer were filled up with PbS QD-ink. This is followed by deposition of a planar PbS QD-EDT layer of 30 nm and 100 nm of Au. Figure 2.1c shows the seamless interface between the ZnO and QD layers, highlighting the effectiveness of the hole infiltration with QD ink. It also becomes clear from the figure that the nanopattern is confined to the interface between ZnO and QDs, which means that the i-type material exhibits a planar surface morphology. Hence, conformal deposition of p-type QDs and the Au layer is possible in the same way as for a planar cell.

2.4. Optical optimization

Following the successful realization of QD pillars embedded in ZnO, we investigate the specific dimensions required to optimize the efficiency gain. We first study the optical properties of bulk PbS QD layers and maximize the absorption per unit volume in the patterned absorber by means of finite difference time domain (FDTD) simulations.

The optical properties of bulk PbS QD layers derive from a combination of the properties of PbS, which is a narrow bandgap semiconductor (0.41 eV [152]), the quantum confinement effect that occurs in nanocrystals with diameters smaller than the Bohr radius of electron-hole pairs [128], and the effective refractive index of the organic matrix that contains the individual PbS QDs and consists of the ligands that cap them. The effective medium formed by ligands and nanocrystals determines the refractive index of the bulk QD layer and is dominated by the choice of ligands.

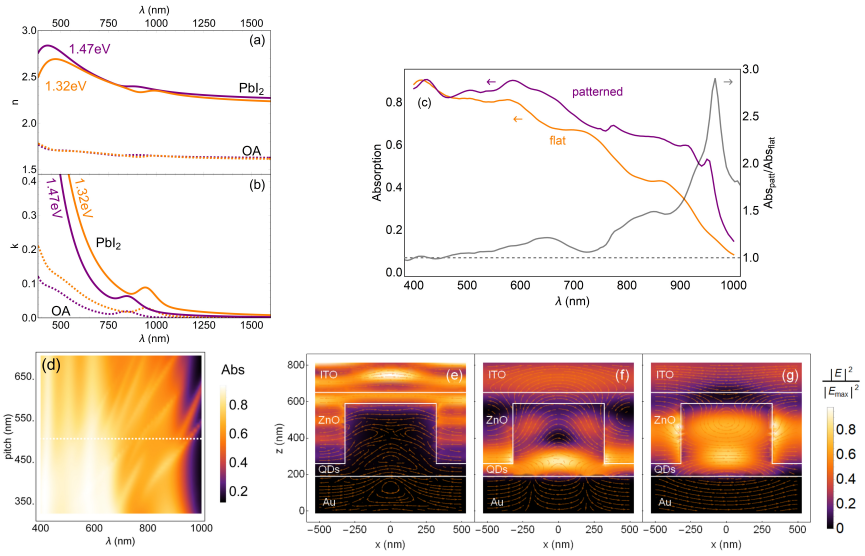

Figure 2.2: Real (a) and imaginary (b) parts of the refractive index of PbS QDs. For QDs with the first exciton peak at 1.47 eV (purple) and 1.32 eV (orange) and with either PbI_2 (solid) or oleic acid (OA, dashed) ligands. (c) Absorption versus wavelength for a planar cell of 180 nm absorber thickness (orange) and a patterned cell that uses the same absorber volume (purple). Relative increased absorption for the patterned case is plotted on the right axis (grey line). Pillar dimensions of patterned case: 330 nm height, 320 nm diameter, 500 nm pitch; (d) Absorption versus wavelength and array pitch of the QD pillars. The color scale represents the absorption value. Data at the white dashed line corresponds to the purple absorption spectrum for the patterned case in (c). (e-g) Relative electric field intensities (color scale) across the solar cell's cross-section through the center of a pillar for wavelengths of 425 nm, 915 nm, and 950 nm, respectively. White lines and labels are used to distinguish between different cell regions. Orange arrows are used to indicate the orientation of the electric field in the x-z planes.

Figure 2.2a,b shows the real (n) and imaginary (k) part of the refractive index of PbS QD films with different first exciton peaks and ligands, determined by spectroscopic ellipsometry (SE). We show data for first exciton peaks at 1.32 eV and 1.47 eV, as well as data for QDs capped with oleic acid (OA) ligands and PbI_2. The low energy peak in k corresponds to the homogenously broadened first exciton peak which is further inhomogenously broadened due to the size dispersion of the QDs. In general, absolute values and spectral shapes of the curves for n and k are in good agreement with literature [153]. PbI_2-capped QDs show a higher real part of n and stronger absorption compared to those with OA, which can be explained by the much denser film in the case of the short PbI_2 ligand (3 atoms) compared to the large separations induced by the much longer OA ligand (18 C-atoms [154]). The absorption for the QDs with the small bandgap (large QDs) is higher than for the large bandgap QDs. This is the case because larger QDs have a higher density of states available for absorption. The energy labels assigned to the graphs in Figure 2.2a represent the first exciton peak energies. The actual semiconductor bandgap of the QD layer, that is conventionally defined by a tauc-plot [155], is lower. In fact, the bandgap for the QDs with a first exciton peak at 1.47 eV is around 1.34 eV. This is very close to the ideal bandgap according to the detailed balance limit [99], and we will be using this

particular set of optical constants for our optical simulations.

Using FDTD (Lumerical), we now investigate by how much the absorption per unit volume in a QD pillar can be increased by nanopatterning the layer, assuming the solar spectrum (AM1.5G). We systematically vary height, diameter, and pitch of the cylinders. Furthermore, the residual QD layer thickness that separates the ZnO layer and the Au backcontact is optimized. We also considered the following boundary conditions: The residual layer is restricted to a minimum thickness of 30 nm (corresponding to 2 layers of EDT-capped QDs) and the final thickness is chosen to be 70 nm because the gain in absorption is lower for thicker layers. The pillar height was constrained to a maximum QD layer height of 400 nm, including residual layer, which corresponds to the thickness of many of the currently best performing devices[136]. A thicker layer would suffer from large recombination losses which makes that range less interesting for our investigation.

As Figure of Merit (FOM) we choose the enhancement of absorption per unit volume, defined as the ratio of the absorption within the QD volume of a patterned cell and the absorption in a planar cell with the same QD volume. Figure 2.2c shows the results optimized for the patterned cell and planar cell that use the same amount of QD volume. A clear enhancement in absorption is found across most of the investigated spectrum. It is largest towards the infrared range, peaking at 2.8-fold enhancement close to the bandgap and corresponds to an integrated gain of 19.5% for the spectral range considered. Overall, the spectrum shows a better IR-response due to an effectively sharper absorption onset at the bandgap energy, a mitigated dip/plateau towards the short wavelength side of the first exciton peak, as well as a more gradual increase in absorption towards the UV range, in comparison to the planar case. The difference found in the comparison of these spectra is indicative of optical enhancement beyond what one would expect from differences due to interference minima and maxima in planar solar cells.

The sharp onset of the absorption around the bandgap energy is induced by two quasi-guided modes[156–158] in the plane of the nanopatterned layer as seen from the modal field profiles at 915 nm (f) and 950 nm (g) respectively. Towards shorter wavelengths, another sharp peak (780 nm) can be identified, also related to a quasi-guided mode. The cancellation of the dip next to the first exciton peak stems from a Fabry-Perot resonance that was placed in that wavelength range by adjusting the height of the QD pillar, effectively forming a cavity. The UV range is not significantly influenced by the pattern for two reasons. Firstly, the dimensions obtained from the optimization are most ideal for the IR range, as there is more to gain and hence the FOM mainly is optimized within that range. Secondly, higher energy light is absorbed well within the first 100 nm of the QD absorber, which means that UV light does not penetrate far enough into the absorber for it to excite resonant modes in the nanostructure (Figure 2.2e).

To confirm the nature of the resonances, we first study the dependence of the resonant peak wavelength on the periodicity of the QD pillar lattice (Figure 2.2d). We find that with increasing separation of the pillars, the sharp resonances continuously shift towards longer wavelengths, which indicates that they are not a property of the QD pillar itself but a property of the pillar lattice, as determined by its periodicity (pitch). In principle, adjacent pillars can couple and exhibit collective resonances[159], but we rule these out as the sharp features do not vanish with increasing pillar-pillar separation, but only shift in wavelength. To investigate this further, we investigate the electric field

line profiles for wavelengths of interest at the cross-section through the patterned solar cell. This analysis shows that 780 nm and 950 nm (Figure 2.2e,g) peaks corresponds to quasi-waveguide modes that propagate within the complex of the structured QD-ZnO interface. Furthermore, the 915 nm peak (Figure 2.2f) corresponds to field line profiles that can be associated with surface plasmon polaritons that propagate at the QD-Au interface. While surface plasmon polaritons are lossy due to modal overlap with the metal, enough of the mode's electric field distribution resides within the absorber layer to yield a net absorption gain.

2.5. Electronic analysis

Next, we investigate how the nanostructured geometry performs electronically, by using Lumerical CHARGE, which is a drift-diffusion equation solver. We use literature data [137,139,146,160–163] for energy levels, doping density, recombination, and to account for bulk QD specific properties like hopping as charge transfer mechanism and voltage loss due to the fact that an effective conduction band slightly below the conduction band is formed by defects.

In general, for planar quantum dot solar cells, the efficiency as function of thickness peaks at an absorber thickness for which the trade-off between charge-carrier generation and extraction is at its optimum. PbS QD solar cells utilize electric field-associated drift to guide charges towards their extraction interfaces. As these electric fields only span across the depletion region within the cell, diffusion rather than drift is the dominant charge extraction mechanism for absorber layers much thicker than the depletion region. This leads to increased recombination with increasing absorber thickness.

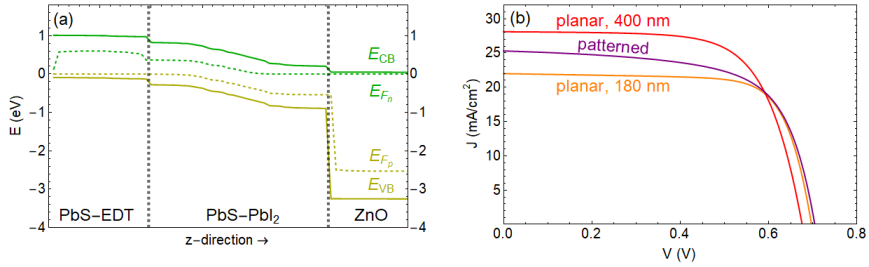

Figure 2.3: (a) Band diagram of a PbS QD solar cell (here: 180 nm absorber layer) at short-circuit current (J_{SC}) condition (V=0). From top to bottom: Conduction band (ECB), electron quasi fermi level (EFn), hole quasi fermi level (EFp), valence band (EVB). Grey dashed lines are used to distinguish between different regions in the p-i-n junction. Light incident from the right site. (b) Simulated current density (J) as function of voltage (V) for planar cells with absorber thicknesses of 180 nm (orange) and 400 nm (red), as well as a patterned absorber layer (purple).

An electronic band diagram of a planar cell with 180 nm absorber thickness is shown in Figure 2.3a (applied voltage of 0 V). The graphs can be separated into three distinct regions along the z-directions, corresponding to the p-, i-, and n-type layers. Band bending occurs across the full range of the i-type layer, and corresponds to the presence of electric fields and is typical of depleted heterojunction solar cells12. The energy offset of the p-type QD layer compared to the i-type QD layer results from the fact that dipole

moments of ligands affect the energy landscape of bulk QDs. Similar conduction and valence band profiles and offsets can be found in literature [164].

To investigate the electronic performance of the patterned QD solar cells, we show simulated current-voltage ($I-V$) curves of a patterned cell and planar cells of 180 nm and 400 nm thickness under AM1.5G illumination in Figure 2.3b. The patterned cell corresponds to the set of dimensions that we obtained from the maximization of absorption per unit volume shown in Figure 2.2c. The thin (180 nm) planar cell uses the same amount of absorber volume as the patterned cell, and the thick (400 nm) planar cell corresponds to the thickness of QD pillar and residual layer of the absorber structure in the patterned case. Interestingly, the patterned cell shows a short-circuit current (J_{sc}) that is 3.2 mA/cm^2 larger than that of the thin planar cell, and it exhibits an open-ciruit voltage (V_{oc}) that is slightly above that of the thin planar reference. The fill factor FF is decreased for the patterned case compared to the thin planar case. Overall, the efficiency increased by 0.4% to 11.6% in comparison to the thin reference (11.2%). Compared to the 400 nm planar reference, the patterned cell shows a slightly lower current (2.8 mA/cm^2), an increased V_{oc}, and a lower FF, yielding an overall lower efficiency. From these two comparisons it becomes obvious that the main obstacle for a higher efficiency of the patterned cell appears to be the FF.

We now investigate aspects of the differences in J_{sc}, V_{oc}, and FF for the three cases, by investigating profiles of charge carrier generation (Figure 2.4a-c), recombination (Figure 2.4d-f), and potential gradients (Figure 2.4g-i). The strongly enhanced J_{sc} for the patterned cell compared to the thin cell results from the fact that it absorbs light much better for the same volume due to resonant light absorption in the nanostructure. Given the QD volume of the patterned device is 45% of that of the thick reference cell (400 nm), the J_{sc} results indicate that the largely reduced volume comes with a much smaller relative difference in J_{sc} (10%). We also note that compared to the J_{sc} that is directly calculated from the absorption spectrum, the actual J_{sc} value in the patterned case is slightly lowered, by 0.8 mA/cm^2. This is due to some recombination occurring already at V=0 (see fig 4e).

The V_{oc} is similar for patterned and thin cells (704 mV and 697 mV, respectively) while in the thicker planar cell with the larger volume we find that the V_{oc} is lowered to 676 mV. The reason for this can be found in the static electric (E) fields across the absorber (Figure 2.4g-f). While the thick planar cell exhibits a maximum E-field strength (z-component) of 1.5x10^6 V/m, the thin planar cell's E-field goes up to 3.6x10^6 V/m. This means that the thin cell can effectively resist external bias up to higher values and extract charges at larger applied voltages. In the case of the patterned cell, the E-field strength is well below 1.5x10^6 V/m around the top of the pillar, but it increases significantly towards the bottom, also reaching around 3.6x10^6 V/m in the very centre, and even larger values towards the edges. We note that while we do not show simulated dark-IV curves here, their comparison leads to the same conclusions as this V_{oc} comparison.

So far, we have found that the nanopattern has two distinct advantages. First, it strongly enhances light absorption, which enables the use of less absorber material and increases the current, and second, the electric field strength is comparable to that of the thin cell, which leads to an optimized V_{oc}. At the same time, the FF of the patterned cell is strongly reduced in these simulations. To find the origin of this, we first have to

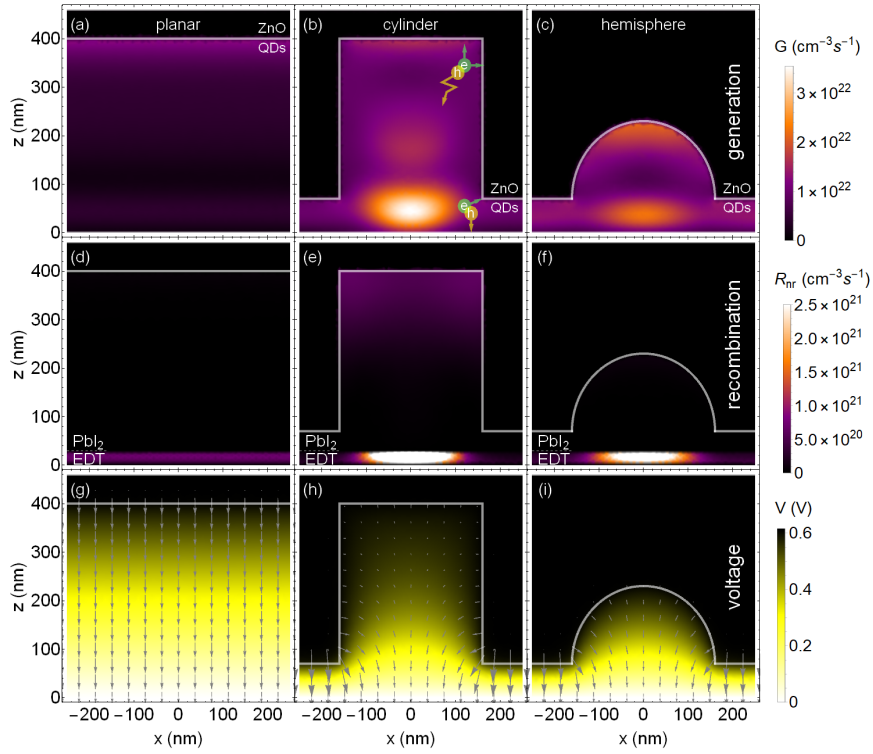

Figure 2.4: (a,b,c) Charge-carrier generation rates (G) across the cross-section of a planar QD solar cell (a) and a cell with cylindrical (b) and hemispherical nanopattern (c). The color scale shows regions with high or low generation rates. (d,e,f) Non-radiative recombination rates (Rnr) of charge carriers for the planar (d), cylindrical, and hemispherical (f) case. The interface between QD layers with different ligands is indicated by PbI_2 and EDT. (g,h,i) Electric potential across p-i-n junction for planar (g), cylindrical (h), and hemispherical (i) patterned cases. The arrows show the electric field orientation and strength. Grey lines are used to show the interface between the ZnO and PbS QDs. A schematic of characteristic electron-hole pairs is shown in (b).

consider the generation profiles shown in Figure 2.4a-c, then consider Figure 2.4d-f to evaluate the associated recombination profiles, and will then find the connection between generation and recombination by considering the potential gradients in Figure 2.4g-i.

The generation profiles in Figure 2.4a-c are derived from electric field distributions such as those shown for three selected wavelengths in Figure 2.2e-g, integrating profiles over the full wavelength range until the bandgap. For the planar case (Figure 2.4a) the generation rate gradually decreases with depth, according to the Beer-Lambert law. In the patterned cell most of the generation occurs at the bottom of the centre of the nanopillar. The hotspots in the generation profile towards the bottom of the cell correspond mostly to absorption of light close to the bandgap that creates a well-defined resonant mode. The reason why this hotspot is found so close to the Au backcontact is that close to the backcontact incident and reflected light interfere more strongly with each other. While this creates a hotspot-like shape in the patterned case, this behaviour

can also be found at the back of planar solar cells, where usually the carrier generation increases again, deviating from a classical Beer-Lambert law absorption profile. This deviation can be understood as a sum of the incident light's Beer-Lambert profile and the profile of the light reflected from the Au interface, which has highest values at the back of the cell and a decreasing exponential tail towards the front. The region of high generation at the top of the pillar corresponds to Beer-Lambert-like absorption of more energetic light.

In QD solar cells, charges that are generated in the vicinity of interfaces, within the depletion zone, have significantly higher chance of extraction, and thus do not cause losses to the J_{sc}. In the nanopatterned cell, generated electrons are on average much closer to the ZnO carrier collection interface that surrounds the nanopillars than in the case of the thick cell where carriers have to travel to the top or bottom interface. Effectively, the nanopatterned structure forms a bulk heterojunction geometry similar to that in other bulk heterojunction quantum dot (/organic, /dye-sensitized) solar cells, where tailored nanogeometries reduce the distance that charge carriers have to travel to the extraction interfaces and result in carrier generation in regions with stronger extraction fields. Furthermore, most holes are generated much closer to their extracting interface (bottom part of panel 4b) (QD EDT – QD PbI_2) than in the planar case, where most generation happens in the front. The schematic drawings of electrons (green) and holes (yellow) in Figure 2.4b indicate the required directions in which charges need to migrate.

Figure 2.4d (planar) and 4e (patterned) show where most of the non-radiative recombination occurs in the two cell types. For all cells, recombination is highest in the back, due to poor carrier mobilities in the PbS-QD EDT layer. Besides that, for the planar case recombination occurs homogeneously through the QD layer. In the patterned case, enhanced recombination occurs in the top region of the pillar, increasing radially away from the bottom centre of the pillar.

To understand why this region is exposed to so much non-radiative recombination, the internal potential distribution for the two cell types is shown in Figure 2.4g and 4h. For the planar case (Figure 2.4e), we find a gradient across the depletion region, which extends across the whole absorber. In contrast, the gradient in the patterned case is radially aligned from the ZnO interface to the base of the pillar. The top region of the pillar shows only a very small potential gradient, explaining the strong recombination in that area. This explains the origin of the low FF in the patterned cells. For increasing cell voltages, the internal field decreases, and the weak-E-field region grows in volume - from the top of the pillar downwards - and hence recombination increases strongly with applied voltage, yielding a lower collected current density (Figure 2.3). This is equivalent to stating that the depletion region narrows with applied voltage and an increasing portion of charges is generated outside the depletion region and thus not contributing to the collected current.

This behaviour can already affect the extracted current at V=0. We use the simulated absorption spectrum from optical simulations and weigh it with the AM1.5G spectrum, to obtain an upper bound for J_{sc} based on optical simulations. The ratio between this current and the current obtained from the electronic simulations yields the extraction efficiency of generated charges. Here, we define the internal quantum efficiency (IQE)

for the absorber layer only, i.e. considering only photons that are absorbed by the absorber (PbS-PbI_2, PbS-EDT), and neglecting parasitic absorption by the ITO and Au layers. The extraction efficiencies for 400 nm planar, 180 nm planar, and the patterned case are 99.5%, 97.5%, and 95.0%, respectively. This confirms the reduced extraction capabilities of the patterned structure at V=0. Furthermore, the discrepancy between 400 nm and 180 nm planar layers implies that charges generated in the PbS-EDT layer at the back (relatively more generation happening there in the 180 nm case) are more likely to be lost to recombination than to be extracted. This suggests that charge carrier generation should ideally fully happen in the PbS-PbI_2 layer, where charges can be separated more easily with the help of stronger electric fields (Figure 2.3a).

Experimentally measured $I-V$ curves (Supplementary Information) serve as further evidence regarding the subtle interplay between local fields, absorption/generation distance to the charge separating/collecting interfaces, and charge recombination. First of all, the increased J_{sc} confirms the enhanced light trapping observed in EQE measurements (Figure 2.5) and in simulations (Figure 2.2). Second, the reduced FF confirms the reduced carrier collection due to less optimal carrier extraction in the patterned case. Third, it is notable that the additional surface area does not create additional recombination as shown by the unchanged V_{oc} of the patterned cell.

In summary, the strong E-field at the pillar bottom allows for a larger V_{oc}, while the weak E-field at the top induces the low FF due to extraction losses caused by holes that do not get extracted at the bottom of the cell. This realization immediately inspires further advanced cell designs that decouple the beneficial effects of local charge generation and collection near the collection interfaces and the detrimental effect of enhanced carrier recombination in field-free regions of the cell. For example, one could consider using a hemispherical shape (Figure 2.4c,f,i) instead of the pillar feature to create optical resonances. This would avoid weak-E-field regions at the top (Figure 2.4i), whilst the light absorption per unit volume is still enhanced (Figure 2.4c). In fact, by comparing expected J_{sc} values from optical and electronic simulations, we can get an extraction efficiency of 95.9% for this initial structure guess, which is already 0.9% higher than for the cylindrical structure. With respect to absorption, such a structure might come very close to a cylinder with an aspect ratio of 1, due to the similarity of the shapes. This would essentially correspond to cutting off part of the top of the cylinder that our optical optimization yielded in Figure 2.2c. As our optical optimization found different parameters for the cylinder dimensions than for those of the hemisphere, the hemisphere would come with some absorption loss relative to the optimized cylinder.

One option to circumvent this trade-off would be the introduction of an electronically inert material in place of the top half of the cylinder. With a real part of the refractive index similar to that of the QDs, and with a negligible imaginary part, this material would deliver the same optical resonances, but with essentially all generation happening in the bottom half of the cylinder. This would solve the issue of the low FF while keeping V_{oc} and J_{sc} at similarly high values.

Another potential option to tackle the weak extraction from the top of the cylinder would be the utilization of a graded bandgap, which is a well-investigated concept for PbS QD solar cells[163]. By having a few layers of QDs with consecutively smaller bandgaps towards the top of the cylinder (the bandgap would approach the desired

overall bandgap towards the bottom), a gradient would emerge in the conduction and valence bands, due to the bandgap shrinking towards the top. This would aid with directing the diffusing carriers in the right direction. Naturally, such a structure would have a lower V_{oc}, due to the addition of QDs with slightly smaller bandgaps. But this loss might be overcome by a significantly increased FF.

In general, the observations made so far can potentially help bring the efficiency of PbS quantum dot solar cells beyond current record power conversion efficiencies. So far, one of the main goals for PbS QD solids within the scientific community has been the improvement of the charge carrier diffusion length [165]. While this is an important objective, our simulations outline an alternative road towards highly efficient solar cells. Better control over the charge carrier generation profile could potentially allow for a weakening of the constraints that are imposed by short diffusion lengths. Generating charges closely to extraction interfaces requires shorter average charge migration, and hence less susceptibility to carrier recombination. We have also shown that there is no benefit if the distribution of the electric fields is affected negatively by the structured absorber. More strongly doped p-, and n-type layers [164] could potentially help with mitigating the effect of weakened electric fields due to structuring, and lead to overall gains, if diffusion lengths in these materials are much lower than in the materials used in this study. If the diffusion length of the absorber is much longer, then the charge extraction is also improved for the patterned case. This favours shapes that strongly interact optically, as electronic constraints are alleviated. In this case, the structure is more competitive compared to thicker planar cases, as the strong optical performance is coupled with lower extraction losses. Finally, the results so far put emphasis on the role of shapes within the device architecture, and while fabrication of planar structures is in many cases easier, there is no obvious reason why the ideal solar cell geometry should consist of such a highly planar geometry.

2.6. Electronic characterization of patterned junction

Finally, we characterize the electronic performance of a patterned and planar QD solar cell by measuring the wavelength-resolved external quantum efficiency (EQE). Figure 2.5 shows a comparison between EQE and light transmitted into the cell (1-R) for thick planar and patterned cells. In the initial experiments the QD pillars have a radius of 190 nm, a height of 100 nm, a pitch of 513 nm, and the residual layer is 400 nm thick. The EQE represent the number of electrons and holes that arrive at the metal contacts and are extracted, relative to the incident photon flux. The EQE of the planar device clearly shows the first exciton peak (900 nm), as well as two Fabry-Perót cavity features (450 nm and 650 nm). For the patterned device we can identify the first exciton peak at the same wavelength, but no Fabry-Perót resonances are distinguished. A flat EQE spectrum is found for wavelengths shorter than 700 nm. Importantly, we find a considerably higher EQE towards the bandgap (950-1200 nm) for the patterned case. The reflection spectra confirm those features, except for the range around the first exciton peak.

Several conclusions can be drawn from the EQE results. First of all, the comparison of the two EQE spectra shows that the complex nanopatterning procedure to fabricate these QD bulk heterojunction cell geometry yields devices with better EQE than the planar cells, demonstrating the applicability of SCIL to fabricate good-quality devices.

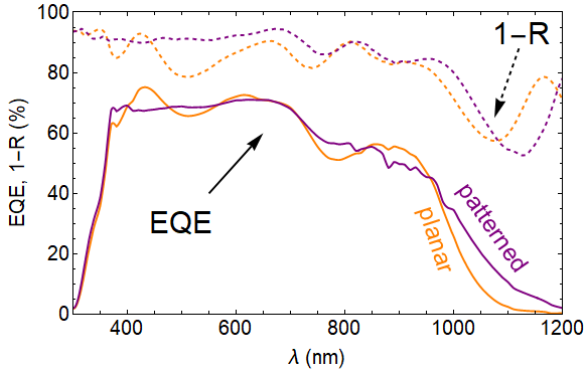

Figure 2.5: External quantum efficiency (EQE) and reflection losses (1-R) of a fabricated planar (orange) and patternd (purple) PbS QD solar cell, as a function of wavelength. Solid lines describe EQE curves and dashed lines correspond to the upper limits for the EQE, given by the cell reflection and represented by 1-R.

Secondly, the IR response (1000-1200 nm) is significantly better in the patterned case. This is indicative of longer effective path length that light experiences within the absorber layer and in good agreement with the wavelength dependent enhancement presented in Figure 2.2b, which is highest close to the bandgap, similar to the EQE measurement.

Thirdly, in both cases the EQE and reflection loss align well with each other for wavelengths below 750 nm. The gap between EQE and (1-R) curves corresponds to charges that are lost either to parasitic absorption or to extraction losses. For wavelengths around the first exciton peak, the EQE and (1-R) data have a bigger gap, indicating that the charges generated by lower energy light are extracted less efficiently. We attribute this to generation of charges in regions that are too far away from extracting interfaces. Alternatively, the light may be lost to parasitic absorption in the ITO layer.

We note that the experimental geometry used here is quite different than the optimum obtained from simulations. Notably, the pillar height (100 nm vs. 330 nm for the optimum) and residual thickness (400 nm vs. 70 nm), and further enhancements can be expected in further improved experiments.

From the reflection spectra, we derive a maximum enhanced J_{sc} gain of 2.00 mA/cm^2 for the nanopatterned cell. However, the integrated EQE spectra indicate a J_{sc} gain of 0.74 mA/cm^2 for the patterned case. The difference, 1.26 mA/cm^2, is lost by incomplete extraction or to parasitic absorption. This incomplete extraction is further confirmed by an IV-analysis (Supplementary Information), which shows that experimental planar and patterned cells suffer from a lower FF than in the simulations, associated to more strongly decreasing charge extraction with increasing voltage. Overall, the EQE shows a higher J_{sc} for the patterned case, mainly owing to mitigation of Fabry-Perót cavity related dips in the short wavelength region and a better EQE response around the bandgap (1000-1200 nm), due to effective path length enhancement for near-infrared photons.

2.7. Conclusion

Optically resonant heterojunctions can benefit the charge collection of solar cells with short carrier diffusion lengths in addition to the advantages of enhanced light incoupling and trapping. We demonstrate a nanopatterned p-n junction for a QD solar cell and present a novel method for fabrication of such structures, using soft nanoimprint. We then use optical simulations to maximize the absorption per unit volume in a QD solar cell and significantly increase absorption in comparison to a reference structure. Additionally, the optical optimization yields a charge carrier generation profile that is vastly different from the conventional Beer-Lambert law-like profile of planar cells.

The impact of such a pattern on the IV characteristics of a device is investigated in electronic simulations and indicates that such structuring allows for both improved J_{sc} and V_{oc} values. Our initial design shows a reduced FF, which is attributed to inhomogeneous electric field distribution across the absorber that leads to locally weaker charge extraction for increased voltage. For the same absorber volume, an efficiency gain of 0.4% is found in the patterned case.

Based on these insights, we suggest two pathways for further improving the efficiency by dealing with the low FF. One option entails introduction of an electronically inert material with similar optical properties as the QDs, that serves as an effective optical antenna, while the generation of charges occurs closer to the collecting contact layers. The other option would utilise a graded bandgap structure to direct diffusing charges towards the space charge region from where they can be extracted more easily.

Finally, we show experimental results for a nanopatterned heterojunction design, and find that the EQE spectrum of the patterned cell differs considerably from the planar case, corresponding to an enhanced J_{sc} of 0.74 mA/cm^2. Overall, our work shows a novel solar cell architecture that optimizes light management and charge carrier extraction. These observations are independent of the absorber material and apply also to other materials with short diffusion lengths.

2.8. Methods

2.8.1. ZnO nanoparticle synthesis

The synthesis of zinc oxide (ZnO) nanoparticles was performed according to previously published methods[151]. 2.95 g zinc acetate dihydrate ($Zn(Ac)_2$*$2H_2O$) was dissolved by 125 ml methanol at 60°C and the solution was kept stirring at 60°C. 1.48 g potassium hydroxide (KOH) was dissolved by 65 ml methanol. Then the KOH-methanol solution was added to the $Zn(Ac)_2$ solution drop-by-drop. Next, the solution was kept at 60°C and stirred for 2.5 hours. The product was precipitated by centrifugation and washed by using methanol twice. The washed ZnO nanoparticles were dissolved by 10 ml of methanol and chloroform (1:1 v/v).

2.8.2. ZnO patterning using SCIL

For the patterned ZnO NP layer, commercial glass substrates with 200 nm ITO, were cleaned by sonicating for 10 minutes each in detergent, acetone and IPA. Then, the ZnO NPs solution was dropped onto the ITO substrate and the solution was spread and thinned briefly using a spin-coater. After 3.5 s at 2000 RPM, the sample with the thin liq-

uid ZnO layer was taken out of the spin-coater and the PDMS stamp was applied onto it, to transfer the nano-pattern into the ZnO NP layer. After 6 minutes of room temperature curing, the stamp was peeled off, which concluded the patterning process.

2.8.3. PbS QD synthesis

PbS colloidal quantum dots (CQD) were synthesized according to previously published methods. Firstly, 460 mg lead (II) oxide (PbO, 99.999%, Sigma-Aldrich) was mixed with 10 ml octadecene (technical grade, Sigma-Aldrich) and 2 ml oleic acid (technical grade, Sigma-Aldrich). The solution was heated to 120 °C and degassed for 1 hour. Then the temperature was reduced to 90 °C and 5 ml octadecene solution with 140 µL hexamethyldisilathiane (TMS_2S) (synthesis grade, Sigma-Aldrich) was injected swiftly. After the injection, heating was turned off and the solution was allowed to cool to room temperature gradually. The as-synthesized CQD-solution was purified by adding acetone (VWR) before centrifugation at 6000 RPM for 5 min, followed by re-dispersing with hexane (95%, Sigma-Aldrich). This washing process was repeated twice, and the precipitate was dispersed by octane (50 mg/ml).

2.8.4. PbS QD ink preparation

PbS ink was prepared by using previously published solution ligand-exchange process [166]. 553.2 mg lead (II) iodide (PbI_2), 174.1 mg lead (II) bromide ($PbBr_2$), and 55.5 mg ammonium acetate (NH_4Ac) were dissolved by 12 ml N,N-Dimethylformamide (DMF). 7.5 ml 10 mg/ml PbS-octane solution was added into the solution. The mixture was shaken by using a vortex mixer for 5 min. The upper layer of the solution was removed. The solution was washed in octane 2-3 times. Then toluene was added into the solution followed by centrifuging at 6000 RPM for 5 min to precipitate the quantum dots. The precipitate was dried by vacuum and dispersed by butylamine. The final concentration was 300 mg/ml.

2.8.5. PbS QD spin-coating

40 µl PbS ink was applied on substrates followed by spin-coating at 1000 RPM for 3 s, and then 2000 RPM for 30 s. The film was annealed at 80°C for 2 min.

2.8.6. PbS QD-EDT layer and Au layer

Afterwards, two thin PbS QD OA layers of 15 nm each were deposited, and each was subjected to solid-state ligand exchange to obtain PbS QD EDT (ethanedithiol) layers. The backcontact was fabricated by evaporation of Au at an initial rate of 0.01 nm/s for the first 10 nm and then 0.1 nm/s to get to 100 nm final thickness.

2.8.7. Ellipsometry

The required samples were prepared by spin-coating thin layers (30-150 nm) of PbS QDs onto Si substrates. Subsequently, spectroscopic ellipsometry (SE) datasets were taken at angles of incidence of 60-80°, using a Woolam Ellipsometer. The spectra were analysed using CompleteEASE: A Cauchy model was used to obtain the thickness and refractive index of the QD layer in the infrared (IR) range where absorption is negligible. After fixing these values, the Cauchy model was replaced by a b-Spline model and initially fitted

for the non-absorbing wavelength range in the IR only. Then the fitted range was incrementally increased towards the UV, to get a first approximation of the optical constants, according to the used b-Spline model. That model was then replaced by a Gaussian oscillator model. As the inhomogenous broadening is much stronger than the homogenous broadening[167] for the first exciton peak, it is modelled by a Gaussian. The onset of the continuous, bulk PbS part of the absorption spectrum is also modelled by the tail of a Gaussian. For PbS QD films with OA ligands, a third oscillator was included as that greatly improved the fit accuracy.

2.8.8. Optical simulations: Lumerical FDTD

Except for the QD layers and the ITO layer, optical constants from the Lumerical FDTD library were used for ZnO and Au. After convergence testing, the simulation mesh accuracy was set to "5" and "conformal variant 1". Symmetric/antisymmetric boundary conditions were employed along the cell's plane and perfectly matched layers (PML) were used at the top and bottom of the simulation geometry.

2.8.9. Electronic simulations: Lumerical CHARGE

The simulation geometry was described by a triangular mesh which was sufficiently fine to accurately describe all features of the simulated device. Planar structures were simulated in 2D, patterned structures in 3D. Parameters for the p-, i-, and n-layers are listed in Table 2.1 in the supplementary information. Both contact layers were defined as Ohmic contacts with parameters specified in Table 2.2. For performance under AM1.5G solar irradiation, a charge carrier generation profile was imported from Lumerical FDTD, using the dedicated "Solar Generation" function. To obtain an $I-V$-curve, the simulation geometry is evaluated separately for a range of voltage values across the relevant voltage range. For simplicity, recombination processes that have not received much attention in recent years (interface recombination of PbS QDs and ZnO) have not been included in the simulations. Depending on the interface structure/roughness, this might lead to minor gains or losses in the overall performance[168], but the literature does not provide reliable values that could be used in the simulations.

2.8.10. *EQE* and reflection measurements

We used a PV Measurements QEX7 system for the *EQE* measurements. The spot size of the incident light beam was 1 mm x 4 mm and smaller than the contact area, which is necessary to not loose charges generated in non-active areas. In parallel, we measured reflection spectra for the same samples, with a PerkinElmer1050 tool. The samples were fixated at the backside of an integrating sphere, and the reflection spectrum was collected for an angle of incidence of 8°, to include specular reflection. For this step, Au was evaporated over the full backside area of the cell.

2.9. Supporting information

2.9.1. Current-voltage curves of fabricated samples

Figure 2.6 shows a current density - voltage ($J-V$) curve comparison between fabricated planar and patterned PbS QD solar cells under 1-sun AM1.5G illumination. The pattern

Table 2.1: List of parameters [137,139,146,160–163] used for the semiconductors in the 3D drift-diffusion simulations in Lumerical CHARGE.

Quantity	Unit	ZnO	PbS-PbI2	PbS-EDT
DC permittivity		66	20	20
Work function	eV	5.95	4.7	4.55
High symmetry point at the conduction band minimum		Γ	Γ	Γ
Effective electron mass	$1/m_e$	0.24	0.54	0.54
Effective hole mass	$1/m_e$	0.59	0.54	0.54
Bandgap	eV	3.3	1.1	1.1
Electron mobility	$cm^2/(Vs)$	100	0.02	0.0002
Hole mobility	$cm^2/(Vs)$	25	0.02	0.0002
Non-radiative electron lifetime	s	$1.0x10^{-9}$	$2.4x10^{-7}$	$2.4x10^{-7}$
Non-radiative hole lifetime	s	$1.0x10^{-9}$	$2.4x10^{-7}$	$2.4x10^{-7}$
Trap state energy level offset	eV	1.1	0.4	0.4
Optical capture rate coefficient	cm^3/s	-	$5x10^{-13}$	$5x10^{-13}$
Donor doping density	cm^{-3}	10^{18}	10^{15}	10^{14}
Acceptor doping density	cm^{-3}	0	10^{15}	10^{17}

Table 2.2: List of parameters [137,139,146,160–163] used for the semiconductor-metal interfaces in the 3D drift-diffusion simulations in Lumerical CHARGE.

Quantity	Label in software	Unit	Au-PbSEDT interface	ITO-ZnO interface
Metal workfunction	Workfunction	eV	5.1	4.7
Interface recombination velocity	SRV	cm/s	$1.0x10^9$	$1.0x10^9$

dimensions are the same as stated in the main manuscript (section: Electronic Characterization of the Patterned Junction), and the fabrication details can be found in the Methods section. Different solar cells were fabricated for the light-$J-V$ measurements than for the EQE characterization, as $J-V$ measurements require smaller Au backcontacts (100-nm-thick Au disks with 1 mm radius), to minimize the impact of fabrication defects on the electronic properties. Both cells originate from the same batch, and every cell contains 9 subcells with distinct backcontacts.

The trends for short-circuit density (J_{sc}), open-circuit voltage (V_{oc}), fill factor FF, and efficiency (η) observed in Figure 2.6 correspond well with the trends predicted by simulations (Figure 2.3b). The J_{sc} is increased significantly. The average V_{oc} shows a slight gain within the error bar range. The FF is reduced in the patterned case. The efficiency shows a slight gain within the error bar range. We note that the observed trends are sometimes confined to the error bar range.

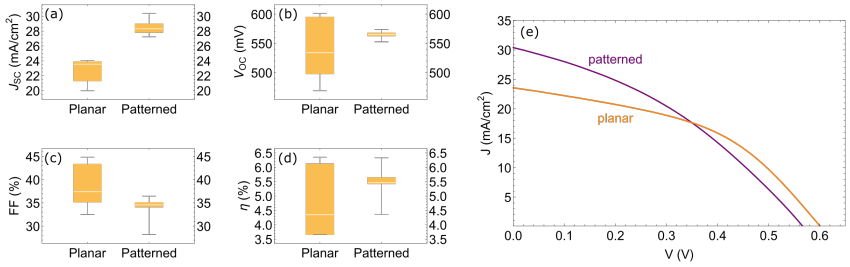

Figure 2.6: Left: Box-plot diagrams of short-circuit current density (J_{sc}), open-circuit voltage (V_{oc}), fill factor FF and efficiency (η) of a planar and a patterned solar cell. Each cell contains 9 subcells. Right: $J-V$-curves of the best planar (orange) and patterned (purple) subcell.

Furthermore, the planar reference cell exhibits a fairly low FF. To investigate the quality of the baseline and the degree to which the data shown in Figure 2.6 is representative, we fabricated a separate batch of planar samples (Figure 2.7). This batch was fabricated after the batch that yielded the comparison between planar and patterned samples, and shows improved electronic parameters. However, we expect that the conclusions on the sample-to-sample variation are equally valid.

The investigation of the baseline shows that the difference in the electronic parameters from cell-to-cell can be larger than the error bars that are derived from individual subcells. One reason for this is that the Au backcontact area is associated with an error of up to 20% for the Au disk radius, due to variations in evaporation mask procedure . This affects the J_{sc} as it is calculated by normalising the measured current to the backcontact area. Furthermore, it was difficult to control the quality and deposition conditions (air flow) of the PbS QD ink precisely, which affected the electronic quality of the cells.

The difference in J_{sc} in the patterned-planar comparison (Figure 2.6) is larger than the baseline sample to sample variation observed in Figure 2.7. The differences in V_{oc} and FF in the patterned-planar comparison are within the baseline sample-to-sample variation observed in Figure 2.7. This suggests that the impact of the patterned structure on the electronic properties (V_{oc}, FF) is not very detrimental. Finally, the efficiency

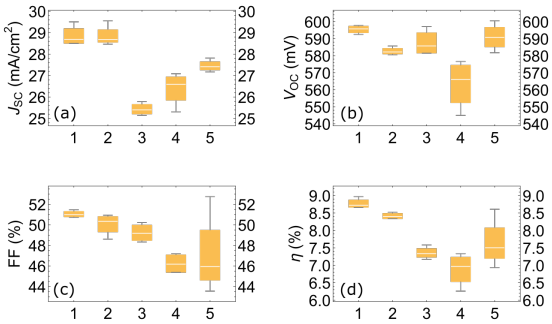

Figure 2.7: Box-plot diagrams of short-circuit current density (J_{sc}), open-circuit voltage (V_{oc}), fill factor FF and efficiency (η) of five planar solar cells from a single fabrication batch. The numbers on the x-axis denote different cells, with 9 subcells each.

statistics do not allow for identifying a superior geometry, but do confirm that the realisation of a nanopatterned p-n junction yields properly functioning electronic devices.

2.10. Acknowledgements

SWT thanks Dimitry Lamers for valuable discussions and technical support. This work is part of the research program of the Dutch Research Council (NWO). The authors acknowledge the facilities and scientific and technical assistance of the UNSW-Node of the Australian National Fabrication Facility (ANFF). The authors acknowledge the facilities and the scientific and technical assistance of Microscopy Australia at the Electron Microscope Unit (EMU) within the Mark Wainwright Analytical Centre (MWAC) at UNSW Sydney. This work is also supported by the Australian Renewable Energy Agency (ARENA) via their Collaboration Grant Funding.

2.11. Author contributions

S.W. Tabernig performed the optical and electronic simulations and characterization, and fabricated the nanopatterned layer. L. Yuan contributed to the electronic characterization. L.Y., Z.L. Teh, and Y. Gao fabricated the absorber layer. S.W.T., A. Cordaro, and A.Polman interpreted/analyzed the optical data. S.W.T., A.C., A.Pusch, and A.P. interpreted the electronic data. R. Patterson gave feedback on the fabrication. S. Huang and A.P. supervised the project. S.W.T., L.Y., A.Pu., S.H., and A.P. wrote the paper and gave feedback.

3

Avoiding shading losses in concentrator photovoltaics using a soft-imprinted cloaking geometry

3.1. Abstract

Shading losses are a longstanding obstacle in photovoltaic devices, particularly in concentrator photovoltaics where the trade-off between shading and resistive losses limits the concentration at which the highest power conversion efficiency is achieved to values far below the capabilities of concentrator optics. Here we demonstrate a simple and scalable fabrication method that enables large front metal coverage, while keeping shading losses to a minimum. Soft-imprint lithography is used to create trenches in a transparent polymer above the metal contacts, enabling cloaking via refraction at a range of angles near normal incidence. Using optical characterization techniques, we first confirm that the metal contacts are indeed optically cloaked. We then demonstrate an increase in short-circuit current density from 29.95 mA/cm^2 to 39.12 mA/cm^2 for a Si solar cell with 25% front metal coverage before and after patterning, respectively. We investigate the angular performance of the trench pattern and further demonstrate how such a cloaking strategy could be implemented in concentrator photovoltaics to enable efficiency peaks at concentrations beyond 1000 suns.

3.2. Introduction

In recent years electricity generation from mainstream photovoltaic (PV) technologies, dominated by rooftop solar and utility scale solar plants, has established itself as one of the cheapest sources of electricity [169], considerably cheaper than alternative non-renewable energy sources (coal, gas, nuclear) [170]. Aided by this, formerly niche applications of PV such as building-integrated PV [80,124,125], vehicle-integrated PV [126], and space PV [171–173] have also experienced considerable growth in recent years. Besides these, concentrator photovoltaics (CPV) [174] remains promising for utility scale power generation, as its Levelized Cost of Electricity (*LCOE*) [175] is predicted to drop rapidly and may soon reach the *LCOE* of conventional PV in high-irradiation regions [176].

While CPV requires more elaborate infrastructure than conventional PV, it offers a range of benefits. Firstly, the fundamental detailed balance efficiency limit is significantly higher, due to a logarithmic gain in open-circuit voltage (V_{oc}) as a function of the concentration factor [89]. So far, the current world record for CPV is 47.1% (143 suns), which is 7.9% absolute above the 1-sun efficiency of the same device [177]. This is also 7.6% higher than the currently best performing non-concentrator solar cell (39.5%) [178]. Secondly, CPV requires much less active solar cell area as it employs concentrator optics to focus light onto a small cell area. Thus, with increasing concentration the cost of the cell becomes less significant compared to the cost of the overall system. This allows for large-scale implementation of solar cells that are based on highly efficient albeit expensive technologies such as III-V solar cells. Furthermore, CPV can be combined with solar thermal concentrator/storage architectures [179] to make more efficient use of sub-bandgap infrared radiation, and thus increase the overall system efficiency beyond the efficiency of the CPV sub-system alone.

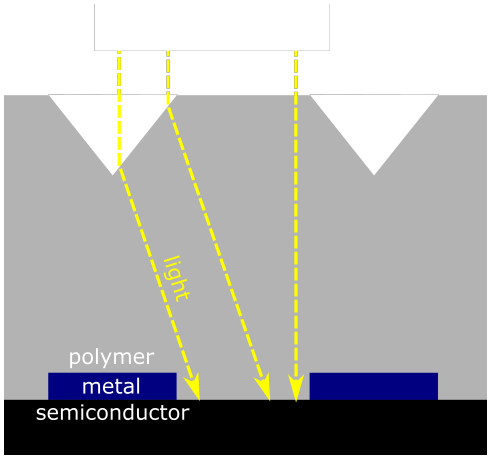

Figure 3.1: Schematic representation of refractive contact cloaking (not to scale). Normal incident light is refracted by triangular polymer trenches onto the underlying semiconductor absorber and away from the metal contacts.

The concentration factors at which the highest efficiencies are achieved are currently

limited to values on the order of one hundred [177,178]. For higher concentration, the efficiency decreases due to a rise in resistive losses which scale quadratically with the current density in the front metal contact grid [180]. To counteract this, the front metal grid coverage is often in the range of 10-15% for concentrator solar cells [181], compared to only 4% for conventional solar cells [181]. While this improves extraction, it also increases the optical shading of the solar cell, resulting in exchanging one loss against another. Hence, the final CPV front contact grid designs are usually derived from a trade-off between shading losses and resistive losses, with efforts to push the highest efficiency region to a concentration closer to 1000 suns requiring avoiding this trade-off.

This work proposes a strategy to overcome this trade-off by making the front metal grid invisible to the incident light. We achieve this by coating a transparent, UV-curable polymer onto the front of a solar cell and subsequently patterning it. Following geometric optics, the patterned structures redirect light onto the semiconductor absorber and away from the metal grid, and thus eliminate the effect of shading to increase the short-circuit current density (J_{sc}). The angular optical performance of the new design enables concentration values of well above 1000. We therefore demonstrate a path towards 1000-fold concentration for a front metal coverage of 25%, with low shading losses of only 1.8%.

Similar approaches towards effectively transparent contacts have been attempted in the past, but they either rely on a more complex fabrication procedure [182–185], are difficult to upscale [184], or involve potentially parasitic reflection from metals [183,186–189]. While a few [182–184] have looked into the dependence on the illumination angle, the overall shading as a consequence of concentration geometry and angular performance has only been discussed for one of these approaches [188,189]. While the different approaches used in these studies yield different angular dependencies of the external quantum efficiency (EQE), we find that the best devices lie within the same range as our device at normal incidence, although our device has the highest front metal coverage reported.

3.3. Design

Figure 3.1 shows the general design of the proposed structure. The underlying semiconductor absorber, along with the front metal grid, are covered by a transparent polymer that contains triangular trenches aligned with the metal contacts. The light that would reach the metal contacts in a planar structure now is refracted towards the midpoint between the contacts and thus reaches the semiconductor absorber. This requires a certain refractive index contrast between air and the polymer, adding a loss channel due to reflection. However, a glass(/polymer)-air interface is standard for any solar cell that is embedded in a module, and the proposed layer structure should thus be seen as the first piece of the solar module, instead of the solar cell alone.

While multiple patterns of lines of various widths and pitches were investigated, a fixed width (10 µm) and pitch (40 µm) form the core of this study, which corresponds to 25% shading. We note that to achieve this 25% metal coverage we have already fixed a range of parameters for our final structure. The last remaining free parameter, the separation between the top of the metal contacts and the bottom of the polymer trenches (d), is chosen such that the light refracted at the bottom of the trench misses the contact and that the light refracted at the top of the trench does not hit a neighboring contact.

All dimensions and relevant parameters are summarized in the appendix in Figure 3.8 and Table 3.1.

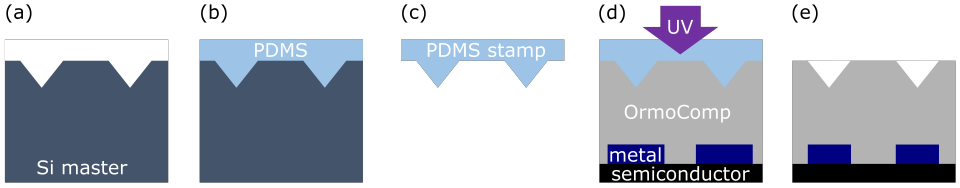

Figure 3.2: Main fabrication steps towards a solar cell with the patterned polymer on top. Polymer in gray, metal contacts in yellow, and absorber layer in black. (a) Wet-etching of trenches into a Si wafer with KOH to get the Si master. (b) Filling up of the trenches with PDMS to form the pattern for the PDMS stamp. (c) Peeling-off of the PDMS stamp from the Si master. (d) Si solar cell covered with OrmoComp (liquid polymer), stamp in contact with OrmoComp and aligned with the metal grid. Subsequent UV-exposure hardens the polymer. (e) Final patterned sample after separation from the PDMS-stamp.

3.4. Fabrication

Substrate conformal soft-imprint lithography (SCIL [107]) in combination with a UV-curing transparent polymer (OrmoComp [190]) was used to create the refractive layer. This entails the fabrication of a Si wafer that contains the pattern for the polymer (master wafer), a PDMS-mold (stamp), and subsequent patterning of the actual sample (Figure 3.2). The master wafer was made from a (100) Si wafer and patterned via KOH-wet-etching (Figure 3.2a). The anisotropic nature of KOH-wet-etching results in an exposure of the (111) facet, which is at an angle of 54.74° towards the (100) facet. By masking the Si wafer appropriately, triangular trenches inside the Si (Figure 3.2b) were created and subsequently filled with PDMS.

The hardened PDMS was peeled off and became the stamp pattern for the sample fabrication (Figure 3.2c). To transfer the pattern onto the samples, we combined SCIL and UV-lithography by using the transparent PDMS stamp. The stamp was brought into contact with the liquid OrmoComp polymer and aligned with the metal contacts (Figure 3.2d). Subsequent UV exposure and stamp removal yielded the finished sample (Figure 3.2e). We refer to the methods section (Appendix) for more details on the complete fabrication sequence.

Figure 3.3a shows a detailed scheme of the master wafer fabrication. These steps yield a Si wafer with a grooved pattern as shown in Figure 3.3b-d. The trenches are visible at the top of the wafer and the edges appear clean. The top edge appears to have some residue, which most likely comes from the cleaving of the sample that was necessary to obtain a cross-section image. Thin lines are visible inside the trenches, corresponding to steps in the (111) Si plane, commonly observed during Si KOH-etching. Those step features are negligible as they will not affect the intended light refraction. The region imaged in the SEM is one of many fields of varying dimensions that we introduced onto the Si surface to test the stamp fabrication process. The different fields can be seen as separated squares on the PDMS stamp, as shown in Figure 3.3e.

The first step of the sample fabrication entails deposition of a polymer spacer layer

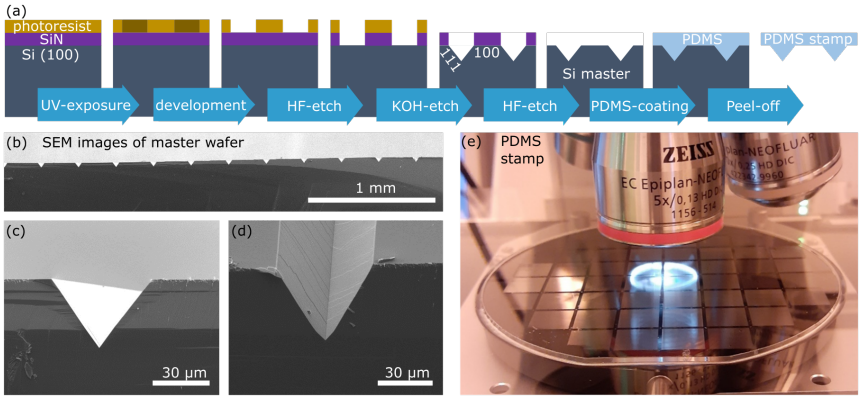

Figure 3.3: (a) Detailed scheme of the required fabrication steps for a Si master wafer. PDMS in light blue. The photoresist-SiN_x-Si(100) structure experiences masked UV-exposure, development, HF-etching of SiN_x, photoresist removal, KOH-etching of Si, SiN_x-removal via HF-etching, PDMS coating, and PDMS peel-off to obtain the stamp. (b) SEM cross-sectional image of Si master. (c) Close-up of cross-section of a single trench. (d) 45°-view of trench. (e) Photo of the finished PDMS stamp under a microscope objective. The different squares are 1 cm^2 in size and contain trenches of various widths and pitches. Note: SEM images in (b,c,d) were taken on a test field with larger pitch and trench width than used for the sample fabrication later on.

on top of the sample/solar cell. This introduces the required metal-trench separation (d). Then, the planar polymer layer is covered with the polymer layer that is to be patterned. For the patterning, one of the stamp fields was selected and brought into contact with the liquid polymer and the sample. The contacts and trenches are aligned by minimizing Moiré interference and sample brightness via rotation and translation of the samples. This is followed by UV-exposure and stamp-sample separation, to obtain the final samples. More details can be found in the methods section (Appendix).

The patterned samples were first investigated with SEM and optical microscopy. Figure 3.4a shows an SEM cross-section image of a sample with metal contacts and the patterned polymer on top. The interface between the first and second polymer layers cannot be distinguished, indicating that no interface defects such as voids were generated. Furthermore, the polymer was coated conformally around the metal contacts despite the roughness of the evaporated contacts.

In Figure 3.4b we can see an optical microscope image that shows that the metal contacts are indeed cloaked by refraction by the polymer pattern. This is highlighted by the air bubble defect in the image. The metal (Au) finger is clearly visible there, as an air bubble replaced the polymer during the imprint and exposure stage. We note that Au contacts were used for samples intended for optical characterization, while we used Al contacts for solar cells. Across the rest of the sample, two dark lines are seen on each side of the trench walls of the cloaked metal contacts. The lower intensity compared to the flat section is due to the difference in backscattered light depending on whether light

hits the trench or the flat surface. The light that hits the planar regions experiences an ordinary reflection either at the polymer surface or at the semiconductor surface while light that reaches the trenched region is refracted onto the semiconductor and can only couple out via a planar surface as it is totally internally reflected by the trench walls.

The elimination of shading can also be observed by naked eye. Figure 3.4c and Figure 3.4d show a Si cell with a planar and a patterned polymer layer, respectively. Since the pattern directs light away from the metal and onto the absorber, the reflection of the sample is reduced, making it appear dark blue, due to the anti-reflection coating (on top of the Si cell). Air bubble defects can also be observed for both samples. These can arise when the PDMS stamp is brought into contact with the liquid polymer before UV-exposure and translate into imperfectly uniform polymer coverage. This effect can be avoided if the SCIL process is further optimized for large throughput processing.

Note that from the master fabrication to the finished patterned solar cell, we mainly used well-established scalable processes and materials. Furthermore, the most crucial step, the trench-contact alignment, can be done by minimization of reflection by naked eye. For large scale applications, automated reflection intensity monitors can optimize for minimum reflection. Additionally, the feature resolution limit for SCIL is 6 nm [107], well below the resolution requirements for the refractive trenches discussed in this work. One potential bottleneck could be the use of OrmoComp (relatively expensive) as the polymer on a large scale, though this material might be replaced by a range of other, less expensive UV-curing transparent polymers. PMMA is such an interesting candidate for replacement of the polymer, provided cross-linking molecules that allow for PMMA as a negative UV-resist are used [191].

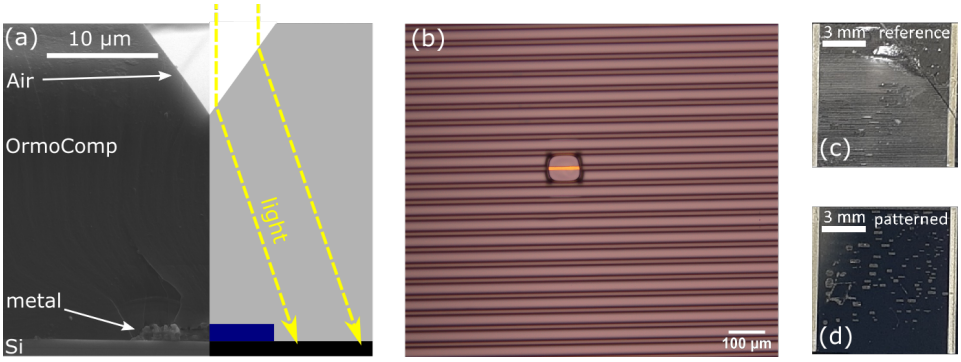

Figure 3.4: SEM and microscope characterization of patterned samples. (a) Direct comparison between a cross-sectional SEM image of the fabricated geometry and schematic design from Figure 3.1. (b) Optical microscope image of the top view of a patterned sample with an air bubble defect. (c) Photo of metal (Al) covered Si solar cells with planar polymer on top. Top right: Crack through cell from fabrication. Centre: air bubble defects. (d) Photo of cell from same batch but with patterned polymer on top. Air bubbles appear grey.

3.5. Optical characterization

To investigate the optical performance of the transparent polymer layer, transparent quartz samples with Au grids and the patterned polymer on top were fabricated. Addi-

tionally, two reference samples were used, the first consisting of a quartz sample, with a metal grid, and a planar polymer. The second consisting of a pure quartz sample. These references represent the best (100% transparency) and worst (0% transparency) case that a patterned sample can attain in our comparison. The transparency describes the fraction of incident light that is refracted away from the metal. Note that the reference for the best case (100% transparency) is a bare quartz sample that does not include a planar polymer layer on top, as this corresponds to a comparison of the sample before and after deposition of our structure.

To assess the quality of the transparency (Q_T) under normal incidence, we use integrating sphere (IS) measurements to measure the reflection of the sample (Figure 3.5a). Then we use the measured absorption of the sample combined with the known spectral dependence of parasitic absorption by Au to assess the angular performance of our fabricated samples (Figure 3.5b-d). Additional data for reflection, resolved for different reflection angles, can be found in the Appendix (Figure 3.11).

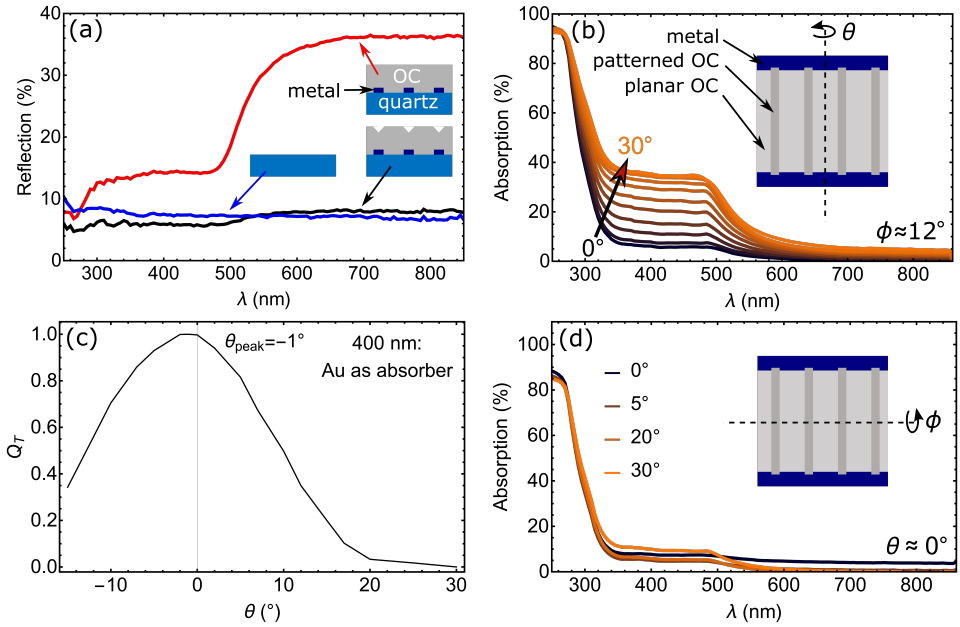

Figure 3.5: Optical characterization of patterned samples. (a) Comparison of total reflection between a patterned quartz sample with Au grid (black), a planar sample with Au grid (red) and a bare quartz sample (blue). In this case, the metal (Au) coverage was 30%. (b) Total absorption by the patterned quartz + Au-finger sample for a range of AOI (θ). The inset drawing shows the rotation axis (parallel to contacts). These measurements were conducted with ϕ <12°. The change in graph color from black towards orange corresponds to an increase in angle from 0° (black) to 30° (orange). (c) Change in quality of the transparency (Q_T) as function of angle θ at 400 nm wavelength. (d) Total absorption by the patterned quartz + Au-finger sample for various AOI (ϕ). The inset drawing shows the rotation axis (perpendicular to contacts).

The reflection (R) was measured with the samples mounted at the back of the IS, opposite to the inlet port. To get an adequate comparison between the different samples, performance values were derived from the range between 700 nm to 800 nm, for which

all materials on the samples are either good reflectors (Au), or non-absorbing (OrmoComp, quartz). Figure 3.5a shows the comparison between the two references and the patterned quartz sample. The reflection of the patterned sample ($R_{patterned}$) is similar to that of the fully transparent quartz reference (R_{quartz}). For wavelengths shorter than 550 nm the patterned cell shows even lower reflection than the quartz sample. This is due to a decrease in reflection and an increase in absorption of Au in that range. The same trend is much stronger for the sample with a planar polymer coating (R_{planar}). Further towards the UV range, below 365 nm, the polymer strongly absorbs, leading to a dip in reflection for the two polymer-coated samples (see SI for optical data). Considering all this, the range between 700 nm and 800 nm is the most appropriate range for the quantification of the transparency of the patterned sample, as Au is an almost perfect reflector in that range. This yields Q_T = 95.2%, calculated using the expression

$$Q_T(\lambda) = \frac{R_{planar}(\lambda) - R_{patterned}(\lambda)}{R_{planar}(\lambda) - R_{quartz}(\lambda)} \tag{3.1}$$

An analogous set of measurements was conducted with the samples in the transmission configuration of the IS, and the corresponding analysis can be found in the appendix.

As in a solar concentrating geometry sunlight will hit the solar cell at a range of angles, the full angular performance of the structure was investigated as shown in Figure 3.5b-d. The IS measurements were performed with samples mounted in the center of the sphere. The light that was collected in this measurement mode corresponds to the sum of reflected light (R) and transmitted light (T) for all angles. From this we deduced the absorption of the measured sample, using $A = 1 - R - T$. As the investigated sample contained quartz (absorbing below 200 nm), OrmoComp (absorbing below 365 nm), and Au (strongly absorbing below 550 nm), we used this measurement mode to determine parasitic absorption within the Au layer, by investigating the range between 365 nm and 550 nm. Furthermore, the sample was slightly (>12°) tilted along ϕ (the rotation axis perpendicular to the Au contacts) to prevent the specular reflection from escaping through the inlet for small sample rotation angles of θ<12°.

Figure 3.5b shows the parasitic absorption by the Au grid for rotations around the rotation axis parallel to the Au contacts (θ) in the range 0°<θ<30°. Rotation around this axis changes the optical paths such that light is directed onto the Au contacts, thus reducing the beneficial effect of the trenches. The data shows that the absorption in the system increases gradually with increasing angle θ and saturates towards θ=30°. Between 365 and 550 nm, the absorption is dominated by the increased absorption in Au in this range, and for wavelengths shorter than 365 nm the polymer also contributes. Note that the absorption saturates at a value that corresponds well with the Au coverage and it shows a wavelength dependence that agrees well with the optical constants of Au.
Figure 3.5c summarizes the data from 5b by calculating the dependence of Q_T on θ from the absorption values (A) taken at 400 nm. With the best performance at $\theta = 0$ deg and worst performance at $\theta = \theta_{max}$, we can calculate $Q_T(\theta)$ from (3.2), for λ=400 nm.

$$Q_T(\theta) = Q_T(0)\frac{A(\theta_{max}) - A(\theta)}{A(\theta_{max}) - A(0)} \tag{3.2}$$

Figure 3.5c also includes data measured for the rotation in the opposite direction. From the peak position, it becomes apparent that there was a slight offset of 1° from the alignment of the sample in the IS. In general, the data shows that the transparency vanishes at incoming angles θ larger than 20°. However, there is a plateau of high transparency for small angles as the trench width is wider than the Au width. This tolerance to rotation along θ can be improved if the trenches are made even wider relative to the contacts. In a first approximation, which neglects the impact of extended trenches with regards to refraction onto adjacent contacts, a 40% wider trench compared to the contact width would cause the plateau to extend to θ=5° (see Appendix, for an analysis of the influence of the trench width relative to the contact width).

Finally, Figure 3.5d shows the absorption with respect to rotation around ϕ. For rotation along ϕ, the absorption by the Au contacts does not increase towards larger angles. Since the trenches run perpendicular to this rotation direction, no significant degradation in performance as a function of angle of incidence (AOI) is expected up to the Brewster angle. That the absorption at ϕ=0° appears slightly higher is due to the fact that θ was also set to 0° and hence the specular reflection was lost through the entrance and not collected by the IS.

3.6. Electronic characterization

So far, the optical data suggest that shading was eliminated almost entirely for the investigated samples at small AOI. To confirm that this also translates into stronger light absorption in a solar cell we compared the external quantum efficiency (EQE) of cells before and after deposition of the transparent polymer. The samples used were textured silicon solar cells with a SiN_x antireflection coating and a 25% Al metal coverage (see methods in Appendix for fabrication details). While the intended application of the patterned polymer coating is on top of III-V concentrator solar cells, Si solar cells serve as a relevant platform for an investigation of the improvements in EQE due to contact cloaking.

Figure 3.6 shows the improvement of the normal incidence EQE due to the introduction and patterning of the polymer. The EQE measurement sampled an accurate ratio of metal contacts and absorber regions to represent the metal coverage of 25%. The data for a sample without the polymer and with the patterned polymer were measured on the same sample, the data for the sample with the planar polymer layer was obtained from a different sample of the same batch.

We can see how the EQE increases just by introduction of the planar polymer layer. The reason for this is that this extra layer has a refractive index (n=1.564) between that of Si and air, and hence lowers the overall sample reflection. Furthermore, as the cell has a pyramidal texture on top, the polymer also acts as a trapping layer for light that is scattered into shallow angles from the Si absorber or the Al contacts. The drop in EQE below 365 nm is related to the absorption of the polymer. Furthermore, the gradual decrease in the EQE improvement compared to the reference that occurs below 700 nm is possibly associated to increased absorption in the metal grid from enhanced light trapping.

The EQE of the patterned sample peaks at 95.0%. To get a value for Q_T we use equation (3.8) and first take into account that a fraction of 70% of the patterned sample's polymer surface is planar, and that the loss from a planar OrmoComp reflection is

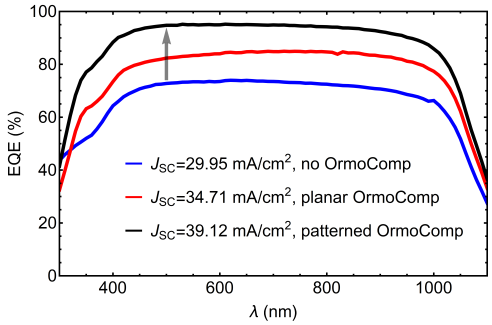

Figure 3.6: External quantum efficiency (EQE) as function of wavelength. Curves shown for Si solar cells with front Al-grid, pyramidal texture and SiN_x antireflection-coating. Performance of bare cell (blue) improves significantly after deposition of planar polymer (red) and makes another jump with the patterned polymer (black). The grey arrow indicates the fabrication order.

3.4%. The reflection of light scattered out by reflecting off two trench walls, taking into account the reflection angle of first (54.7°,R_1=7.9%) and second (15.8°,R_2=4.9%) reflection, contributes to the overall reflection by (7.9%)*(4.9%)*0.3=0.1%. The remaining 1.5% EQE loss can be attributed to fabrication defects associated with the polymer trenches and could be avoided by using further optimized patterning procedures and tools. This means that the shading was reduced to from 25% to 1.5% and we can calculate the quality of the transparency in the electronic experiments to be Q_T=1-0.015/0.25=0.94.

We have derived Q_T for planar samples in optical (95.2%) and textured samples in electronic (94.0%) experiments, as well as established the angular dependence of Q_T. The difference between these Q_T values can partially be explained by a difference in spot size and shape in optical and electronic measurements. Furthermore, different samples were used in the two experiments, so a sample-to-sample deviation is also possible.

3.7. Prospective performance in a concentrator setup

Using the results obtained in the previous section, we can estimate the level of solar concentration at which the cloaking trenches perform as desired. Assuming negligible influence from variation in ϕ, the effective shading (S_{eff}) can be calculated by integrating $Q_T(\theta)$ over a chosen θ range. The derivation of (3.3) can be found in the Appendix.

$$S_{eff}(\theta) = S\left(1 - \frac{1}{sin(\theta)}\int_0^{\theta} Q_T(\theta')cos(\theta')d\theta'\right) \tag{3.3}$$

Figure 3.7a shows the maximum concentration that we can achieve depending on the concentration pattern (Figure 3.7b,c). The Brewster angle of the polymer is 57.4°, which marks the upper limit for ϕ such that increased reflection does not lower the performance of the cell. We can see that small θ angles can be sufficient to reach 1000 suns concentration, if a large angular range along ϕ is concentrated onto the cell. In fact, for full exhaustion of the Brewster-limited ϕ-range, a θ-range of up to 2° is already sufficient to reach 1000-fold concentration (Figure 3.7b). Combining this with the analysis of the angular performance shown in Figure 3.5c, we get an effective shading of 1.8% for this

choice of angles. Furthermore, we show that if one were to increase both angles at the same rate, to get a circular concentration pattern (Figure 3.7c), 1000-fold concentration could only be reached at S_{eff} beyond 5.0%. The second y-axis in Figure 3.7a outlines the potential absolute efficiency gain that one could expect for a single-junction GaAs solar cell, according to the detailed balance limit (see Appendix for the calculation). These gains would be even larger if calculated for the current world record 6-junction solar cell[177].

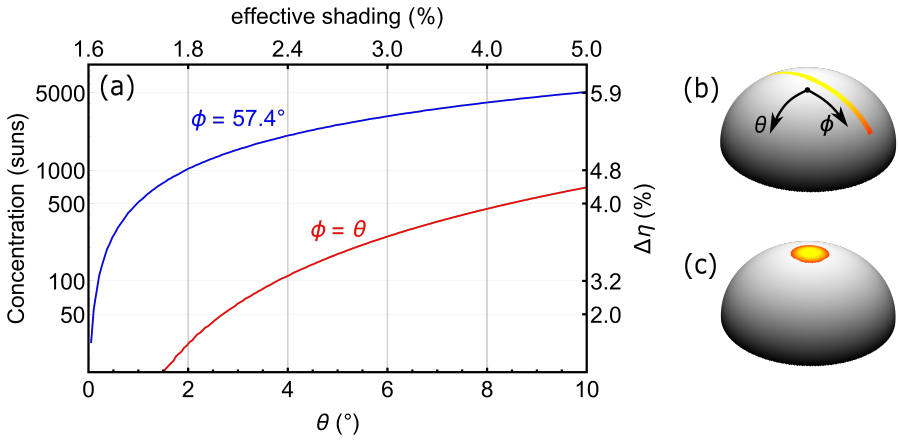

Figure 3.7: Prospects for integration into a CPV setup. (a) Achievable concentrations as a function of the limiting angle θ, plotted for values of $\phi = 57.4°$ (blue) and for $\phi = \theta$ (red). The total effective shading associated to a given maximum angle θ is shown along the top x-axis. The right y-axis shows the calculated absolute efficiency gain for a given concentration. (b) Illustration of the concentration pattern for 1000 suns at $\phi = 57.4°$ and $\theta = 2°$. The yellow-to-red color gradient corresponds to the deviation from 0° incidence. (c) Illustration of the concentration pattern for 1000 suns with $\phi = \theta$.

We show the visualization of the concentration pattern necessary for 1000 suns at the lowest possible S_{eff} in Figure 3.7b. The solar cell sits in the center of the hemisphere and is exposed to light across that hemisphere. Instead of the sun occupying only a small area of the hemisphere, we see the extend of the solid angle that 1000 suns require on a hemispherical surface. In this case, the area is shaped such that it is limited by the Brewster angle (57.4°) in ϕ direction and by 2° along θ. This slice of the hemisphere surface minimizes the effective shading and hence would lead to the best possible performance for a cell with the transparent contact design we propose. Figure 3.7c visualizes what 1000 suns concentration look like for a circular concentration pattern, and it becomes obvious that this extends much further into the unfavorable θ direction. The concentration pattern shown in Figure 3.7b can be achieved using a trough concentrator[192,193] whereby light is focused along one direction only and hence corresponds to 1 sun along θ such that concentration along ϕ would allow for 252-fold concentration. Higher concentration can be achieved by also focusing light along θ to achieve the proposed concentration pattern for 1000 suns. At this point it should be noted that another important aspect is the stability of the used polymer under such large concentrations, in terms of

heat and UV exposure. This should be investigated prior to the experimental demonstration of such cells under concentrated sunlight.

3.8. Conclusions

In this work we have demonstrated a path towards the reduction of shading losses in solar cells, with a focus on allowing for much higher front contact coverage, that can minimize resistive losses in concentrator solar cells. We discussed the full fabrication procedure, optical properties, and electronic output for a V-groove polymer coating geometry that cloaks the metal contacts on a solar cell.

SEM images showed good agreement with design and optical images indicate that the patterned polymer cloaks the metal contacts effectively. This was further confirmed by optical characterization of quartz samples with Au grids that were made effectively transparent. From this, we derive the first estimate for the quality factor Q_T to be 95.2%.

We also investigated the performance under varying angles of incidence and find that Q_T only decreases by rotation around the axis that is parallel to the metal contacts (θ). Rotation around the axis that is normal to the metal contacts (ϕ) does not affect Q_T.

Electronic measurements show that the shading loss of the EQE from a dense metal grid can be recovered almost completely. The electronic data also yields a second estimate for Q_T, which is 94.0%. Finally, we take Q_T and its angular dependence into account to come up with a simple concentration geometry that would allow for concentration intensities of 1000 suns, while mitigating the shading/resistance-loss trade-off almost completely. In fact, the proposed structure can translate a metal coverage of 25% into an effective shading of only 1.8% at 1000 suns.

Considering the potential gains in conversion efficiencies at higher concentrations that this approach enables (4.8% for a single junction GaAs cell) we have outlined a path beyond 50% laboratory power conversion efficiencies for multi-junction solar cells[177]. The reduction in cell area and increase in efficiency with concentration enabled by this design may render III-V multi-junction solar cells commercially viable for large-scale power generation.

3.9. Appendix

3.9.1. Methods

Design

The exact dimensions were subject to a few design constraints (Figure 3.8). The function of the patterned polymer layer relies on optical behavior that can be described by geometric optics. Therefore, the crosscut of the (symmetric) trenches needs to be at least a few microns in size to avoid influences from (sub-)wavelength-scale scattering effects. Secondly, the choice of the trench angles (top angle α=54.7°, bottom angle β=70.6°) was fixed to be the same as the angles obtained from the (111) and (100) facets of silicon, which serves as the material for the master wafer. The separation between the tip/bottom of the trench and the metal contacts needs to be large enough to allow for all light to be refracted away from the metal ($d_{min} = w_{metal}/(2tan(\gamma))$), with γ being the angle at which light refracted from the trenches enters the polymer layer (γ=23.2°). At the same time, the separation should not be too large, so that the light is not refracted

Table 3.1: Design parameters

Property	Value
$n_{polymer}$	1.564
w_{metal}	10.0 µm
p	40.0 µm
w_{trench}	12.0 µm
d	25.0 µm
h_{trench}	8.5 µm
h_{metal}	0.2 µm

onto adjacent metal fingers ($d_{max} = (p - w_{trench})/(tan(\gamma))$). Here, w_{metal} was replaced with w_{trench}, as w_{trench} can be larger, to allow for some tolerance for alignment of the trenches and the metal contacts. The metal finger height h_{metal} is 200 nm, which is much smaller than any of the other dimensions and hence negligible in the optical design. Consequently, all dimensions involved follow directly from the choice of finger width w_{metal} and finger pitch p (see Table 3.1).

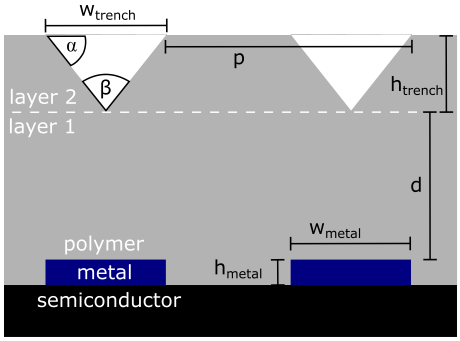

Figure 3.8: Designed geometry and parameter labels (black). White labels are used to identify the different materials and to mark the interface between the first and second polymer layer (dashed white line).

Master and stamp fabrication

To achieve a well-defined geometry of parallel trenches, a 50 nm thick SiN_x mask was used. The SiN_x was deposited via plasma enhanced physical vapor deposition (PECVD) and subsequently patterned according to the desired trench width for the master wafer. This was done using AZ6632 photoresist in combination with photolithography. The patterned photoresist on top of the SiN_x served as a wet-etch-mask for HF (4.9%). For a sufficiently thin SiN_x layer, a wet-etch with HF allows to break through the SiN_x in areas determined by the photoresist-mask, without significant under-etching. We used this SiN_x-mask and a 20% KOH-solution to etch down a (100) Si wafer. The SiN_x mask acted as an etch-stop towards the edges and caused the initially random pyramids that are created by the KOH-etch to merge into triangular (111)-plane trenches given sufficient etch time. Measurements from SEM-images (Figure 3.3b) suggest that the actual achieved

angle between wafer surface and trench wall is slightly smaller than the angle between the (100) and (111)-planes, in line with recent investigation of scattering angles of pyramidal Si surfaces[194].
The fabrication of the PDMS stamp is described extensively by Verschuuren et al.[107] and we refer to that work for details. The only major difference is that Verschuuren et al. describe the stamp fabrication mainly in combination with Si masters that contain patterns of nanoscale objects which do not change along the surface normal of the stamp. In our case, the fabricated structures are on the microscale and do change along the surface normal, but this does not influence the stamp fabrication, highlighting the universality of the approach.

Fabrication of patterned sample
To make the PDMS stamp compatible with the UV lithography tool used for alignment and UV-curing of the samples, the glass carrier onto which the PDMS mold is glued was diced to make the stamp fit into the tool. Furthermore, it was fixated onto a thick glass carrier to prevent it from breaking during fabrication. The UV-lithography tool used is a MBJ3 tool from SÜSS MicroTec with manual pressure control, which is beneficial when dealing with liquid photoresist as the range of applied pressure via the stamp can be monitored and adjusted more accurately than possible in some automated tools that focus on solid state UV-lithography. For larger-scale application, the manual pressure control could be replaced by an automated pressure control system that stops upon contact with liquids. Before the imprint process, a 25 µm base layer of the transparent polymer (OrmoComp) is deposited via spin-coating (30 s, 3000 RPM), heat-cured (2 min, 80°C), UV-cured (1500 mJ/cm^2), and again heat cured (2 min, 80°C). The second layer of the transparent polymer is prepared and processed at the same spinning and curing conditions to obtain the structure in Figure 3.8.

Before UV-exposure, the PDMS stamp is brought into contact with the liquid polymer layer on top of the sample in the UV-lithography tool. Once in contact, the stamp features and the metal finger lines on the sample are aligned with each other to achieve the desired transparency. This alignment is done by using the attached optical microscope and comparing the position of the metal grid and trench lines of the stamp. During alignment the microscope is focused onto the plane containing the metal grid at low magnification. Higher magnification would mean that a greater range of incident angles is sampled and hence the fingers would appear non-transparent, even though they might be perfectly aligned with the trenches.

We found that a more general and effective method is alignment by minimizing the reflection by eye (making the sample appear as dark as possible). At the initial stage of the alignment, the orientation of trenches and metal contacts, which are usually not parallel to each other, leads to clearly visible Moiré patterns. The pattern alternates between dark and bright regions, which correspond to the absorber and metal reflection, respectively. By rotating the sample such that those regions become larger and hence the number of alternations across the sample less, the trenches and contacts are aligned in a parallel fashion. Next, the sample is translated such that the trenches and contacts are not only parallel, but also on top of each other. This is visible by a change in brightness of the sample during translation, and the position for which the sample appears darkest corresponds to ideal alignment. We note that the simple alignment method described in

this paragraph suggests that it should be fairly straightforward to transfer the procedure to the industrial scale.

For samples with front texture, this manual method is the only way of aligning the metal grid and the trenches, as the front texture scatters too much to be able to distinguish the metal covered area from the bare absorber in the microscope. This suggests that in a more advanced alignment setup the alignment could work best by placing a light detector above the sample and minimizing the photon counts it receives. After exposure, the sample is carefully separated from the PDMS stamp and again heat-cured as was done for the first layer.

Optical characterization

The optical characterization was based on integrating sphere (IS) measurements. We used a Perkin Elmer Lambda1050 tool, along with its designated focusing and sample rotation kits. For reflection measurements, the sample was mounted behind the backside opening of the IS. An opening smaller than the sample was used, and the beam was focused such that it was also smaller than the opening. The distance between the focusing lens and sample was large enough to be able to assume that the range of AOI is negligible, and that the effective AOI was indeed 0°, with respect to θ. To measure the angular dependence of the absorption, the samples were fixed in the center of the IS, by using a designated holder clip. The holder clip can be rotated from outside the IS, which allows to vary the angle without having to reopen the tool. Furthermore, this measurement collects the sum of reflection and transmission. Hence, we assumed that all light that was not collected was lost to absorption. Similar to the reflection measurements, the beam was focused onto the sample with a corresponding lens. Again, the distance between lens and sample was large enough to neglect widening of the range of AOI.

Angle-resolved reflection measurements

These measurements (Figure 3.11) were conducted using an in-house custom built system [195] based at Macquarie University. The system uses a collimated super continuum laser as an illumination source that is passed through a Glan-Taylor prism to create the desired linear polarization. The illuminating light is then directed to reflect off the sample into a mini integrating sphere detector fibre-coupled to a silicon or InGaAs CCD spectrometer. The system is configured in single beam configuration, and is able to measure wavelengths in the range of 400-1800 nm. Measurements are taken sequentially, with a single measurement consisting of one angle of incidence and one angle of reflection. The angle of incidence for the illumination and the angle of detected reflected light are able to be independently changed across almost the entire range of 0 - 90 degrees relative to the samples normal.

Fabrication of the Si solar cells

An industrial 6 inch silicon solar cell was obtained with a PERC structure on the rear and SiN_x on the front. The cell was cleaved into 2x2 cm^2 pieces for the test structure. Photolithography was done on the front to remove parts of the passivation layer (with a buffered oxide etchant) and to create the desired Al fingers via evaporation, creating 1x1 cm^2 devices. The metal fingers are 10 μm in width with a pitch spacing of 40 μm,

which correspond to 25% metal coverage. While the devices are not isolated on the wafer, this enables accurate measurement of the EQE.

Electronic characterization
The external quantum efficiency measurements were done with a PV Measurements QEX7 system. The samples were brought into a focal spot with dimensions 1 mm x 4 mm. Samples were aligned such that the metal fingers were perpendicular to the light spot line.

3.9.2. Derivation of effective shading in equation (3.3)

Q_T is a function of the angular coordinate θ of the light source on a (hemi-)spherical surface with the solar cell located in the center, given by equation (3.2) from the main text. To obtain an angle-average over the shading up to a certain maximum angle θ we have to weigh $Q_T\ (\theta)$ by the surface area taken up by an infinitesimal slice of this hemispherical surface at the angle θ. Using a spherical coordinate system this amounts to:

$$\begin{aligned}
S_{eff}(\theta) = & S\left(1-\frac{\int dA\, Q_T(A)}{\int dA}\right) = \\
& S\left(1-\frac{\int\int dxdy\, Q_T(x,y)}{\int\int dxdy}\right) = \\
& S\left(1-\frac{\int\int r\, d\theta'\, r\, cos(\theta')\, d\phi'\, Q_T(\theta')}{\int\int r\, d\theta'\, r\, cos(\theta')\, d\phi'}\right) = \\
& S\left(1-\frac{r^2\int d\phi'\int d\theta'\, cos(\theta')\, Q_T(\theta')}{r^2\int d\phi'\int d\theta'\, cos(\theta')}\right) = \\
& S\left(1-\frac{\int_0^\theta d\theta'\, cos(\theta')\, Q_T(\theta')}{\int_0^\theta d\theta'\, cos(\theta')}\right) = \\
& S\left(1-\frac{\int_0^\theta d\theta'\, cos(\theta')\, Q_T(\theta')}{sin(\theta)}\right) = \\
& S\left(1-\frac{1}{sin(\theta)}\int_0^\theta Q_T(\theta')\, cos(\theta')\, d\theta'\right)
\end{aligned} \tag{3.4}$$

3.9.3. Optical constants of OrmoComp

The optical constants of OrmoComp were determined using spectroscopic ellipsometry, and by subsequently matching simulated and experimental reflection data for a film of 200 nm on top of a Si substrate. The data in Figure 3.9 shows a strong absorption onset around 360 nm, typical of UV-photoresists.

3.9.4. Relevance of ratio of trench and contact width

The ratio of the widths of the trenches and the metal contacts determines the plateau width in Figure 3.5c, for which no performance loss at all is experienced with respect to θ. Figure 3.10 illustrates this. The parameter f_W represents the ratio of the trench width to the contact width and is larger than 1 when the trenches are wider.

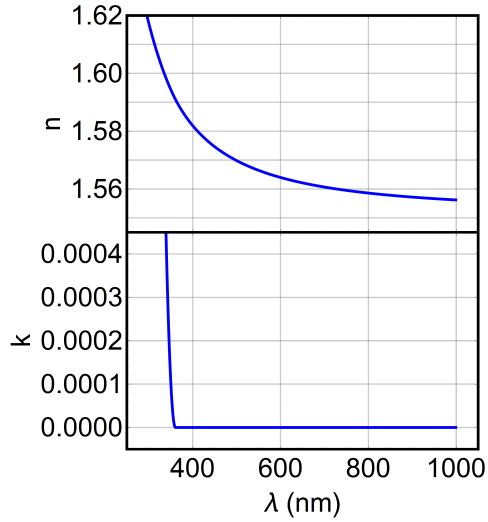

Figure 3.9: Real (top) and imaginary (bottom) components of the refractive index of OrmoComp.

The experimental data corresponds well with f_W=1.1 up to θ=8°. Beyond that value the experimental data shows worse performance, which can be attributed to the fact that the modelled data does not take neighboring contacts into account, hence only describes the transparency for the contacts right under the trench. However, for increasing angle, refracted light rays may hit adjacent contacts. This contributes to a decrease in the experimental data beyond θ=8°.

The relevance of width ratio between trenches and contacts is also apparent from the figure. While trenches thinner than the contacts obviously let light pass onto the contacts, wider trenches lead to more resilience towards the angle of incidence, and hence suggest an improved performance as function of angle. However, the discrepancy that we see between the experimental curve and the modeled data for f_W=1.1 would already arise at angles below 8° as the trench is closer to the adjacent contacts.

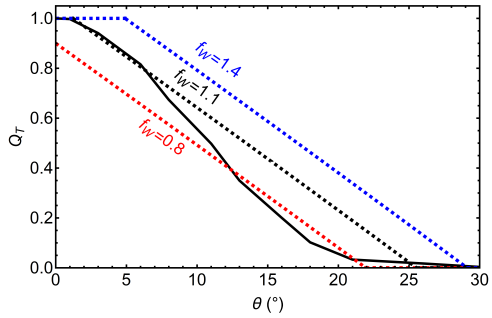

Figure 3.10: Comparison of experimental angular dependence of Q_T (solid) and modeled dependences (dashed) for different values of f_W.

3.9.5. Detailed balance limit calculations

To obtain the right y-axis in Figure 3.7a, the detailed balance limit[88] was calculated by balancing the generated current-density (J_G, Equation (3.5)), with the recombination current density (J_R, Equation (3.6)), which yields an overall extracted current (J, Equation (3.7)). The generated current density is a sum of the generation from sunlight (1st term) and the received radiation from the ambient (2nd term, insignificant for the investigated bandgap range).Via iteration at different voltages, a current-voltage curve can be constructed, from which short-circuit current density (J_{sc}), open-circuit voltage (V_{oc}), fill factor (FF), and efficiency (η) can be predicted. By including a concentration factor (f_c), the calculation can be expanded towards concentrations different from 1 sun.

$$J_G(E_{BG}, f_c) = f_c q \int_{E_{BG}}^{\infty} \phi_{AM1.5D}(E) dE + \left(\frac{f_{c,max} - f_c}{f_{c,max}} \right) q \frac{2\pi}{c^2 h^3} \int_{E_{BG}}^{\infty} \frac{E^2}{e^{\frac{E}{kT}} - 1} dE \tag{3.5}$$

$$J_R(E_{BG}, V) = q \frac{2\pi}{c^2 h^3} \int_{E_{BG}}^{\infty} \frac{E^2}{e^{\frac{E-V}{kT}} - 1} dE \tag{3.6}$$

$$J(E_{BG}, V, f_c) = J_G(E_{BG}, f_c) - J_R(E_{BG}, V) \tag{3.7}$$

Where q is the electron charge, c the speed of light in vacuum, h the Planck constant, k the Boltzmann constant, T the temperature of the solar cell (assumed to be at room temperature), and $f_{c,max}$ is the maximum possible concentration. Furthermore, $\phi_{AM1.5D}$ corresponds to the photon flux described by the AM1.5D solar spectrum, E_{BG} is the bandgap energy (set to 1.441 eV, which corresponds to GaAs), E the energy of the incoming photon and V the applied voltage.

3.9.6. Angle-resolved reflection

Angle-resolved reflection measurements were conducted to confirm that the trench-structure functions as intended, by refracting light into a specific angle, given by the trench angle. This was done for the same samples as in Figure 3.5. We can see from Figure 3.11(a-c), that the reflection angle that one would expect for light that is first refracted by the trench, then reflected by the sample, and finally out-coupled by the planar surface (dashed line) indeed matches well with the angle at which an intensity maximum is observed in the experimental data. There is a slight offset which could be related to a slightly different trench angle or refractive index of the fabricated sample. In general, the figure further confirms that the refractive behavior works as intended.

3.9.7. Transmission of patterned quartz samples

Analogous to reflection measurements, transmission measurements were conducted using the integrating sphere. Figure 3.12 shows the corresponding transmission spectra. In this case, the samples were mounted in front of the inlet of the integrating sphere, which is very close to the focusing optics of the setup, in comparison to the large optics-sample distance for the reflection measurement. This means that the angular range of incident light was larger than the normal incidence that was sampled in the case of the reflection

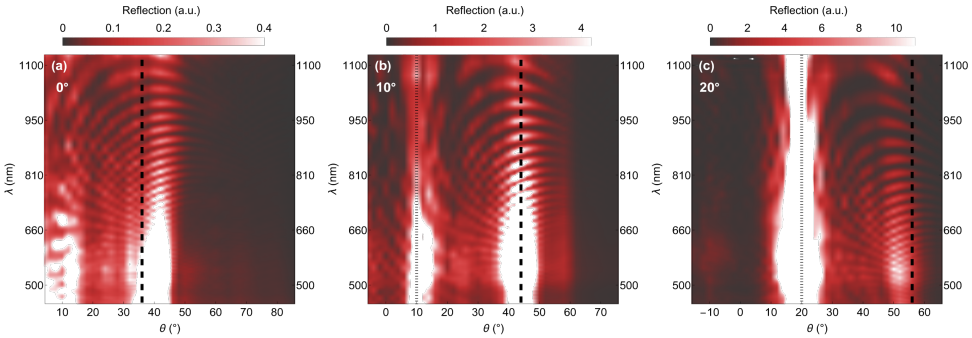

Figure 3.11: Experimental data on reflected light intensity for specific receiving angles (θ) and wavelengths (λ). White corresponds to higher reflection intensity. (a), (b), and (c) correspond to angles of incidence of 0°, 10° and 20°. The dashed line corresponds to the expected out-coupling angle for light that enters the sample via a trench and is out-coupled via a planar surface. The dotted line corresponds to the specular reflection of the incident beam.

measurements. As a consequence, the patterned sample appears to perform worse in transmission than in reflection, as unfavorable, larger angles of incidence are sampled as well. Using (3.1) between 700 to 800 nm, we find Q_T=83.7%, for the transmission for this geometry.

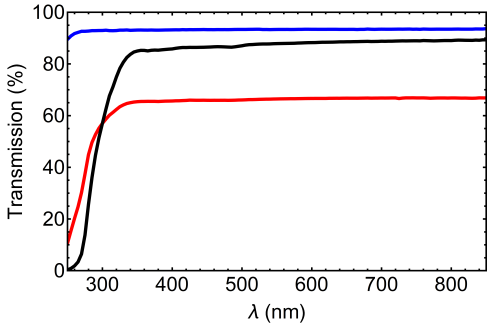

Figure 3.12: Comparison of total transmission between a patterned quartz sample with Au grid (black), a planar sample with Au grid (red) and a bare quartz sample (blue). In this case, the metal (Au) coverage was 30%.

3.9.8. Derivation of the transparency from the external quantum efficiency

For the quantification of Q_T in the electronic case, the peak value of the EQE of the patterned sample was used, and by taking reflection losses from the polymer into account, Q_T = 94% was calculated. This approach can be extended to the full wavelength range, although it assumes an ideal AR-coating effect, which is only true for the peak wavelength. Hence, Q_T is systematically underestimated for off-peak wavelengths. Figure 3.13 shows the results that one would obtain using (3.8) for the patterned case, but also for the planar polymer case, for which the light-trapping effect of the planar layer also yields Q_T values of up to 60%.

$$Q_T(\lambda) = 1 - \frac{1 - EQE(\lambda) - (1 - f_g) r_{planar} - f_g r_{patt}}{f_m} \tag{3.8}$$

Where f_g is the fraction of polymer area covered with grooves, f_m the fraction of solar cell area covered with metal, and r_{planar} and r_{patt} correspond to reflection from the planar and grooved polymer areas, respectively. It becomes apparent that this approach for calculating Q_T is only suitable for the range in which the combination of SiN AR-coating and pyramidal texture is at an optimum.

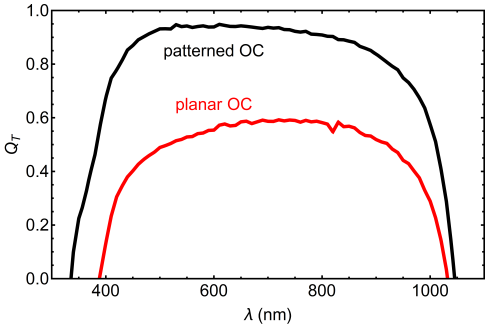

Figure 3.13: Electronically derived Q_T as a function of wavelength, calculated using (3.8). With the patterned case in black, and the planar case in red.

3.10. Acknowledgements

This work was performed in part at the NSW Node of the Australian National Fabrication Facility (ANFF). This work was performed in part at the Research and Prototype Foundry Core Research Facility at the University of Sydney - part of the Australian National Fabrication Facility. The authors acknowledge the facilities and the scientific and technical assistance of Microscopy Australia at the Electron Microscope Unit (EMU) within the Mark Wainwright Analytical Centre (MWAC) at UNSW Sydney. This work has been supported by the Australian Government through the Australian Renewable Energy Agency (ARENA), the Australian Centre of Advanced Photovoltaics (ACAP). This work has been supported by the Australian Government through the Australian Research Council's DECRA program (DE210100453). Responsibility for the views, information or advice expressed herein is not accepted by the Australian Government. MPN acknowledges the support of the UNSW Scientia Program. This work is part of the research program of the Dutch Research Council (NWO).

3.11. Author contributions

S.W. Tabernig, A. Soeriyadi, D. Lamers, and U. Römer fabricated the master and stamp. A.S. fabricated the solar cells. S.W.T and A.S. patterned the solar cells. S.W.T., U.R., M. Nielsen, and A.S. performed the electronic characterization. S.W.T., M.N., U.R., A.S., M. Juhl, and D. Payne performed the optical characterization. A. Pusch designed the pattern. S.W.T. and A.Pu. performed theoretical analyses. N. Ekins-Daukes, M.N., and A.

Polman supervised the project and gave feedback. All authors contributed to the writing of the manuscript and gave feedback on it.

4

Broadband nanopatterned anti-reflection coatings for planar Si solar cells

4.1. Abstract

Crystalline Si solar cells based on thin wafers, with thicknesses in the range 5-50 micrometer can find applications in a wide range of markets where flexibility and bendability are important. For very thin Si cells, avoiding the common macroscopic texture would be desirable to increase structural integrity and reduce surface area to minimize recombination. In this work we first introduce a patterned SiN_x anti-reflection (AR) coating that consists of 190-nm-diameter and 117-nm-height nanocylinders arranged in a square lattice on a thin SiN_x layer. The layer combines Fabry-Perót anti-reflection, refractive index grading, and forward scattering by Mie resonances to achieve high transmission over a broad spectral band. We add the nanocoating on a commercial interdigitated back contact (IBC) Si solar cell, and we find a short-circuit current density (J_{sc}) of 36.9 mA/cm^2 (2.3 mA/cm^2 higher in comparison to a single-layer AR coated cell), and an efficiency of 16.3% at a thickness of around a 100 μm. We predict that an annealing step could boost the J_{sc} up to 39 mA/cm^2. Further investigation shows that the incoupling efficiency is comparable to that of pyramidal texture, while the absorption in the infrared is lower, due to less effective light trapping. We then demonstrate the integration of a hyperuniform nanostructure with tailored angular and spectral scattering profiles into the top surface of a 100 μm-thick IBC cell and use electronic simulations to predict the surface passivation quality that is needed to mitigate losses from the additional surface area. We find that losses due to increased surface area are negligible for surface recombination velocities below 10 cm/s.

4.2. Introduction

Crystalline Si is the dominant photovoltaic (PV) material . In the past thin-film solar cells based on CIGS [196,197], CdTe [198], and amorphous Si (a-Si) [199] temporarily looked like they could take up large market shares [200], but Si PV has always bounced back and currently holds a market share of 95% [200]. Silicon PV is so important as it is the currently most efficient and inexpensive option for large-scale single-junction PV. However, PV modules based on novel thin-film materials, such as organic [112,172,201] and perovskite [113,172] absorbers are also making their way into the commercial PV market, and thin-film PV is becoming increasingly important for several reasons.

First, thin-film absorbers, in principle, require less material, making them cheaper and more sustainable. The use of less material also implies that the deposition time per unit area is shorter, making the throughput larger and costs lower [72,200]. Furthermore, thin-film PV can be flexible and bendable, which is important for integration of aesthetically pleasing PV in buildings (BIPV [202,203]), curved PV on vehicles (VIPV [202,204–206]) for extended driving range (around 18 km/day/kWp [207]), and for integration with textiles [208]. Flexible and durable solar cells can also be shaped and diced into arbitrary shapes, allowing for mass customization [202].

The perspective of using thin, monocrystalline wafers of Si, the commercially most mature absorber material for thin-film PV is an appealing prospect. Silicon is very easy to bend and cut to a desired shape at thicknesses below 50 µm [209,210], which is well below the common thickness of Si solar cells [211] (140-170 µm). From the electronic perspective, a thinner cell can have a larger open-circuit voltage (V_{oc}) [212] due to reduced bulk recombination. However, to ensure significant light absorption, the Si absorber needs to be thicker than 100 µm, as Si is a poor light absorber due to its indirect bandgap [213].

To achieve efficient thin-film Si wafer-based solar cells, the issue of incomplete absorption needs to be addressed. This is where proper light management strategies become essential. The maximum possible absorption is given by the Lambertian light trapping limit [116,210,214]: in an ideal geometry light is scattered at the front or back interface of a solar cell by a Lambertian scattering surface, which distributes the light intensity inside the absorber evenly, such that the intensity per unit solid angle is uniform. The escape cone for light inside the absorber is related to an escape probability and depends on the absorber's refractive index, n. By balancing the escaped light with the incoming light, one can obtain a pathlength enhancement of $4n^2$ for light inside the absorber.

Micrometer-sized random pyramidal texture is the industry standard [215] for creating path length enhancements within the absorber and for improving incoupling of light through multiple reflections at the front side. It is also comparatively easy to fabricate by dipping the Si wafer in KOH solution [194]. However, it is not always possible to process the wafer this way, and it may be beneficial to come up with other textures that minimize surface area and reduce surface recombination losses [216]. Additionally, in the limit of very thin Si (<5 µm), Si volume cannot be sacrificed to create the pyramidal texture, as the KOH would then affect the structural integrity of the wafer or even etch through it.

There are alternatives that do not exhibit large surface features and provide good incoupling or strong scattering. Previous work [217] has investigated the back interface of the absorber and designed it to trap the light by using nanoscale grids of Mie- and plasmonic resonators. Incoupling can also be improved by using multi-layer AR coatings [218]

and nanotextured "black" silicon[219] or nanoscale scatterers that preferentially scatter light forward, such as, for example, TiO_2 resonators[220] or nanostructures that preferentially direct light into angular channels at which it is totally internally reflected within the absorber[221–225].

In the following we demonstrate that a single-layer periodic nanopattern of cylindrical SiN_x nanoparticles on a planar front surface of a Si solar cell has the potential to outperform the conventional SiN_x single-layer AR coating, bringing the incoupling efficiency closer to that of front surface pyramidal texture. At the same time, we use pyramidal texture at the back to create efficient light trapping. We demonstrate our nanoscale surface incoupling geometry on a commercial interdigitated back contact (IBC) Si solar cell for which we planarize and repassivate the front surface. We demonstrate enhancement of the short-circuit current density from 27.7 mA/cm^2 for the flat Si surface with 200 nm SiN_x to 36.9 mA/cm^2 by patterning the nanostructure into the SiN_x layer. The results indicate that the nano patterned front surface is well suited as an efficient light incoupling layer for thin Si solar cells.

Furthermore, we use the same commercial IBC cell platform to investigate the viability of hyperuniform Si nanostructures on the front surface of the cell for light trapping. In previous work[221], optical measurements of such structures on a 1 μm Si membrane have resulted in absorption spectra that predict a J_{sc} of well above 20 mA/cm^2 (78% of the Lambertian limit). Here we fabricate this structure onto a Si IBC solar cell and simulate the electronic passivation requirements of such a large-surface-area Si structure using experiments and simulations.

4.3. Nanopatterned SiN_x anti-reflection coating for improved light incoupling

4.3.1. Optical optimization of the nanopatterned SiN_x layer

This work aims to demonstrate efficient light incoupling using a layer with optical and electronic functionality for Si solar cells. Optically, the layer should appear textured, for improved incoupling of light, while electronically, it should appear flat, minimizing surface area, which is important for electronic passivation. We choose SiN_x because it fulfils the optical requirements[226] of weak parasitic absorption in the visible and near-infrared (NIR) range (in contrast to a-Si[227]) and a relatively high refractive index[226] (n) of 2.0, and can also be used for surface and bulk passivation[228].

To simulate the optical performance we solve Maxwell's equations using Ansys Lumerical FDTD[229] for an air – cylinder (SiN_x) – bottom layer (SiN_x) – Si stack (Figure 4.1a inset). We maximize the AM1.5G-spectrum-weighted transmission into the absorber using a particle-swarm optimization routine[230]. By maximizing transmission at the SiN_x/Si interface, rather than doing a more canonical total reflectance minimization, unintentional maximization of absorption in the patterned SiN_x layer is avoided. The structural parameters optimized are the height of the SiN_x bottom layer, the height of the cylinder, its diameter, and the cylinder lattice pitch, using a square lattice.

Figure 4.1a shows the reflectance (R) from the surface (SiN_x & Si layers), transmittance into the Si (T), and the absorptance (Abs) of the optimized SiN_x structure. At wavelengths shorter than 650 nm, the absorption gradually increases due to parasitic

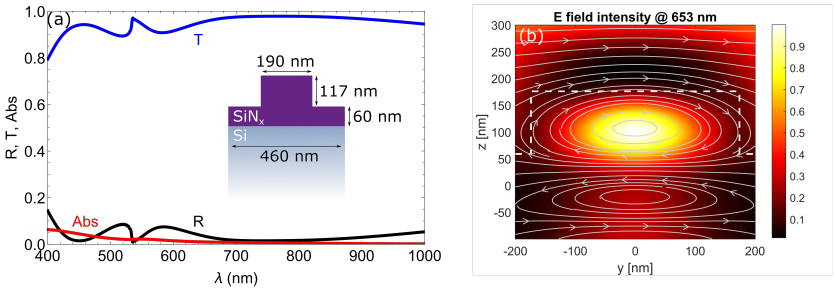

Figure 4.1: (a) Transmittance (blue), reflectance (black), and absorptance (red) as a function of wavelength. The inset shows the structure (SiN_x purple, Si gray) and dimensions for which the curves are simulated (60 nm bottom layer, 117 nm cylinder height, 190 nm cylinder diameter, 460 nm pitch). (b) Crosscut through a single SiN_x cylinder. The air-SiN_x interface is marked with dashed white lines. The color scale shows the normalized E-field intensity at 653 nm and the arrows show a snapshot of the electric field lines.

absorption in the SiN_x. The average reflectivity is 3.7% and we observe three minima, a sharp minimum at 535 nm, and two broader minima centred at 450 nm and 740 nm. The shape of the transmittance spectrum curve is complementary to the reflectance spectrum and is slightly reduced at shorter wavelengths due to the parasitic absorption in the SiN_x.

The high transmission can be explained by a combination of a graded-index antireflection coating with a preferential forward scattering of light. The graded index is created by the stack of four layers: it increases from air to the Si layer (n given for a wavelength of 600 nm): air (n=1) - effective medium that is described by the layer of SiN_x cylinders in air (n= 1.14) – SiN_x planar layer (n=2.0) – Si (n=3.9). Furthermore, the electric field distribution in Figure 4.1b indicates that the cylinder dimensions allow for the excitation of Mie resonances inside the SiN_x pillar. The crosscut through the simulated structure shows an electric field profile that indicates the presence of a Mie-like electric dipole mode[231] at 653 nm. This wavelength coincides with the transition from higher transmission (longer wavelengths) to lower transmission (shorter wavelengths). Furthermore, a sharp feature in transmission at 535 nm corresponds to a new grating order that opens up for shorter wavelengths[232], and that couples light into large angles for which it is trapped in the solar cell. The peak around 450 nm is close to the optimum wavelength of a 60 nm SiN_x coating, suggesting that the 60-nm-thick bottom layer hosts a Fabry-Pérot resonance in that range. A thorough analysis of how Fabry-Pérot and Mie resonances can be combined in a single metasurface to realize a broadband antireflection response can be found in Cordaro *et al.*[233].

4.3.2. Experimental realization on commercial IBC solar cells

We use commercial interdigitated back contact (IBC) Si solar cells (η=21.5%) for the experimental verification of the simulation results. These cells have random pyramidal texture and a SiN_x AR-coating on both sides, and alternating n- and p-contact patches on the back. To make the cells suitable for our experiments, we remove the front texture, while the rest of the solar cell remains untouched.

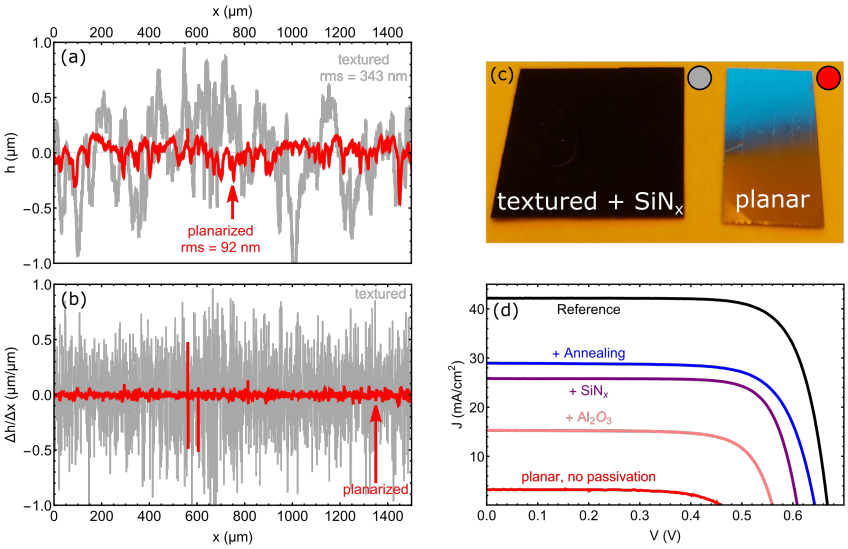

Figure 4.2: (a) Height profiles of textured (gray) and planarized (red) Si solar cells. (b) Slope profiles (change in height over distance) for the same datasets. (c) Measured samples with textured (with SiN_x, left) and planarized (no SiN_x, right) surfaces. The top half of the planarized surface shows a blue reflection from a screen lamp. The more diffuse surface of the textured sample does not. (d) Current density – voltage ($J-V$) curves for all post-processing stages. In order: Before any processing (black), after HF and HNA-etching (red), after Al_2O_3-deposition (pink), after SiN_x-deposition (purple), and after annealing (blue). Except for the reference $J-V$ curve (textured), all $J-V$ curves correspond to planar solar cells.

To planarize the front surface of the cell, first the backside was protected with a 12 µm coating of Parylene-C[234,235], which is resistant to a wide range of chemicals and solutions[234,235]. The SiN_x layer was removed by HF-etching until the surface appears gray and is hydrophobic. To planarize the cell, it was transferred into a HNA solution (Hydrofluoric acid, nitric acid, and acetic acid) that etches Si isotropically. For the case of pyramidal texture this implies that the pyramids gradually become rounder upon etching until they vanish, depending on the etch duration. In principle, this procedure allows etching solar cells down to very thin absorber layers. The etching was stopped as soon as the reflection from the Si surface became specular.

Substrate conformal imprint lithography (SCIL) was then used to pattern the planarized Si surface. Figure 4.2a shows the sample roughness before and after the HF & HNA processing. The root-mean-square roughness (rms) drops by a factor 4. Visually, this translates into a much more specularly reflecting sample (Figure 4.2c). At the same time, Figure 4.2a indicates there is residual roughness left, which as we will show slightly affects the fidelity of the SCIL imprint. Figure 4.2b shows the derivative of the line scans in Figure 4.2a; a much bigger contrast is observed between the textured and etched surfaces. This means the chemical etching planarization eliminated short-range roughness more strongly than long-range roughness. This made the surface well suited for SCIL imprinting.

At this stage, the solar cell had a planar front surface but no passivating layers. Figure 4.2d shows that the cell performance was severely impacted by the processing steps (η=1%). Removing the AR-coating and pyramidal texture strongly reduces the incoupling efficiency of light and results in a 30-40%[236] lower short-circuit current density (J_{sc}), purely based on reduced light incoupling. However, a much stronger reduction in short-circuit current is observed in Figure 4.2d (black and red curves), which we ascribe to strongly increased surface recombination at the front surface due to the absence of surface passivation[237]. Figure 4.2d shows how passivating the etched front surface with Al_2O_3 (10 nm, deposited by atomic-layer deposition (ALD), pink curve)[238–240], followed by deposition of SiN_x (200 nm, by plasma-enhanced chemical vapor deposition (PECVD), purple curve), and a subsequent annealing step in air (10 min at 400°C, blue curve) led to a much improved short-circuit current density and open-circuit voltage (V_{oc}).

Assuming an ideal-diode model[241], the difference in V_{oc} between the reference and the fully processed sample (25 mV) cannot fully be explained by only the difference in J_{sc} ($\Delta V_{oc,J_{sc}}$ = 9.5 mV), and we attribute the remaining difference to a 1.8-times higher front surface recombination current density ($J_{0,f}$), for the processed sample. Overall, the planarization and passivation of the front surface yielded solar cells that form an effective platform for the demonstration of front surface light management concepts.

4.3.3. Fabrication of the SiN_x nanocylinder lattice

We then used SCIL to create the mask for the patterning process (Figure 4.3a). We used a Polydimethylsiloxane (PDMS) stamp that was molded from a Si master wafer. A thin layer of silica solgel was spin-coated onto the solar cell, and the PDMS stamp was pressed onto the solgel layer while it was still liquid. After 6 minutes of curing, in which the solvent dries to a solid silica glass layer, the stamp was peeled off and the silica layer was shaped into the desired mask pattern. In our case, we used an additional PMMA interlayer between the solar cell and the solgel for etch-selectivity and easy lift-off at the end. Three different reactive ion etching (RIE) steps broke through the solgel layer, then the PMMA layer, and finally etched into the SiN_x for a duration that was controlled to obtain the desired SiN_x cylinder height. The etch mask was lifted off in acetone afterwards and at that point the solar cell processing was finished.

Figures 4.3b-d show the results of the patterning under the scanning electron microscope (SEM). As we can see, several sections of the surface were not well patterned. This is likely because there is still some residual texture left (Figure 4.2a), which in some cases leads to the accumulation of excess solgel in pockets of microscopically shaped Si. While these regions can be imprinted with the PDMS stamp, the residual solgel layer was thicker than in other regions. This means that the duration of the RIE etch for the solgel is insufficient to break through that layer, and hence this layer prevents the following etch steps from transferring the pattern into the SiN_x. We note that in these areas, light is still coupled into the cell, but at lower efficiency than in the nanopatterned areas. Figures 4.3c,d show high-resolution images of the patterned SiN_x cylinders on an otherwise planar surface.

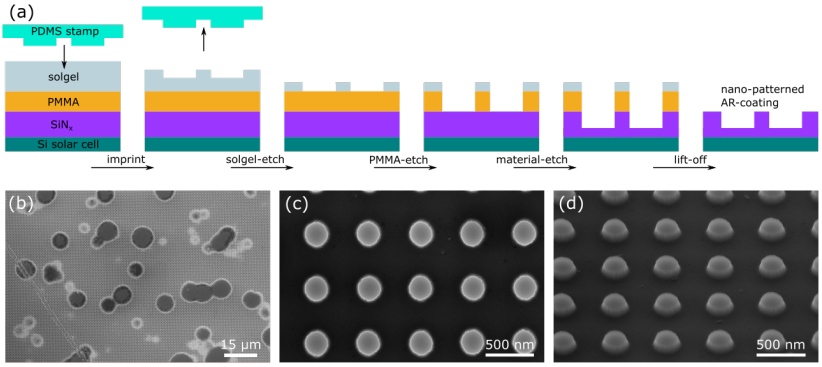

Figure 4.3: (a) Patterning sequence. The PDMS stamp is pushed into the liquid solgel. After the solgel had cured, the stamp was removed. The residual solgel layer was removed by reactive ion etching (RIE), followed by further etching of the PMMA layer. Then, the SiN_x cylinders were created by etching further into that layer. The etch mask was removed by a lift-off in acetone. (b) Large scale SEM image of a patterned solar cell. Darker circular regions correspond to areas where too much solgel was deposited, which prevents breakthrough and patterning of the SiN_x layer. (c) SEM top view of the SiN_x cylinders, which appear as circles. (d) SEM angled view, showing the cylindrical shape.

4.3.4. Electronic performance

To evaluate the effect of the SiN_x nanostructure on the electronic performance, the $I-V$-curves and external quantum efficiency (EQE) of the solar cells were measured before and after patterning of the SiN_x layer. In these initial experiments, the SiN_x layer was not annealed, and the cells thus correspond to not fully optimized geometries that led to a short-circuit current (J_{sc}) that is some 3 mA/cm^2 below that for the annealed cells (see Figure 4.2d). Figure 4.4 shows the comparison for a batch of 5 solar cells that received the same patterning treatment. For all cells, a strong gain in J_{sc} is achieved. The batch statistics in Figure 4.4b confirm that nanopatterning led to a systematic gain in J_{sc} of 8.5 mA/cm^2 average, along with a slight average gain in V_{oc}, and an average reduction in fill factor (FF), dominated by the outlier $I-V$ curve. Nanopatterning the SiN_x layer increased the efficiency (η) by 3.2%-absolute on average compared to the flat cell with SiN_x layer, mainly due to the improved J_{sc}. The best nanopatterned cell had J_{sc}=36.9 mA/cm^2, V_{oc}=0.602 V, FF=73.6%, and η=16.3%. The parameters for the initial textured, unetched cell (reference in Figure 4.2d) were J_{sc}=42.2 mA/cm^2, V_{oc}=0.668 V, FF=76.2%, η=21.5%. We note that the patterned cells showed a somewhat larger variation in J_{sc} than the planar cells (Figure 4.4a). We attribute this to variations in the SCIL process that did not always lead to a full imprint of the surface area (Figure 4.3a). Similarly, the shunting in the outlier $I-V$ curve in Figure 4.4a is attributed to unwanted effects of the SCIL process such as damage caused by wafer handling. We note that these variations can all be avoided by using a fully automated SCIL imprint process, for which commercial systems are now on the market [106].

As noted above, in the experiments of Figure 4.4 the Al_2O_3 and SiN_x layers were not annealed, in contrast to the samples in Figure 4.2d that were annealed to reduce surface

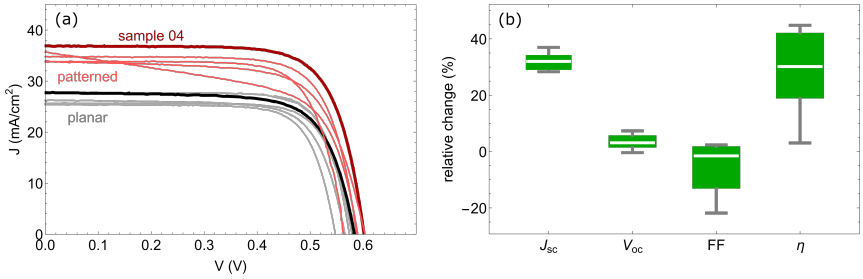

Figure 4.4: (a) Current density – voltage ($J-V$) curves of planarized (gray) and passivated (red) solar cells before and after patterning of the 200-nm-thick SiN_x layer. The curves that correspond to the best cell are indicated by darker colors. (b) Boxplot diagram showing the electronic parameters short-circuit current density (J_{sc}), open-circuit voltage (V_{oc}), fill factor (FF), and efficiency (η). The units are the relative change of the parameter after patterning compared to before.

recombination, leading to an enhanced short-circuit current as shown in Figure 4.2d. This explains why the observed V_{oc} values in Figure 4.4a for the patterned cells are lower than for the optimum case for the planar cells in Figure 4.2d even though the short-circuit currents are higher. Based on the results in Figure 4.2b we estimate that annealing of the patterned cells, leading to better passivation and hence carrier collection could add another 2 mA/cm^2 to the short-circuit current. Experiments are presently underway to investigate this. We refer to Figure 4.8 in the appendix, which shows a further comparison between the characteristics of annealed and not annealed solar cells.

The large gain in J_{sc} between patterned and flat SiN_x coated solar cells (9.2 mA/cm^2 for the best cell) is consistent with the strongly enhanced incoupling of light into the solar cell. To study this in detail, Figure 4.5 shows the external quantum efficiency (EQE) of the best solar cell shown in Figure 4.4. Optical limits for the EQE are also shown, and these were derived from the theoretical reflection from the cell surface, assuming all the transmitted light contributes to the EQE, irrespective of the bandgap. Before patterning, the 200-nm-thick SiN_x layer resulted in an EQE spectral shape with three peaks, and only a small range (490-620 nm) showed an EQE above 80%. Figure 4.5 also shows the calculated optical limits for the EQE of a Si solar cell with a planar front surface and a 200-nm SiN_x layer on top, corresponding to the solar cell before patterning. The curve matches the experimental planar cell well for the 350 and 900 nm wavelength range. For reference, Figure 4.5 shows the EQE and the optical limit for a 75 nm SiN_x layer, for which both curves peak at 600 nm. The cell with the 75 nm SiN_x layer received the same processing as the 200 nm SiN_x cell and showed a slightly larger gap between the theoretical curve and the measured EQE, but an otherwise good agreement between 400 and 900 nm.

The measured EQE for the patterned cell shows significant improvement compared to the measured 200 nm SiN_x planar cell. In the 420-930 nm spectral range the measured EQE for the patterned cell is above 80%. The spectral shape strongly resembles the optimized transmission in the simulations in Figure 4.1a, shifted to slightly lower overall current. The dip in the measured EQE between 450 and 600 nm coincides with the simulated transmission dip (Figure 4.1a), but the sharp feature at 535 nm is not visible in the

experiment and may be smoothened due to variations in the nanofabrication across the cell surface.

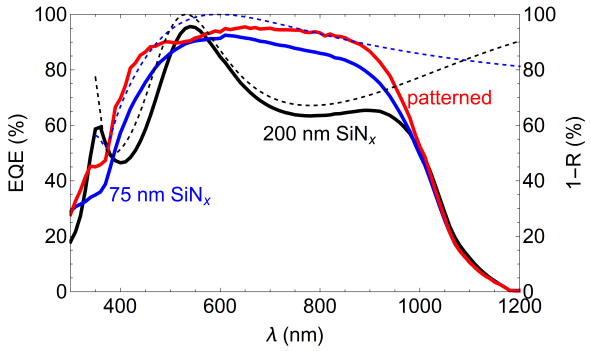

Figure 4.5: External quantum efficiency (*EQE*) of the best cell from Figure 4.4. The *EQE* is shown for the sample before (200 nm SiN_x, black) and after (patterned, red) patterning and for a cell with a single layer AR-coating (75 nm SiN_x, blue). Optical limits for the *EQE*, based on reflection losses, are shown for an air – SiN_x (200 nm) – Si stack (dashed, black), and for an air – SiN_x (75 nm) – Si stack (dashed, blue).

In the future we will apply a passivation anneal to these cells. We expect that the *EQE* of the cells will be enhanced by 5% in the range between 450 and 900 nm, similar to the 5% enhancement observed in short-circuit current that was observed for the planar cells due to annealing (Figure 4.8). For the present experimental cells, integrating the *EQE* spectrum leads to a short-circuit current that is 2.3 mA/cm^2 above that for the planar cell with a 75 nm SiN_x AR coating. Compared to a front surface with pyramidal texture (reference cell from Figure 4.2d), the SiN_x patterned device loses only 2.4 mA/cm^2 in the 300-900 nm range (from which the maximum current that can be harvested is 33.7 mA/cm^2). In the near-infrared spectral range between 900 and 1200 nm (12.7 mA/cm^2 available) the nanopatterned cells harvests 4.2 mA/cm^2 less which is due to the fact that microscopic texturing strongly enhances light trapping in this spectral range. Note that the overall J_{sc} difference (6.6 mA/cm^2) measured during *EQE* measurements is larger than measured during $I-V$ measurements (5.3 mA/cm^2). This might be related to a light bias dependence of the *EQE* or uncertainties associated with the illumination intensity and spectrum of the light sources.

4.4. Nanostructured hyperuniform Si surfaces for improved light trapping

The nanopatterned SiN_x broadband anti-reflection coating shows a high incoupling efficiency, however, it does not trap light well in the near-bandgap spectral range. Here, we investigate a front surface structure that can trap light efficiently. In recent work, Tavakoli *et al.*[221] have designed and fabricated a hyperuniform (HUD) structure that provides a large number of scattering channels across a broad wavelength range, yielding a short-circuit current density (J_{sc}) of 26.3 mA/cm^2 for a 1 µm thick absorber, as derived from to absorption measurements. Complementary recent investigations of HUD scattering pattern also showed efficient light trapping in solar cells[222–225] demonstrat-

ing the power of this concept. Moreover, this nanostructure enables ultrathin flexible Si solar cells.

4.4.1. Fabrication of the hyperuniform Si surface

To assess the viability of the HUD surface pattern for application in thin Si solar cells, the planarized IBC cells from the previous section were used as a platform. The patterning process used was similar to the process in the previous section, with the important difference that this time the Si was patterned, instead of SiN_x. Figure 4.6a shows the patterning sequence for these solar cells. Compared to the process shown in Figure 4.3a, there is no PMMA layer between the silica solgel mask and the layer that was patterned. The Si layer was RIE etched, and the mask was removed with an HF-dip. The methods section provides further details.

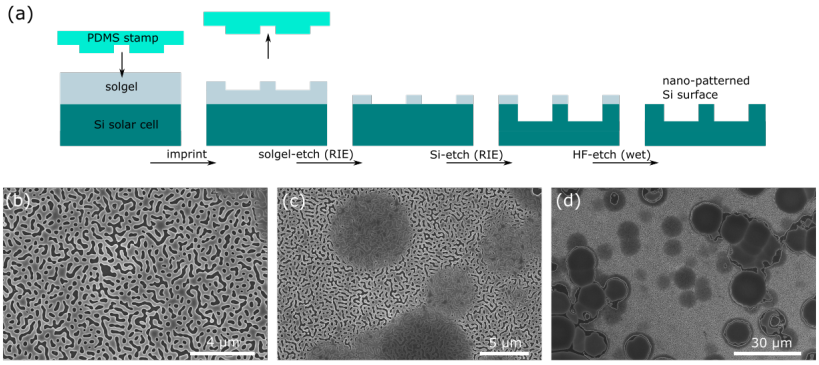

Figure 4.6: (a) Patterning sequence. The PDMS stamp was pushed into the liquid solgel. After the solgel had cured, the stamp was removed. The residual solgel layer was removed by reactive ion etching (RIE). Then, the Si surface was patterned by etching (RIE) into it. The etch mask was removed by lift-off in HF-solution. (b) SEM top-view of a spinodal HUD pattern[221] etched into Si. (c) Zooming out reveals darker patches which correspond to areas where the breakthrough was not successful. (d) On a very large scale, the pattern did not cover the full sample. The pattern coverage improves for thinner and hence more planar Si IBC cells. The solgel mask was still on the sample in (b)-(d).

Figures 4.6b-d give insight into the Si solar cell surface after the patterning process. On the small scale (Figure 4.6b), we found that the patterning works well and yields clean structures. On larger scales (Figure 4.6c&d), circular patches could be found across the sample, which we attribute to inhomogeneities in the stamping, as discussed for Figures 4.3b-d. Note that the fraction of unsuccessfully patterned Si likely decreases for thinner Si solar cells, as these are more planar.

4.4.2. Electronic simulations of the impact of surface recombination velocity and surface area on the electronic passivation for nanopatterns in Si

Patterning the Si absorber layer directly increases its surface area, which means that the electronic surface passivation quality requires special consideration. In the following, we

perform 2D finite element drift-diffusion simulations, using Ansys Lumerical CHARGE. Simulations were run for different surface recombination velocities (SRV) and different surface areas, and $I-V$ curves were extracted for every simulation. The charge carrier generation was set to 30 mA/cm^2 and the Si wafer was 3 µm thick. Such high generation in a thin Si slab is an optimistic scenario[86], but very suitable to the final goal of our work, achieving high carrier generation in very thin Si solar cells. The methods section provides further details.

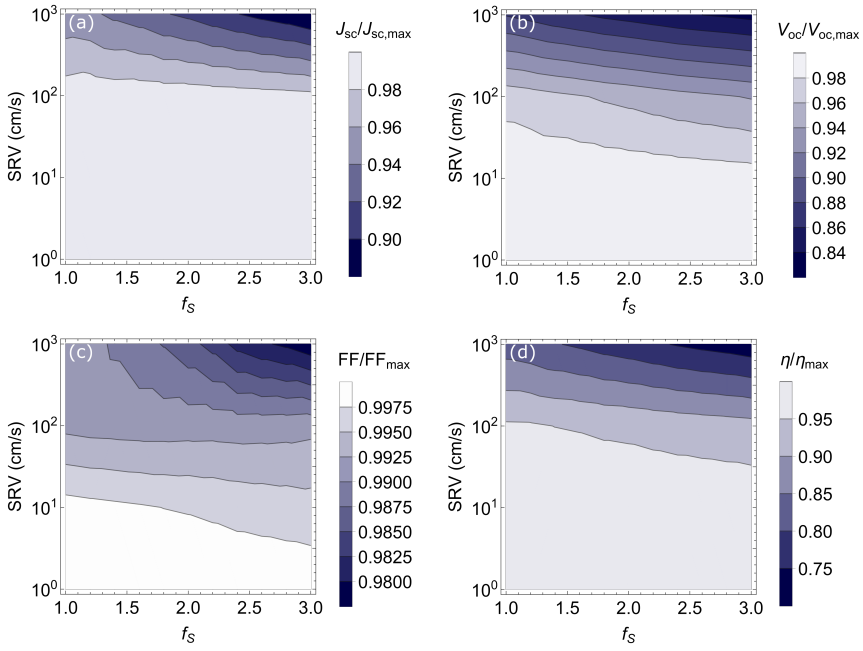

Figure 4.7: Simulated electronic parameters as a function of surface recombination velocity (SRV), and surface area enhancement factor (f_S). The colorscale corresponds to the value of the parameter relative to the maximum value found in the simulations. Darker colors indicate lower values. The panels show (a) the short-circuit current density (J_{sc}), (b) the open-circuit voltage (V_{oc}), (c) the fill factor (FF), and (d) the efficiency (η).

Figure 4.7 shows the solar cell parameters relative to the performance of a planar (f_S=1) cell with a SRV of 1 cm/s. The effect of the SRV on the J_{sc} is negligible (less than 2%) for SRV lower than 100 cm/s, irrespective of surface area. The V_{oc} was affected more strongly by the surface area and the SRV, but losses stayed below 2% for an SRV of 30 cm/s and lower. The changes in FF were negligible in comparison and are less than 2% across the full parameter range investigated. For a SRV of 30 cm/s and 3-times larger surface area (f_S=3) than in the planar case (f_S=1), an efficiency loss of 5%-relative was predicted. For comparison, a planar surface yields 5% efficiency loss at an SRV of 100 cm/s, which implies that a 3-times larger surface roughly translates to the effect of a 3-times larger SRV, for this specific parameter range. Overall, for high-quality passivation[238–240] below 10 cm/s, the relative efficiency loss for a 3-times larger surface is only 0.7% compared to a planar surface, showing that losses due to the increased surface

area are negligible. As light trapping architectures are typically designed to improve the efficiency by more than 0.7%-relative, they can compensate for this loss and yield a net efficiency gain. For reference, pyramidal texture corresponds[242] to an f_S between 1.3 and 1.8, while the HUD designs described by Tavakoli *et al.*[221] range from 1.8 to 3.3.

4.5. Conclusion

We have fabricated SiN_x nanocylinders arranged in a periodic lattice as an electronically flat and optically patterned anti-reflection coating on interdigitated back contact Si solar cells. The layer of nanocylinders formed an effective anti-reflection coating embedded with Mie resonators that efficiently forward scatter light in a broad spectral band. The nanopatterned solar cells showed significant current gains after patterning, compared to cells with a planar surface, with the best cell achieving a J_{sc} of 36.9 mA/cm^2 (up from 27.7 mA/cm^2 for planar cells), and a power conversion efficiency of 16.3%. The measured *EQE* showed good agreement between simulated and measured data, validating the combined effect of Fabry-Pérot and Mie resonances leading to enhanced light incoupling. The SCIL nanopatterning technique was found to be well suited for cell processing, with some surface inhomogeneities that can be avoided by using an automated imprint system. Based on our experimental data, we expect that annealing to further improve surface passivation will further enhance the short-circuit current by 2.0 mA/cm^2 to about 39 mA/cm^2. Using the planar nanopatterned geometry instead of conventional macroscopic surface texture led to a short-circuit current deficit of about 4.2 mA/cm^2 due to reduced light trapping in the 900-1200 nm spectral band. We also presented the first steps towards integrating a hyperuniform Si structure, that is capable of efficient light trapping, on the front surface of thin Si solar cells. We achieved comparable pattern quality as for the nanopatterned SiN_x AR coating and evaluate the electronic passivation requirements by means of electronic simulations. We predict that recombination losses from the increased surface area become negligible for surface recombination velocities below 10 cm/s. Overall, the data provide a roadmap for the development of wafer-based flexible solar cells, where the nanopatterned SiN_x can replace the conventional macroscopic surface texture for efficient incoupling, and at same time we present planarized and thinned commercial IBC solar cells as a demonstrator platform for other research questions, such as the electronic passivation requirements for nanostructured Si surfaces.

4.6. Appendix

4.6.1. Dependence of electronic parameters on annealing treatment for improved passivation

Annealing (400°C, 10 min, ambient) of the solar cell to improve the Al_2O_3 passivation[243] usually does not affect the solar cell negatively (Figure 4.2d). In some cases, we have found that it affected the *FF* negatively. Figure 4.8 shows a comparison between two batches (11-12 samples each) that were fabricated identically during the same fabrication run, with the only difference being that one was annealed after Al_2O_3 and SiN_x deposition, and the other was not.

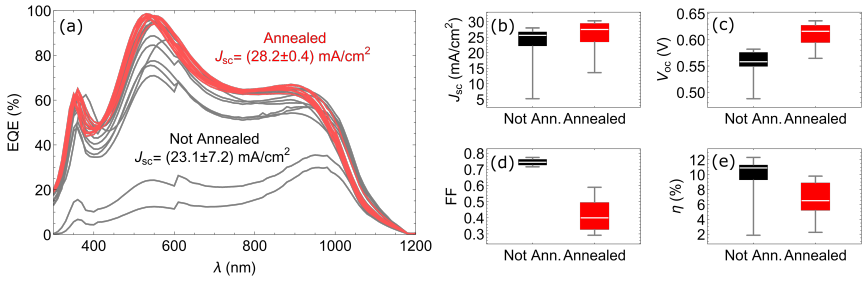

Figure 4.8: External quantum efficiency (EQE) of cells of two distinct batches. One batch of samples was annealed (red), the other batch not (gray). (b)-(e) Short-circuit current density (J_{sc}), open-circuit voltage (V_{oc}), fill factor (FF), and efficiency (η) for the annealed (red) and not annealed (black) batch.

4

It becomes clear that annealing improves the J_{sc} and EQE significantly (2 mA/cm^2 on average). At the same time, also the V_{oc} strongly increases (60 mV on average), but these gains are offset by a large loss in FF (from 75% down to 40%). This large drop in FF does not always occur, but to ensure that the solar cell devices remain comparable to one another, we chose to work with the not annealed batch for the fabrication. We believe that this significant drop in FF was related to proprietary features of the commercial IBC solar cells used in this work. Consequently, we would recommend annealing post dielectric film deposition to activate surface passivation fully.

4.6.2. Methods

Optical simulations

For Figure 4.1, Ansys Lumerical FDTD[229] was used to solve Maxwell's equations numerically. The simulation mesh accuracy was set to "3", and "conformal variant 0". Periodic boundary conditions were used to reproduce the unit cell in both directions along the Si surface plane. Perpendicular to the plane, perfectly matched layers (PML) were used at the boundaries. A broadband plane wave source was used, and the monitor used to detect the transmission was inserted at the SiN_x – Si interface. The simulation was conducted for various structure parameters, which were adapted according to a particle swarm optimization. The field profile was obtained from a single particle scattering simulation, which uses PML at all simulation boundaries, and a total-field scattered-field (TFSF) source.

Electronic simulations

For Figure 4.7, Ansys Lumerical CHARGE[244] was used to solve 2D drift-diffusion equations numerically using the finite element method. The simulation geometry was adapted from the standard example for a silicon solar cell[245]. The cell design was changed such that it represents an IBC cell and front contacts and associated doped regions are moved to the rear. The bulk was set to be n-type doped with a carrier concentration of 10^{15} cm^{-3}. After convergence testing, the minimum mesh triangle length was set to 10 nm. To simulate increasing surface area, Si pillars were placed on top of the main Si slab. They had a width of 250 nm, and a pitch of 500 nm, which are dimensions that represent many

nanostructures fairly well, amongst which the one of Tavakoli *et al.*[221]. The pillar height (h) was varied to simulate the larger surface area (Figure 4.9), which was parameterized by the surface area enhancement factor (f_S) and given by $f_S = 1 + \frac{2h}{500}$ with h in nm. The surface recombination velocity (SRV) was varied at the interface between Si and the passivation layer (set to the same value for holes and electrons). $I-V$ curves were obtained by sweeping the applied voltage for one of the back contacts. Note that the generation is confined to the bulk Si layer (Figure 4.9), does not extend into the Si pillars, and is described by a Beer-Lambert profile. More realistic light trapping structures would exhibit generation in the pillars, as well as an overall more uniform generation profile in the bulk.

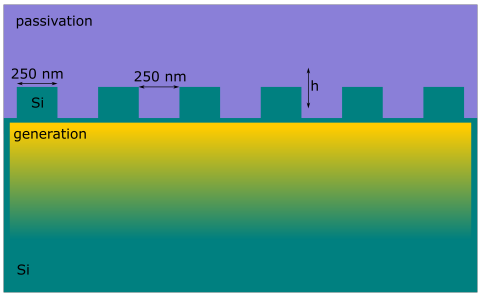

Figure 4.9: Simulation setup scheme. 2D Si pillars are placed on the Si front surface. Width and pillar-pillar separation are both 250 nm. The height is varied during simulations. The optical generation profile (yellow gradient) is confined to the bulk Si layer. The passivation layer fills the half space to the top.

Planarization

To planarize the front side of the double-textured solar cells, their backside is protected using the parylene-C polymer. It was deposited by vaporizing a solid parylene dimer precursor and by splitting it into monomers at high temperature (650°C). The hot vapour was channeled into a cool (room temperature) chamber that contains the cells, where the vapour forms the polymer on all exposed surfaces. Parylene-C is resistant to all chemicals used for the processing. For the electronic characterization, the parylene layer that covered the contacts was removed with a reactive ion etch (O_2 at 20 sccm, 200 W , 15 mTorr, 90-150 min). The initial SiN_x layer on the solar cell was removed by dipping the parylene-protected solar cell into HF solution (4.5%, approximately 10 minutes, no agitation) until the front surface appears gray and appears hydrophobic. The planarization is done by HNA-etching. Great care for personal safety must be taken during this process, as the used chemicals are extremely hazardous in their individual and combined form. Hydrofluoric acid (HF, 49%), nitric acid (HNO_3, 70%), and acetic acid (CH_3COOH, glacial) were mixed at a ratio 10:73:17, according to Yu *et al.*[246]. A stirring bar is added to 500 ml of HNA solution and accelerates the etch rate (typically by a factor 4). The parylene-protected solar cell was dipped in the solution, and the planarization was monitored by looking at the gradually increasing specularity of the initially diffuse Si surface. Depending on the agitation and the HNA volume, planarization took 15–60 minutes. Thinning to 30 µm Si thickness took another 40-60 minutes. Afterwards, the

samples were taken out of the solution and thoroughly rinsed in water.

Patterning
We used substrate conformal soft-imprint lithography (SCIL) [106,107] for the patterning. Silica solgel was spin-coated at 2000 RPM for 8 s, to form a layer of 74 nm thickness. The stamp was pushed into the liquid silica gel, and removed after 6 min of curing at room temperature. The stamp dimensions are the same as in Figure 4.1, except for the height of the pillars. The height of the pillars and the thickness of the bottom layer is regulated with the initial SiN_x thickness and the etch duration. To etch specific layers, we used the following reactive ion etch (RIE) chemicals, of which the durations were adjusted depending on the desired thickness: silica solgel was etched with CHF_3/Ar. Si is etched with a short (11 s) pre-etch using Cl_2, and followed by the main HBr/O_2 etch. PMMA was etched by O_2. SiN_x is etched by CHF_3/O_2.

Passivation
For the passivation of the planar front surface with Al_2O_3, the solar cell surface was cleaned with an RCA cleaning procedure [247]. Sequentially, the sample was dipped in RCA-1 ($H2O_2$:NH_4OH:H_2O (1:1:5); 80°C; 10 min), RCA-2 (H_2O_2:HCl:H_2O (1:1:5); 80°C; 10 min), and HF (4.5%, 2 min). The sample was blow-dried with a N_2-gun after the HF cleaning step. Within 30 minutes after the last cleaning step, the sample was loaded and under vacuum in a Picosun R-200 atomic layer deposition (ALD) system. The cell was heated to 200°C, and 100 cycles of a water (H_2O) and tetramethylammonium hydroxide (TMA) deposition sequence were run to deposit 10 nm of Al_2O_3. The SiN_x layer was deposited by plasma-enhanced chemical vapour deposition (PECVD), using a Oxford Instruments Plasmalab 100 PECVD tool. The SiN_x layer (180-200 nm) was deposited at 300°C from silane (SiH_4) and ammonia (NH_3) precursors. To improve the Al_2O_3 passivation, an annealing step was done in some cases. The cells were deposited on a 400°C hot Si wafer on a hotplate and left there for 10 minutes, in air.

Electronic characterization
For the electronic characterisation, the solar cells were mounted on a stage with an aperture that is smaller than the solar cell area. The cell was contacted from the back, with 2 (EQE) or 4 ($I-V$) contacting probes pressing the cell onto the aperture rim, thereby fixing its position. The stage was then flipped over so that the front surface of the solar cell faced upward in the AM1.5 solar simulator. For the external quantum efficiency (EQE) measurements, a PV measurements QEX7 system was used. The samples were brought into a focal spot with dimensions 1×4 mm^2 under bias light. Current – voltage ($I-V$) curves were measured using a WaveLabs SINUS 220 tool. The obtained current values were normalized by the aperture size (8x8 mm^2 in most cases) to obtain the current density.

4.7. Author contributions

A. Cordaro performed optical simulations. S.W. Tabernig, M. Pollard, and C. Yi fabricated and characterized the IBC cells. S.W.T., A.C., A. Lambertz, and M.P. characterized the patterned solar cells. B. Hoex, E. Alarcón Lladó, M.P., and A. Polman supervised the project. All authors contributed to the writing of the manuscript and gave feedback.

5

Detailed-balance efficiency limits of two-terminal perovskite/silicon tandem solar cells with planar and Lambertian spectral splitters

5.1. Abstract

We derive the photovoltaic conversion efficiency limit for two-terminal tandem solar cells with a perovskite top cell and silicon bottom cell with an embedded spectrum splitter. For large-bandgap top-cells a spectrum splitter strongly enhances the efficiency because of enhanced light absorption and trapping. A Lambertian spectral splitter shows a significantly improved effect compared to a planar splitter: we find an ideal efficiency enhancement for a 500 nm thick top cell of 6% absolute for bandgaps above 1.75 eV. Vice versa, the use of a spectral splitter geometry enables the use of a thinner top cell. Using experimental parameters for perovskite cells we show that for a top-cell bandgap of 1.77 eV a 2.7% absolute efficiency enhancement can be achieved. The calculations in this work show that integration of a spectral splitter into perovskite/silicon tandem cells for which the top cell is limiting the overall current can lead to a large increase in efficiency, even with realistic experimental losses and non-unity reflection of the spectral splitter.

5.2. Introduction

At present, solar photovoltaics (PV) has an installed capacity of around 600 GWp worldwide[248]. Following the IRENA roadmap, by 2050 PV should reach an installed capacity of 8.5 TWp to account for 43% of the total installed power capacity for electricity generation[249]. With the costs of the cells determining only a small part of the costs of a PV system, raising their efficiency is a key method to reduce the cost of PV per kWp. Also, higher-efficiency panels take up less space, which is essential as PV is applied at very large scale. Therefore, in PV research it is crucial to fight for every digit that can be gained in cell efficiency. With 95% of the total production in 2019, the market is strongly dominated by single-junction Si-wafer based PV technology[200]. Silicon-based tandem solar cells have the potential to raise the efficiency beyond the theoretical limit of 29.4% for Si-only cells[250]. The combination of perovskite and Si in a 2-terminal (2T) or 4-terminal (4T) tandem configuration is one of the most growing and promising concepts. Recently, a Si-perovskite 2T tandem solar cell was presented with an efficiency of 29.15%[251] well above the record for a single-junction Si cell of 26.7%[252].

One aspect that is of high importance to improve the performance of tandem cells is light management to optimize the coupling and distribution of sunlight in the tandem subcells[253–256]. Recent work has focused on minimizing reflection from the top or interlayers[257–260] and reducing parasitic absorption in the inactive layers such as transparent conductive layers[255,261,262], and to optimize light trapping in the top and bottom cells[263,264]. A concept that has not been studied in much detail is to control the spectral splitting of light directed into the two subcells[265]. We note that other light management strategies to enhance efficiency such as enhanced light incoupling and backreflection from the bottom cell are also relevant; they are not discussed here[266]. Spectral splitting can be achieved by an additional interlayer between the top- and bottom cells that effectively reflects the part of the spectrum with energy above the bandgap of the top cell, and that transmits the remainder to the bottom cell. In an ideal case, the low- and high-energy spectral bands are fully split between the cells, so that maximum current and voltage can be harvested. However, in practical geometries a low-energy tail close to the top-cell bandgap is always transmitted due to incomplete light absorption in the top cell and is then absorbed in the underlying cell (Figure 5.1a). This transmitted tail creates higher thermalization losses in the bottom cell and should thus be avoided.

Earlier, spectral splitting in 4T tandem cells has been modelled[265] and it was predicted that, by integrating a spectral splitting light trapping layer, an efficiency gain between 0.5% and 3% (absolute) and a two- to threefold reduction in thickness of the top cell can be reached, depending on the diffusion length of the absorber material. The benefits of spectral splitting in 2T tandem concepts have been studied previously to achieve current matching between top and bottom cell, using Bragg reflectors[268–271] or three-dimensional photonic crystals[272–274] as intermediate layers, and small spectrum splitting improvements for Si-based top and bottom cells could be shown. Current matching is a limiting factor in 2T perovskite/Si tandems for perovskites with a bandgap below E_{BG}=1.73 eV. In that case the current generated in the perovskite can exceed that in the Si, depending on the absorption in the top cell, in which case no spectral splitter is needed. However, a spectral splitter enables the use of a smaller perovskite cell thickness to obtain current matching with low-gap perovskites. This can already lead

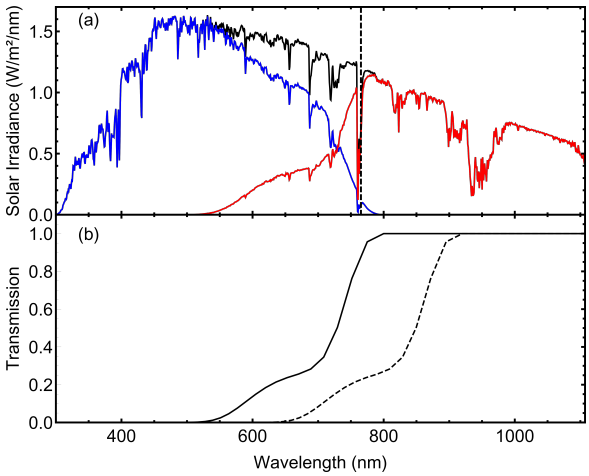

Figure 5.1: (a) AM1.5G solar spectrum (black line) with theoretical absorption in 500-nm-thick perovskite top cell (blue line) and spectrum directed into Si bottom cell (red line). The vertical dashed line marks the position of the bandgap E_{BG} = 1.62 eV. (b) Transmission spectrum of 500-nm-thick perovskite with E_{BG} = 1.62 eV (solid black line) from Werner *et al.*[267] and modelled transmission for 500-nm-thick perovskite with E_{BG} = 1.4 eV (dashed black line).

to cheaper solar cells and higher throughput in fabrication, as well as lower toxicity per unit cell area. In addition, for tandems with higher perovskite bandgaps, which have the largest potential tandem efficiency, and which have applications in photoelectrochemical splitting of water because of their high voltage[275,276], for example, spectrum splitting has significant potential to enhance the efficiency. In the following, we show for which conditions a spectral splitter in a 2T perovskite/Si tandem cell is beneficial and what efficiency gains can be achieved. We make a distinction between planar spectral splitters with specular reflectivity, and spectral splitters with a Lambertian scattering distribution that enhances light trapping in the perovskite top cell.

5.3. Methods

Throughout the article, we use detailed-balance calculations[95] to determine the theoretical maximum efficiencies of the different 2T tandem configurations. These calculations are based on balancing the bandgap dependent absorption flux (light generated current from the AM1.5G spectrum) with the bandgap and voltage dependent emission flux (via Planck's equation). From this, current-voltage curves can be constructed. Auger recombination in Si and other non-radiative processes are not taken into account and we assume full current collection from light that is absorbed in the top and bottom cells, meaning ideal electronic properties. While such theoretical maximum efficiencies cannot be reached in reality, they allow a more systematic comparison between different configurations. Similar trends as we find here will also apply for tandem designs in realistic experimental geometries, as we will discuss further on. We differentiate between three cases of light absorption in the perovskite top cell:

1. Full absorption up to the bandgap as is typically done in detailed-balance limit calculations;
2. Ideal current splitting that assumes that the top cell absorbs exactly the amount of light such that half of the maximum possible current of the bottom cell (as a single-junction cell) is generated in the top cell;
3. Single pass absorption of a semi-transparent top cell with finite thickness d:

$$A_{TTC} = 1 - e^{-\alpha d} \tag{5.1}$$

with α the absorption coefficient for the transmitting top cell (TTC). To model the bandgap-dependent absorption in the perovskite top cell we use the wavelength-dependent absorption coefficient of CsFAPbIBr with a bandgap of E_{BG} = 1.62 eV[267] which is in the bandgap range of the most frequently used perovskite top cells. Figure 5.1b shows the transmission of a 500 nm thick layer of this material (black solid line). The transmission for perovskites with the same thickness but different bandgap was then modelled by shifting the graph by the bandgap shift (Fig. 1b), similarly to Köhnen *et al.*[277]. Our simplified model of light absorption might not fully reflect transmission for specific perovskites with different material compositions and bandgaps, however, it allows us to systematically compare the effect of transparency of the top cell for different bandgaps.

5.4. 2-terminal tandem efficiencies with semitransparent top cells

The limiting efficiency for 2T tandems, assuming perfect absorption up to the bandgap in the top cell of the perovskite/Si tandem, is maximal for E_{BG}=1.73 eV with an efficiency of 45.1%[278] (Fig. 2). This limit strictly adheres to the assumptions that are made for the single-junction detailed balance limit, and will be referred to as infinite (top cell) thickness (IT) limit. The limiting efficiency gradually decreases as the top-cell bandgap approaches the Si bandgap (1.12 eV), where all light up to that energy is absorbed in the top cell with no current left for the bottom cell. We then define the current splitting (CS) limit as a condition, for a given perovskite bandgap, where the top cell is not fully absorbing up to its bandgap, but rather absorbs an optimized smaller fraction to obtain current matching (Fig. 2). In this ideal case the top cell absorbs light such that exactly half of the maximum possible current of the bottom cell (as a single-junction cell) is generated in the top cell. This requires a top cell with a bandgap below 1.73 eV. For bandgaps below 1.73 eV the CS limit is well above that for the IT limit of fully absorbing top cells. For higher perovskite bandgaps full absorption in the top cell is always optimal and equal to the CS limit.

As described above, for any perovskite bandgap the optimized absorption, or equivalently transmission, of the top cells can be realized by selecting the proper top cell thickness (see method section). We calculate the detailed-balance limiting efficiency using the modeled transmission (1) for thicknesses in the range 250-1000 nm as a function of bandgap of the top cell (Fig. 2). Several trends can be observed in this figure. First, the shape of every individual TTC limit is similar to the shape of the IT limit, with a pronounced maximum efficiency that is quickly decreasing for lower or higher bandgaps.

This is because of the large sensitivity of 2T tandem cells to unbalanced currents in the top and bottom cells. For bandgaps below 1.73 eV the maximum efficiency for every thickness is much higher than the one derived from the IT limit assuming full absorption. The maximum of all four graphs for different thicknesses match the CS curve at the bandgaps where the currents are matched.

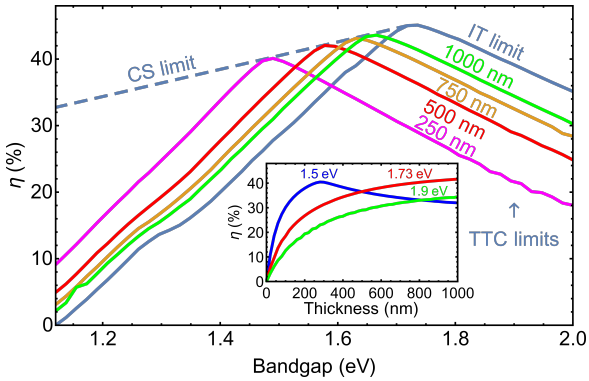

Figure 5.2: Detailed-balance efficiency limits for 2T tandem solar cells with Si bottom cell: Infinite (top cell) thickness limit (IT) assuming perfect absorption in the top cell (solid blue line); Current splitting (CS) limit assuming ideal splitting of the spectrum for perfect current matching in top and bottom cell (dashed blue line); Transmitting top cell (TTC) limit assuming realistic absorption/transmission in a perovskite top cell for top cell thickness in the range 250-1000 nm. Inset: Comparison of dependence of efficiency on top cell thickness for three different perovskite top cell materials with E_{BG} = 1.5 eV, E_{BG} = 1.73 eV and E_{BG} = 1.9 eV.

Figure 5.2 shows there is a wide range of perovskite bandgaps (1.5 to 1.7 eV) for which very high 2T tandem efficiencies can be reached by optimizing the perovskite thickness in the practical range of 250-1000 nm. For top cells with bandgaps higher than E_{BG}=1.73 eV, the TTC limit is much lower than the IT limit, because incomplete absorption in the top cell due to the limited thickness limits the overall current. This is where a spectral splitting light trapping layer could be of special interest. Transmitted light above the bandgap is then reflected and trapped in the top cell, such that the infinite thickness limit could be approached for those bandgaps even with finite top cell thicknesses. This is discussed in detail in the next section. The described trends are illustrated by the inset in Figure 5.2 where the TTC limit versus thickness of the top cell is plotted for three different bandgaps. For a bandgap below E_{BG} =1.73 eV an ideal thickness can be chosen to reach the maximum TTC efficiency for that bandgap (e.g. 280 nm at 1.5 eV, see the inset). For bandgaps of E_{BG} =1.73 eV and higher, the cell ideally is 'infinitely' thick to absorb all light above the bandgap energy.

5.5. Planar and Lambertian spectral splitter

Next we discuss the effect of a spectral splitter in between the top and bottom cell of a 2T tandem cell. We distinguish between: (1) a planar spectral splitter that reflects the light specularly back to the top cell and creates one extra path for absorption in the top cell; (2) a Lambertian spectral splitter that reflects the light back in a cosine angular fashion such that enhanced light trapping can be achieved in the top cell. Figure 5.3a shows a

schematic of both spectral splitter geometries. The reflectivity $R(\lambda)$ of the spectral splitter is defined as a step function with tunable step wavelength λ_{step} and reflectance r:

$$R(\lambda) = \begin{cases} 0, & \lambda > \lambda_{step} \\ r, & \lambda \leq \lambda_{step} \end{cases} \tag{5.2}$$

In both cases, we assume that light that is not reflected is transmitted losslessly to the underlying Si substrate. We add one additional absorption path in the top perovskite cell with length d for the planar splitter and length $d_{eff} = d\frac{2+x}{1-x}$ with $x = a(\alpha d)^b$, $a = 0.935$ and $b = 0.67$ to represent the angular distribution scattered by the Lambertian splitter[214,265]. The absorption in the bottom cell is modified to account for the reflectivity R.

First, we assume that the reflectivity is split at the bandgap of the top cell ($\lambda_{step} = \lambda_{BG}$) and assume r=1. In that case for both spectral splitter configurations the absorption in the Si bottom cell is identical to the one in the infinite thickness limit as no light below the top cell bandgap energy is transmitted to the bottom cell. Figure 5.3b shows the tandem efficiencies for a 500 nm thick perovskite top cell, comparing the TTC limit with the planar and Lambertian spectral splitting limits. Figure 5.3c shows the corresponding top and bottom cell currents. For a 500 nm top cell the planar or Lambertian spectral splitters strongly improve the tandem efficiency. At 1.70 eV the Lambertian splitter increases the tandem efficiency by more than 5% to 42.9%. Interestingly, this is even beyond the TTC maximum of 42.0% that occurs for a bandgap of 1.58 eV, reflecting the trend that the higher the absorption in the top cell, the closer the ultimate IT limit that assumes full absorption, which occurs at 1.73 eV, is achieved.

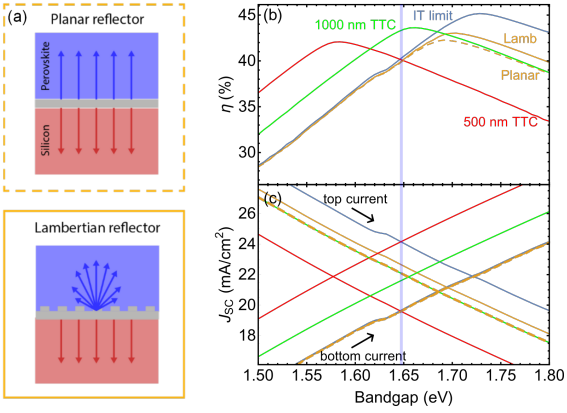

Figure 5.3: Spectral splitter in 2T tandem cell. (a) Schematics of planar and Lambertian spectral splitter (in gray). Light is selectively scattered back to the perovskite top cell (blue). The remainder of the spectrum is transmitted to the underlying Si cell (red). (b) IT limiting efficiency for full absorption in the top cell (blue line), TTC limit with 500 nm (red) and 1000 nm (green) thick perovskite top cell. Limiting efficiencies of 2T tandems with 500 nm thick perovskite top cell and planar (dashed yellow line) and Lambertian spectral splitter (solid yellow line). (c) J_{sc} of top and bottom cell of tandem cells for all limits from (b). The graphs increasing and decreasing with bandgap represent the current of the top and bottom cells, respectively. The bottom cell curves for Planar, Lamb, and IT overlay with each other.

To further illustrate the benefit of the spectrum splitters, we show the TTC limit of a 1000 nm top cell in the same figure and compare the short-circuit current J_{sc} of the top and bottom cells in in the lower panel. The top cell J_{sc} for the 1000-nm-thick cell and the 500 nm cell with planar spectral splitter is identical for all bandgaps as the top cell thickness is effectively doubled by the planar spectral splitter. The bottom cell current, however, is always lower for the 500-nm-thick cell with spectrum splitter. This is because for the planar geometry above-bandgap light that is not absorbed in the top cell is transmitted into the Si bottom cell, while with the spectral splitter it is reflected and lost from the front side of the top cell. For the larger bandgaps, the efficiencies of the 1000-nm-thick cell and the 500 nm cell with planar spectral splitter become equal as the identical top cell currents are the limiting factor in both tandems.

The benefit of the Lambertian splitter over the planar splitter is twofold: it further enhances absorption in the top cell due to the larger angular scattering range, and, as a result, less light is lost from the front of the cell. Consequently, the top cell current of the cell with Lambertian spectral splitter is consistently higher than that of the planar spectral splitter while the bottom cell current of both cases is equal.

The bumps in current and efficiency around 1.63 eV that can be observed for the IT limit as well as the planar and Lambertian spectral splitters come from the fact that within the range between 1.60 eV and 1.63 eV the AM1.5G spectrum contains almost no photons, and hence the change in current within the top and bottom cells is negligible.

5.6. Splitting conditions

Next, we investigate the influence on the efficiency of an offset (ΔE) of the step energy from the top cell bandgap energy as well as incomplete reflectance from the spectrum splitter. This is of interest because it has been found that for 4T tandem cells, especially for planar reflectors, the escape losses from the front side of the cell for light at energies just above the top cell bandgap can be detrimental for the overall tandem performance[265]. To avoid this, we shift the reflection spectrum to slightly higher energy, so that the non-absorbed spectral band just above the top-cell bandgap is transmitted to the Si bottom cell. Figures 5.4a and b show the efficiency gains/losses $\Delta\eta$ for a 500 nm top cell with a bandgap of 1.7 eV as a function of ΔE and r, with and without planar and Lambertian spectral splitter, respectively. The gain/loss $\Delta\eta$ is calculated from the difference between a cell with spectral splitter and a cell without, meaning only with realistic reflection (5 to 6% within relevant range) that arises from the difference in refractive index at the perovskite-Si interface. In both cases (planar/Lambertian) the best result is found for the highest reflectivity of the spectral splitter, but the figure shows that also for non-ideal splitters with r<1, as they may be made experimentally, large efficiency gains are expected. For the planar splitter a maximum achievable efficiency enhancement of 4.2% is found; for the Lambertian one a gain of 5.1% is expected. In both cases, the optimum is found for a shift in the reflectance edge by about 20 meV above bandgap of the top cell. The maxima are marked with black stars in Figure 5.4a,b.

To further study the impact of the reflectance r we calculate the possible efficiency gain as a function of top cell bandgap for a Lambertian spectral splitter with 500 nm top cell thickness (Fig. 4c), again in comparison to a tandem cell with realistic perovskite-Si interface reflection. In agreement with what is described above, efficiency gain is ob-

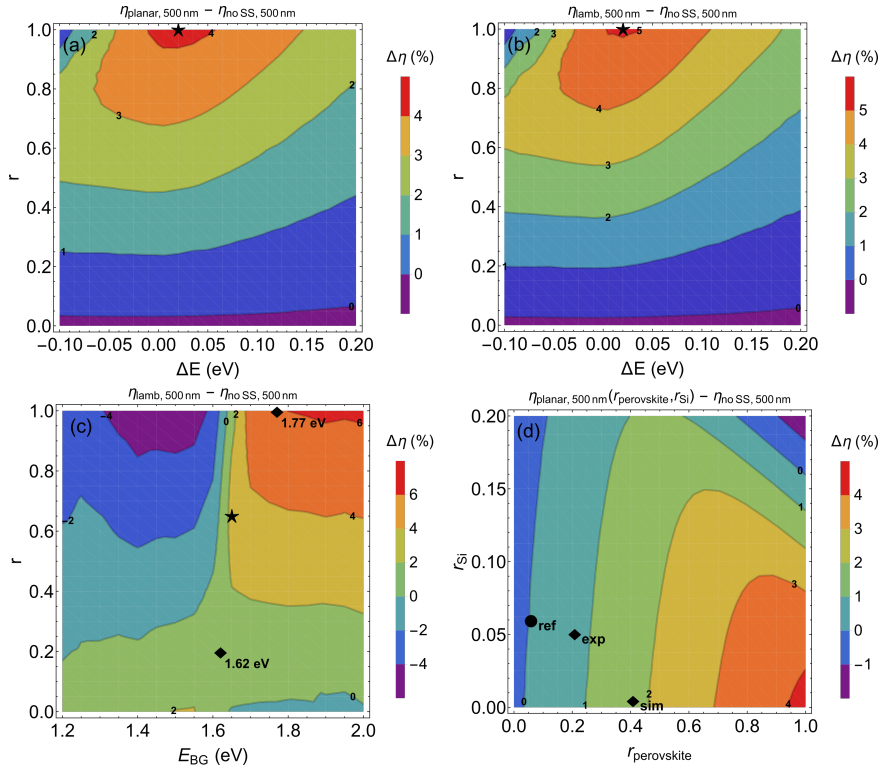

Figure 5.4: Absolute efficiency gain of 2T tandem cells depending on reflectance of the spectral splitter, the step wavelength and parasitic absorption in the spectral splitter. Efficiency gain for tandem cells with planar (a) and Lambertian (b) spectral splitter and 500-nm-thick perovskite top cell with E_{BG}=1.7 eV compared to TTC limit of the same cell, as function of ΔE and r. The stars in (a) and (b) represent the largest efficiency enhancement. (c) Efficiency gain for tandem cell with Lambertian spectral splitter and 500-nm-thick top cell as function of top cell bandgap and reflectance r with ΔE=0.02 eV. The star indicates the ideal spectral splitting condition for maximal efficiency gain for a tandem cell with a 500-nm-thick perovskite top cell with E_{BG}=1.65 eV. The diamonds mark the position of maximum gain for two examples of realistic perovskite-silicon cells with E_{BG}=1.62 eV and E_{BG}=1.77 eV. (d) Efficiency gain using a planar spectral splitter as function of reflection above ($r_{perovskite}$) and below (r_{Si}) the cutoff energy. The perovskite bandgap is 1.7 eV and ΔE=0.02 eV. The diamonds mark experimental (exp) and simulated (sim) results for a 4T spectral splitter[279]. The dot (ref) refers to the calculated reflection at a realistic perovskite-Si interface. All figures assume no parasitic absorption.

served for the highest top cell bandgaps, while a loss is observed for the lowest gaps. However, we find that variation of r allows further optimization depending on the top-cell bandgap. An interesting subtlety occurs just at the cutoff energy 1.65 eV. Contrary to what was observed for the spectral splitter with r=1 in Figure 5.3b, also for smaller bandgaps a spectral splitter geometry can be beneficial if the reflectivity is reduced. In Fig. 4c one can see that also here a Lambertian spectral splitter is beneficial and increases the efficiency by 2.7% absolute (marked with black star in Figure 5.4c), if the reflectance is set to be r=0.65. In detailed balance calculations, an equal increase can be reached by increasing the thickness of the top cell, however, in practice an increase in

thickness leads to losses in the V_{oc}. For very low reflectivity and small bandgaps (around 1.5 eV), the efficiency gain goes up as well because for these low bandgaps the bottom cell is limiting and for reflectivity values below 0.05 more light is transmitted into the Si bottom cell, compared to the reference that assumes realistic reflection values at the interface. While the combined bandgap and reflection range for this phenomenon is small, such gains could for example be achieved with a graded intermediate layer, effectively acting as an interface AR coating[260]. However, for larger bandgaps and low reflectivity, exactly this transmission into the Si layer causes efficiency loss, as the Si cell is not current limiting in this case.

So far, we have assumed r=0 for energies below the cut-off energy. To investigate how a non-zero value for r affects the overall performance, we plot the efficiency enhancement as a function of the reflectivity above ($r_{perovskite}$) and below (r_{Si}) the energy cut-off for a planar case compared to realistic interface reflection (Figure 5.4d). For small r_{Si}, $r_{perovskite}$ should ideally be as large as possible for highest efficiencies. In this case each subcell receives most of the light in the relevant spectral range. However, with increasing r_{Si}, the ideal $r_{perovskite}$ shifts to lower reflectivity values. This can be explained by considering that high r_{Si} corresponds to current loss in the bottom cell. As soon as the bottom cell is current limiting, the overall tandem current profits from a lower reflectivity above the cut-off energy, as this will mitigate the current losses in the limiting bottom cell. For example, at r_{Si}=0.15, the ideal $r_{perovskite}$ is found to be around 0.60. At this point the currents in the two sub-cells are matched. For larger $r_{perovskite}$ values, the efficiency gain decreases because the bottom cell current decreases, while the top cell current decreases for smaller $r_{perovskite}$ values. The circular marker in figure 4d is the calculation assuming realistic reflectivity of a perovskite-Si interface. The diamond-shaped markers indicate values of $r_{perovskite}$ and r_{Si} for experimentally realized and simulated 4T spectral splitters[279], showing that spectral splitting geometries with these reflectivities can be realized in practice.

We note that all calculations so far were based on an idealized set of assumptions. To get an idea of what efficiency enhancement can be expected in the Lambertian case for realistic materials, we applied detailed-balance calculations using data from selected record cells[280]. As a first estimate, we took a state-of-the-art perovskite/Si tandem cell with a top-cell bandgap of 1.62 eV. The corresponding EQE-spectra and thickness for the top cell layer were used to approximate the absorption coefficient around the bandgap, by assuming unity internal quantum efficiency. The resulting absorption coefficient was used to investigate the potential performance of a Lambertian spectral splitter for a 500 nm thick perovskite layer on top of Si. Figure 5.4c contains markers (diamonds) representing this comparison. In the case of the 1.62 eV perovskite, it turns out that an efficiency loss of 0.13% absolute is to be expected (in the detailed-balance limit) for an ideal reflectance of r=0.2.

So far, this analysis assumed detailed-balance-derived open-circuit voltage (V_{oc}) and fill-factor (FF) values. To get a more accurate estimate for realistic conditions, we approximate the tandem cell as a non-ideal diode under illumination described by 5.3:

$$J(V) = J_{sc} - J_0\left(e^{\frac{qV}{nkT}} - 1\right) \tag{5.3}$$

The overall current density $J(V)$ depends on the short-circuit current density J_{sc} and

the voltage dependent diode current density term with the voltage V, the reverse saturation current density J_0, an ideality factor n, Boltzmann's constant k and the temperature T=298.15K (standard test conditions). Using this equation, we can fit the effective recombination current J_0,tandem and ideality factor n_{tandem} of the full tandem device from the cell's IV-curve. The V_{oc} was calculated by using the J_{sc} for the Lambertian case as derived above in the detailed-balance calculations, plugging it into the non-ideal diode equation and solving the equation for $J(V) = 0$. Furthermore, we account for the local FF minimum around the current matching condition [281] by applying the same relative FF-loss that is observed in the detailed-balance analysis above on the listed FF value of the experimental cell. This comparison yields 0.17% absolute efficiency loss (r=0.2), just slightly lower compared to the initial estimate that was based on only adjusting the absorption coefficient to the experimental value.

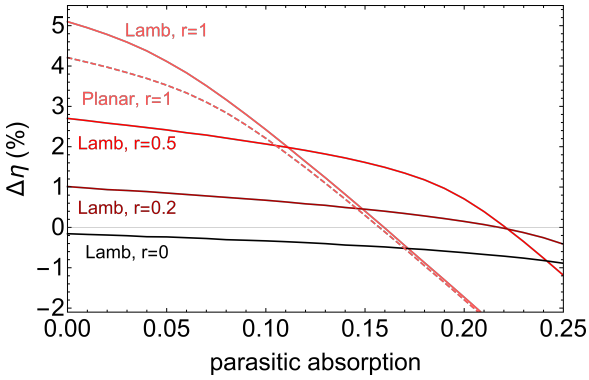

Figure 5.5: Efficiency gain for a 2T perovskite/Si tandem cell with Lambertian (solid lines) and planar (dashed pink line) spectral splitter and 500-nm-thick top cell, as function of parasitic absorption of the spectral splitter. The efficiency gains are with respect to a cell with realistic interface reflection and no parasitic absorption. ΔE=0.02 eV, E_{BG}=1.7 eV and r refer to reflection above the cut-off energy. The Lambertian case was plotted for different reflectivity values above the bandgap.

To get an estimate for a tandem cell with a higher perovskite bandgap, we take the top cell from the current perovskite/perovskite record tandem cell (1.77 eV) [280] and determine the absorption coefficient. In this case, due to the nature of the available data, we are limited to an estimation according to the first method used above. For the imagined case of such a top cell on top of a Si bottom cell, this analysis yields an efficiency enhancement of 2.7% absolute at a reflectance of r=1, highlighting that the significance of a Lambertian spectral splitter increases with the top cell bandgap.

We note that the efficiency gains according to this estimate are less than what Figure 5.4c suggests (diamonds). This is attributed to the fact that for the comparison with the record devices we derived the absorption coefficient from stated EQE spectra. This procedure tends to overestimate the absorption coefficient, as it also includes absorption beyond the first pass. Hence the absorption coefficient shows a sharper onset, which weakens gains from spectrum splitting layers. This is a fact that should be kept in mind. For absorption coefficients that strongly deviate in slope (either less or more direct bandgaps), the optimal bandgap values shift but the associated conclusions and

trends do not. Overall, this analysis underlines how much more relevant a spectral splitter is for large bandgap perovskite top cell than for small bandgaps.

Finally, an important parameter in the experimental realization of a spectral splitter are the losses that such a layer could introduce into the system. Figure 5.5 shows the efficiency gain/loss as a function of parasitic absorption, assuming spectrally flat parasitic absorption for a 500 nm thick cell at the perovskite-Si interface. We find that for a bandgap of 1.7 eV and ΔE=0.02 meV, the range for which a planar/Lambertian spectral splitter is still beneficial strongly depends on the reflection above the bandgap. To understand this, we need to remind ourselves that due to the placement of the spectrum splitter, all light that passes into the bottom cell will encounter it, but the light that is absorbed within the first pass inside the top cell will not. In the case of the top cell, only light that has been scattered back by the spectrum splitter will be affected by parasitic absorption. This means that the current in the bottom cell is linearly dependent on the parasitic absorption, while in the top cell only the fraction of the current that is generated due to reflection from the spectral splitter decreases linearly with parasitic absorption. Thus, when the top cell is current limiting, the dependence of the efficiency gain on parasitic absorption is much weaker compared to cases with a current limiting bottom cell. With increasing parasitic absorption, the loss in the bottom cell increases more rapidly, which means that in the limit of very high parasitic absorption, the bottom cell will always be the current limiting cell. For a bandgap of 1.7 eV, we find the interesting case that for maximum reflection (r=1) the top and bottom cells are roughly current matched, while for lower values of r the top cell is limiting and hence we see a shallower slope with decreasing r. The initial slope at r=0 is non-zero because current losses in the non-limiting subcell still affect the subcell's V_{oc} and FF and hence contribute to a slight loss in performance.

5.7. Realization

Considering the theoretical analysis above, and the estimates for what a realistic device with integrated spectral splitter could achieve, we will now give an outline of potential pathways towards realizing such a structure. One important property the spectral splitter needs to have is a sharp step in reflection at the desired cut-off energy, close to the perovskite bandgap. Such steps can be achieved using periodic nanostructures and have been shown for 4T SS devices[279], while other concepts, such as graded index interlayers[260] exhibit broadband features and hence cannot deliver step function-like reflection. While a Bragg reflector can enable a stepwise reflection as well, it can be difficult to retain the electronic performance of the cell and introducing Lambertian scattering from the interface is not possible with such a design. Furthermore, for the optical performance of nanopatterns, it is desirable that the materials that form such a layer exhibit a large contrast in refractive index. Lastly, integration of a spectral splitter in a 2T device requires careful assessment of the influence of used materials on the electronic performance of the cell, and hence two distinct pathways could be explored: fabrication by reshaping the perovskite-Si interface, or introduction of a new, electronically inert material to the interface region.

In the first case, we envision patterning an element of the interface, be it Si, perovskite, or another incorporated layer. Substrate conformal imprint lithography (SCIL[106])

could be used to transfer a nanopattern onto the cell. From this point, by using material removal techniques such as reactive ion etching, wet-etching, or lift-off in combination with deposition techniques, such as spin-coating, evaporation, and sputtering, the chosen material can be patterned. A specific example could for example be the patterning of a specific shape, such as in Neder *et al.*[279] into Si, and following this up by spin-coating perovskite on top, to surround these shapes. Taking into account the refractive index of perovskite as the surrounding medium, this could lead to similar resonances as shown previously for Si features on top of Si[231], and these can then be tailored into a spectral splitter layer with desired reflection features. From an electronic perspective, increasing the surface area of Si may lead to higher surface recombination.

In the second pathway we envision the introduction of a dielectric material that can passivate Si well, such as SiN or Al_2O_3, providing refractive index contrast and passivation at the same time. Provided that band-alignment and surface charge effects do not interfere with the migration of charges through the tandem cell, this could be another option of patterning the Si-perovskite interface. Other materials and patternable regions, such as the backside of the perovskite absorber, can also be considered, provided they do not introduce too large additional electronic losses at the interface. We also note that any pattern at the Si-perovskite interface can translate into a patterned front surface if the top layer is deposited conformally. In principle this can contribute to enhanced incoupling of light via mechanisms such as Mie-scattering, as is discussed in Ferry *et al.*[282].

These two pathways involve 1-2 steps for the creation of a patterned interface. For an efficiency gain of 2.7%, as calculated for large band gap perovskites, this corresponds to a range of 1.3% to 2.7% efficiency gain per fabricated layer. For a range between 0.75% to 1.33% efficiency gain per perovskite top cell layer that is added to a silicon bottom cell, Werner *et al.*[283] have estimated manufacturing costs between 46.2 to 19.5 €cts/W, respectively. The referenced range for c-Si modules goes from 25 to 30 €cts/W, which shows that perovskite/Si tandems can be economically interesting. Assuming similar costs for the fabrication steps, and no significant loss in spectrum splitting performance with upscaling, the efficiency gains per fabricated layer found in this work lie within a economically competitive range.

5.8. Conclusion

In this work, we derive the detailed-balance efficiency limit of two-terminal tandem solar cells with a perovskite top cell and a Si bottom cell, considering realistic incomplete absorption conditions for the perovskite top cell. We calculate the theoretically possible efficiency gain due to the introduction of a spectral splitter in between the top and bottom cell. For industrially relevant top cells with bandgaps of 1.7 eV and higher[277], a spectral splitter strongly enhances light absorption in the top cell, leading up to 5-6% absolute efficiency gain in the infinite thickness limit for a 500 nm thick top cell. Using experimental parameters of realistic cells, we predict an efficiency gain for a practical perovskite-tandem cell with Lambertian spectral splitter of 2.7% for a top cell with a bandgap energy of 1.77 eV and unity spectrum splitter reflectivity. In optimizing the reflectivity of the spectral splitter, we find small subtleties in the 1.6 to 1.7 eV bandgap range, due to unwanted outscattering of light from the front side of the cell. The effect

of parasitic absorption that will occur in experimental spectral splitters is also derived. Overall, our work shows there is a bright perspective for the integration of spectral splitters in perovskite-Si tandem solar cells, even if unity reflectivity cannot be achieved experimentally.

5.9. Acknowledgements

This work is part of the research program of the Dutch Research Council (NWO).

5.10. Author contributions

V. Neder and S.W. Tabernig performed the calculations. A. Polman supervised the project. All authors contributed to the manuscript and gave feedback.

6

Zn_3P_2-TiO_2 selective contact-based thin-film solar cell device design

6.1. Abstract

Electricity generation via photovoltaic energy conversion has just reached a deployed capacity of 1 TW. The majority of commercial solar panels is based on Si. For some applications that involve flexible photovoltaics Si is not well-suited, as Si solar cells are roughly 100-times thicker than the more versatile thin-film solar cells. However, most thin-film absorbers suffer from drawbacks such as material scarcity, bad stability, toxicity, or a low efficiency potential and so the ideal candidate for thin-film solar cells has not been determined yet. In this work we present a solar cell design that addresses these issues by using Zn_3P_2 as the absorber. By combining optical and electronic simulations, we investigate the energy band level requirements for the front and rear layers of a Zn_3P_2 solar cell. We identify Au as an ideal candidate, and Ni as a potential low-cost alternative for the back contact. TiO_2 is identified as the ideal electron extraction layer at the front, with ITO serving as the front electrode on top of it. Overall, the proposed device could achieve 20% power conversion efficiency, with room for further improvements via light management, suggesting a bright perspective for Zn_3P_2 as a thin-film absorber.

6.2. Introduction

The exponentially growing interest and installation of photovoltaics (PV) in recent years, especially of silicon-based PV, has led to an increasing demand in resources and energy by the PV industry. With these new scales of PV, the impact and requirements of the PV industry with regards to earth abundance, fabrication speed, energy intensity, and material efficiency becomes increasingly important. Thus, while high solar cell efficiencies are still a prime requirement for many applications, it is increasingly important how these are achieved, considering invested processing energy, manufacturing speed and materials consumption. While silicon is efficient and abundant, the typical thickness that is required for absorption of most of the incident light is about two orders of magnitude larger than for other PV materials, such as CIGS[196], GaAs[284], CdTe[198] and perovskite[285]. Such thin films excel with their potential of high fabrication speed[286], lower manufacturing energy requirements[287], and low demand in absorber material. However, these thin-film materials in turn suffer from components that are scarce in the earth's crust or difficult to mine.

Zinc phosphide (Zn_3P_2) is a material that has potential in this respect, as it is fully composed of earth-abundant elements[288]. Zinc phosphide has a large absorption coefficient[289,290], comparable to GaAs, and carrier diffusion lengths as high as 5 to 10 µm[117] have been demonstrated. However, limited work has been performed on Zn_3P_2 solar cells, and the record solar cell efficiency so far is only 6.0%[291], which is far from the 31.5%[292] theoretical efficiency for Zn_3P_2. Until recently, device designs have been constrained by the fact that high-purity Zn_3P_2 could only be grown on a limited range of substrates, mainly gallium arsenide[293] or indium phosphide[294,295], which are parasitically absorbing and from which a clean separation of the absorber is difficult. Thanks to recent developments[296], it is now possible to separate the grown Zn_3P_2 from its growth substrate, which means that the back and the front of the absorber can be freely accessed to add carrier collection layers, opening up many opportunities to optimize the solar cell design.

In Zn_3P_2 the diffusion length is large compared to the absorption depth, which means that most generated carriers can reach the interface to the bottom/top layer, as the absorber can be made relatively thin. However, it is not clear what the ideal top and bottom layers for charge extraction should be. Zn_3P_2 is intrinsically p-type, and no suitable n-type doping strategy for Zn_3P_2 has been reported yet, which eliminates homojunctions as a possibility. This is also confirmed by density functional theory (DFT) calculations, which have found that most of the common dopants yield p-type[297–299] Zn_3P_2. Studies of interfaces between Zn_3P_2 and potential carrier-selective layers and/or heterojunction partners[300,301] are also scarce. This means that there is little existing knowledge on the charge extraction from Zn_3P_2.

In the following, we introduce a zinc phosphide p-n heterojunction solar cell design[302], by using an intrinsically p-type[299] Zn_3P_2 layer together with an n-type selective contact, sandwiched between a transparent front contact (ITO) and a metal back contact. We use electronic drift-diffusion simulations to derive the requirements for energy band levels and work functions to optimize the solar cell efficiency, and identify materials that fit within these optimized parameters.

6.3. Design

We have chosen a selective contact-based cell design, that allows for charge carrier selectivity at the interface between Zn_3P_2 and a n-type window layer (Figure 6.1). A 100-nm-thick n-type window layer is placed on top of the 300-nm-thick Zn_3P_2 absorber (1.51 eV). We investigate a range of n-type window layer materials and use their conduction band (CB) and valence band (VB) energy levels to calculate the cell output parameters, varying the thickness of the Zn_3P_2 layer and taking into account the work function (ϕ) of a metal back contact. We use indium-tin-oxide (ITO) as a transparent top electrode. ITO is the most commonly used transparent electrode in photovoltaics[303], but it should be noted that alternatives exist such as fluorine-tin-oxide (FTO)[304], or Ag nanowire grids[305], that have comparable transparency and conductivity.

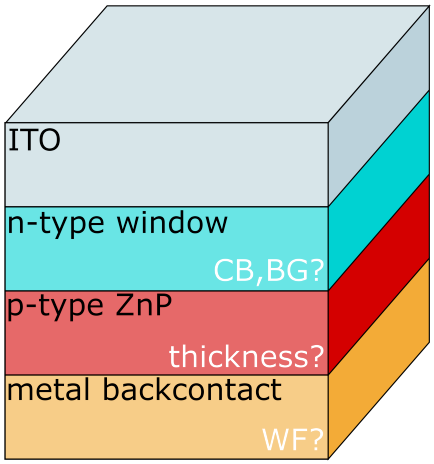

Figure 6.1: Layer stack of a solar cell with Zn_3P_2 as the absorber layer. Known specifications in black, properties investigated in this work in white. Light comes from the top. CB=conduction band, BG=band gap, WF=work function.

The simple solar cell design presented here enables fundamental insight into the parameters that determine the optimized cell design. A further optimized design may include additional barrier and contact layers, such as a highly doped p+-type layer (p+-Zn_3P_2 or another material) between the metal back contact and the Zn_3P_2 to improve selectivity at the back interface. Furthermore, additional light trapping can be achieved with an antireflection layer (e.g. MgF[306,307], LiF[307]) on top of the ITO, and by structuring the solar cell either at the front[308,309] or the back[310,311], as commonly done in other thin-film solar cell designs[309–311].

6.4. Methods

In order to determine the appropriate ranges for the energy levels of the n-type layer and the metal back contact, we use a combination of optical and electronic simulations for

the solar cell device. In a first step, we obtain the charge-carrier generation profile within the device from optical simulations. This is used as an input for the electronic simulations, where we simulate the charge carrier dynamics in the device for a range of applied voltages, and then obtain a current-voltage (IV) curve for the solar cell. From these curves we calculate the short-circuit current density (J_{sc}), open-circuit voltage (V_{oc}), fill factor (FF), and power conversion efficiency (η). These simulations are iterated for different parameters to evaluate their impact on the device efficiency.

We use a finite-difference time-domain (FDTD)-based solver (Ansys Lumerical FDTD) to solve Maxwell's equations for the layer stack and calculate the light field intensities inside the device. We start by using ZnO as the n-type carrier collection layer and simulate the following device stack (top to bottom): ITO (200 nm), ZnO (100 nm), Zn_3P_2 (300 nm), Au (500 nm); The used optical constants and a detailed description of the simulation setup can be found in the Appendix. For simplicity we use the optical constants of ZnO and Au when studying alternative carrier collection layers and metal back contacts. This is justifiable as the n-type layers have similarly large bandgaps as ZnO, and thus are also transparent. Slight differences in parasitic absorption and reflection are negligible in comparison to the impact of the band alignment on the electronic output parameters. Similarly, using Au as a highly reflective back contact serves as a reference for the reflection of light at the back of the solar cell.

A finite element method-based drift-diffusion equation solver (Ansys Lumerical CHARGE) is used to calculate the electronic device performance. Metals (back contact, ITO) are parameterized by their work function, while the Zn_3P_2 absorber layer and the n-type collection layer are parameterized by a wider range of properties, summarized in the Appendix.

We define the ideal ranges for the energy levels of the n-type semiconductor and the metal back contact in the proposed device and find that the ideal design is composed of a Type-II heterojunction, with a slight conduction band offset (TiO_2: 0.4 eV), as well as a metal back contact with a work function of 5.1 eV or higher.

6.5. Results & discussion

6.5.1. Impact of back contact work function on device performance

First we determine the ideal material for the metal back contact by finding the best range for the metal work function (ϕ). Figure 6.2 shows the solar cell characteristics (J_{sc}, V_{oc}, FF, and η) for a metal-Zn_3P_2-ZnO-ITO solar cell stack as a function of the metal work function. Note that we assume that the relative energy level alignment at the Zn_3P_2 - n-type layer interface does not affect the charge extraction at the metal-Zn_3P_2 interface, as long as the energy levels for the CB and bandgap (BG) are within a sensible range (n-type layer: CB = 3.6 eV, BG = 3.3 eV). Note that we refer to a "higher" energy level if the magnitude of the energy level is larger, irrespective of the sign.

The J_{sc} (Figure 6.2a) increases moderately with ϕ, while the V_{oc} (Figure 6.2b) increases more strongly, for ϕ up to around 5.2 eV, at which point the V_{oc} saturates. The FF (Figure 6.2c) also levels off above ϕ = 5.2 eV. These trends lead to an overall strong dependence of η on ϕ (Figure 6.2d); it gradually increases until it levels off at ϕ = 5.2 eV. Figure 6.2e shows the IV-curves for three specific cases (4.6 eV, 5.0 eV, 5.4 eV) and it be-

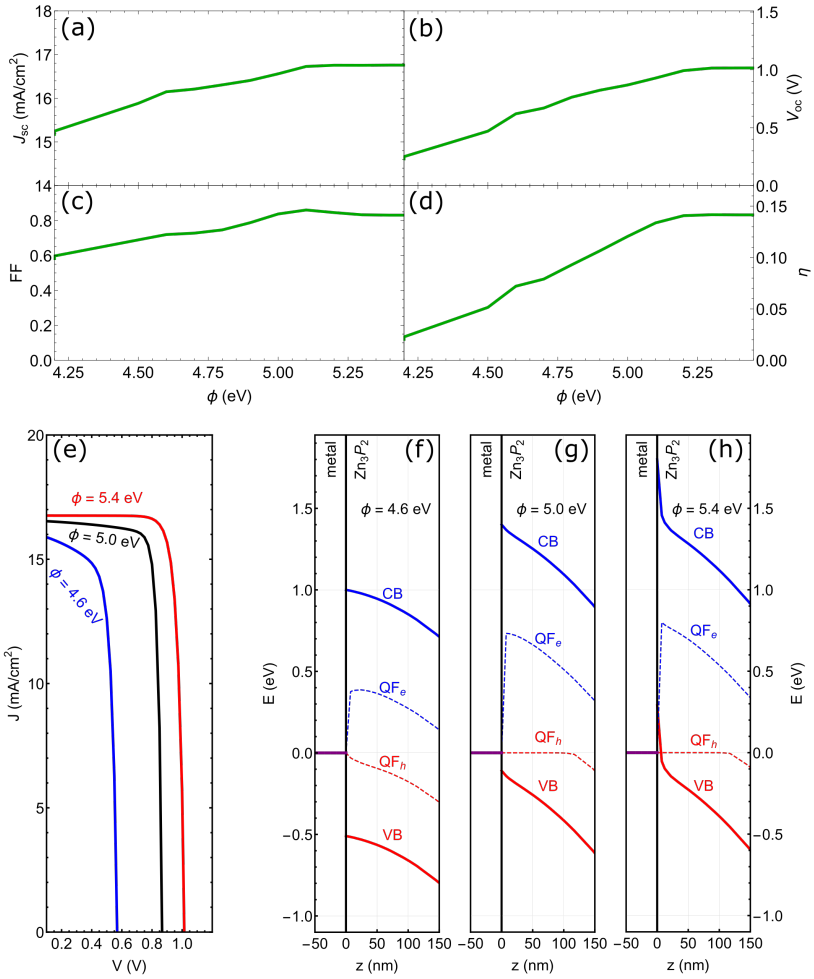

Figure 6.2: (a-d) J_{sc}, V_{oc}, FF, η for a metal-Zn_3P_2-ZnO-ITO layer stack as function of the metal back contact work function (ϕ). (e) Current-voltage (IV) curves for three values of the metal work function (ϕ). (f-h) Band diagrams at the metal-Zn_3P_2 interface for three values of ϕ indicated in the graphs. Energy levels are shown with respect to the hole quasi-Fermi-level (QF_h) at the hole-extracting interface (back contact). The lines correspond to conduction band (CB, solid-blue), electron quasi-Fermi-level (QF_e, dashed-blue), QF_h (dashed-red), and valence band (VB, solid-red).

comes clear from their shapes that the FF decreases for smaller work functions due to a shunting effect, while the series resistance does not change with ϕ. Figures 6.2b-d show the band diagrams for those three cases at the J_{sc} condition (V=0) under illumination. We observe band bending across the full range in the Zn_3P_2 that is plotted. Towards higher metal work functions, very strong band bending occurs within the vicinity of the metal-semiconductor interface (10 nm), bringing the hole-quasi-fermi level (QF_h) closer

to the VB of the Zn_3P_2 layer. At the same time, the energetic barrier for electrons flowing towards the back contact increases.

The interface between Zn_3P_2 and the metal back contact corresponds to the interface of a p-type semiconductor and a conductor, as described by Dittrich[90]. The direction of the band bending depends on the difference between the metal work function and the Fermi level of the semiconductor. In Figure 6.2b-d we can see how the band bending changes with the metal work function, and that the band bending at higher ϕ benefits extraction of holes. The semiconductor bands bend upwards in the vicinity of the interface, which promotes hole migration towards the back contact and limits carrier losses, and at the same time the matching Fermi-level of the metal and the holes in the semiconductor limits energetic losses. On the other hand, strong band bending prevents electrons from reaching that interface, reducing the recombination current and increasing charge carrier separation at the rear interface. It appears that 5.2 eV is a critical threshold above which there is negligible influence of ϕ on the electronic device performance. This value is slightly above the Zn_3P_2 VB at 5.11 eV.

The relations between the band diagrams and the IV curves are the following: We observe upward band bending in the vicinity (10 nm) of the rear interface for the 5.4 eV case compared to the 4.6 eV case. This corresponds to a decrease in potential energy for the holes towards the interface, which promotes hole flow towards and electron flow away from the rear interface, benefitting the J_{sc}. The V_{oc} increases towards larger work functions, as extraction of holes at the energy of the VB means that there is no additional loss in potential energy, and because of improved charge separation at the rear interface. Lastly, the FF benefits from strong band bending because this limits electron flow in the wrong direction, which manifests itself as shunting behavior in an IV curve (Figure 6.2e).

These calculations show that any back contact metal with a work-function of 5.1 eV or higher is worth considering. We note that the back contact should ideally be highly reflective, and hence Au (ϕ = 5.10–5.40 eV)[312,313] is a good candidate for an initial device, albeit expensive. Nickel (ϕ = 5.04–5.35 eV)[314] is an interesting alternative. We note that these results show a general trend based on the work function, and that the effect of interface defects that can sometimes occur at an interface between two materials is not taken into account here.

6.5.2. Conduction band energy as the critical parameter for the n-type window layer

So far, we have established the lower boundary for the work function of the metal back contact. Setting ϕ_{bc}=5.3 eV, we now investigate the energy bands that are desirable for the n-type window layer. As parasitic absorption should be avoided as much as possible, wide-bandgap semiconductors are the most interesting candidates. The n-type layer should function as a charge carrier selective contact and at the same time it constitutes a heterojunction with the absorber layer. We consider Type-I and Type-II heterojunctions[315]. Type-I heterojunctions pair the absorber with a wide-bandgap material that has a lower CB level and a higher VB level than the absorber itself. In a Type-II heterojunction, the CB and VB levels of the wide-bandgap material are both either higher or lower (for n-type: higher), than the CB and VB levels of the paired absorber, but the bandgaps overlap. We note that the CB is synonymous with the often used electron

affinity (χ_e), and that for semiconductors, ϕ refers to the energy level in the middle of the bandgap (undoped).

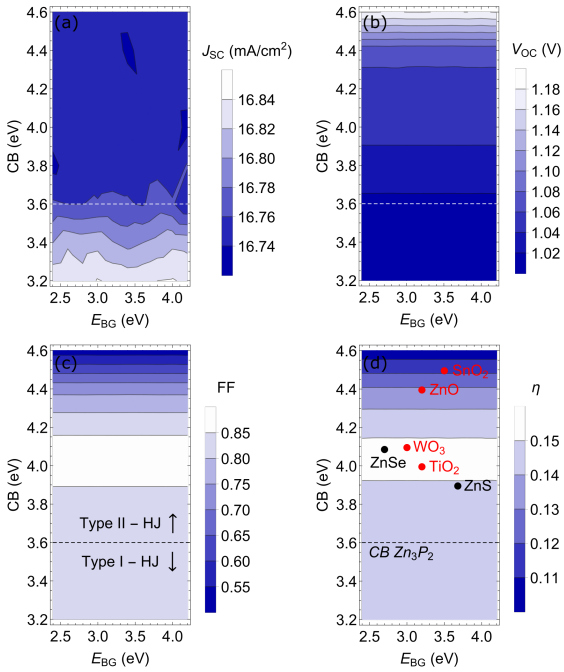

Figure 6.3: (a-d) Cell parameters (J_{sc}, V_{oc}, FF, η) as function of the n-type layer BG energy (BG) and the conduction band level (CB). In te panel of the FF, the ranges for the type-I and type-II heterojunctions are indicated. In the panel for the efficiency (d), the conduction band of Zn_3P_2 is also indicated, along with values of a range of potentially interesting materials. ZnS(e) compounds in black, oxides in red.

Figure 6.3 shows the dependence of the cell characteristics on CB and BG energies. As expected, the cell characteristics do not depend strongly on the BG within the investigated range. The J_{sc} (Figure 6.3a) is slightly higher towards low CB levels that correspond to a Type-I heterojunction. The V_{oc} increases moderately towards high CB levels (Figure 6.3b). The FF shows peaks at 4.0 eV, and decreases again towards larger CB levels (Figure 6.3c). The overall efficiency follows the trend of the FF, as this parameter shows the strongest dependence on the CB level (Figure 6.3d).

By looking at the shape of the IV curves (Figure 6.4a), it becomes clear that the dependence of the FF on the CB level arises from a change in the series resistance of the cell. Furthermore, for very high CB levels, the IV curve becomes S-shaped around the V_{oc}. The band diagrams in Figure 6.4b-d show how the energy landscape at the p-n interface changes from Type-I (CB = 3.4 eV) to Type-II (CB = 4.0 eV & 4.6 eV). CB levels below 3.6 eV correspond to a Type-I heterojunction geometry, for which electrons and holes have to bridge an energy barrier to enter the n-type layer. In a Type-II heterojunction (above 3.6 eV) the photogenerated electrons in the absorber can freely flow into the n-type layer. By contrast, photogenerated holes encounter a large barrier, making this

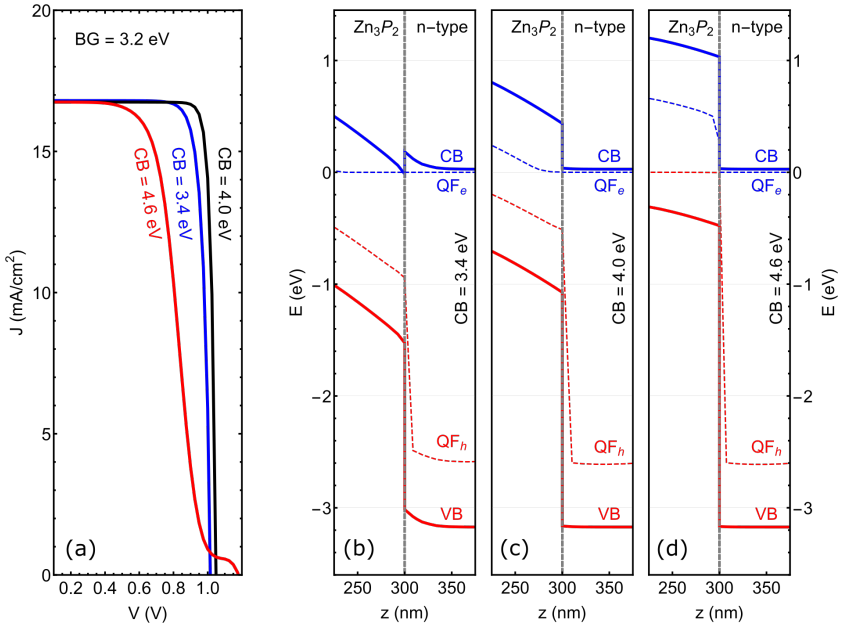

Figure 6.4: (a) Current-voltage (IV) curves for three conduction band levels (CB), for bandgap BG = 3.2 eV. (b-d) Corresponding band diagrams for the Zn_3P_2-n-type layer interface (left to right). The energy levels are shown with respect to the electron quasi-Fermi-level (QF_e) at the extraction interface. The lines correspond to CB (solid-blue), QF_e (dashed-blue), quasi-fermi-level of the holes (QF_h, dashed-red), and valence band (VB, solid-red).

architecture intrinsically carrier-selective, as desired. While we observe band bending in the n-type layer for the Type-I heterojunction, the CB and VB are flat in the Type-II case. The band bending in the Zn_3P_2 layer is stronger for lower n-type CB levels. The VB and QF_h levels are otherwise unaffected in all three diagrams. The QF_e level is matched at both sides of the interface for CB levels of 3.4 eV and 4.0 eV, while a large step in the QF_e level is observed for CB = 4.6 eV.

A key feature we observe is that the large step in the CB causes an S-shaped IV curve for CB = 4.6 eV. With increasing voltage, the band bending becomes weaker, until it is inverted and prevents electrons from reaching the p-n interface. At the same time, the applied voltage is not sufficient to push electrons in the reverse direction across the junction. This reduces the current density for the voltage range for which the band bending in the absorber can be overcome, but the CB offset cannot. For larger applied voltages, the energetic barrier can be overcome and the recombination current begins to dominate. This feature is not observed for lower CB energies because the voltage that overcomes the band bending is sufficiently large to overcome the CB offset. A more detailed explanation based on band diagrams at different voltages can be found in the Appendix (Figure 6.7).

We attribute the moderately higher J_{sc} in the case of the Type-I heterojunction to im-

proved extraction due to stronger band bending across the Zn_3P_2 layer for lower n-type CB levels (Figure 6.4b-d). The V_{oc} does increase towards very large CB energies due to the fact that with a larger CB offset it becomes more energy-intensive to push electrons in the reverse direction. The increased V_{oc} goes hand-in-hand with an S-shaped IV-curve (Figure 6.4a) as explained in the previous paragraph. In contrast to the case for the metal back contact, where we found shunting behavior to dominate the FF-dependence, the change in FF now mainly depends on the series resistance for electrons across the p-n junctions. We find that the FF is highest at the CB energy for which Zn_3P_2 and the n-type layer have matching quasi-Fermi energy levels for the electrons. Overall, highest efficiencies are achieved at a CB offset of 0.4 eV in favor of a Type-II heterojunction (CB = 4.0 eV).

Figure 6.3d also shows the approximate BG and CB values for some state-of-the art n-type wide-bandgap oxides[301,316], as well as n-type ZnS(e) compounds[301] that deserve special attention in this context. We find that TiO_2 (Anatase phase), ZnSe, WO_3, and ZnS have parameters close to what our analysis suggests is the optimum, with TiO_2 showing best performance. TiO_2 has been used as a n-type window layer in combination with a wide range of absorber layers (perovskite, PbS QDs, dyes) in the past. Furthermore, a wide range of deposition methods exists for it, ranging from solgel-deposition[317] to atomic-layer deposition (ALD)[318,319] approaches. Considering these aspects, especially in comparison to the other candidates, we deem TiO_2 a promising option for combining it with Zn_3P_2 in a p-n heterojunction.

6.6. Proposed cell design and the impact of the absorber thickness

Having established the work function requirements for the metal back contact and identified TiO_2 as a suitable n-type material, we calculate the full energy band diagram of our solar cell device design under illumination, at the J_{sc} condition (V = 0). The simulations predict a photovoltaic efficiency of 15% and consists of the following layers, from bottom to top: Au (back contact), Zn_3P_2 (absorber, 300 nm thick, acceptor doping level (N_A): 10^{16} cm^{-3}), TiO_2 (n-type layer, 100 nm thick, donor doping level (N_D): 10^{18} cm^{-3}), and ITO (front contact). Starting at the back of the solar cell (ϕ_{Au} = 5.1 eV), we find steep band bending within the first 10-20 nm of the absorber, induced by the large ϕ of the metal back contact. This favors hole extraction and blocks electrons. Furthermore, the QF_h and VB levels align well at the back contact interface, creating an Ohmic contact. In the active layer (Zn_3P_2) we see a steady decrease in the accumulation of holes until similar charge carrier densities are reached for electrons and holes (indicated by QF_h and QF_e). At the p-n heterojunction interface electrons are transferred into the TiO_2 layer, assisted by a shallow band bending slope that spans across most of the absorber. The TiO_2 layer blocks the holes and is strongly n-doped, as indicated by the proximity of the CB and QF_e levels. Holes can enter the Zn_3P_2 from the TiO_2, while electrons are blocked by a barrier of 0.4 eV. The TiO_2-ITO interface is set to be Ohmic throughout the simulations.

While we have so far optimized the device performance for a thin absorber layer (300 nm), the long diffusion lengths in Zn_3P_2 allow for much thicker devices. Figure 6.6

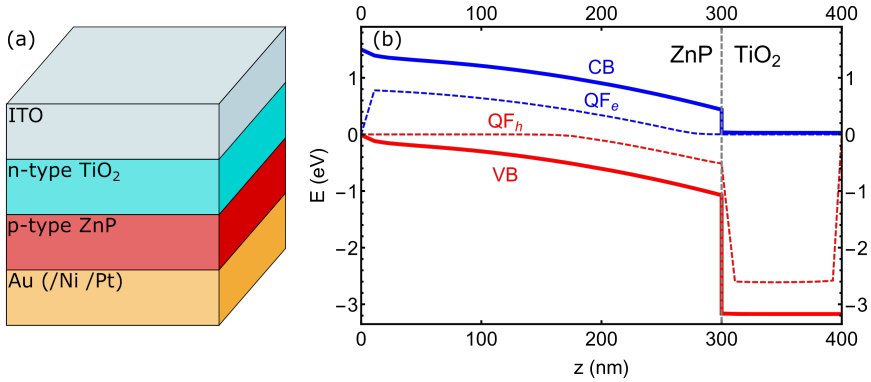

Figure 6.5: (a) Solar cell stack of a heterojunction solar cell with Zn_3P_2 as the absorber layer. This work simulated an ideal architecture that contains TiO_2 as the n-type window layer and ITO and Au (/Ni) as front and back contacts, respectively. Light comes from the top. (b) Corresponding band diagram, light comes from the right. The band diagram corresponds to the J_{sc} condition (V=0), under illumination. Conduction band (CB, solid-blue), electron quasi-Fermi-level (QF_e, dashed-blue), hole quasi-Fermi-level (QF_h, dashed-red), and valence band (VB, red) are plotted for the full p-n heterojunction. The gray-dashed line marks the interface between Zn_3P_2 and TiO_2.

6

shows how the efficiency can be increased significantly from 15% at a thickness of 300 nm up to 20% at 2000 nm, beyond which the efficiency levels off. As the V_{oc} and FF are not impacted on this length scale, we find that this significant increase in efficiency can be solely attributed to better light absorption leading to a higher J_{sc}.

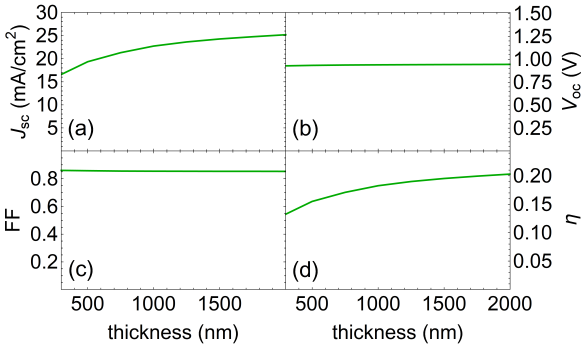

Figure 6.6: (a-d) Solar cell parameters (J_{sc}, V_{oc}, FF, η) for the Au-Zn_3P_2-TiO_2-ITO heterojunction design as function of the Zn_3P_2 thickness.

At this point it is important to note that while these simulations largely neglect the impact of recombination losses, they do not serve as an upper bound. Simple light management strategies, such as an anti-reflection coating, or more advanced strategies, such as texture, have not been considered in this work, and can improve the J_{sc} significantly, by minimizing reflection loss and increasing the average path length of light within the absorber.

6.7. Conclusion

We propose a novel p-n heterojunction thin-film solar cell design, based on Zn_3P_2 as an absorber. We numerically solve Maxwell's equations and couple them to electronic drift-diffusion equations, to investigate the performance of a range of device geometries. We identify work functions larger than 5.1 eV as ideal for the metal back contact, and find suitable material candidates in Au and Ni. Analyzing the requirements for the conduction band of the n-type window layer, we find that TiO_2 is the best candidate for the n-type layer. We predict a potential device efficiency of 20% in absence of significant carrier recombination and without light management strategies, leaving room for further efficiency enhancement. Overall, these findings serve as a promising guide towards the fabrication of earth-abundant and efficient Zn_3P_2 based solar cell devices.

6.8. Appendix

6.8.1. Optical simulations

We use a finite-difference time-domain (FDTD) solver (Ansys Lumerical FDTD) for optical simulations. The following device stack was simulated (top to bottom): ITO (200 nm), ZnO (100 nm), Zn_3P_2 (300 nm), Au (500 nm); The mesh accuracy was set to "2" for a "auto non-uniform" mesh type. The mesh refinement was set to "conformal variant 1". The simulations were done in 3D, with periodic boundary conditions along the plane of the cell (500 nm range in x-/y-direction;), and perfectly matched layers (PMLs) at both ends of the simulation region in z-direction. A plane-wave source at a distance of 2.2 µm from the front of the solar cell was used as input, and dedicated "Transmission box" and "Solar generation rate" analysis groups were used to obtain absorption spectra and generation profiles, respectively.

6.8.2. Electronic simulations

A finite-element method-based drift-diffusion equation solver (Ansys Lumerical CHARGE) is used to calculate the electronic device performance. The device stack is the same as for the optical simulations. The mesh edge lengths are limited to a range between 10 nm and 1 µm via "Global Mesh Constraints". The device is simulated in the steady-state solver mode, and in 2D, with a "norm length" of 1 cm for the 3rd dimension. To simulate the device within an electric circuit, the front and back contacts are identified as electronic connection points. The front contact (ITO, ϕ = 4.7) is set to "force ohmic = true", while the back contact (ϕ was tuned) is set to "force ohmic = false", which is necessary to evaluate the impact of the work function on the device performance. Surface/interface recombination is neglected, and the generation profile from the optical simulations is imported via the designated import function. Band diagrams are recorded with the dedicated "Band Structure Monitor", and IV curves are directly extracted from the "CHARGE"-solver window. A detailed listing of the parameter values used for the semiconductors (Zn_3P_2, TiO_2) can be found in Table 6.1.

6.8.3. Explanation of S-shaped $I-V$ curves

The S-shaped $I-V$ curve in Figure 6.4a is a consequence of the electrons getting stuck inside the absorber, due to the barrier at the Zn_3P_2 - n-type layer interface that prevents

electron flow in the reverse direction. Figure 6.7 illustrates the band bending at the J_{sc} condition (0 V, Figure 6.7a), close to the maximum power point (0.7 V, Figure 6.7b), and close to the V_{oc} condition (1.1 V, Figure 6.7c). The comparison of the CB shows that the electrons can be extracted via the n-type layer for low voltages, but with increasing voltage, an energy barrier arises, and current flow in both directions is inhibited. Only for very high voltages the barrier at the front interface becomes low enough to bridge it, and electrons can flow in the reverse direction. This leads to the uncharacteristically large V_{oc} found in Figure 6.4a.

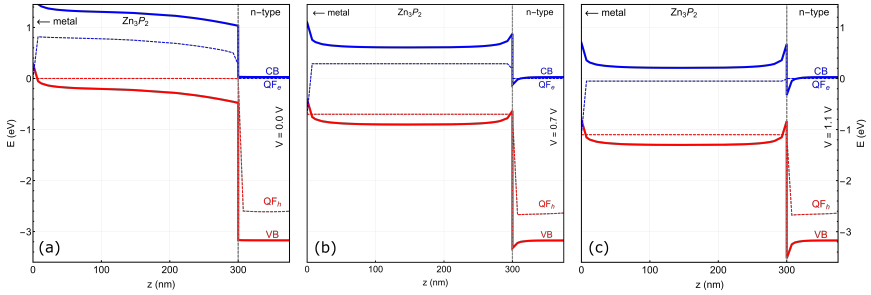

Figure 6.7: Band diagrams for the Zn_3P_2 solar cell at different voltages. Metal contact (WF=5.4 eV) at the rear, n-type layer (CB=4.6 eV, BG=3.2 eV) at the front interface. (a) 0.0 V, (b) 0.7 V, and (c) 1.1 eV. The energy levels are shown with respect to the electron quasi-Fermi-level (QF_e) at the front extraction interface. The lines correspond to CB (solid-blue), QF_e (dashed-blue), QF_h (dashed-red), and VB (solid-red).

6.9. Author contributions

S.W. Tabernig performed the simulations. M. Dimitrievska provided feedback and data for the simulations. M.D., E. Alarcón Lladó, A. Fontcuberta i Morral, and A. Polman supervised the project. All authors contributed to writing the manuscript and gave feedback.

Table 6.1: List of parameters[301,320–325] used for the semiconductors in the drift-diffusion simulations.

Quantity	Label in software	Unit	Zn_3P_2	TiO_2
DC permittivity	DC permittivity		11 (lit.[322,325])	66
Work function	Work function	eV	4.355 (lit.[301])	5.6
Electron affinity	—	eV	3.6 (lit.[301])	4.0
High symmetry point at the conduction band minimum	Ec valley		Γ	Γ
Effective electron mass	Effective mass mn	$1/m_e$	0.268	0.24
Effective hole mass	Effective mass mp	$1/m_e$	1.069	0.59
Bandgap	Eg	eV	1.51 (lit.[323])	3.2
Electron mobility	Mun	$cm^2/(Vs)$	1000 (lit.[321])	100
Hole mobility	Mup	$cm^2/(Vs)$	20 (lit.[324])	25
Non-radiative electron lifetime	Taun	s	$2.7x10^{-8}$ (lit.[321])	$1x10^{-9}$
Non-radiative hole lifetime	Taup	s	$2.7x10^{-8}$	$1x10^{-9}$
Trap state energy level offset	Ei offset	eV	0	1.1
Donor doping density	ND:n	cm^{-3}	0	$1x10^{18}$
Acceptor doping density	NA:p	cm^{-3}	$1x10^{16}$ (lit.[320])	0

7

Soft-imprint nanopatterning for optoelectronic improvements in solar cells

7.1. Abstract

The integration of nanostructures has become a prominent pathway for the enhancement of the optical performance in photovoltaic (PV) devices. Substrate conformal soft-imprint lithography (SCIL) serves as a useful tool for effective and large-scale integration of nanostructures in PV device stacks. However, with increasing integration, care needs to be taken during fabrication to minimize fabrication-associated degradation of the device. We investigate three different patterning approaches that are based on SCIL and evaluate their impact on solar cells, and observe improvements in the short-circuit current density in all cases. In some cases the open-circuit voltage and the fill factor also benefit. We identify a direct imprinting approach, for which the solgel material immediately serves as the functional layer, to minimize cell degradation during nanofabrication, provided an adequate solgel is found. Furthermore, direct imprint also serves as a tool to investigate the potential of nanostructures with optical and electronic functionalities.

7.2. Introduction

New records for photovoltaic (PV) devices are often achieved by structuring a device layer to enhance its intrinsic function, or to add another functionality to that layer. For the optical performance of a solar cell, texture is often used at the front[308,309] to improve light incoupling, or at the back[310,311] to increase the path length for light within the absorber. These approaches allow for an increased generation of charges. Charge extraction can also benefit from similar approaches, such as bulk heterojunctions[201], which allow for shorter diffusion paths for the charges. Very recent records in key PV technologies highlight the relevance of structured surfaces for PV, such as the current record for 2T perovskite-Si tandem solar cells, which was achieved thanks to nano-texturing[326].

Imprint lithography[106,107,327,328] has established itself as a very popular approach to pattern materials, as it can be upscaled fairly easily. Complete patterning of 300 mm wafers is a commercially viable process, and can either be done in cassette-based systems[106], or by using roll-to-roll processes[328], for high throughput. Those advantages set imprint-based lithography apart from UV[329–331]- and e-beam[330–332] approaches, for example. Substrate conformal soft-imprint lithography (SCIL)[106,107] exhibits the advantages of imprint lithography and is fabrication-defect resistant, which makes it appealing for large-scale applications, where strict requirements on cleanliness are often not wanted.

In fact, imprint lithography has already proven to be a great success in PV-labs, and produced black silicon[333], efficient back reflectors[311], colored PV[125], spectrum splitters[279], transparent electrodes[305], patterned p-n heterojunctions[334], and nanopatterned AR coatings[333]. Imprint lithography approaches are also highly relevant in many other fields, such as electronic integrated circuits[335,336], and applications in photonics[337]. Its scalability is especially interesting for PV, for which the industry is continuously shifting to larger wafer sizes[338].

Most of the work in the past has focused on introducing nanopatterns in the solar cell geometry in a way that would benefit the optical performance, while ideally the patterned geometries do not get in contact with critical electronic layers. Often this has led to approaches where, for example, a glass window is introduced between an optical nanopattern and the solar cell[125]. In the following, we focus on pathways that introduce nanostructures in regions which require careful consideration of the solar cell electronic properties as well. We describe the most efficient routes for the integration of nanostructures in solar cells, and will discuss the important aspect of electronic compatibility and functionality of the layers, which have previously received most of the attention from an optical perspective.

The previous chapters of this thesis focus on the interplay of optical and electronic effects that arise from nanostructures, and how they can be used to benefit solar cells. Several approaches for the experimental integration of such structures in PV devices are introduced. We directly imprint ZnO and fill it up with PbS quantum dots (Chapter 2)[334], pattern V-grooves into a transparent polymer on top of a solar cell (Chapter 3)[339], nanopattern and passivate the surface of silicon solar cells (Chapter 4), and simulate how nanopatterns can benefit 2-terminal (2T) perovskite-Si tandem solar cells (Chapter 5)[340]. Here we also present results on the direct patterning of TiO_x and dielectric nanopatterns for CZTS and CIGS. This chapter aims to summarize these fabrication

approaches, which all have in common that they are derived from SCIL. Detailed descriptions of the electronic cell performance are provided in the corresponding chapters and published papers. We will discuss the fabrication routes and at the same time evaluate how they impact the structural, optical, and electronic integrity of PV devices.

7.3. Fabrication approaches

The basic approach for patterning of specific layers relies on pushing a PDMS-stamp into a liquid silica-solgel layer after spin-coating. The silica solgel composition is optimized to make it cure within a few minutes at room temperature. The PDMS stamp consists of three different PDMS layers with different Young's modulus [106,107] on a thin glass carrier that allow for it to retain in-plane features on the nanoscale while being flexible on the wafer-scale [106,107]. See Verschuuren *et al.* [106,107] for technical details of the SCIL process. In the following we describe direct and indirect patterning processes using the SCIL process for several PV geometries.

7.3.1. Indirect patterning in combination with lift-off

Indirect patterning refers to using the patterned silica solgel as a mask for further processing, in order to structure a specific layer. In combination with lift-off, this usually involves patterning of the solgel on top of another sacrificial layer. The pattern is transferred into that layer via etching and the empty features are filled up using evaporation as a deposition method. Subsequent lift-off of the sacrificial layer yields the final structure, which is a negative of the initially imprinted pattern (Figure 7.1).

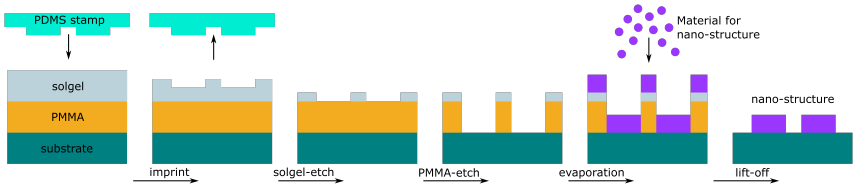

Figure 7.1: Indirect patterning in combination with lift-off. A sacrificial (PMMA) layer is deposited on the substrate, followed by a liquid silica solgel layer. From left to right: A PDMS-stamp is pushed into the liquid solgel. After curing, the stamp is removed, and a solgel-etch removes the residual layer of the solgel. Then a PMMA etch is used to expose the substrate. The desired material is then evaporated into the gaps that were formed in the PMMA. Lift-off of the sacrificial PMMA layer yields the nanostructure on the substrate.

Provided the substrate and patterned layer are compatible with the etch used for the sacrificial layer, as well as the solvent used for lift-off, this approach serves as a universal approach for patterning of many materials. A key prerequisite is the existence of a suitable evaporation source for the required material. Electron-beam and thermal evaporation are well compatible, while sputtering and atomic-layer deposition (ALD) make lift-off more difficult due to the conformality of deposited material.

We have employed the indirect patterning technique to fabricate arrays of SiO_2 nanoscatterers at the backside (on ITO) of a bifacial copper-indium-gallium-sulfide (CIGS) solar cell [341] (Figure 7.2a,b), and transferred this process to deposit SiO_2 nanoscatterers on Mo, the backcontact for CZTS solar cells (Figure 7.2c,d). We have also studied the growth of

CZTS over the dielectric scatterers (Figure 7.2e,f).

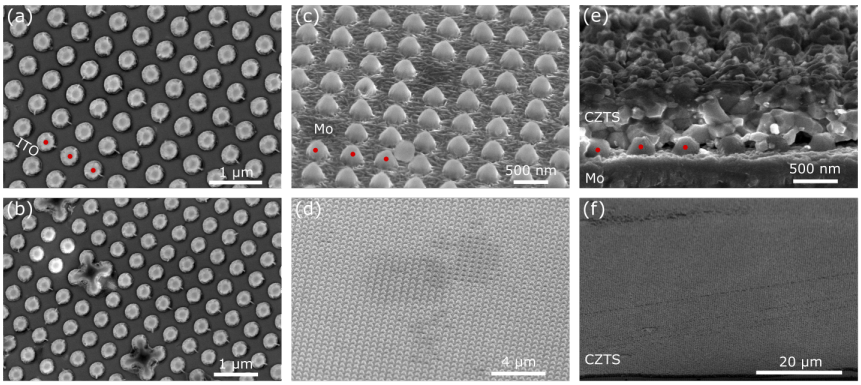

Figure 7.2: (a) Top view of 200-nm-high SiO_2 nanopillars on top of an ITO-coated glass. Three pillars are marked with red dots (b) SiO_2 nanopillar lattice with some defects composed of fused pillars. (c) View under an angle onto 200-nm-high SiO_2 nanopillars on top of a Mo film on a glass substrate. Two empty spots are visible, and we find that the shape deviates from a cylindrical pillar shape due to non-perfect alignment during evaporation in combination with sample rotation. Three nanopillars are marked with red dots. (d) Large-area image of SiO_2 nanopillars on top of a Mo film on a glass substrate. (e) Cross-cut view of 200-nm-high SiO_2 nanopillars on a Mo film on a glass substrate, with CZTS grown over the pillars. Three pillars are marked with red dots. (f) Large-area image of CZTS grown over the SiO_2 nanopillars. The pattern of the pillars on the backside was transferred to an array of corrugations on the front side of the CZTS layer.

7

7.3.2. Indirect patterning in combination with etching

Indirect patterning can also be combined with a pure etching approach. In this case, the silica solgel can serve as a sacrificial layer on its own, but an additional sacrificial layer under the solgel layer can be used as well. In both cases the sacrificial layers are etched through first, and then a different etching recipe is used to transfer the pattern into the substrate material. After the substrate material has been patterned, the sacrificial layer is removed with solvents to obtain the desired structure (Figure 7.3).

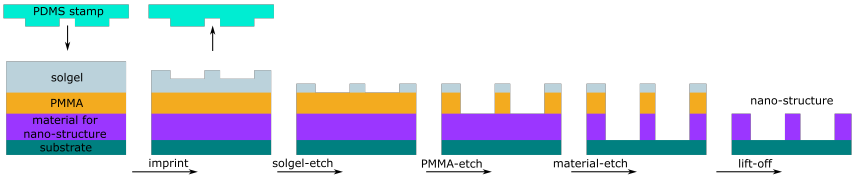

Figure 7.3: Indirect patterning in combination with reactive ion etching (RIE). The process starts with a planar layer of the material that needs to be patterned, on top of a substrate. A sacrificial PMMA layer is deposited followed by a liquid solgel layer. Processing from left to right: A PDMS-stamp is pushed into the liquid silica solgel. After curing, the stamp is removed, and a solgel-etch removes the residual layer of the solgel. Then a PMMA etch is used to reach the substrate. The material that is to be patterned is etched during the next step. Lift-off of the sacrificial PMMA layer yields the nanostructure on the substrate.

For this line of processing to work, it is important that the etch for the substrate layer

exhibits high selectivity towards the substrate material, to not affect the etch-mask during the patterning. The etching is usually done by reactive ion etching (RIE). Side effects from this process can be degradation of the substrate due to ion-bombardment or UV-radiation and contamination of other layers can be a concern when it involves solar cell layers that are sensitive to electronic defects.

We have used this approach to pattern hyper-uniform light trapping patterns that were etched into silicon[221] (Figure 7.4a-c) and to fabricate nanopatterned SiN_x anti-reflection coatings on top of silicon (Figure 7.4d-f).

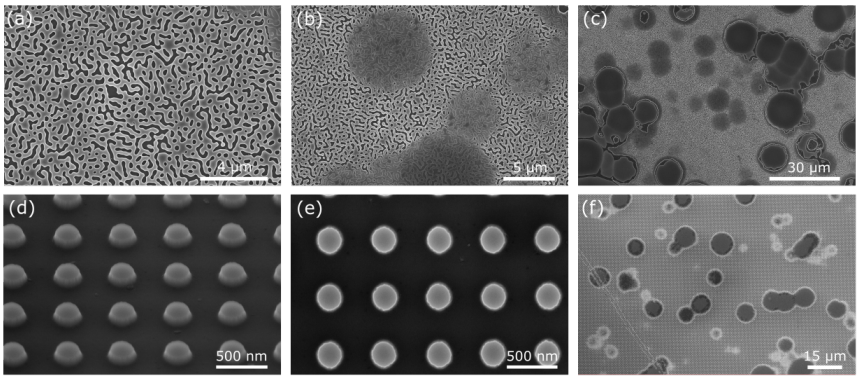

Figure 7.4: (a) Top view of a hyper-uniform spinoidal[221] structure etched into the surface of a Si solar cell using a nanopatterned silica mask layer. (b) Larger area, same structure with some patches (dark regions) where the solgel etch did not break through the solgel layer. (c) Even larger area for the same structure. The non-patterned areas correspond to residual surface indents in the Si wafer that stem from initial pyramidal texture that was removed by polishing to create a flat solar cell. These pockets accumulate thicker solgel layers for which the solgel etch cannot break through. (d) Angled view of periodic (pitch = 530 nm) square array of SiN_x pillars of 255 nm width and 120 nm height on top of a planar 60 nm SiN_x layer on a Si solar cell. (e) Top view. (f) Larger area, similar defects as in (c) are visible, stemming from the not perfectly planarized surface of the originally textured Si surface.

7.3.3. Direct patterning

Direct patterning refers to using the cured solgel material as the functional layer after patterning (Figure 7.5). The advantage of this is that it is a one-step approach that only involves spin-coating of the solgel solution and subsequent imprinting. The only potentially detrimental impact on the substrate in this case is the mechanical pressure that is induced during the moment of contact between the PDMS stamp and the solgel. This means that this approach causes the least possible degradation of substrate layers and the functional layer, and hence is the best option, if available.

The possibility of using this approach depends on the existence of a suitable solgel that exhibits the right spin-coating and curing behavior, as is the case for the used silica solgel[106,107]. Furthermore, this approach limits the achievable feature height to the feature depth in the PDMS-stamp, and limits the residual layer thickness in proportion to the solgel volume used during spin-coating.

Figure 7.6 shows how directly patterned layers have been achieved using TiO_x solgel

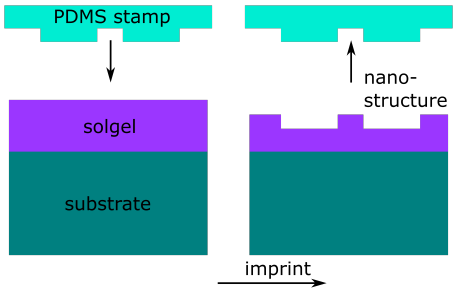

Figure 7.5: Direct patterning. The process starts with a liquid solgel layer of the desired material composition on top of a substrate. A PDMS-stamp is pushed into the solgel, and after curing, is peeled-off. This yields the final nanostructure, that consists of the cured solgel material.

(on CZTS/CdS and on ITO, Figure 7.6a,b), and ZnO with varying residual layer thickness (on ITO, Figure 7.6c,d)[334]to achieve a template for a PbS QD absorber (Figure 7.6e,f). Control over the ZnO residual layer thickness is especially interesting, as this affects the series resistance of the solar cell device. The TiO_x was deposited from Titanium diisopropoxide bisacetylacetonate ($C_{16}H_{32}O_6Ti$)[342] dissolved in isopropanol, and the ZnO was synthesized according to Chuang *et al.*[151].

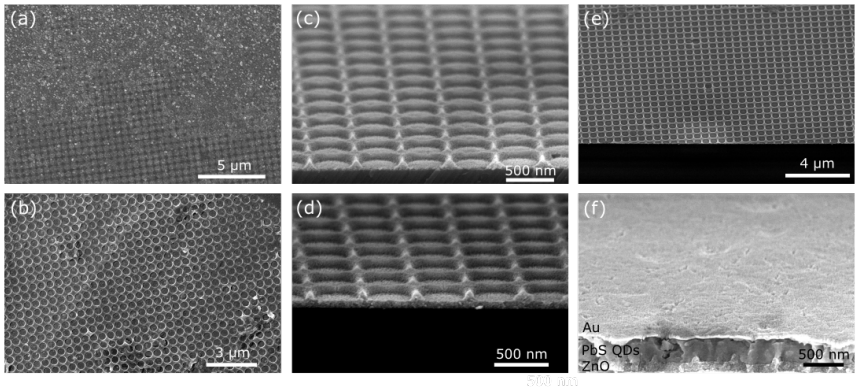

Figure 7.6: (a) Top view of patterned TiO_x on top of a CZTS/CdS heterojunction. Due to the roughness of this substrate material, the TiO_x coverage is not perfect. (b) Patterned TiO_x on top of ITO-coated glass. (c) Side view of patterned ZnO on Si, with negligible residual layer thickness, due to the use of a diluted ZnO solgel. (d) Similar to (c) but with thicker residual layer using undiluted ZnO solgel. (e) Larger-area view of patterned ZnO, showing good coverage. (f) Crosscut view of a patterned p-n heterojunction in a PbS QD solar cell, that uses patterned ZnO on top of ITO, and infiltrates the pattern with PbS QDs. The Au layer on top is fairly planar, showing that the pattern is not transferred through the PbS layer.

7.4. Impact of fabrication on functional layer and cell

7.4.1. Structure

Indirect patterning allows for best control of the final feature depth/height, and thus is preferred for applications that only depend on feature geometry. Comparing Figure 7.2c and Figure 7.4d, we can also see that the RIE-only indirect patterning approach best conserves the desired shape. However, often it is desirable to use a fabrication approach that avoids potentially damaging processes such as RIE. In such a case direct imprint serves as a non-invasive alternative, at little loss in the pattern quality.

The impact on the cell structure depends on the degree of integration of the nanostructure into the cell. In the case of an array of optical scatterers at the front of the cell, which can help with incoupling of light, the fabrication can be essentially decoupled from the cell itself, and hence the rest of the cell is not impacted structurally. If the nanostructures are integrated in between different layers, their impact on the following layers can be large. For example, the overgrowth process of CZTS (co-sputtering and sulfurization[343]) on SiO_2-nanopillars on top of a Mo-film leads to an overall smaller CZTS grain size than for planar CZTS layers and also causes a periodic pattern to be visible on the front side of the CZTS layers (Figure 7.2e,f). As shown before for a-Si:H[344], this can enhance the incoupling of light at the front side due to the excitation of Mie resonances with forward scattering distributions. However, in the case of spin-coated PbS quantum dots, the structural impact of the patterned ZnO layer (Figure 7.6f) is confined to the interface of those two materials, and does not transfer through to other layers, because the material is deposited in liquid and not solid form.

7.4.2. Optical & electronic function

How important is the choice of fabrication approach for the optical and electronic properties of the solar cell? Some options produce more accurate structures than others, and some are more likely to contaminate the solar cell.

Optically, most materials can sustain a certain degree of contamination with other materials without serious impact on their optical constants[345], eliminating contamination during processing as a concern. Obviously, for best optical performance it is important to fabricate the structure as accurately as possible, and all three fabrication strategies serve as viable options for sufficient accuracy, with the RIE-only indirect imprint approach standing out as the best.

Electronically, many materials are vulnerable to small amounts of contaminants, like Au creates effective carrier traps in Si[346]. While these defects typically do not largely affect the optical constants of the semiconductor (e.g. absorption), they can form a non-radiative recombination site, and compromise charge separation and extraction. During imprint lithography, such defects could be introduced by ion-bombardment (RIE), the use of contaminated deposition chambers (evaporation, sputtering,...), or via liquids used in processing (lift-off).

Direct imprint stands out in this regard, as it uses none of these potential sources of contamination, in comparison to the two indirect approaches. Figure 7.6c-f shows examples for TiO_x and ZnO, which can be patterned without the need to worry about unintentionally changing the oxidation state during a RIE-etch with O_2 or introducing

bulk or surface defects from ion bombardment. However, to increase the applicability of this approach (for example to directly pattern the absorber), more research on solgels for various materials of interest is required.

7.5. Conclusion

We have evaluated substrate conformal soft-imprint lithography (SCIL) as an important tool for introducing nanostructures in solar cells. The main benefits are the scalability of this approach, as well as the relative simplicity. Three potential paths for the patterning of functional layers are outlined, differing in complexity as well potential impact on the solar cell performance. Indirect patterning strategies that use lift-off and reactive ion etching allow for the use of a wider range of material. In contrast, direct patterning requires the material to be dissolved in solution beforehand and serves as an effective one-step approach with negligible impact on the solar cell performance. For materials for which a solgel exists, we identify this approach as most suitable for the integration of nanostructures that are not only optically, but also electronically functional.

7.6. Author contributions

S.W. Tabernig, A. Cordaro A. Lambertz, K. Sun, and S. Zhou took the SEM images. S.W.T., K.S., S.Z., Y. Li, A.L., A.C. contributed to the fabrication. M. Pollard, B. Hoex, E. Alarcón Lladó, M. Schmid, X. Hao, and A. Polman supervised the various projects from which the data in this chapter was taken. S.W.T. wrote the manuscript and A.P. gave feedback.

8

Summary

This summary is written in July of 2022, and the most recent data point for the CO_2 concentration on Mauna Loa is 420.99 ppm. I was born in April 1994, at 361.36 ppm. Stopping the rapid rise of greenhouse gas concentration in our atmosphere to combat the climate crisis is the biggest challenge of this century and has to be set on track this decade. And we are lucky enough to have the capabilities to make the tools to get there. Changing our ways of generating energy from polluting fossil fuels towards sustainable and renewable energy sources like wind, water and sunlight will significantly contribute to mitigation of global warming. Electricity generation from sunlight, photovoltaics (PV), is on track to carry part of the burden, and can benefit from further innovations in power conversion efficiency, technological versatility (flexible, bendable, durable, ...), and cost reduction.

In this thesis, these aspects are addressed for a range of technologies. We design novel photovoltaic architectures for a range of established (Si, III-V materials) and novel (PbS quantum dots, Zn_3P_2, perovskites) absorber materials. Light management concepts are used to evaluate and improve the absorption of light for photovoltaic devices, solar cells. The improvements are based on nano- and micrometer sized structures at the front, centre, or rear of the solar cells and aim to enhance the absorption inside the absorber layer as a primary goal. Additionally, the spatial distribution of the absorbed light is also considered, to not just ensure successful generation of charge carriers from photons, but also successful extraction of the carriers. We demonstrate many of these designs experimentally, evaluate their electronic performance, and use commercially relevant scalable processes to maximize the application relevance of our designs.

The thesis starts by elaborating on the looming consequences of the rise of greenhouse gas concentration in our atmosphere (Chapter 1). Global warming is identified as a serious danger and the main challenge of the century. This, amongst other reasons, provides important motivation and justification for switching to energy generation from renewable sources. The basic principles of photovoltaic energy conversion are discussed, as well as the thermodynamic detailed-balance limit, as a physical limitation. Special attention is giving to the trends in increase of device efficiencies for different ab-

sorbers over the years, and their distinct advantages for PV applications are presented.

The first technology we look at are solution-processed thin-film PbS quantum dot solar cells (Chapter 2), for which we introduce an optically resonant bulk heterojunction solar cell design. The cell is designed to consist of a square lattice of PbS QD cylinders of 330 nm height, 320 nm diameter, and a pitch of 500 nm, embedded in ZnO. The QD cylinder dimension are chosen such that they support optical resonances, maximizing the absorption per unit volume by 20% compared to a planar reference. Electronic simulations predict a gain in short-circuit current density (J_{sc}) of 3.2 mA/cm^2, and an efficiency gain of 0.4%-absolute. In experiment, we first use substrate conformal imprint lithography (SCIL) to demonstrate patterning of ZnO solgel and find optical trends confirmed in the fabricated devices, along with an increased external quantum efficiency (EQE) that shows a J_{sc} gain of 0.74 mA/cm^2. Finally, this chapter highlights the importance of considering the charge carrier generation profile as the quantity that interfaces optical and electronic solar cell design. PbS quantum dot solar cells have a tunable bandgap, are thin, and solution processable, making them interesting prospects for ink-jet printed or slot-die coated solar cells, as well as potentially indoor light harvesting devices. Advances in PbS quantum dots solar cells often also have positive implications for the design of light emitting diode (LED) devices based on this absorber.

Concentrator photovoltaics (CPV) is a high-efficiency technology that relies on concentration of sunlight onto relatively small solar cells, and the concentration factor causes a logarithmic increase in the open-circuit voltage (V_{oc}), which allows for more efficient devices. Furthermore, the usage of much smaller cells (factor 100-1000) allows for consideration of expensive III-V technologies, such as GaAs-based solar cells. However, CPV requires large front metal contact coverage to collect the high generated currents, which causes significant reflection losses. In Chapter 3, we demonstrate contact cloaking by means of optical refraction from V-shaped grooves that are patterned into a glass-like polymer. We demonstrate high optical transparency (95.2%) and apply the layer to a Si solar cell. For a front metal coverage of 25%, the optical cloaking layer increases the J_{sc} from 29.95 mA/cm^2 to 39.12 mA/cm^2. Finally, a concentrator optics design is presented that allows for an effective shading of 1.8% at a concentration of 1000 suns, for which we predict an efficiency gain of 4.8%-absolute, according to the detailed-balance limit. Concentrator solar cells are the most efficient PV technology on record, with a maximum power conversion efficiency of 47.1%. Furthermore, they are well suited for combination with concentrated solar thermal setups in high irradiance regions on earth, making these architectures capable of sourcing electricity and heat from the sun simultaneously.

Silicon PV is currently the commercially most relevant technology, owing to low end-user costs and high module efficiencies (above 20%). At the same time, thin-film PV applications are becoming increasingly important. The maturity of Si technology would make it an interesting contender for that market, but absorption in thin crystalline Si wafers is inhibited by poor absorption of light close to the bandgap (1000-1200 nm). Chapter 4 introduces a fabrication approach for two optical designs that can improve incoupling and light trapping in Si absorbers with flat surfaces to mitigate this issue. For incoupling, we demonstrate a square lattice of SiN_x nanocylinders (117 nm height, 190 nm diameter, 460 nm pitch) that acts as a broadband anti-reflection coating. The design currently yields a measured J_{sc} of 36.9 mA/cm^2, with the potential of achieving

up to 39 mA/cm^2 on a 100 µm Si wafer. Such designs can also be used on thinner wafers to create high-efficiency flexible solar cells. Finally, we experimentally demonstrate a hyperuniform Si nanostructure on the surface of a Si solar cell, that can efficiently trap light in a thin Si cell, and investigate electronic passivation requirements for the strongly corrugated geometry. Thin crystalline Si wafers may find applications in vehicle-integrated PV, building-integrated PV, and in wearable and foldable electronics, and may enable a further cost reduction due to the use of a thinner absorber layer.

A highly promising path to enhance the power conversion efficiency of Si based PV is by the addition of a second absorber on top, creating a tandem solar cell device. The detailed-balance efficiency limit for such a cell is 45.1% for a perovskite top cell with a bandgap of 1.73 eV, which is significantly larger than the limit for a Si cell alone (33%). We adapt (Chapter 5) the detailed balance formalism to predict realistic efficiency limits, by tailoring the optical interface between Si and perovskite. We optimize the spectrally selective light reflection, so that the energy of the incoming photons can be harvested more efficiently. The calculations predict that a spectrally selective Lambertian light trapping layer can yield an efficiency gain of 2.7%-absolute for a 500-nm-thick perovskite layer with a bandgap that is close to the optimum (1.77 eV). With increasing bandgap, this effect becomes stronger, and can yield efficiency gains up to 6%-absolute. Perovskite/Si tandem devices have just achieved laboratory efficiencies of 31.3% and are already being commercialized. The high voltages that such tandem devices enable are also interesting for electrolysis applications such as solar-to-hydrogen conversion, where power from the solar cell facilitates water splitting.

Zn_3P_2 is an absorber material with long diffusion lengths and strong absorption but has received very limited attention in PV until just recently. New developments that allow for high-purity Zn_3P_2 crystals and removal of the absorber from the growth substrate now enable new design opportunities for the cell architecture. We propose (Chapter 6) a thin-film Zn_3P_2-TiO2 heterojunction solar cell design that consists of a cell stack of Au (back contact) – Zn_3P_2 (p-type absorber) – TiO_2 (n-type layer) – ITO (front contact). The design is derived from electronic drift-diffusion simulations and predicts a power conversion efficiency of 20% for 2-µm-thick Zn_3P_2. Improved light incoupling could increase the efficiency further. Zn_3P_2 consists of materials that are abundant in the earth's crust, and thus have the potential to become relevant for PV on a large scale due to lower material extraction costs, next to its good optoelectronic qualities.

For light management concepts to become interesting on an industrial scale, it is important that fitting nanofabrication processes are found. Substrate conformal imprint lithography (SCIL) is such a process and is used in many chapters of this thesis. In Chapter 7 we review further nanofabrication approaches for PV based on SCIL. Relying on the experience from the previous chapters, we identify three possible approaches. Next to indirect approaches that use SCIL to provide an etch mask for further lithography steps, we highlight direct imprinting as a simple one-step approach, that can be applied using dedicated solgels. SCIL has already been commercialized for a cassette-based wafer patterning approach and roll-to-roll soft-imprint patterning also exists commercially, so that these novel insights may find their way to large-scale applications.

Conceptually, this thesis integrates the optimization of light management with charge carrier management by carefully optimizing the three-dimensional charge carrier gener-

ation and collection profiles. We emphasize the importance of spatial control of absorption for the electronic solar cell performance. We investigate how absorption-enhancing nanostructures influence the electronic integrity of solar cells for a wide range of established as well as novel photovoltaic technologies. The insights derived in this thesis can lead to solar cells with thinner absorber layers, higher efficiencies, and may introduce the use of novel absorber materials and cell designs.

Samenvatting

Op het moment dat deze samenvatting is geschreven, juli 2022, is het meest recente datapunt voor de CO_2-concentratie op Mauna Loa 420,99 ppm. Ik ben geboren in april 1994, met 361,36 ppm. Om de klimaatcrisis te bestrijden, is het stoppen van de snelle stijging van de broeikasgasconcentratie in onze atmosfeer één van de grootste uitdagingen van deze eeuw, daarom moet het dit decennium nog op het schema worden gezet. We hebben het geluk dat we de mogelijkheden hebben om de werktuigen te maken om daar te komen. Het veranderen van de manieren waarop wij energie opwekken — weg van vervuilende fossiele brandstoffen en richting duurzame en hernieuwbare energiebronnen zoals wind, water en zon — zal aanzienlijk bijdragen aan het beperken van de opwarming van de aarde. Elektriciteitsopwekking uit zonlicht, fotovoltaïsche energie (PV), ligt op schema om een deel van de last te dragen en deze groei kan profiteren van verdere innovaties op het gebied van efficiënte stroomconversie, technologische veelzijdigheid (flexibel, buigzaam, duurzaam, etc.) en kostenreductie.

In dit proefschrift komen deze aspecten aan de orde voor verschillende technologieën. We ontwerpen nieuwe fotovoltaïsche architecturen voor een reeks gevestigde (Si, III-V-materialen) en nieuwe (PbS-quantum dots, Zn_3P_2, perovskieten) absorberende materialen. Lichtmanagementconcepten worden gebruikt om de absorptie van licht voor fotovoltaïsche apparaten, zonnecellen, te evalueren en te verbeteren. De verbeteringen zijn gebaseerd op structuren van nano- en micrometer dimensie aan de voorkant, het midden of de achterkant van de zonnecellen en hebben als primair doel de absorptie in de absorberende laag te verbeteren. Bovendien wordt ook rekening gehouden met de ruimtelijke verdeling van het geabsorbeerde licht, om niet alleen een succesvolle opwekking van ladingsdragers uit fotonen te garanderen, maar ook het succesvol extraheren van de ladingsdragers. We demonstreren veel van deze ontwerpen experimenteel, evalueren hun elektronische prestaties en gebruiken commercieel relevante schaalbare processen om de toepassingsrelevantie van onze ontwerpen te maximaliseren.

Het proefschrift begint met een uiteenzetting van de dreigende gevolgen van de stijging van de broeikasgasconcentratie in onze atmosfeer (Hoofdstuk 1). De opwarming van de aarde wordt gezien als een ernstig gevaar en de grootste uitdaging van deze eeuw. Dit is onder meer een belangrijke motivatie en rechtvaardiging om over te stappen op energieopwekking uit hernieuwbare bronnen. De basisprincipes van fotovoltaïsche energieconversie worden besproken, evenals de thermodynamische limiet, als een fysieke grens. Speciale aandacht wordt besteed aan de trends in de toename van de celefficiëntie voor verschillende halfgeleiders door de jaren heen, en hun duidelijke voordelen voor PV-toepassingen worden gepresenteerd.

De eerste technologie waar we naar kijken zijn dunne-film PbS quantum dots (kwantumdeeltjes, QD) zonnecellen, gemaakt vanuit oplossing (Hoofdstuk 2). Hiervoor introduceren we een bulk heterojunctie zonnecelontwerp dat optisch resonant is. De cel is

ontworpen als een vierkant rooster van PbS QD-cilinders met een hoogte van 330 nm, een diameter van 320 nm en een roosterafstand van 500 nm, ingebed in ZnO. De afmetingen van de QD-cilinder zijn zo gekozen dat ze optische resonanties ondersteunen, waardoor de absorptie per volume-eenheid met 20% wordt verbeterd in vergelijking met een vlakke referentie. Elektronische simulaties voorspellen een winst in kortsluitstroomdichtheid (J_{sc}) van 3,2 mA/cm^2 en een efficiëntiewinst van 0,4% - absoluut. In het experiment gebruiken we eerst substraat-conforme afdruklithografie (SCIL) om patroonvorming van ZnO-solgel aan te tonen en de verwachte optische trends in de gefabriceerde cellen te vinden. Ook laten we een verhoogde externe kwantumefficiëntie (EQE) zien, die leidt tot een J_{sc}-verhoging van 0,74 mA/cm^2. Ten slotte benadrukt dit hoofdstuk het belang om het generatieprofiel van ladingsdragers te beschouwen als de grootheid die het optische en elektronische ontwerp van zonnecellen verbindt.

PbS QD zonnecellen hebben een verstelbaare bandgap, zijn dun en ze zijn te verwerken in oplossing, waardoor ze interessante kandidaten zijn voor geprinte zonnecellen, evenals cellen voor het oogsten van licht binnenshuis. Vooruitgangen in PbS QD zonnecellen hebben vaak ook positieve implicaties voor het ontwerp van op deze halfgeleider gebaseerde licht-emitterende diodes (LED).

Een geconcentreerd fotovoltaïsch systeem (CPV) is een hoogrenderende technologie die afhankelijk is van de concentratie van zonlicht op relatief kleine zonnecellen, en de concentratiefactor veroorzaakt een logaritmische toename van de nullastspanning (V_{oc}), wat efficiëntere cellen mogelijk maakt. Bovendien maakt het gebruik van veel kleinere cellen (factor 100-1000) het mogelijk om dure III-V-technologieën in overweging te nemen, zoals op GaAs gebaseerde zonnecellen. CPV vereist echter om een groot oppervlakte aan de voorkant te bedekken met metaal om de hoge gegenereerde stroom te verzamelen, wat aanzienlijke reflectieverliezen veroorzaakt. In Hoofdstuk 3 introduceren we transparante contacten van een glasachtig polymeer, door gebruik te maken van optische breking in V-vormige groeven. We brengen de laag aan op een Si-zonnecel en demonstreren een hoge optische transparantie (95,2%). Voor een frontale metaaldekking van 25% verhogen de transparante contacten de J_{sc} van 29,95 mA/cm^2 naar 39,12 mA/cm^2. Ten slotte wordt een CPV-ontwerp gepresenteerd dat een “effectieve schaduw” van 1,8% mogelijk maakt bij een concentratie van 1000 zonnen, waarvoor we een efficiëntiewinst van 4,8%-absoluut voorspellen, volgens de thermodynamische limiet.

CPV zonnecellen zijn de meest efficiënte PV-technologie ooit, met een maximale energieconversie-efficiëntie van 47,1%. Bovendien zijn ze zeer geschikt om te combineren met geconcentreerde thermische zonne-installaties in gebieden met een hoge instraling op aarde. Deze architecturen zijn in staat om gelijktijdig elektriciteit en warmte op te wekken.

Silicium-PV is momenteel de commercieel meest relevante technologie, vanwege de lage eindgebruikerskosten en de hoge module-efficiëntie (boven de 20%). Tegelijkertijd worden dunne-film PV-toepassingen steeds belangrijker. De volwassenheid van Si-technologie zou het een interessante concurrent voor die markt maken, maar absorptie in dunne kristallijne Si-wafers wordt beperkt door slechte absorptie van licht rond de bandgap (1000-1200 nm). Hoofdstuk 4 introduceert een fabricagebenadering voor twee optische ontwerpen die inkoppeling en light trapping (lichtopsluiting) in Si-

halfgeleiders met vlakke oppervlakken kunnen verbeteren om dit probleem te verminderen. Voor inkoppeling demonstreren we een vierkant rooster van SiNx-nanocilinders (117 nm hoogte, 190 nm diameter, 460 nm roosterafstand) dat fungeert als een breedband antireflectielaag. Het ontwerp levert momenteel een gemeten J_{sc} op van 36,9 mA/cm^2, met het potentieel om tot 39 mA/cm^2 te bereiken op een 100 µm Si-wafer. Dergelijke ontwerpen kunnen ook worden gebruikt op dunnere wafers om zeer efficiënte flexibele zonnecellen te maken. Ten slotte demonstreren we experimenteel een hyperuniforme Si-nanostructuur op het oppervlak van een Si-zonnecel, die licht efficiënt kan vangen in een dunne Si-cel, en onderzoeken we elektronische passiveringsvereisten voor deze geometrie.

Dunne kristallijne Si-wafers kunnen worden toegepast in voertuigen, in gebouwen en in draagbare en opvouwbare elektronica, en kunnen een verdere kostenverlaging mogelijk maken door het gebruik van een dunnere absorberende laag.

Een veelbelovend pad om de energieconversie-efficiëntie van op Si gebaseerde PV te verbeteren, is door de toevoeging van een tweede halfgeleider bovenop, waardoor een tandem-zonnecel ontstaat. De efficiëntielimiet voor een dergelijke cel is 45,1% voor een perovskiet-topcel met een bandgap van 1,73 eV, wat aanzienlijk groter is dan de limiet voor een Si-cel alleen (32%). We passen (Hoofdstuk 5) het formalisme voor de thermodynamische limiet aan om realistische efficiëntielimieten te voorspellen, door het optische grensvlak tussen Si en perovskiet aan te passen. We optimaliseren de golflengte-selectieve lichtreflectie, zodat de energie van de binnenkomende fotonen efficiënter kan worden gewonnen. De berekeningen voorspellen dat een golflengte-selectieve Lambertiaanse lichtvanglaag een efficiëntiewinst van 2,7% kan opleveren voor een 500 nm dikke perovskietlaag met een bandkloof die dicht bij het optimum ligt (1,77 eV). Met toenemende bandgap wordt dit effect sterker en kan efficiëntiewinsten tot 6% absoluut opleveren.

Perovskiet/Si tandem-zonnecellen hebben onlangs een laboratoriumefficiëntie van 31,3% behaald en worden al op de markt gebracht. De hoge spanningen die dergelijke tandemcellen mogelijk maken zijn ook interessant voor elektrolysetoepassingen zoals zonneenergie-naar-waterstofconversie, waarbij stroom van de zonnecel het splitsen van water vergemakkelijkt.

Zn_3P_2 is een absorberend materiaal met lange diffusielengtes en sterke absorptie, maar heeft tot voor kort zeer weinig aandacht gekregen in PV. Nieuwe ontwikkelingen, die zorgen voor zeer zuivere Zn_3P_2-kristallen en verwijdering van de halfgeleider van het groeisubstraat, bieden nu nieuwe ontwerpmogelijkheden voor de celarchitectuur. We stellen (Hoofdstuk 6) een dunne-film Zn_3P_2-TiO_2 heterojunctie zonnecelontwerp voor dat bestaat uit een celstapel van Au (achtercontact) – Zn_3P_2 (p-type halfgeleider) – TiO_2 (n-type halfgeleider) – ITO (voorcontact). Het ontwerp is afgeleid van elektronische drift-diffusiesimulaties en voorspelt een energieconversie-efficiëntie van 20% voor 2 µm dik Zn_3P_2. Een verbeterde lichtinkoppeling zou de efficiëntie verder kunnen verhogen.

Zn_3P_2 bestaat uit materialen die overvloedig aanwezig zijn in de aardkorst en dus de potentie hebben om op grote schaal relevant te worden voor PV vanwege lagere materiaalextractiekosten, naast de goede opto-elektronische eigenschappen.

Om lichtmanagementconcepten op industriële schaal interessant te maken, is het belangrijk dat er passende nanofabricageprocessen worden gevonden. Substraat con-

forme afdruk lithografie (SCIL) is zo'n proces en wordt in veel hoofdstukken van dit proefschrift gebruikt. In Hoofdstuk 7 bespreken we verdere nanofabricagebenaderingen voor PV op basis van SCIL. Op basis van de ervaring uit de vorige hoofdstukken onderscheiden we drie mogelijke benaderingen. Naast indirecte benaderingen waar SCIL wordt gebruikt om etsmaskers te maken voor verdere lithografiestappen, benadrukken wij directe afdrukken als een eenvoudige eenstapsbenadering, die kan worden toegepast met behulp van speciale solgels.

SCIL is al gecommercialiseerd voor een op cassettes gebaseerde waferpatroonbenadering en roll-to-roll zachte-afdruk patronen bestaan ook commercieel. Deze nieuwe inzichten kunnen dus snel op grote schaal worden toegepast.

Conceptueel integreert dit proefschrift de optimalisatie van lichtbeheer en ladingdragerbeheer door zorgvuldig de driedimensionale opwekking van ladingsdragers en extractie te optimaliseren. We benadrukken het belang van ruimtelijke controle van absorptie voor de elektronische prestaties van zonnecellen. We onderzoeken hoe absorptieverhogende nanostructuren de elektronische integriteit van zonnecellen beïnvloeden voor een breed scala aan gevestigde en nieuwe fotovoltaïsche technologieën. De inzichten die in dit proefschrift zijn verkregen kunnen leiden tot zonnecellen met dunnere absorberende lagen, hogere efficiënties en kunnen het gebruik van nieuwe halfgeleider materialen en celontwerpen introduceren.

Zusammenfassung

Diese Zusammenfassung wurde im Juli 2022 geschrieben, und der jüngste Messwert für die CO_2-Konzentration auf Mauna Loa beträgt 420,99 ppm. Ich wurde im April 1994 bei 361,36 ppm geboren. Das Stoppen des schnellen Anstiegs der Treibhausgaskonzentration in unserer Atmosphäre - zur Bekämpfung der Klimakrise - ist eine der größten Herausforderungen dieses Jahrhunderts und die Weichen dafür müssen noch in diesem Jahrzehnt gestellt werden. Wir haben das große Glück, dass wir auch über die technischen Voraussetzungen, um dieses Ziel zu erreichen, verfügen. Die Umstellung unserer Energieerzeugung, weg von umweltschädlichen fossilen Brennstoffen und hin zu nachhaltigen und erneuerbaren Energiequellen wie Wind, Wasser und Sonne, wird erheblich zur Eindämmung der Erderwärmung beitragen. Die Stromerzeugung aus Sonnenlicht, Photovoltaik (PV), wird hierbei einen großen Beitrag leisten, und kann von weiteren Innovationen in Bezug auf Effizienz, technologische Vielseitigkeit (Flexibilität, Langlebigkeit, etc.) und Kostensenkung profitieren.

In dieser Doktorarbeit betrachten wir die genannten Aspekte für eine Reihe von Technologien. Wir entwerfen neue photovoltaische Architekturen für etablierte (Si, III-V Materialien) und neuartige (PbS-Quantum Dots, Zn_3P_2, Perowskite) Halbleiter. Lichtmanagementkonzepte werden zur Bewertung und Verbesserung der Lichtabsorption in den photovoltaischen Einheiten – Solarzellen - verwendet. Die Verbesserungen basieren auf Nano- und Mikrostrukturen, die in, auf oder unter den Solarzellen installiert werden, um die Absorption innerhalb der Halbleiterschicht zu verbessern. Zusätzlich wird auch die räumliche Verteilung des absorbierten Lichts berücksichtigt, um nicht nur eine erfolgreiche Erzeugung von Ladungsträgern mittels Photonen, sondern auch eine erfolgreiche Extraktion der Ladungsträger zu ermöglichen. Viele dieser Designs werden dann experimentell realisiert, um ihre elektronische Leistung zu bewerten. Dafür werden kommerziell relevante, skalierbare Prozesse verwendet, um die Anwendungsrelevanz unserer Designs zu demonstrieren.

Wir befassen uns zuerst mit den drohenden Folgen des Anstiegs der Treibhausgaskonzentration in unserer Atmosphäre (Kapitel 1). Die Erderwärmung wird als ernsthafte Gefahr und größte Herausforderung des Jahrhunderts identifiziert. Dies ist eine wichtige Motivation für den Umstieg auf Energieerzeugung aus erneuerbaren Quellen. Es werden die physikalischen Grundprinzipien der photovoltaischen Energieumwandlung sowie das thermodynamische Limit als Effizienzgrenze diskutiert. Besonderes Augenmerk wird auf die Trends zur Steigerung der Zelleffizienz für verschiedene Halbleiter im Laufe der Jahre gelegt, wobei deren individuellen Vorteile für PV-Anwendungen vorgestellt werden.

Die erste Technologie, die wir betrachten, sind Dünnschicht-PbS-Quantum Dot (Quantenpunkt, QD) Solarzellen (Kapitel 2), für die wir ein optisch resonantes Bulk-Heterojunction Solarzellendesign vorstellen. Die Zelle besteht aus einem quadratischen Gitter von PbS-QD-Zylindern mit einer Höhe von 330 nm, einem Durchmesser von 320 nm

und einem Abstand von 500 nm, eingebettet in ZnO. Die QD-Zylinderabmessungen sind so gewählt, dass sie optische Resonanzen unterstützen und die Absorption pro Volumen-einheit im Vergleich zu einer planaren Referenzzelle um 20 % erhöhen. Elektronische Simulationen sagen eine Zunahme der Kurzschlussstromdichte (J_{sc}) um 3,2 mA/cm^2 und eine Effizienzsteigerung um 0,4 %-absolut voraus. Im Experiment verwenden wir zunächst substratkonforme Weichdrucklithographie (SCIL), um ZnO-Solgel mit einem Muster zu versehen. Die hergestellten Zellen bestätigen die simulierten optischen Trends, welche zu einer erhöhten externen Quanteneffizienz (EQE) führen, die eine J_{sc} Verstärkung von 0,74 mA/cm^2 zur Folge hat. Abschließend betont dieses Kapitel, wie wichtig es ist, das Ladungsträgererzeugungsprofil als die Größe zu betrachten, die optisches und elektronisches Solarzellendesign vereint.

PbS-QD-Solarzellen haben eine verstellbare Bandlücke und können in Lösung verarbeitet werden, was sie zu interessanten Kandidaten für tintenstrahlgedruckte Solarzellen sowie potenzielle Lichtsammelzellen für den Innenbereich von Gebäuden macht. Fortschritte bei PbS-QD-Solarzellen haben oft auch positive Auswirkungen auf das Design von Leuchtdioden (LEDs), die auf diesem Halbleiter basieren.

Konzentrator-Photovoltaik (CPV) ist eine hocheffiziente Technologie, die auf der Konzentration von Sonnenlicht auf relativ kleine Solarzellen beruht. Das Erhöhen der Konzentration führt zu einem logarithmischen Anstieg der Leerlaufspannung (V_{oc}), was effizientere Zellen ermöglicht. Darüber hinaus ermöglicht die Verwendung viel kleinerer Zellen (Faktor 100-1000) die Berücksichtigung teurer III-V-Technologien, wie z. B. Solarzellen auf GaAs-Basis. CPV erfordert jedoch eine große Frontmetallkontaktdichte, um die hohen Ströme zu sammeln, was wiederum erhebliche Reflexionsverluste verursacht. In Kapitel 3 demonstrieren wir unsichtbare Kontakte mittels optischer Brechung von V-förmigen Rillen, die in ein glasartiges Polymer gedruckt sind. Wir demonstrieren eine hohe optische Transparenz (95,2 %) und bringen die Schicht auf einer Si-Solarzelle auf. Bei einer Frontmetallbedeckung von 25 % erhöht die optische Deckschicht die J_{sc} von 29,95 mA/cm^2 auf 39,12 mA/cm^2. Am Ende wird ein Konzentratordesign vorgestellt, das einen effektiven Kontaktschatten von 1,8 % bei einer Konzentration von 1000 Sonnen ermöglicht, für das wir gemäß des thermodynamischen Limits einen Effizienzgewinn von 4,8 %-absolut vorhersagen.

Konzentrator-Solarzellen sind die effizienteste PV-Technologie die es je gab, mit einer zurzeit maximalen Energieumwandlungseffizienz von 47,1 %. Darüber hinaus eignen sie sich gut für die Kombination mit solarthermischen Konzentratoranlagen in Erdregionen mit hoher Sonneneinstrahlung, da diese Architekturen in der Lage sind intensives Sonnenlicht gleichzeitig in Strom und Wärme umzuwandeln.

Aufgrund niedriger Endverbraucherkosten und hoher Moduleffizienzen (über 20 %) ist Silizium (Si) PV derzeit die kommerziell interessanteste Technologie. Gleichzeitig werden Dünnschicht-PV-Anwendungen immer wichtiger. Die Reife der Si-Technologie würde sie zu einem interessanten Konkurrenten für diesen Markt machen, aber die Absorption in dünnen, kristallinen Si-Wafern wird durch schlechte Lichtabsorption nahe der Bandlücke (1000–1200 nm) gehemmt. Kapitel 4 stellt zwei optische Designs vor, die das Einkoppeln und das Speichern von Licht (Light Trapping) in Si-Zellen mit flachen Oberflächen verbessern können, um dieses Problem zu beheben. Zur Einkopplung demonstrieren wir ein quadratisches Gitter aus SiNx-Nanozylindern (117 nm Höhe,

190 nm Durchmesser, 460 nm Abstand), das als Breitbandantireflexionsbeschichtung fungiert. Das Design ergibt derzeit eine gemessene J_{sc} von 36,9 mA/cm^2, mit dem Potenzial, bis zu 39 mA/cm^2 auf einem 100 µm Si-Wafer zu erreichen. Solche Designs können auch für dünnere Wafer verwendet werden, um hocheffiziente, flexible Solarzellen herzustellen. Des Weiteren demonstrieren wir eine hyperuniforme Si-Nanostruktur auf der Oberfläche einer Si-Solarzelle, womit Licht in einer dünnen Si-Zelle effizient einfangen werden kann, und untersuchen die Anforderungen an den elektronischen Passivierungsgrad für solche Architekturen.

Dünne, kristalline Si-Wafer können in fahrzeugintegrierter PV, gebäudeintegrierter PV und in tragbarer und faltbarer Elektronik genutzt werden und zudem ermöglicht die dünnere Halbleiterschicht eine signifikante Materialkostensenkung.

Ein vielversprechender Weg zur Verbesserung der Effizienz von PV auf Si-Basis ist das Hinzufügen eines zweiten Halbleiters auf der Oberseite, wodurch eine Tandemsolarzelle entsteht. Die Effizienzgrenze für eine solche Zelle beträgt 45,1 % für eine Solarzelle mit einer Perowskitschicht (Bandlücke von 1,73 eV) oberhalb der Siliziumschicht, was deutlich höher ist als die Grenze für eine Si-Zelle ohne Perowskit (32 %). Wir passen (Kapitel 5) den Formalismus für das thermodynamische Limit an, um realistische Effizienzgrenzen für Tandemsolarzellen mit optisch modifizierten Grenzflächen zwischen Si-und Perowskit vorherzusagen. Wir optimieren die spektral selektive Lichtreflexion, damit die Energie der einfallenden Photonen effizienter geerntet werden kann. Die Berechnungen sagen voraus, dass eine spektral selektive, Lambertsche Lichteinfangschicht einen Effizienzgewinn von 2,7 % für eine 500 nm dicke Perowskitschicht mit einer Bandlücke nahe dem Optimum (1,77 eV) erzielen kann. Mit zunehmender Bandlücke wird dieser Effekt stärker und kann zu Effizienzgewinnen von bis zu 6 % führen.

Perowskit/Si-Tandemzellen haben gerade einen Laboreffizienz von 31,3 % erreicht und werden bereits kommerzialisiert. Die hohen Spannungen, die solche Tandemzellen ermöglichen, sind auch für Elektrolyseanwendungen, wie die Umwandlung von Solarenergie in Wasserstoff interessant, wobei der Strom und die Spannung der Solarzelle die Wasserspaltung ermöglichen.

Zinkphosphid (Zn_3P_2) ist ein Halbleitermaterial mit hoher Absorption und Diffusionslänge, hat aber bis vor kurzem nur sehr begrenzte Aufmerksamkeit in der PV erhalten. Neue Fortschritte, die hochreine Zn_3P_2-Kristalle und die Separation des Halbleiters vom Wachstumssubstrat ermöglichen, erlauben es nun, effizientere Zellarchitekturen anzufertigen. Wir schlagen (Kapitel 6) ein Dünnschicht-Zn_3P_2-TiO_2-Solarzellendesign vor, das aus einem Zellstapel aus Au (Rückkontakt) – Zn_3P_2 (p-Typ-Halbleiter) – TiO_2 (n-Typ-Halbleiter) – ITO (Frontkontakt) besteht. Das Design wird von elektronischen Driftdiffusionssimulationen hergeleitet und wir prognostizieren eine Effizienz von 20 % für 2 µm dickes Zn_3P_2. Eine verbesserte Lichteinkopplung kann die Effizienz noch weiter steigern.

Zn_3P_2 besteht aus Materialien, die in der Erdkruste reichlich vorhanden sind und daher, neben den sehr guten optoelektronischen Eigenschaften, das Potenzial haben, aufgrund niedriger Materialgewinnungskosten für die PV relevant zu werden.

Damit Lichtmanagementkonzepte im industriellen Maßstab interessant werden, ist es wichtig, dass geeignete Nanofabrikationsverfahren gefunden werden. Die substratkonforme Weichdrucklithographie (SCIL) ist ein solches Verfahren und wird in vielen Kapiteln

dieser Arbeit verwendet. In Kapitel 7 besprechen wir weitere Nanofabrikationsansätze für PV basierend auf SCIL. Aufbauend auf den Erfahrungen aus den vorangegangenen Kapiteln illustrieren wir drei mögliche Vorgehensweisen. Neben indirekten Ansätzen, die SCIL verwenden, um eine Ätzmaske für weitere Lithographieschritte zu fertigen, heben wir den direkten Weichdruck als einfachen, einstufigen Ansatz hervor, der mithilfe spezieller Solgels angewandt werden kann.

SCIL wurde bereits für einen kassettenbasierten Ansatz zur Waferstrukturierung kommerzialisiert, und auch rollenbasierte Weichdruckstrukturierung existiert kommerziell, was den Weg dieser neuartigen Erkenntnisse hin zur Anwendung erleichtert.

Zusammenfassend verbindet diese Arbeit die Optimierung von Lichtmanagement mit Ladungsträgermanagement. Wir betonen die Bedeutung der räumlichen Steuerung des Absorptionsprozesses für die Effizienz von Solarzellen. Des Weiteren untersuchen wir für ein breites Spektrum etablierter und neuartiger Photovoltaiktechnologien, wie absorptionserhöhende Nanostrukturen die elektronische Integrität von Solarzellen beeinflussen. Die in dieser Arbeit gewonnenen Erkenntnisse können zu Solarzellen mit dünneren Halbleiterschichten und höheren Effizienzen führen und sie ermöglichen die Verwendung neuartiger Halbleitermaterialien und Zelldesigns.

References

[1] R. Pierrehumbert, *There is no Plan B for dealing with the climate crisis,* Bulletin of the Atomic Scientists **75**, 215 (2019).

[2] D. Archer and S. Rahmstorf, *The Climate Crisis: An Introductory Guide to Climate Change* (Cambridge University Press, 2009).

[3] EPA, *Climate change and social vulnerability in the United States. A Focus on Six Impacts*, Tech. Rep. September (U.S. Environmental Protection Agency, 2021).

[4] I. M. Otto, D. Reckien, C. P. Reyer, R. Marcus, V. Le Masson, L. Jones, A. Norton, and O. Serdeczny, *Social vulnerability to climate change: a review of concepts and evidence,* Regional Environmental Change **17**, 1651 (2017).

[5] W. N. Adger and P. M. Kelly, *Social vulnerability to climate change and the architecture of entitlements,* Mitigation and Adaptation Strategies for Global Change **4**, 253 (1999).

[6] W. Steffen, K. Richardson, J. Rockström, S. E. Cornell, I. Fetzer, E. M. Bennett, R. Biggs, S. R. Carpenter, W. De Vries, C. A. De Wit, C. Folke, D. Gerten, J. Heinke, G. M. Mace, L. M. Persson, V. Ramanathan, B. Reyers, and S. Sörlin, *Planetary boundaries: Guiding human development on a changing planet,* Science **347** (2015), 10.1126/science.1259855.

[7] L. Persson, B. M. Carney Almroth, C. D. Collins, S. Cornell, C. A. de Wit, M. L. Diamond, P. Fantke, M. Hassellöv, M. MacLeod, M. W. Ryberg, P. Søgaard Jørgensen, P. Villarrubia-Gómez, Z. Wang, and M. Z. Hauschild, *Outside the Safe Operating Space of the Planetary Boundary for Novel Entities,* Environmental Science and Technology **56**, 1510 (2022).

[8] S. J. Lade, W. Steffen, W. de Vries, S. R. Carpenter, J. F. Donges, D. Gerten, H. Hoff, T. Newbold, K. Richardson, and J. Rockström, *Human impacts on planetary boundaries amplified by Earth system interactions,* Nature Sustainability **3**, 119 (2020).

[9] K. Thoning, A. Crotwell, and J. Mund, *Atmospheric Carbon Dioxide Dry Air Mole Fractions from continuous measurements at Mauna Loa, Hawaii, Barrow, Alaska, American Samoa and South Pole. 1973-2021,* National Oceanic and Atmospheric Administration (NOAA), Global Monitoring Laboratory (GML) **50**, 1 (2022).

[10] S. Solomon, G. K. Plattner, R. Knutti, and P. Friedlingstein, *Irreversible climate change due to carbon dioxide emissions,* Proceedings of the National Academy of Sciences of the United States of America **106**, 1704 (2009).

[11] N. W. Arnell, M. G. R. Cannell, M. Hulme, R. S. Kovats, J. F. B. Mitchell, R. J. Nicholls, M. L. Parry, M. T. J. Livermore, and A. White, *The consequences of CO_2 stabilisation for the impacts of climate change,* Climatic Change **53**, 413 (2002).

[12] S. A. Montzka, E. J. Dlugokencky, and J. H. Butler, *Non-CO_2 greenhouse gases and climate change,* Nature **476**, 43 (2011).

[13] S. Manabe and R. J. Stouffer, *Sensitivity of a global climate model to an increase of CO_2 concentration in the atmosphere.* Journal of Geophysical Research **85**, 5529 (1980).

[14] S. Manabe and R. Wetherald, *The Effects of Doubling the CO_2 Concentration on the climate of a General Circulation Model,* Journal of the Atmospheric Sciences **32**, 3 (1975).

[15] P. C. Jain, *Greenhouse effect and climate change: scientific basis and overview,* Renewable Energy **3**, 403 (1993).

[16] I. Dincer and C. Zamfirescu, *Sustainable Energy Systems and Applications*, Vol. 1 (Springer, 2011) pp. 1–823.

[17] T. Kåberger, *Progress of renewable electricity replacing fossil fuels,* Global Energy Interconnection **1**, 48 (2018).

[18] I. Lazkano, L. Nøstbakken, and M. Pelli, *From fossil fuels to renewables: The role of electricity storage,* European Economic Review **99**, 113 (2017).

[19] L. Gustavsson, P. Börjesson, B. Johansson, and P. Svenningsson, *Reducing CO_2 emissions by substituting biomass for fossil fuels,* Energy **20**, 1097 (1995).

[20] N. Abas, A. Kalair, and N. Khan, *Review of fossil fuels and future energy technologies,* Futures **69**, 31 (2015).

[21] W. F. Lamb, T. Wiedmann, J. Pongratz, R. Andrew, M. Crippa, J. G. Olivier, D. Wiedenhofer, G. Mattioli, A. A. Khourdajie, J. House, S. Pachauri, M. Figueroa, Y. Saheb, R. Slade, K. Hubacek, L. Sun, S. K. Ribeiro, S. Khennas, S. De La Rue Du Can, L. Chapungu, S. J. Davis, I. Bashmakov, H. Dai, S. Dhakal, X. Tan, Y. Geng, B. Gu, and J. Minx, *A review of trends and drivers of greenhouse gas emissions by sector from 1990 to 2018,* Environmental Research Letters **16**, 073005 (2021).

[22] A. Arrigoni, D. K. Panesar, M. Duhamel, T. Opher, S. Saxe, I. D. Posen, and H. L. MacLean, *Life cycle greenhouse gas emissions of concrete containing supplementary cementitious materials: cut-off vs. substitution,* Journal of Cleaner Production **263**, 121465 (2020).

[23] A. Shakoor, S. Shakoor, A. Rehman, F. Ashraf, M. Abdullah, S. M. Shahzad, T. H. Farooq, M. Ashraf, M. A. Manzoor, M. M. Altaf, and M. A. Altaf, *Effect of animal manure, crop type, climate zone, and soil attributes on greenhouse gas emissions from agricultural soils—A global meta-analysis,* Journal of Cleaner Production **278**, 124019 (2021).

[24] Hans-O. Pörtner and Debra C. Roberts, *Climate Change 2022: Impacts, Adaption and Vulnerability,* Intergovernmental Panel on Climate Change , 1 (2022).

[25] D. Gielen, F. Boshell, D. Saygin, M. D. Bazilian, N. Wagner, and R. Gorini, *The role of renewable energy in the global energy transformation,* Energy Strategy Reviews **24**, 38 (2019).

[26] J. Gong, C. Li, and M. R. Wasielewski, *Advances in solar energy conversion,* Chemical Society Reviews **48**, 1862 (2019).

[27] M. B. Hayat, D. Ali, K. C. Monyake, L. Alagha, and N. Ahmed, *Solar energy—A look into power generation, challenges, and a solar-powered future,* International Journal of Energy Research **43**, 1049 (2019).

[28] S. A. Vargas, G. R. T. Esteves, P. M. Maçaira, B. Q. Bastos, F. L. Cyrino Oliveira, and R. C. Souza, *Wind power generation: A review and a research agenda,* Journal of Cleaner Production **218**, 850 (2019).

[29] P. Breeze, *Wind Power Generation* (Elsevier Science, 2016).

[30] E. F. Moran, M. C. Lopez, N. Moore, N. Müller, and D. W. Hyndman, *Sustainable hydropower in the 21st century,* Proceedings of the National Academy of Sciences of the United States of America **115**, 11891 (2018).

[31] O. Paish, *Small hydro power: Technology and current status,* Renewable and Sustainable Energy Reviews **6**, 537 (2002).

[32] G. Coro and E. Trumpy, *Predicting geographical suitability of geothermal power plants,* Journal of Cleaner Production **267**, 121874 (2020).

[33] A. Thakur, C. E. Canter, and A. Kumar, *Life-cycle energy and emission analysis of power generation from forest biomass,* Applied Energy **128**, 246 (2014).

[34] M. Gillespy, V. Ukropcova, and N. Brennan, *The Money Trees*, Tech. Rep. (CDP Worldwide, 2019).

[35] J. Hill and S. Friggens, *Biomass in a low-carbon economy*, Tech. Rep. 1 (Climate Change Comitee, 2018).

[36] M. S. Booth, *Not carbon neutral: Assessing the net emissions impact of residues burned for bioenergy,* Environmental Research Letters **13**, 035001 (2018).

[37] A. Verbruggen, E. Laes, and S. Lemmens, *Assessment of the actual sustainability of nuclear fission power,* Renewable and Sustainable Energy Reviews **32**, 16 (2014).

[38] N. Shykinov, R. Rulko, and D. Mroz, *Importance of Advanced Planning of Manufacturing for Nuclear Industry,* Management and Production Engineering Review **7**, 42 (2016).

[39] D. Abbott, *Is nuclear power globally scalable?* in *Proceedings of the IEEE,* Vol. 99 (Institute of Electrical and Electronics Engineers Inc., 2011) pp. 1611–1617.

[40] M. Zucchetti, L. Di Pace, L. El-Guebaly, J. H. Han, B. N. Kolbasov, V. Massaut, Y. Someya, K. Tobita, and M. Desecures, *Recent advances in fusion radioactive material studies,* Fusion Engineering and Design **88**, 652 (2013).

[41] J. Ongena and Y. Ogawa, *Nuclear fusion: Status report and future prospects,* Energy Policy **96**, 770 (2016).

[42] D. Grosspietsch, M. Saenger, and B. Girod, *Matching decentralized energy production and local consumption: A review of renewable energy systems with conversion and storage technologies,* Wiley Interdisciplinary Reviews: Energy and Environment **8**, 1 (2019).

[43] Sun Cable Pty Ltd, *Sun Cable (website),* `https://suncable.energy/` (2018), accessed: 2022-08-01.

[44] O. Majeed Butt, M. Zulqarnain, and T. Majeed Butt, *Recent advancement in smart grid technology: Future prospects in the electrical power network,* Ain Shams Engineering Journal **12**, 687 (2021).

[45] J. D. Hunt, B. Zakeri, R. Lopes, P. S. F. Barbosa, A. Nascimento, N. J. d. Castro, R. Brandão, P. S. Schneider, and Y. Wada, *Existing and new arrangements of pumped-hydro storage plants,* Renewable and Sustainable Energy Reviews **129**, 109914 (2020).

[46] A. G. Olabi, A. s. bahri, A. A. Abdelghafar, A. Baroutaji, E. T. Sayed, A. H. Alami, H. Rezk, and M. A. Abdelkareem, *Large-vscale hydrogen production and storage technologies: Current status and future directions,* International Journal of Hydrogen Energy **46**, 23498 (2021).

[47] M. Aziz, A. TriWijayanta, and A. B. D. Nandiyanto, *Ammonia as effective hydrogen storage: A review on production, storage and utilization,* Energies **13**, 1 (2020).

[48] S. F. Leung, H. C. Fu, M. Zhang, A. H. Hassan, T. Jiang, K. N. Salama, Z. L. Wang, and J. H. He, *Blue energy fuels: Converting ocean wave energy to carbon-based liquid fuels: Via CO_2 reduction,* Energy and Environmental Science **13**, 1300 (2020).

[49] J. W. Ager and A. A. Lapkin, *Chemical storage of renewable energy,* Science **360**, 707 (2018).

[50] M. Stocks, R. Stocks, B. Lu, C. Cheng, and A. Blakers, *Global Atlas of Closed-Loop Pumped Hydro Energy Storage,* Joule **5**, 270 (2021).

[51] N. Camacho and D. Jurburg, *Hydrogen fuel cell heavy-duty trucks : Review of main research topics,* International Journal of Hydrogen Energy **47**, 29505 (2022).

[52] ACER, *Transporting Pure Hydrogen by Repurposing Existing Gas Infrastructure: Overview of existing studies and reflections on the conditions for repurposing,* European Union Agency for the Cooperation of Energy Regulators , 1 (2021).

[53] I. R. Souza Filho, H. Springer, Y. Ma, A. Mahajan, C. C. da Silva, M. Kulse, and D. Raabe, *Green steel at its crossroads: Hybrid hydrogen-based reduction of iron ores,* Journal of Cleaner Production **340**, 130805 (2022).

[54] D. Hidalgo and J. M. Martín-Marroquín, *Power-to-methane, coupling CO_2 capture with fuel production: An overview,* Renewable and Sustainable Energy Reviews **132**, 110057 (2020).

[55] Y. Zheng, *Advanced Catalytic Materials for Ethanol Oxidation,* **10(2)**, 166 (2020).

[56] E. Valsera-Naranjo, A. Sumper, P. Lloret-Gallego, R. Villafáfila-Robles, and A. Sudria-Andreu, *Electrical vehicles: State of art and issues for their connection to the network,* in *2009 10^{th} International Conference on Electrical Power Quality and Utilisation* (2009) pp. 1–3.

[57] A. Kalair, N. Abas, M. S. Saleem, A. R. Kalair, and N. Khan, *Role of energy storage systems in energy transition from fossil fuels to renewables,* Energy Storage **3**, 1 (2021).

[58] K. Darcovich, B. Kenney, D. D. MacNeil, and M. M. Armstrong, *Control strategies and cycling demands for Li-ion storage batteries in residential micro-cogeneration systems,* Applied Energy **141**, 32 (2015).

[59] X. Fan, B. Liu, J. Liu, J. Ding, X. Han, Y. Deng, X. Lv, Y. Xie, B. Chen, W. Hu, and C. Zhong, *Battery Technologies for Grid-Level Large-Scale Electrical Energy Storage,* Transactions of Tianjin University **26**, 92 (2020).

[60] W. Palz, *Power for the World The Emergence of Electricity from the Sun*, 1st ed., edited by W. Palz (Jenny Stanford Publishing, 2010) pp. 1–575.

[61] D. M. Chapin, C. S. Fuller, and G. L. Pearson, *A new silicon p-n junction photocell for converting solar radiation into electrical power [3],* Journal of Applied Physics **25**, 676 (1954).

[62] John Perlin, *Let It Shine: The 6000-Year Story of Solar Energy* (New World Library, 2022) pp. 1–544.

[63] IRENA, *Renewable Power: Sharply Falling Generation Costs,* International Renewable Energy Agency , 15 (2016).

[64] IEA, *Renewables 2020 - Analysis and forecast to 2025,* International Energy Agency , 1 (2020).

[65] IRENA, *Global Renewables Outlook: Energy transformation 2050,* International Renewable Energy Agency , 1 (2020).

[66] S. Madeddu, F. Ueckerdt, M. Pehl, J. Peterseim, M. Lord, K. A. Kumar, C. Krüger, and G. Luderer, *The CO_2 reduction potential for the European industry via direct electrification of heat supply (power-to-heat),* Environmental Research Letters **15**, 124004 (2020).

[67] M. Wei, C. A. McMillan, and S. de la Rue du Can, *Electrification of Industry: Potential, Challenges and Outlook,* Current Sustainable/Renewable Energy Reports **6**, 140 (2019).

[68] R. Gross, R. Hanna, A. Gambhir, P. Heptonstall, and J. Speirs, *How long does innovation and commercialisation in the energy sectors take? Historical case studies of the timescale from invention to widespread commercialisation in energy supply and end use technology,* Energy Policy **123**, 682 (2018).

[69] Oxford PV Germany GmbH, *Oxford PV (website),* `https://www.oxfordpv.com/` (2022), accessed: 2022-08-01.

[70] Saule Spółka Akcyjna, *Saule Technologies (website),* `https://sauletech.com/` (2022), accessed: 2022-08-01.

[71] P. Buchholz and T. Brandenburg, *Demand, Supply, and Price Trends for Mineral Raw Materials Relevant to the Renewable Energy Transition Wind Energy, Solar Photovoltaic Energy, and Energy Storage,* Chemie-Ingenieur-Technik **90**, 141 (2018).

[72] A. W. Bett, *Sustainable PV manufacturing in Europe*, Tech. Rep. (Fraunhofer ISE, 2020).

[73] R. Deng, N. L. Chang, Z. Ouyang, and C. M. Chong, *A techno-economic review of silicon photovoltaic module recycling,* Renewable and Sustainable Energy Reviews **109**, 532 (2019).

[74] M. A. Green, E. D. Dunlop, J. Hohl-Ebinger, M. Yoshita, N. Kopidakis, K. Bothe, D. Hinken, M. Rauer, and X. Hao, *Solar cell efficiency tables (Version 60),* Progress in Photovoltaics: Research and Applications **30**, 687 (2022).

[75] NREL, *Best research cell efficiencies*, Tech. Rep. (NREL, 2022).

[76] S. Joshi, S. Mittal, P. Holloway, P. R. Shukla, B. Ó Gallachóir, and J. Glynn, *High resolution global spatiotemporal assessment of rooftop solar photovoltaics potential for renewable electricity generation,* Nature Communications **12**, 5738 (2021).

[77] A. Shekhar, V. K. Kumaravel, S. Klerks, S. De Wit, P. Venugopal, N. Narayan, P. Bauer, O. Isabella, and M. Zeman, *Harvesting roadway solar energy-performance of the installed infrastructure integrated pv bike path,* IEEE Journal of Photovoltaics **8**, 1066 (2018).

[78] M. A. Z. Abidin, M. N. Mahyuddin, and M. A. A. M. Zainuri, *Solar photovoltaic architecture and agronomic management in agrivoltaic system: A review,* Sustainability (Switzerland) **13**, 18 (2021).

[79] S. Oliveira-Pinto and J. Stokkermans, *Assessment of the potential of different floating solar technologies – Overview and analysis of different case studies,* Energy Conversion and Management **211**, 112747 (2020).

[80] R. A. Agathokleous and S. A. Kalogirou, *Status, barriers and perspectives of building integrated photovoltaic systems,* Energy **191**, 116471 (2020).

[81] N. Ekins-Daukes, M. Kay, A. Ciesla, J. Y. Jiang, Z. Yang, I. Perez-Wurfel, R. Hopkins, and J. Mcdonald, *The Potential for Vehicle Integrated Photovoltaics,* in *Asia-Pacific Solar Research Conference* (2021) pp. 1–2.

[82] A. I. Osman, M. Hefny, M. I. Abdel Maksoud, A. M. Elgarahy, and D. W. Rooney, *Environmental Chemistry Letters*, Vol. 19 (Springer International Publishing, 2021) pp. 797–849.

[83] I. A. Digdaya, I. Sullivan, M. Lin, L. Han, W. H. Cheng, H. A. Atwater, and C. Xiang, *A direct coupled electrochemical system for capture and conversion of CO_2 from oceanwater,* Nature Communications **11**, 1 (2020).

[84] R. Haight, T. Gershon, O. Gunawan, P. Antunez, D. Bishop, Y. S. Lee, T. Gokmen, K. Sardashti, E. Chagarov, and A. Kummel, *Industrial perspectives on earth abundant, multinary thin film photovoltaics,* Semiconductor Science and Technology **32**, 033004 (2017).

[85] A. G. Aberle, *Thin-film solar cells,* Thin Solid Films **517**, 4706 (2009).

[86] I. Massiot, A. Cattoni, and S. Collin, *Progress and prospects for ultrathin solar cells,* Nature Energy **5**, 959 (2020).

[87] Q. Tai and F. Yan, *Emerging Semitransparent Solar Cells: Materials and Device Design,* Advanced Materials **29**, 1700192 (2017).

[88] W. Shockley and H. J. Queisser, *Detailed balance limit of efficiency of p-n junction solar cells,* Journal of Applied Physics **32**, 510 (1961).

[89] H. J. Queisser, *Detailed balance limit for solar cell efficiency,* Materials Science and Engineering B: Solid-State Materials for Advanced Technology **159-160**, 322 (2009).

[90] T. Dittrich, *Material Concepts for solar cells*, 2nd ed. (World Scientific, 2018) pp. 1–551.

[91] P. Würfel and U. Würfel, *Physics of Solar Cells: From Basic Principles to Advanced Concepts* (Wiley, 2016) p. 288.

[92] D. R. Williams, *Sun Fact Sheet (website),* `https://nssdc.gsfc.nasa.gov/planetary/factsheet/sunfact.html` (2018), accessed: 2022-08-01.

[93] American Society for Testing and Materials (ASTM) Terrestrial Reference Spectra for Photovoltaic Performance Evaluation, *Reference Solar Spectral Irradiance: Air Mass 1.5 (website),* `http://rredc.nrel.gov/solar/spectra/am1.5/#about`, accessed: 2022-08-01.

[94] S. Sadasivam, M. K. Chan, and P. Darancet, *Theory of Thermal Relaxation of Electrons in Semiconductors,* Physical Review Letters **119**, 1 (2017).

[95] A. D. Vos, *Detailed balance limit of the efficiency of tandem solar cells,* Journal of Physics D: Applied Physics **13**, 839 (1980).

[96] M. F. Müller, M. Freunek, and L. M. Reindl, *Maximum efficiencies of indoor photovoltaic devices,* IEEE Journal of Photovoltaics **3**, 59 (2013).

[97] H. Shpaisman, O. Niitsoo, I. Lubomirsky, and D. Cahen, *Can up- and down-conversion and multi-exciton generation improve photovoltaics?* Solar Energy Materials and Solar Cells **92**, 1541 (2008).

[98] D. K. Ferry, S. M. Goodnick, V. R. Whiteside, and I. R. Sellers, *Challenges, myths, and opportunities in hot carrier solar cells,* Journal of Applied Physics **128**, 220903 (2020).

[99] B. Ehrler, E. Alarcón-Lladó, S. W. Tabernig, T. Veeken, E. C. Garnett, and A. Polman, *Photovoltaics reaching for the Shockley-Queisser limit,* ACS Energy Letters **5**, 3029 (2020).

[100] A. Polman, M. Knight, E. C. Garnett, B. Ehrler, and W. C. Sinke, *Photovoltaic materials: Present efficiencies and future challenges,* Science **352**, 307 (2016).

[101] M. Yamaguchi, F. Dimroth, J. F. Geisz, and N. J. Ekins-Daukes, *Multi-junction solar cells paving the way for super high-efficiency,* Journal of Applied Physics **129** (2021), 10.1063/5.0048653.

[102] K. Jäger, P. Tillmann, and C. Becker, *Detailed illumination model for bifacial solar cells,* Optics Express **28**, 4751 (2020).

[103] J. S. Van Der Burgt, D. R. Needell, T. Veeken, A. Polman, E. C. Garnett, and H. A. Atwater, *Unlocking Higher Power Efficiencies in Luminescent Solar Concentrators through Anisotropic Luminophore Emission,* ACS Applied Materials and Interfaces **13**, 40742 (2021).

[104] Q. Chen, Y. Liu, Y. Wang, W. Chen, J. Wu, Y. Zhao, and X. Du, *Optical properties of a random inverted pyramid textured silicon surface studied by the ray tracing method,* Solar Energy **186**, 392 (2019).

[105] T. Braun, A. Schubert, and S. Zsindely, *Nanoscience and nanotechnology on the balance,* Scientometrics **38**, 321 (1997).

[106] M. A. Verschuuren, M. Megens, Y. Ni, H. Van Sprang, and A. Polman, *Large area nanoimprint by substrate conformal imprint lithography (SCIL),* Advanced Optical Technologies **6**, 243 (2017).

[107] M. A. Verschuuren, M. Knight, M. Megens, and A. Polman, *Nanoscale spatial limitations of large-area substrate conformal imprint lithography,* Nanotechnology **30**, 345301 (2019).

[108] K. Cooper, *Scalable nanomanufacturing - a review,* Micromachines **8**, 20 (2017).

[109] S. Shen, A. Narayanaswamy, and G. Chen, *Surface phonon polaritons mediated energy transfer between nanoscale gaps,* Nano Letters **9**, 2909 (2009).

[110] J. M. Pitarke, V. M. Silkin, E. V. Chulkov, and P. M. Echenique, *Theory of surface plasmons and surface-plasmon polaritons,* Reports on Progress in Physics **70**, 1 (2007).

[111] M. Woodhouse, B. Smith, A. Ramdas, and Robert Margolis, *Crystalline Silicon Photovoltaic Module Manufacturing Costs and Sustainable Pricing: 1H 2018 Benchmark and Cost Reduction Roadmap,* National Renewable Energy Laboratory , 1 (2019).

[112] K. Fukuda, K. Yu, and T. Someya, *The Future of Flexible Organic Solar Cells,* Advanced Energy Materials **10**, 1 (2020).

[113] J. Y. Kim, J. W. Lee, H. S. Jung, H. Shin, and N. G. Park, *High-Efficiency Perovskite Solar Cells,* Chemical Reviews **120**, 7867 (2020).

[114] F. Martinho, *Challenges for the future of tandem photovoltaics on the path to terawatt levels: A technology review,* Energy and Environmental Science **14**, 3840 (2021).

[115] C. Wadia, A. P. Alivisatos, and D. M. Kammen, *Materials availability expands the opportunity for large-scale photovoltaics deployment,* Environmental Science and Technology **43**, 2072 (2009).

[116] Eli Yablonovitch, *Statistical ray optics,* J. Opt. Soc. Am. **72**, 899 (1982).

[117] N. C. Wyeth and A. Catalano, *Spectral response measurements of minority-carrier diffusion length in Zn_3P_2*, Journal of Applied Physics **50**, 1403 (1979).

[118] *Electrical Properties of Gallium Arsenide (website),* `https://www.ioffe.ru/SVA/NSM/Semicond/GaAs/electric.html`, accessed: 2022-08-01.

[119] A. Haddout, A. Raidou, and M. Fahoume, *A review on the numerical modeling of CdS/CZTS-based solar cells,* Applied Physics A: Materials Science and Processing **125**, 1 (2019).

[120] B. Chen, S. W. Baek, Y. Hou, E. Aydin, M. De Bastiani, B. Scheffel, A. Proppe, Z. Huang, M. Wei, Y. K. Wang, E. H. Jung, T. G. Allen, E. Van Kerschaver, F. P. García de Arquer, M. I. Saidaminov, S. Hoogland, S. De Wolf, and E. H. Sargent, *Enhanced optical path and electron diffusion length enable high-efficiency perovskite tandems,* Nature Communications **11**, 1257 (2020).

[121] P. Uprety, I. Subedi, M. M. Junda, R. W. Collins, and N. J. Podraza, *Photogenerated Carrier Transport Properties in Silicon Photovoltaics,* Scientific Reports **9**, 19015 (2019).

[122] C. Ding, D. Wang, D. Liu, H. Li, Y. Li, S. Hayase, T. Sogabe, T. Masuda, Y. Zhou, Y. Yao, Z. Zou, R. Wang, and Q. Shen, *Over 15% Efficiency PbS Quantum-Dot Solar Cells by Synergistic Effects of Three Interface Engineering: Reducing Nonradiative Recombination and Balancing Charge Carrier Extraction,* Advanced Energy Materials **12**, 2201676 (2022).

[123] David R. Lide, *CRC Handbook of Chemistry and Physics*, edited by David R. Lide, Vol. 88 (CRC Press/Taylor & Francis Group, 2007) p. 2640.

[124] F. Uleman, V. Neder, A. Cordaro, A. Alù, and A. Polman, *Resonant Metagratings for Spectral and Angular Control of Light for Colored Rooftop Photovoltaics,* ACS Applied Energy Materials **3**, 3150 (2020).

[125] V. Neder, S. L. Luxembourg, and A. Polman, *Efficient colored silicon solar modules using integrated resonant dielectric nanoscatterers,* Applied Physics Letters **111**, 850183 (2017).

[126] M. Heinrich, C. Kutter, F. Basler, M. Mittag, L. E. Alanis, D. Eberlein, A. Schmid, C. Reise, T. Kroyer, D. H. Neuhaus, and H. Wirth, *Potential And Challenges Of Vehicle Integrated Photovoltaics For Passenger Cars,* Presented at the 37^{th} European PV Solar Energy Conference and Exhibition **7**, 11 (2020).

[127] E. C. Garnett, B. Ehrler, A. Polman, and E. Alarcon-Llado, *Photonics for Photovoltaics: Advances and Opportunities,* ACS Photonics **8**, 61 (2021).

[128] I. Moreels, K. Lambert, D. Smeets, M. D. De, T. Nollet, J. C. Martins, F. Vanhaecke, A. Vantomme, C. Delerue, G. Allan, and Z. Hens, *Size-Dependent Optical Properties of Colloidal PbS Quantum Dots,* ACS Nano **3**, 3023 (2009).

[129] X. Zhang, P. K. Santra, L. Tian, M. B. Johansson, H. Rensmo, and E. M. Johansson, *Highly Efficient Flexible Quantum Dot Solar Cells with Improved Electron Extraction Using MgZnO Nanocrystals,* ACS Nano **11**, 8478 (2017).

[130] G. V. Shcherbatyuk, R. H. Inman, C. Wang, R. Winston, and S. Ghosh, *Viability of using near infrared PbS quantum dots as active materials in luminescent solar concentrators,* Applied Physics Letters **96**, 13 (2010).

[131] X. Wang, G. I. Koleilat, J. Tang, H. Liu, I. J. Kramer, R. Debnath, L. Brzozowski, D. A. R. Barkhouse, L. Levina, S. Hoogland, and E. H. Sargent, *Tandem colloidal quantum dot solar cells employing a graded recombination layer,* Nature Photonics **5**, 480 (2011).

[132] R. W. Crisp, G. F. Pach, J. M. Kurley, R. M. France, M. O. Reese, S. U. Nanayakkara, B. A. Macleod, D. V. Talapin, M. C. Beard, and J. M. Luther, *Tandem Solar Cells from Solution-Processed CdTe and PbS Quantum Dots Using a ZnTe-ZnO Tunnel Junction,* Nano Letters **17**, 1020 (2017).

[133] V. Wood and V. Bulović, *Colloidal quantum dot light-emitting devices,* Nano Reviews **1**, 5202 (2010).

[134] W. Chen, H. Tang, N. Li, M. A. Scheel, Y. Xie, D. Li, V. Körstgens, M. Schwartzkopf, S. V. Roth, K. Wang, X. W. Sun, and P. Müller-Buschbaum, *Colloidal PbS quantum dot stacking kinetics during deposition: Via printing,* Nanoscale Horizons **5**, 880 (2020).

[135] M. Li, W. Zhang, G. Shao, H. Kan, Z. Song, S. Xu, H. Yu, S. Jiang, J. Luo, and H. Liu, *Sensitive NO_2 gas sensors employing spray-coated colloidal quantum dots,* Thin Solid Films **618**, 271 (2016).

[136] B. Sun, A. Johnston, C. Xu, M. Wei, Z. Huang, Z. Jiang, H. Zhou, Y. Gao, Y. Dong, O. Ouellette, X. Zheng, J. Liu, M. J. Choi, Y. Gao, S. W. Baek, F. Laquai, O. M. Bakr, D. Ban, O. Voznyy, F. P. García de Arquer, and E. H. Sargent, *Monolayer Perovskite Bridges Enable Strong Quantum Dot Coupling for Efficient Solar Cells,* Joule **4**, 1542 (2020).

[137] N. Yazdani, S. Andermatt, M. Yarema, V. Farto, M. H. Bani-Hashemian, S. Volk, W. M. Lin, O. Yarema, M. Luisier, and V. Wood, *Charge transport in semiconductors assembled from nanocrystal quantum dots,* Nature Communications **11**, 41467 (2020).

[138] X. Lan, O. Voznyy, A. Kiani, F. P. García De Arquer, A. S. Abbas, G. H. Kim, M. Liu, Z. Yang, G. Walters, J. Xu, M. Yuan, Z. Ning, F. Fan, P. Kanjanaboos, I. Kramer, D. Zhitomirsky, P. Lee, A. Perelgut, S. Hoogland, and E. H. Sargent, *Passivation Using Molecular Halides Increases Quantum Dot Solar Cell Performance,* Advanced Materials **28**, 299 (2016).

[139] D. K. Ko, P. R. Brown, V. Bulovic, and M. G. Bawendi, *P-i-n heterojunction solar cells with a colloidal quantum-dot absorber layer,* Advanced Materials **26**, 4845 (2014).

[140] A. G. Pattantyus-Abraham, I. J. Kramer, A. R. Barkhouse, X. Wang, G. Konstantatos, R. Debnath, L. Levina, I. Raabe, M. K. Nazeeruddin, M. Grätzel, and E. H. Sargent, *Depleted-heterojunction colloidal quantum dot solar cells,* ACS Nano **4**, 3374 (2010).

[141] I. J. Kramer, D. Zhitomirsky, J. D. Bass, P. M. Rice, T. Topuria, L. Krupp, S. M. Thon, A. H. Ip, R. Debnath, H. C. Kim, and E. H. Sargent, *Ordered nanopillar structured electrodes for depleted bulk heterojunction colloidal quantum dot solar cells,* Advanced Materials **24**, 2315 (2012).

[142] J. Jean, S. Chang, P. R. Brown, J. J. Cheng, P. H. Rekemeyer, M. G. Bawendi, S. Gradečak, and V. Bulovic, *ZnO nanowire arrays for enhanced photocurrent in PbS quantum dot solar cells,* Advanced Materials **25**, 2790 (2013).

[143] S. W. Baek, P. Molet, M. J. Choi, M. Biondi, O. Ouellette, J. Fan, S. Hoogland, F. P. García de Arquer, A. Mihi, and E. H. Sargent, *Nanostructured Back Reflectors for Efficient Colloidal Quantum-Dot Infrared Optoelectronics,* Advanced Materials **31**, 1 (2019).

[144] S. Kim, J. K. Kim, J. Gao, J. H. Song, H. J. An, T. S. You, T. S. Lee, J. R. Jeong, E. S. Lee, J. H. Jeong, M. C. Beard, and S. Jeong, *Lead sulfide nanocrystal quantum dot solar cells with trenched ZnO fabricated via nanoimprinting,* ACS Applied Materials and Interfaces **5**, 3803 (2013).

[145] E. Parcham and S. A. Miandoab, *Introducing nanostructure patterns for performance enhancement in PbS colloidal quantum dot solar cells,* International Journal of Nano Dimension **11**, 18 (2020).

[146] Y. Fu, A. G. Dinku, Y. Hara, C. W. Miller, K. T. Vrouwenvelder, and R. Lopez, *Modeling photovoltaic performance in periodic patterned colloidal quantum dot solar cells,* Optics Express **23**, A779 (2015).

[147] A. Mihi, F. J. Beck, T. Lasanta, A. K. Rath, and G. Konstantatos, *Imprinted electrodes for enhanced light trapping in solution processed solar cells,* Advanced Materials **26**, 443 (2014).

[148] M. M. Adachi, A. J. Labelle, S. M. Thon, X. Lan, S. Hoogland, and E. H. Sargent, *Broadband solar absorption enhancement via periodic nanostructuring of electrodes,* Scientific Reports **3**, 2928 (2013).

[149] O. Ouellette, A. Lesage-Landry, B. Scheffel, S. Hoogland, F. P. García de Arquer, and E. H. Sargent, *Spatial Collection in Colloidal Quantum Dot Solar Cells,* Advanced Functional Materials **30**, 1 (2020).

[150] H. Aqoma, N. Barange, I. Ryu, S. Yim, Y. R. Do, S. Cho, D. H. Ko, and S. Y. Jang, *Simultaneous Improvement of Charge Generation and Extraction in Colloidal Quantum Dot Photovoltaics Through Optical Management,* Advanced Functional Materials **25**, 6241 (2015).

[151] C. H. M. Chuang, P. R. Brown, V. Bulović, and M. G. Bawendi, *Improved performance and stability in quantum dot solar cells through band alignment engineering,* Nature Materials **13**, 796 (2014).

[152] R. Dalven, *A review of the semiconductor properties of PbTe, PbSe, PbS and PbO,* Infrared Physics **9**, 141 (1969).

[153] B. T. Diroll, E. A. Gaulding, C. R. Kagan, and C. B. Murray, *Spectrally-Resolved Dielectric Functions of Solution-Cast Quantum Dot Thin Films,* Chemistry of Materials **27**, 6463 (2015).

[154] S. Ghosh, K. Das, K. Chakrabarti, and S. K. De, *Effect of oleic acid ligand on photophysical, photoconductive and magnetic properties of monodisperse SnO_2 quantum dots,* Journal of the Chemical Society. Dalton Transactions **42**, 3434 (2013).

[155] N. Ghobadi, *Band gap determination using absorption spectrum fitting procedure,* International Nano Letters **3**, 2 (2013).

[156] S. Fan and J. D. Joannopoulos, *Analysis of guided resonances in photonic crystal slabs,* Physical Review B - Condensed Matter and Materials Physics **65**, 1 (2002).

[157] S. S. Wang, M. G. Moharam, R. Magnusson, and J. S. Bagby, *Guided-mode resonances in planar dielectric-layer diffraction gratings,* Journal of the Optical Society of America A **7**, 1470 (1990).

[158] S. S. Wang and R. Magnusson, *Theory and applications of guided-mode resonance filters,* Applied Optics **32**, 2606 (1993).

[159] G. W. Castellanos, P. Bai, and J. Gómez Rivas, *Lattice resonances in dielectric metasurfaces,* Journal of Applied Physics **125**, 213105 (2019).

[160] T. Kim, X. Jin, J. H. Song, S. Jeong, and T. Park, *Efficiency Limit of Colloidal Quantum Dot Solar Cells: Effect of Optical Interference on Active Layer Absorption,* ACS Energy Letters **5**, 248 (2020).

[161] A. Thabet, S. Abdelhady, and Y. Mobarak, *Design modern structure for heterojunction quantum dot solar cells,* International Journal of Electrical and Computer Engineering **10**, 2918 (2020).

[162] D. Zhitomirsky, O. Voznyy, L. Levina, S. Hoogland, K. W. Kemp, A. H. Ip, S. M. Thon, and E. H. Sargent, *Engineering colloidal quantum dot solids within and beyond the mobility-invariant regime,* Nature Communications **5**, 1 (2014).

[163] C. Ma, C. Shi, K. Lv, C. Ying, S. Fan, and Y. Yang, *Gradient-band-gap strategy for efficient solid-state PbS quantum-dot sensitized solar cells,* Nanoscale **11**, 8402 (2019).

[164] P. R. Brown, D. Kim, R. R. Lunt, N. Zhao, M. G. Bawendi, J. C. Grossman, and V. Bulovi, *Energy Level Modification in Lead Sulfide Quantum Dot Thin Films through Ligand Exchange,* ACS Nano **8**, 1 (2014).

[165] S. Zheng, J. Chen, E. M. Johansson, and X. Zhang, *PbS Colloidal Quantum Dot Inks for Infrared Solar Cells,* iScience **23**, 101753 (2020).

[166] D. Jia, J. Chen, S. Zheng, D. Phuyal, M. Yu, L. Tian, J. Liu, O. Karis, H. Rensmo, E. M. Johansson, and X. Zhang, *Highly Stabilized Quantum Dot Ink for Efficient Infrared Light Absorbing Solar Cells,* Advanced Energy Materials **9**, 1 (2019).

[167] I. Moreels, G. Allan, B. De Geyter, L. Wirtz, C. Delerue, and Z. Hens, *Dielectric function of colloidal lead chalcogenide quantum dots obtained by a Kramers-Krönig analysis of the absorbance spectrum,* Physical Review B - Condensed Matter and Materials Physics **81**, 1 (2010).

[168] S. Kumar, R. Upadhyay, and B. Pradhan, *Performance enhancement of heterojunction ZnO/PbS quantum dot solar cells by interface engineering,* Solar Energy **211**, 283 (2020).

[169] L. Cozzi, T. Gould, S. Bouckart, D. Crow, T.-Y. Kim, C. McGlade, P. Olejarnik, B. Wanner, and D. Wetzel, *World Energy Outlook 2020,* **2050**, 1 (2020).

[170] E. Bellini, *Solar retains it LCOE edge in latest Lazard analysis,* PV magazine Global (2021).

[171] S. M. Hubbard, *Nanostructured photovoltaics for space power,* Journal of Nanophotonics **3**, 031880 (2009).

[172] I. Cardinaletti, T. Vangerven, S. Nagels, R. Cornelissen, D. Schreurs, J. Hruby, J. Vodnik, D. Devisscher, J. Kesters, J. D'Haen, A. Franquet, V. Spampinato, T. Conard, W. Maes, W. Deferme, and J. V. Manca, *Organic and perovskite solar cells for space applications,* Solar Energy Materials and Solar Cells **182**, 121 (2018).

[173] A. W. Ho-Baillie, H. G. Sullivan, T. A. Bannerman, H. P. Talathi, J. Bing, S. Tang, A. Xu, D. Bhattacharyya, I. H. Cairns, and D. R. McKenzie, *Deployment Opportunities for Space Photovoltaics and the Prospects for Perovskite Solar Cells,* Advanced Materials Technologies **2101059**, 1 (2021).

[174] S. P. Philipps, A. W. Bett, K. Horowitz, and S. Kurtz, *Current Status of Concentrator Photovoltaic (CPV) Technology,* National Renewable Energy Laboratory , 1 (2015).

[175] J. Aldersey-Williams and T. Rubert, *Levelised cost of energy – A theoretical justification and critical assessment,* Energy Policy **124**, 169 (2019).

[176] S. P. Philipps and A. W. Bett, *III-V Multi-junction solar cells and concentrating photovoltaic (CPV) systems,* Advanced Optical Technologies **3**, 469 (2014).

[177] J. F. Geisz, R. M. France, K. L. Schulte, M. A. Steiner, A. G. Norman, H. L. Guthrey, M. R. Young, T. Song, and T. Moriarty, *Six-junction III–V solar cells with 47.1% conversion efficiency under 143 Suns concentration,* Nature Energy **5**, 326 (2020).

[178] National Renewable Energy Laboratory, *Best Research Cell Efficiencies,* `https://www.nrel.gov/pv/cell-efficiency.html` (2021), accessed: 2022-08-01.

[179] C. Amy, H. R. Seyf, M. A. Steiner, D. J. Friedman, and A. Henry, *Thermal energy grid storage using multi-junction photovoltaics,* Energy and Environmental Science **12**, 334 (2019).

[180] A. W. Blakers, *Shading losses of solar-cell metal grids,* Journal of Applied Physics **71**, 5237 (1992).

[181] M. F. Stuckings and A. W. Blakers, *A study of shading and resistive loss from the fingers of encapsulated solar cells,* Solar Energy Materials and Solar Cells **59**, 233 (1999).

[182] M. F. Schumann, M. Langenhorst, M. Smeets, K. Ding, U. W. Paetzold, and M. Wegener, *All-Angle Invisibility Cloaking of Contact Fingers on Solar Cells by Refractive Free-Form Surfaces,* Advanced Optical Materials **5**, 1 (2017).

[183] R. Saive, M. Boccard, T. Saenz, S. Yalamanchili, C. R. Bukowsky, P. Jahelka, Z. J. Yu, J. Shi, Z. Holman, and H. A. Atwater, *Silicon heterojunction solar cells with effectively transparent front contacts,* Sustainable Energy and Fuels **1**, 593 (2017).

[184] F.-h. Chen, S. Pathreeker, J. Kaur, and I. D. Hosein, *Increasing light capture in silicon solar cells with encapsulants incorporating air prisms to reduce metallic contact losses,* Optics Express **24**, A1419 (2016).

[185] P. Jahelka, R. Saive, and H. Atwater, *Total Internal Reflection for Effectively Transparent Solar Cell Contacts,* arXiv:1610.01047 , 1 (2016).

[186] P. G. Kik, *Catoptric electrodes: transparent metal electrodes using shaped surfaces,* Optics Letters **39**, 5114 (2014).

[187] R. Saive, A. M. Borsuk, H. S. Emmer, C. R. Bukowsky, J. V. Lloyd, S. Yalamanchili, and H. A. Atwater, *Effectively Transparent Front Contacts for Optoelectronic Devices,* Advanced Optical Materials **4**, 1470 (2016).

[188] C. H. Van De Stadt, P. E. Gonzalez, H. A. Atwater, and R. Saive, *A computationally efficient simulation method for optimizing front contacts of concentrator multijunction solar cells,* in *Conference Record of the 46th IEEE Photovoltaic Specialists Conference* (2019) pp. 288–291.

[189] C. H. van de Stadt, P. Espinet Gonzalez, H. A. Atwater, and R. Saive, *A Computationally Efficient Multidiode Model for Optimizing the Front Grid of Multijunction Solar Cells under Concentration,* Journal of Renewable Energy **2020**, 1 (2020).

[190] *OrmoComp (website),* `https://www.microresist.de/en/produkt/ormocomp/` (2022), accessed: 2022-08-01.

[191] F. Rahman, D. J. Carbaugh, J. T. Wright, P. Rajan, S. G. Pandya, and S. Kaya, *A review of polymethyl methacrylate (PMMA) as a versatile lithographic resist – With emphasis on UV exposure,* Microelectronic Engineering **224**, 111238 (2020).

[192] G. M. Giannuzzi, C. E. Majorana, A. Miliozzi, V. A. Salomoni, and D. Nicolini, *Structural design criteria for steel components of parabolic-trough solar concentrators,* Journal of Solar Energy Engineering, Transactions of the ASME **129**, 382 (2007).

[193] R. B. Diver and T. A. Moss, *Practical field alignment of parabolic trough solar concentrators,* Journal of Solar Energy Engineering, Transactions of the ASME **129**, 153 (2007).

[194] T. E. Scheul, E. Khorani, T. Rahman, M. D. Charlton, and S. A. Boden, *Wavelength and angle resolved reflectance measurements of pyramidal textures for crystalline silicon photovoltaics,* Progress in Photovoltaics: Research and Applications **28**, 1248 (2020).

[195] D. N. R. Payne, M. D. B. Charlton, and D. M. Bagnall, *Broadband wavelength and angle-resolved scattering characterization for nanophotonics investigations,* Applied Optics **54**, 7224 (2015).

[196] Y. Osman, M. Fedawy, M. Abaza, and M. H. Aly, *Optimized CIGS based solar cell towardsan efficient solar cell: impact of layers thickness and doping,* Optical and Quantum Electronics **53**, 1 (2021).

[197] A. Mosavi, B. Bertalan, F. Imre, L. Nadai, and N. E. Gorji, *Electrical characterization of CIGS thin-film solar cells by two- and four-wire probe technique,* Modern Physics Letters B **34**, 1 (2020).

[198] N. Amin, K. Sopian, and M. Konagai, *Numerical modeling of CdS/CdTe and CdS/CdTe/ZnTe solar cells as a function of CdTe thickness,* Solar Energy Materials and Solar Cells **91**, 1202 (2007).

[199] B. Rech and H. Wagner, *Potential of amorphous silicon for solar cells,* Appl. Phys. A **69**, 155 (1999).

[200] S. Philipps and W. Warmuth, *Photovoltaics report*, Tech. Rep. February (Fraunhofer Institut für Solare Energieforschung, 2022).

[201] S. Rafique, S. M. Abdullah, K. Sulaiman, and M. Iwamoto, *Fundamentals of bulk heterojunction organic solar cells: An overview of stability/degradation issues and strategies for improvement,* Renewable and Sustainable Energy Reviews **84**, 43 (2018).

[202] A. Groenewolt, J. Bakker, J. Hofer, Z. Nagy, and A. Schlüter, *Methods for modelling and analysis of bendable photovoltaic modules on irregularly curved surfaces,* International Journal of Energy and Environmental Engineering **7**, 261 (2016).

[203] Solarge, *Solarge (website),* `https://solarge.com/`, accessed: 2022-08-01.

[204] Y. Ota, T. Masuda, K. Araki, and M. Yamaguchi, *Curve-correction factor for characterization of the output of a three-dimensional curved photovoltaic module on a car roof,* Coatings **8**, 432 (2018).

[205] T. Tayagaki, K. Araki, M. Yamaguchi, and T. Sugaya, *Impact of Nonplanar Panels on Photovoltaic Power Generation in the Case of Vehicles,* IEEE Journal of Photovoltaics **9**, 1721 (2019).

[206] Lightyear, *Lightyear (website),* `https://lightyear.one/`, accessed: 2022-08-01.

[207] M. Centeno Brito, T. Santos, F. Moura, D. Pera, and J. Rocha, *Urban solar potential for vehicle integrated photovoltaics,* Transportation Research Part D: Transport and Environment **94**, 102810 (2021).

[208] M. Hatamvand, E. Kamrani, M. Lira-Cantú, M. Madsen, B. R. Patil, P. Vivo, M. S. Mehmood, A. Numan, I. Ahmed, and Y. Zhan, *Recent advances in fiber-shaped and planar-shaped textile solar cells,* Nano Energy **71**, 104609 (2020).

[209] S. Wang, B. D. Weil, Y. Li, K. X. Wang, E. Garnett, S. Fan, and Y. Cui, *Large-area free-standing ultrathin single-crystal silicon as processable materials,* Nano Letters **13**, 4393 (2013).

[210] R. Saive, *Light trapping in thin silicon solar cells: A review on fundamentals and technologies,* Progress in Photovoltaics: Research and Applications **29**, 1125 (2021).

[211] Jutta Trube and Susanne Herritsch, *International Technology Roadmap for Photovoltaic (ITRPV),* Tech. Rep. (VDMA, 2022).

[212] A. Augusto, J. Karas, P. Balaji, S. G. Bowden, and R. R. King, *Exploring the practical efficiency limit of silicon solar cells using thin solar-grade substrates,* Journal of Materials Chemistry A **8**, 16599 (2020).

[213] V. Alex, S. Finkbeiner, and J. Weber, *Temperature dependence of the indirect energy gap in crystalline silicon,* Journal of Applied Physics **79**, 6943 (1996).

[214] M. A. Green, *Lambertian light trapping in textured solar cells and light-emitting diodes: Analytical solutions,* Progress in Photovoltaics: Research and Applications **10**, 235 (2002).

[215] M. C. Raval and S. M. Reddy, *Industrial Silicon Solar Cells*, Vol. 1 (IntechOpen, 1970) pp. 1–168.

[216] K. Xiong, S. Lu, D. Jiang, J. Dong, and H. Yang, *Effective recombination velocity of textured surfaces,* Applied Physics Letters **96**, 193107 (2010).

[217] Concetto Eugenio Andrea Cordaro, Nico Tucher, Stefan Tabernig, Hubert Hauser, Oliver Hoehn, Ralph Müller, Benedikt Bläsi, and Albert Polman, *Plasmonic and Mie scattering in nanopatterned back reflectors for III–V-on-silicon solar cells,* in *Photonics for Solar Energy Systems VIII* (2020) p. 1136607.

[218] U. Sikder and M. A. Zaman, *Optimization of multilayer antireflection coating for photovoltaic applications,* Optics and Laser Technology **79**, 88 (2016).

[219] T. H. Fung, T. Veeken, D. Payne, B. Veettil, A. Polman, and M. Abbott, *Application and validity of the effective medium approximation to the optical properties of nano-textured silicon coated with a dielectric layer,* Optics Express **27**, 38645 (2019).

[220] P. Spinelli, B. Macco, M. A. Verschuuren, W. M. Kessels, and A. Polman, Al_2O_3/TiO_2 *nano-pattern antireflection coating with ultralow surface recombination,* Applied Physics Letters **102**, 233902 (2013).

[221] N. Tavakoli, R. Spalding, A. Lambertz, P. Koppejan, G. Gkantzounis, C. Wan, R. Röhrich, E. Kontoleta, A. F. Koenderink, R. Sapienza, M. Florescu, and E. Alarcon-Llado, *Over 65% Sunlight Absorption in a 1 μm Si Slab with Hyperuniform Texture,* ACS Photonics **9**, 1206 (2022).

[222] E. Camarillo Abad, H. J. Joyce, and L. C. Hirst, *Transparent Quasi-Random Structures for Multimodal Light Trapping in Ultrathin Solar Cells with Broad Engineering Tolerance,* ACS Photonics **9**, 2724 (2022).

[223] P. M. Piechulla, L. Muehlenbein, R. B. Wehrspohn, S. Nanz, A. Abass, C. Rockstuhl, and A. Sprafke, *Fabrication of Nearly-Hyperuniform Substrates by Tailored Disorder for Photonic Applications,* Advanced Optical Materials **6**, 1701272 (2018).

[224] P. M. Piechulla, E. Slivina, D. Bätzner, I. Fernandez-Corbaton, P. Dhawan, R. B. Wehrspohn, A. N. Sprafke, and C. Rockstuhl, *Antireflective Huygens' Metasurface with Correlated Disorder Made from High-Index Disks Implemented into Silicon Heterojunction Solar Cells,* ACS Photonics **8**, 3476 (2021).

[225] P. M. Piechulla, B. Fuhrmann, E. Slivina, C. Rockstuhl, R. B. Wehrspohn, and A. N. Sprafke, *Tailored Light Scattering through Hyperuniform Disorder in Self-Organized Arrays of High-Index Nanodisks,* Advanced Optical Materials **9**, 2100186 (2021).

[226] K. Luke, Y. Okawachi, M. R. Lamont, A. L. Gaeta, and M. Lipson, *Broadband mid-infrared frequency comb generation in a Si3N4 microresonator,* in *Conference on Lasers and Electro-Optics Europe - Technical Digest*, Vol. 2015-August (Institute of Electrical and Electronics Engineers Inc., 2015).

[227] A. Paduthol, M. K. Juhl, G. Nogay, P. Löper, and T. Trupke, *Measuring carrier injection from amorphous silicon into crystalline silicon using photoluminescence,* Progress in Photovoltaics: Research and Applications **26**, 968 (2018).

[228] A. G. Aberle, *Overview on SiN surface passivation of crystalline silicon solar cells,* Solar Energy Materials and Solar Cells **65**, 239 (2001).

[229] Ansys Lumerical, *Ansys Lumerical FDTD (website),* `https://www.lumerical.com/products/fdtd/` (), accessed: 2022-08-01.

[230] J. Kennedy and R. Eberhart, *Particle swarm optimization,* in *Proceedings of ICNN'95 - International Conference on Neural Networks*, Vol. 4 (IEEE) pp. 1942–1948.

[231] J. van de Groep and A. Polman, *Designing dielectric resonators on substrates: Combining magnetic and electric resonances,* Optics Express **21**, 26285 (2013).

[232] C. Palmer and E. Loewen, *Diffraction Grating Handbook*, Tech. Rep. (Newport Corporation, 2005).

[233] A. Cordaro, J. Van De Groep, S. Raza, E. F. Pecora, F. Priolo, and M. L. Brongersma, *Antireflection High-Index Metasurfaces Combining Mie and Fabry-Pérot Resonances,* ACS Photonics **6**, 453 (2019).

[234] M. Golda-Cepa, K. Engvall, M. Hakkarainen, and A. Kotarba, *Recent progress on parylene C polymer for biomedical applications: A review,* Progress in Organic Coatings **140**, 105493 (2020).

[235] E. Meng, P. Y. Li, and Y. C. Tai, *Plasma removal of Parylene C,* Journal of Micromechanics and Microengineering **18**, 045004 (2008).

[236] R. Lüdemann, B. M. Damiani, and A. Rohatgi, *Novel processing of solar cells with porous silicon texturing,* in *Conference Record of the IEEE Photovoltaic Specialists Conference*, Vol. 2000-January (Institute of Electrical and Electronics Engineers Inc., 2000) pp. 299–302.

[237] J. Schmidt, F. Werner, B. Veith, D. Zielke, S. Steingrube, P. P. Altermatt, S. Gatz, T. Dullweber, and R. Brendel, *Advances in the surface passivation of silicon solar cells,* Energy Procedia **15**, 30 (2012).

[238] B. Hoex, S. B. Heil, E. Langereis, M. C. Van De Banden, and W. M. Kessels, *Ultralow surface recombination of c-Si substrates passivated by plasma-assisted atomic layer deposited Al_2O_3,* Applied Physics Letters **89**, 9 (2006).

[239] B. Hoex, J. J. Gielis, M. C. Van De Sanden, and W. M. Kessels, *On the c-Si surface passivation mechanism by the negative-charge-dielectric Al_2O_3,* Journal of Applied Physics **104**, 113703 (2008).

[240] B. Hoex, J. Schmidt, P. Pohl, M. C. Van De Sanden, and W. M. Kessels, *Silicon surface passivation by atomic layer deposited Al_2O_3,* Journal of Applied Physics **104**, 044903 (2008).

[241] PV education, *Ideal diode equation (website),* `https://www.pveducation.org/pvcdrom/pn-junctions/diode-equation`, accessed: 2022-08-01.

[242] V. Velidandla, J. Xu, Z. Hou, K. Wijekoon, and D. Tanner, *Texture process monitoring in solar cell manufacturing using optical metrology,* in *Conference Record of the 37^{th} IEEE Photovoltaic Specialists Conference* (2011) pp. 001744–001747.

[243] M. Pawlik, J. P. Vilcot, M. Halbwax, D. Aureau, A. Etcheberry, A. Slaoui, T. Schutz-Kuchly, and R. Cabal, *Electrical and Chemical studies on Al_2O_3 passivation activation process,* in *Energy Procedia*, Vol. 60 (Elsevier Ltd, 2014) pp. 85–89.

[244] Ansys Lumerical, *Ansys Lumerical CHARGE (website),* `https://www.lumerical.com/products/charge/` (), accessed: 2022-08-01.

[245] Ansys Lumerical, *Ansys Lumerical CHARGE - Si solar cell example (website),* `https://optics.ansys.com/hc/en-us/articles/360042165534-Planar-silicon-solar-cell` (), accessed: 2022-08-01.

[246] Z. J. Yu, B. M. Wheelwright, S. Manzoor, and Z. C. Holman, *Silicon wafers with optically specular surfaces formed by chemical polishing,* Journal of Materials Science: Materials in Electronics **27**, 10270 (2016).

[247] W. Kern, *The Evolution of Silicon Wafer Cleaning Technology,* Journal of The Electrochemical Society **137**, 1887 (1990).

[248] IRENA, *Renewable Energy Capacity Highlights 31 March 2020,* International Renewable Energy Agency **00**, 1 (2020).

[249] IRENA, *Global Energy Transformation: A Roadmap to 2050,* International Renewable Energy Agency , 10 (2019).

[250] A. Richter, M. Hermle, and S. W. Glunz, *Reassessment of the limiting efficiency for crystalline silicon solar cells,* IEEE Journal of Photovoltaics **3**, 1184 (2013).

[251] A. Al-Ashouri, E. Köhnen, B. Li, A. Magomedov, H. Hempel, P. Caprioglio, J. A. Márquez, A. B. M. Vilches, E. Kasparavicius, J. A. Smith, N. Phung, D. Menzel, M. Grischek, L. Kegelmann, D. Skroblin, C. Gollwitzer, T. Malinauskas, M. Jošt, G. Matič, B. Rech, R. Schlatmann, M. Topič, L. Korte, A. Abate, B. Stannowski,

D. Neher, M. Stolterfoht, T. Unold, V. Getautis, and S. Albrecht, *Monolithic perovskite/silicon tandem solar cell with >29% efficiency by enhanced hole extraction,* Science **370**, 1300 (2020).

[252] K. Yoshikawa, H. Kawasaki, W. Yoshida, T. Irie, K. Konishi, K. Nakano, T. Uto, D. Adachi, M. Kanematsu, H. Uzu, and K. Yamamoto, *Silicon heterojunction solar cell with interdigitated back contacts for a photoconversion efficiency over 26%,* Nature Energy **2**, 17032 (2017).

[253] Q. Xu, Y. Zhao, and X. Zhang, *Light Management in Monolithic Perovskite/Silicon Tandem Solar Cells,* Solar RRL **4**, 1 (2020).

[254] D. A. Jacobs, M. Langenhorst, F. Sahli, B. S. Richards, T. P. White, C. Ballif, K. R. Catchpole, and U. W. Paetzold, *Light Management: A Key Concept in High-Efficiency Perovskite/Silicon Tandem Photovoltaics,* Journal of Physical Chemistry Letters **10**, 3159 (2019).

[255] H. Shen, D. Walter, Y. Wu, K. C. Fong, D. A. Jacobs, T. Duong, J. Peng, K. Weber, T. P. White, and K. R. Catchpole, *Monolithic Perovskite/Si Tandem Solar Cells: Pathways to Over 30% Efficiency,* Advanced Energy Materials **10**, 1 (2020).

[256] D. T. Grant, K. R. Catchpole, K. J. Weber, and T. P. White, *Design guidelines for perovskite/silicon 2-terminal tandem solar cells: an optical study,* Optics Express **24**, A1454 (2016).

[257] R. Santbergen, R. Mishima, T. Meguro, M. Hino, H. Uzu, J. Blanker, K. Yamamoto, and M. Zeman, *Minimizing optical losses in monolithic perovskite/c-Si tandem solar cells with a flat top cell,* Optics Express **24**, A1288 (2016).

[258] E. R. Martins, A. Martins, B. H. V. Borges, J. Li, and T. F. Krauss, *Photonic intermediate structures for tandem perovskite/silicon solar cells,* in *Asia Communications and Photonics Conference*, Vol. Part F83-A (2017) pp. 1–7.

[259] S. Albrecht, M. Saliba, J. P. Correa-Baena, K. Jäger, L. Korte, A. Hagfeldt, M. Grätzel, and B. Rech, *Towards optical optimization of planar monolithic perovskite/silicon-heterojunction tandem solar cells,* Journal of Optics **18**, 1 (2016).

[260] L. Mazzarella, Y. H. Lin, S. Kirner, A. B. Morales-Vilches, L. Korte, S. Albrecht, E. Crossland, B. Stannowski, C. Case, H. J. Snaith, and R. Schlatmann, *Infrared Light Management Using a Nanocrystalline Silicon Oxide Interlayer in Monolithic Perovskite/Silicon Heterojunction Tandem Solar Cells with Efficiency above 25%,* Advanced Energy Materials **9**, 1 (2019).

[261] M. Chapa, M. F. Alexandre, M. J. Mendes, H. Águas, E. Fortunato, and R. Martins, *All-Thin-Film Perovskite/C-Si Four-Terminal Tandems: Interlayer and Intermediate Contacts Optimization,* ACS Applied Energy Materials **2**, 3979 (2019).

[262] M. Schultes, T. Helder, E. Ahlswede, M. F. Aygüler, P. Jackson, S. Paetel, J. A. Schwenzer, I. M. Hossain, U. W. Paetzold, and M. Powalla, *Sputtered Transparent Electrodes (IO:H and IZO) with Low Parasitic Near-Infrared Absorption for Perovskite-Cu(In,Ga)Se2 Tandem Solar Cells,* ACS Applied Energy Materials **2**, 7823 (2019).

[263] M. Jošt, E. Köhnen, A. B. Morales-Vilches, B. Lipovšek, K. Jäger, B. Macco, A. Al-Ashouri, J. Krč, L. Korte, B. Rech, R. Schlatmann, M. Topič, B. Stannowski, and S. Albrecht, *Textured interfaces in monolithic perovskite/silicon tandem solar cells: Advanced light management for improved efficiency and energy yield,* Energy and Environmental Science **11**, 3511 (2018).

[264] F. Sahli, J. Werner, B. A. Kamino, M. Bräuninger, R. Monnard, B. Paviet-salomon, L. Barraud, L. Ding, J. J. D. Leon, D. Sacchetto, G. Cattaneo, M. Despeisse, M. Boccard, S. Nicolay, Q. Jeangros, B. Niesen, and C. Ballif, *Fully textured monolithic perovskite/silicon tandem solar cells with 25.2% power conversion efficiency,* Nature Materials **17**, 820 (2018).

[265] N. N. Lal, T. P. White, and K. R. Catchpole, *Optics and light trapping for tandem solar cells on silicon,* IEEE Journal of Photovoltaics **4**, 1380 (2014).

[266] K. Jäger, J. Sutter, M. Hammerschmidt, P. I. Schneider, and C. Becker, *Prospects of light management in perovskite/silicon tandem solar cells,* Nanophotonics **10**, 1991 (2021).

[267] J. Werner, G. Nogay, F. Sahli, T. C. J. Yang, M. Bräuninger, G. Christmann, A. Walter, B. A. Kamino, P. Fiala, P. Löper, S. Nicolay, Q. Jeangros, B. Niesen, and C. Ballif, *Complex Refractive Indices of Cesium-Formamidinium-Based Mixed-Halide Perovskites with Optical Band Gaps from 1.5 to 1.8 eV,* ACS Energy Letters **3**, 742 (2018).

[268] A. Hoffmann, U. W. Paetzold, C. Zhang, T. Merdzhanova, A. Lambertz, C. Ulbrich, K. Bittkau, and U. Rau, *Advancing tandem solar cells by spectrally selective multilayer intermediate reflectors,* Optics Express **22**, A1270 (2014).

[269] K. Bittkau, T. Kirchartz, and U. Rau, *Optical design of spectrally selective interlayers for perovskite/silicon heterojunction tandem solar cells,* Optics Express **26**, A750 (2018).

[270] P. G. O'Brien, A. Chutinan, K. Leong, N. P. Kherani, G. A. Ozin, and S. Zukotynski, *Photonic crystal intermediate reflectors for micromorph solar cells: a comparative study,* Optics Express **18**, 4478 (2010).

[271] P. G. O'Brien, Y. Yang, A. Chutinan, P. Mahtani, K. Leong, D. P. Puzzo, L. D. Bonifacio, C. W. Lin, G. A. Ozin, and N. P. Kherani, *Selectively transparent and conducting photonic crystal solar spectrum splitters made of alternating sputtered indium-tin oxide and spin-coated silica nanoparticle layers for enhanced photovoltaics,* Solar Energy Materials and Solar Cells **102**, 173 (2012).

[272] J. Üpping, A. Bielawny, R. B. Wehrspohn, T. Beckers, R. Carius, U. Rau, S. Fahr, C. Rockstuhl, F. Lederer, M. Kroll, T. Pertsch, L. Steidl, and R. Zentel, *Three-dimensional photonic crystal intermediate reflectors for enhanced light-trapping in tandem solar cells,* Advanced Materials **23**, 3896 (2011).

[273] A. Bielawny, J. Üpping, P. T. Miclea, R. B. Wehrspohn, C. Rockstuhl, F. Lederer, M. Peters, L. Steidl, R. Zentel, S. M. Lee, M. Knez, A. Lambertz, and R. Carius, *3D photonic crystal intermediate reflector for micromorph thin-film tandem solar cell,* Physica Status Solidi (A) Applications and Materials Science **205**, 2796 (2008).

[274] S. Fahr, C. Rockstuhl, and F. Lederer, *Sandwiching intermediate reflectors in tandem solar cells for improved photon management,* Applied Physics Letters **101**, 133904 (2012).

[275] J. Jia, L. C. Seitz, J. D. Benck, Y. Huo, Y. Chen, J. W. D. Ng, T. Bilir, J. S. Harris, and T. F. Jaramillo, *Solar water splitting by photovoltaic-electrolysis with a solar-to-hydrogen efficiency over 30%,* Nature Communications **7**, 1 (2016).

[276] M. G. Walter, E. L. Warren, J. R. McKone, S. W. Boettcher, Q. Mi, E. A. Santori, and N. S. Lewis, *Solar water splitting cells,* Chemical Reviews **110**, 6446 (2010).

[277] E. Köhnen, P. Wagner, F. Lang, A. Cruz, B. Li, M. Roß, M. Jošt, A. B. Morales-Vilches, M. Topič, M. Stolterfoht, D. Neher, L. Korte, B. Rech, R. Schlatmann, B. Stannowski, and S. Albrecht, *27.9% Efficient Monolithic Perovskite/Silicon Tandem Solar Cells on Industry Compatible Bottom Cells,* Solar RRL **5**, 1 (2021).

[278] S. Rühle, *The detailed balance limit of perovskite/silicon and perovskite/CdTe tandem solar cells,* Physica Status Solidi (A) Applications and Materials Science **214**, 1600955 (2017).

[279] V. Neder, D. Zhang, S. Veenstra, and A. Polman, *Four-terminal perovskite/silicon tandem solar cell with integrated Mie-resonant spectral splitter metagrating,* arXiv:2012.12649 , 1 (2020).

[280] M. A. Green, E. D. Dunlop, J. Hohl-Ebinger, M. Yoshita, N. Kopidakis, and X. Hao, *Solar cell efficiency tables (version 56),* Progress in Photovoltaics: Research and Applications **28**, 629 (2020).

[281] C. Ulbrich, C. Zahren, A. Gerber, B. Blank, T. Merdzhanova, A. Gordijn, and U. Rau, *Matching of silicon thin-film tandem solar cells for maximum power output,* International Journal of Photoenergy **2013**, 314097 (2013).

[282] V. E. Ferry, M. A. Verschuuren, H. B. Li, R. E. Schropp, H. A. Atwater, and A. Polman, *Improved red-response in thin film a-Si:H solar cells with soft-imprinted plasmonic back reflectors,* Applied Physics Letters **95**, 2007 (2009).

[283] J. Werner, B. Niesen, and C. Ballif, *Perovskite/Silicon Tandem Solar Cells: Marriage of Convenience or True Love Story? – An Overview,* Advanced Materials Interfaces **5**, 1 (2018).

[284] A. Van Geelen, P. R. Hageman, G. J. Bauhuis, P. C. Van Rijsingen, P. Schmidt, and L. J. Giling, *Epitaxial lift-off GaAs solar cell from a reusable GaAs substrate,* Materials Science and Engineering B **45**, 162 (1997).

[285] B. Zhang, M. J. Zhang, S. P. Pang, C. S. Huang, Z. M. Zhou, D. Wang, N. Wang, and G. L. Cui, *Carrier Transport in CH3NH3PbI3 Films with Different Thickness for Perovskite Solar Cells,* Advanced Materials Interfaces **3**, 1600327 (2016).

[286] S. Hegedus, *Thin Film Solar Modules: The Low Cost, High Throughput and Versatile Alternative to Si Wafers,* Prog. Photovolt: Res. Appl. **14**, 393 (2006).

[287] T. Ibn-Mohammed, S. C. Koh, I. M. Reaney, A. Acquaye, G. Schileo, K. B. Mustapha, and R. Greenough, *Perovskite solar cells: An integrated hybrid lifecycle assessment and review in comparison with other photovoltaic technologies,* Renewable and Sustainable Energy Reviews **80**, 1321 (2017).

[288] S. Escobar Steinvall, E. Z. Stutz, R. Paul, M. Zamani, J. B. Leran, M. Dimitrievska, and A. Fontcuberta I Morral, *Nanoscale Growth Initiation as a Pathway to Improve the Earth-Abundant Absorber Zinc Phosphide,* ACS Applied Energy Materials **5**, 5298 (2021).

[289] J. M. Pawlikowski, *Absorption edge of Zn_3P_2,* Physical Review B **26**, 4711 (1982).

[290] E. A. Fagen, *Optical properties of Zn_3P_2,* Journal of Applied Physics **50**, 6505 (1979).

[291] M. Bhushan and A. Catalano, *Polycrystalline Zn_3P_2 Schottky barrier solar cells,* Appl. Phys. Lett. **38**, 39 (1981).

[292] S. Rühle, *Tabulated values of the Shockley-Queisser limit for single junction solar cells,* Solar Energy **130**, 139 (2016).

[293] S. Jeon, J. P. Bosco, S. S. Wilson, S. J. Rozeveld, H. M. Kim, and H. A. Atwater, *Growth Mechanism and Electronic Structure of Zn_3P_2 on the Ga-Rich GaAs(001) Surface,* J. Phys. Chem. C **118**, 12717 (2014).

[294] M. Zamani, E. Stutz, S. Escobar, R. R. Zamani, R. Paul, J. B. Leran, M. Dimitrievska, and A. Fontcuberta i Morral, *The path towards 1 µm monocrystalline Zn_3P_2 films on InP: Substrate preparation, growth conditions and luminescence properties,* Journal of Physics: Energy **3**, 034011 (2021).

[295] V. G. Dubrovskii, S. E. Steinvall, V. De Mestral, R. Paul, J. B. Leran, M. Zamani, E. Z. Stutz, and A. Fontcuberta I Morral, *Modeling the Shape Evolution of Selective Area Grown Zn_3P_2 Nanoislands,* Crystal Growth and Design **21**, 4732 (2021).

[296] R. Paul, N. Humblot, N. Humblot, S. E. Steinvall, E. Z. Stutz, S. S. Joglekar, J. B. Leran, M. Zamani, C. Cayron, R. Logé, A. G. Del Aguila, Q. Xiong, A. F. I. Morral, and A. F. I. Morral, *Van der Waals Epitaxy of Earth-Abundant Zn_3P_2 on Graphene for Photovoltaics,* Crystal Growth and Design **20**, 3816 (2020).

[297] A. Catalano and R. B. Hall, *Defect dominated conductivity in Zn_3P_2,* Journal of Physics and Chemistry of Solids **41**, 635 (1980).

[298] W. J. Yin and Y. Yan, *The electronic properties of point defects in earth-abundant photovoltaic material Zn_3P_2: A hybrid functional method study,* Journal of Applied Physics **113**, 1 (2013).

[299] S. Demers and A. Van De Walle, *Intrinsic defects and dopability of zinc phosphide,* Physical Review B - Condensed Matter and Materials Physics **85**, 1 (2012).

[300] G. M. Kimball, N. S. Lewis, and H. A. Atwater, *Mg doping and alloying in Zn_3P_2 heterojunction solar cells,* in *Conference Record of the 35^{th} IEEE Photovoltaic Specialists Conference* (2010) pp. 1039–1043.

[301] J. P. Bosco, D. O. Scanlon, G. W. Watson, N. S. Lewis, and H. A. Atwater, *Energy-band alignment of II-VI/Zn_3P_2 heterojunctions from x-ray photoemission spectroscopy,* Journal of Applied Physics **113**, 203705 (2013).

[302] S. S. Perlman and D. L. Feucht, *P-N Heterojunctions,* Solid State Electronics **7**, 911 (1964).

[303] M. A. Martínez, J. Herrero, and M. T. Gutiérrez, *Optimisation of indium tin oxide thin films for photovoltaic applications,* Thin Solid Films **269**, 80 (1995).

[304] A. Way, J. Luke, A. D. Evans, Z. Li, J. S. Kim, J. R. Durrant, H. K. Hin Lee, and W. C. Tsoi, *Fluorine doped tin oxide as an alternative of indium tin oxide for bottom electrode of semi-transparent organic photovoltaic devices,* AIP Advances **9** (2019), 10.1063/1.5104333.

[305] J. Van De Groep, P. Spinelli, and A. Polman, *Transparent conducting silver nanowire networks,* Nano Letters **12**, 3138 (2012).

[306] W. A. Syed, N. Rafiq, A. Ali, R. u. Din, and W. H. Shah, *Multilayer AR coatings of TiO_2/MgF_2 for application in optoelectronic devices,* Optik **136**, 564 (2017).

[307] M. Spence, R. Hammond, A. Pockett, Z. Wei, A. Johnson, T. Watson, and M. J. Carnie, *A Comparison of Different Textured and Non-Textured Anti-Reflective Coatings for Planar Monolithic Silicon-Perovskite Tandem Solar Cells,* ACS Applied Energy Materials **5**, 5974 (2022).

[308] J. Van De Groep, P. Spinelli, and A. Polman, *Single-Step Soft-Imprinted Large-Area Nanopatterned Antireflection Coating,* Nano Letters **15**, 4223 (2015).

[309] P. Spinelli, B. Newman, and A. Polman, *Photovoltaics: Light-Trapping in crystalline Silicon and Thin-film Solar Cells by Nanostructured Optical coatings,* in *Nanotechnology for Energy Sustainability*, edited by B. Raj, M. van de Voorde, and Y. Mahajan (Wiley, 2017) 1st ed., Chap. 7, pp. 163–180.

[310] L. Van Dijk, J. Van De Groep, L. W. Veldhuizen, M. Di Vece, A. Polman, and R. E. Schropp, *Plasmonic Scattering Back Reflector for Light Trapping in Flat Nano-Crystalline Silicon Solar Cells,* ACS Photonics **3**, 685 (2016).

[311] G. Yin, M. W. Knight, M. C. van Lare, M. M. Solà Garcia, A. Polman, and M. Schmid, *Optoelectronic Enhancement of Ultrathin CuIn1–xGaxSe2 Solar Cells by Nanophotonic Contacts,* Advanced Optical Materials **5**, 1600637 (2017).

[312] M. Uda A'b', A. Nakamura, T. Yamamoto A'b, and Y. Fujirnoto, *ELSEVIER Journal of Electron Spectroscopy and Related Phenomena 88-91 (1998) 643-648 Work function of polycrystalline Ag, Au and A1*, Tech. Rep. (1998).

[313] H. B. Michaelson, *The work function of the elements and its periodicity,* Journal of Applied Physics **48**, 4729 (1977).

[314] B. G. Baker, B. B. Johnson, and G. L. Maire, *Photoelectric work function measurements on nickel crystals and films,* Surface Science **24**, 572 (1971).

[315] Thomas Ihn, *Semiconductor Nanostructures: Quantum states and electronic transport*, 1st ed. (Oxford University Press, USA, 2009).

[316] M. Parashar, V. K. Shukla, and R. Singh, *Metal oxides nanoparticles via sol–gel method: a review on synthesis, characterization and applications,* Journal of Materials Science: Materials in Electronics **31**, 3729 (2020).

[317] J. i. Fujisawa, T. Eda, and M. Hanaya, *Comparative study of conduction-band and valence-band edges of TiO_2, $SrTiO_3$, and $BaTiO_3$ by ionization potential measurements,* Chemical Physics Letters **685**, 23 (2017).

[318] X. Yang, Q. Bi, H. Ali, K. Davis, W. V. Schoenfeld, and K. Weber, *High-Performance TiO_2-Based Electron-Selective Contacts for Crystalline Silicon Solar Cells,* Advanced Materials **28**, 5891 (2016).

[319] W. Tan, A. R. Bowring, A. S. Babadi, A. C. Meng, R. Tang-Kong, M. D. McGehee, and P. C. McIntyre, *Interfacing Low-Temperature Atomic Layer Deposited TiO_2 Electron Transport Layers with Metal Electrodes,* Advanced Materials Interfaces **7**, 1902054 (2020).

[320] M. Bhushan, *Mg diffused zinc phosphide n/p junctions,* Journal of Applied Physics **53**, 514 (1982).

[321] G. M. Kimball, A. M. Müller, N. S. Lewis, and H. A. Atwater, *Photoluminescence-based measurements of the energy gap and diffusion length of Zn_3P_2*, Applied Physics Letters **95**, 3 (2009).

[322] J. Misiewicz, J. M. Wrobel, and B. P. Clayman, *Lattice modes of Zn_3P_2*, Solid State Communications **66**, 747 (1988).

[323] M. Dimitrievska, F. S. Hage, S. Escobar Steinvall, A. P. Litvinchuk, E. Z. Stutz, Q. M. Ramasse, and A. Fontcuberta i Morral, *The Advantage of Nanowire Configuration in Band Structure Determination,* Advanced Functional Materials **31**, 2105426 (2021).

[324] J. M. Pawlikowski, *Zn_3P_2-based solar cell devices,* Optica Applicata **19**, 31 (1989).

[325] Springer, *Zinc phosphide (Zn_3P_2) optical properties, dielectric constant,* in *Non-Tetrahedrally Bonded Elements and Binary Compounds I*, 0, edited by M. S. O. Madelung, U. Rössler (SpringerMaterials, 2005) pp. 1–16.

[326] E. Bellini, *Helmholtz Center achieves 29.80% efficiency for perovskite/silicon tandem solar cell,* PV magazine Global (2021).

[327] B. D. Gates, Q. Xu, M. Stewart, D. Ryan, C. G. Willson, and G. M. Whitesides, *New approaches to nanofabrication: Molding, printing, and other techniques,* Chemical Reviews **105**, 1171 (2005).

[328] A. Jacobo-Martín, N. Jost, J. J. Hernández, C. Domínguez, G. Vallerotto, S. Askins, I. Antón, and I. Rodríguez, *Roll-to-roll nanoimprint lithography of high efficiency Fresnel lenses for micro-concentrator photovoltaics,* Optics Express **29**, 34135 (2021).

[329] B. Wu and A. Kumar, *Extreme ultraviolet lithography: A review,* Journal of Vacuum Science & Technology B: Microelectronics and Nanometer Structures **25**, 1743 (2007).

[330] R. P. Seisyan, *Nanolithography in microelectronics: A review,* Technical Physics **56**, 1061 (2011).

[331] A. Pimpin and W. Srituravanich, *Reviews on micro- and nanolithography techniques and their applications,* Engineering Journal **16**, 37 (2012).

[332] Y. Chen, *Nanofabrication by electron beam lithography and its applications: A review,* Microelectronic Engineering **135**, 57 (2015).

[333] P. Spinelli, M. A. Verschuuren, and A. Polman, *Broadband omnidirectional antireflection coating based on subwavelength surface Mie resonators,* Nature Communications **3**, 1 (2012).

[334] S. W. Tabernig, L. Yuan, A. Cordaro, Z. L. Teh, Y. Gao, R. J. Patterson, A. Pusch, S. Huang, and A. Polman, *Optically Resonant Bulk Heterojunction PbS Quantum Dot Solar Cell,* ACS Nano **16**, 13750 (2022).

[335] P. Maury, D. Turkenburg, N. Stroeks, P. Giesen, I. Barbu, E. Meinders, A. Van Bremen, N. Iosad, R. Van Der Werf, and H. Onvlee, *Roll-to-roll UV imprint lithography for flexible electronics,* Microelectronic Engineering **88**, 2052 (2011).

[336] H. J. Kim, A. W. Marcia, A. Chaiken, R. Elder, B. Garcia, W. Jackson, A. Jeans, O. Kwon, H. Luo, P. Mei, C. Perlov, C. Taussig, F. Jeffrey, K. Beacom, S. Braymen, J. Hauschildt, and D. Larson, *Roll-to-Roll Manufacturing of electronics on flexible substrates using self-aligned imprint lithography (SAIL),* Proceedings of International Meeting on Information Display **8**, 82 (2008).

[337] O. Bar-On, P. Brenner, T. Siegle, R. Gvishi, H. Kalt, U. Lemmer, and J. Scheuer, *High Quality 3D Photonics using Nano Imprint Lithography of Fast Sol-gel Materials,* Scientific Reports **8**, 1 (2018).

[338] C. Lin, *Transitioning to larger wafers,* PV magazine Global (2021).

[339] S. W. Tabernig, A. H. Soeriyadi, U. Römer, A. Pusch, D. Lamers, M. P. Nielsen, A. Polman, and N. J. Ekins-daukes, *Avoiding shading losses in concentrator photovoltaics using a soft-imprinted cloaking geometry,* IEEE Journal of Photovoltaics **12**, 1116 (2022).

[340] V. Neder, S. W. Tabernig, and A. Polman, *Detailed-balance efficiency limits of two-terminal perovskite/silicon tandem solar cells with planar and Lambertian spectral splitters,* Journal of Photonics for Energy **12**, 1 (2022).

[341] G. Yin, P. Manley, and M. Schmid, *Light trapping in ultrathin CuIn1-xGaxSe2 solar cells by dielectric nanoparticles,* Solar Energy **163**, 443 (2018).

[342] National Center for Biotechnology Information, *Titanium diisopropoxide bis(acetylacetonate) (website),* `https://pubchem.ncbi.nlm.nih.gov/compound/44629995` (2022), accessed: 2022-08-01.

[343] N. Muhunthan, O. P. Singh, S. Singh, and V. N. Singh, *Growth of CZTS thin films by co-sputtering of metal targets and sulfurization in H_2S,* International Journal of Photoenergy **2013**, 1 (2013).

[344] V. E. Ferry, M. A. Verschuuren, M. C. V. Lare, R. E. I. Schropp, H. A. Atwater, and A. Polman, *Optimized Spatial Correlations for Broadband Light Trapping,* Nano Letters **11**, 4239 (2011).

[345] Y. Liu, Y. Li, and H. Zeng, *ZnO-Based Transparent Conductive Thin Films: Doping, Performance, and Processing,* Hindawi Publishing Corporation **2013**, 196521 (2013).

[346] R. C. Newman, *Defects in silicon,* Reports on Progress in Physics **45**, 1163 (1982).

List of publications

This thesis is based on the following publications

- *Photovoltaics reaching for the Shockley–Queisser limit*, B. Ehrler, E. Alarcón Lladó, **S. W. Tabernig**, T. Veeken, E. C. Garnett, and A. Polman, ACS Energy Lett. **5**, 3029 (2020). (**Chapter 1**)

- *Optically resonant bulk heterojunction PbS quantum dot solar cell*, **S. W. Tabernig**, L. Yuan, A. Cordaro, Z. Teh, Y. Gao, R. Patterson, A. Pusch, S. Huang, and A. Polman, ACS Nano **16**, 13750 (2022). (**Chapter 2**)

- *Avoiding shading losses in concentrator photovoltaics using a soft-imprinted cloaking geometry*, **S. W. Tabernig**, A. H. Soeriyadi, U. Römer, A. Pusch, D. Lamers, M. K. Juhl, D. N. R. Payne, M. P. Nielsen, A. Polman, and N. J. Ekins-Daukes, IEEE J. Photovolt. **12**, 1-12 (2022). (**Chapter 3**)

- *Nanopatterned Si and SiN_x structures for improved incoupling and lighttrapping in thin-film Si solar cells* , **S. W. Tabernig***, A. Cordaro*, A. Lambertz*, M. Pollard, C. Yi, E. Alarcón Lladó, B. Hoex, and A. Polman, in preparation. (**Chapter 4**)

- *Detailed-balance efficiency limits of two-terminal perovskite/silicon tandem solar cells with planar and Lambertian spectral splitters*, V. Neder, **S. W. Tabernig**, and A. Polman, J. Photonics Energy **12**, 015502 (2022). (**Chapter 5**)

- *Zn_3P_2-TiO_2 heterojunction-based thin-film solar cell device design*, **S. W. Tabernig**, M. Dimitrievska, A. Polman, A. Fontcuberta i Morral, in preparation. (**Chapter 6**)

- *Beyond light trapping benefits: the effect of SiO_2 nanoparticles in bifacial semi-transparent ultrathin CIGSe solar cells*, Y. Li, **S. W. Tabernig**, G. Yin, A. Polman, M. Schmid, Sol. RRL **6**, 2200695 (2022). (**Chapter 7**)

  *These authors contributed equally

Other publications by the author

- *Nano-patterned back-reflector for enhanced light management in III–V-on-silicon solar cells*, A. Cordaro, R. Müller, **S. W. Tabernig**, N. Tucher, H. Hauser, O. Höhn, B. Bläsi, and A. Polman, (in preparation).

- *Plasmonic indium lattices fabricated via electrochemical depositio*, M. D. Wobben, M. Valenti, Y. Bleiji, A. Cordaro, **S. W. Tabernig**, M. Aarts, R. D. Buijs, S. R. K. Rodriguez, A. Polman, and E. Alarcón Lladó, (in preparation).

- *Bottom-up filling of nanosized trenches with silver and copper to fabricate transparent conducting electrodes*, Y. Bleiji, M. Dieperink, A. Cordaro, **S. W. Tabernig**, A. Polman, and E. Alarcón Lladó, (in preparation).

- *A method to detect triplet exciton transfer from singlet fission materials into silicon solar cells: Comparing different surface treatments*, B. Daiber, S. P. Pujari, S. Verboom, S. L. Luxembourg, **S. W. Tabernig**, M. H. Futscher, J. Lee, H. Zuilhof, and B. Ehrler, Chem. Phys. **152**, 114201 (2020).

- *Enhancing silicon solar cells with singlet fission: the case for Förster resonant energy transfer using a quantum dot intermediate*, **S. W. Tabernig**, B. Daiber, T. Wang, and B. Ehrler, J. Photonics Energy **8**, 022008 (2018).

Publications in conference proceedings

- *Breaking the shackles of the shading/resistance loss trade-off in concentrator solar cells: effectively transparent contacts for elimination of shading losses*, **S. W. Tabernig**, A. H. Soeriyadi, U. Römer, A. Pusch, D. Lamers, M. K. Juhl, D. N. R. Payne, M. P. Nielsen, A. Polman, and N. J. Ekins-Daukes, Photonics for Solar Energy Systems IX, PC121500D (2022).

- *Optically resonant bulk heterojunction PbS quantum dot solar cell*, **S. W. Tabernig**, L. Yuan, A. Cordaro, Z. Teh, Y. Gao, R. Patterson, A. Pusch, S. Huang, and A. Polman, Photonics for Solar Energy Systems IX, PC121500H (2022).

- *Near-infrared bandgap Cd-rich $Pb_xCd_{1-x}S$ quantum dot with record long exciton lifetime*, Z. Teh, R. J. Patterson, **S. W. Tabernig**, A. Sharma, and S. Huang, 2021 IEEE 48$^{\text{th}}$ Photovoltaic Specialists Conference (PVSC), 2475 (2021).

- *Carrier collection in optically resonant nanostructures for quantum dot solar cells*, **S. W. Tabernig**, L. Yuan, Y. Gao, Z. Teh, A. Cordaro, A. Pusch, R. Patterson, S. Huang, and A. Polman, 2021 IEEE 48$^{\text{th}}$ Photovoltaic Specialists Conference (PVSC), 0803 (2021).

- *Plasmonic and Mie scattering in nanopatterned back reflectors for III–V-on-silicon solar cells*, A. Cordaro, N. Tucher, **S. W. Tabernig**, H. Hauser, O. Hoehn, R. Müller, B. Bläsi, and A. Polman, Proc. SPIE 11366 Photonics for Solar Energy Systems VIII, 1136607 (2020).

- *Light management for absorption enhancement in PbS quantum dot solar cells*, **S. W. Tabernig**, Z. Li Teh, A. Cordaro, R. Patterson, G. Conibeer, S. Huang, and A. Polman, Proceedings of the Asia Pacific Solar Research Conference, ISBN: 978-0-6480414-3-6 (2019).

Acknowledgements

The content of the thesis up until now would not have been possible without all the previous work of scientific giants, whose shoulders we are all standing on. And I am lucky that some of those were my mentors, peers, and friends during the last four years.

Albert, you gave me this tremendous opportunity of immersing myself in the research world by being surrounded by amazing science and scientists at AMOLF, UNSW, and all the conferences and workshops I attended. As a supervisor, I always appreciated your ability to spontaneously come up with suggestions for solving problems, but even more so that you gave me the freedom to work at my own pace and in my owns ways. Instead of micromanaging, you always found the right time and place to offer feedback and I appreciated that a lot. As a mentor, you helped me grow in areas where I was less confident, and, as a human, you always stayed kind and humble, despite your successes. I'll always fondly remember our visits to Australia, and all our discussions about the bright future of PV. It is great to share these passions and experiences. Thanks!

Bram, without your support the 2 years at UNSW would not have been possible. You helped me get settled in the for me new, more engineering- and Si-focused research environment at UNSW, and were also integral to the scientific content of many of my research projects. It was amazing to meet again at WCPEC-8 and see how well you are doing at UNSW, pushing the PV agenda forward, not just for yourself but for the whole institute.

Esther, I am very happy that you joined the promotor team as well and it was great seeing you get tenure. I always appreciated your constructive feedback and questions, which often encouraged me to dig deeper into the science and further my understanding. Your curious and calm nature makes you a great addition to the team of LMPV group leaders, providing a comfortable environment for all of us students to grow in.

I would also like to specifically thank the **defense committee** for evaluating my thesis and making time for the defense. **Bruno**, my Master's project in your group is what convinced me to do a PhD in the first place, and it was great to see how the research in your group developed over the years. I also appreciate your public advocacy and commitment to the non-scientific parts of sustainability. **Erik**, I have always been impressed by your ability to ask sharp questions within a wide range of research topics, which I found to be great preparation for conference talks. **Wim**, you were the first one to give me a dedicated PV lecture during the UvA PV classes, and got me much more interested in semiconductors than I had been before. **Christiane**, I really enjoyed the "Optics for Solar Energy" meetup in Berlin and your group's hospitality during those days. **Rebecca**, I fondly remember how your group invited me to visit UTwente. Furthermore, I very much value your many critical questions that make for great discussions. **Florian**, it's great to know that at least one committee member can also understand my Tyrolean dialect. I promise to not use it during the defense though!

At AMOLF, I was surrounded by some of the brightest minds I know. While not always directly involved as supervisors in my research, I have been lucky to receive great feedback and comments from others as well. **Wiebke**, **Said**, **Femius**, and **Ewold**, your expertise and willingness to share it during poster sessions, colloquiums, or informal conversations was very valuable, and I enjoyed these fruitful discussions at AMOLF.

The **Photonic Materials group** has been a great environment to develop myself in, and also a place where always something fun or interesting was happening. **Dion**, thanks for being so creative and quick when it comes to solving lab problems. **Sophie**, we had very little overlap, but it is very cool that you already have your own lab in Toulouse. **Nick**, I am really jealous that you have set yourself up with such a nice position in Brazil. **Verena**, I am still amazed by how you combined your young family with coloring the world of PV. **Magda**, you built the probably most advanced tool at AMOLF, and at the same time were always cheerful in and outside of work. **Tom**, besides being the MVP for making sure the group stays organized, I have always appreciated your kindness as well as our shared excitement for the PV field and football. And our conference trips of course. **Andrea**, I'll never forget the painful but fruitful cleanroom sessions and your readiness to criticize the top 5% of the research field. I hope you'll manage to shape the field a bit in the future. **Matthias L.**, word. Thanks for being an officemate who I could share joy, pain, beers and burritos with, starting and ending the PhD journey together. **Nika**, your cheerfulness is truly contagious, and I am very happy that you share the good taste in beer with me. **Kelly**, I hope you enjoyed Europe and wish you the best of luck back in the US. **Evelijn**, you are a great role model for work life balance, and I always enjoyed the spontaneous coffee breaks we had. I would also like to thank **Saskia**, **Kyra**, **Floris**, **Marnix**, **Heleen**, **Daphne D.**, **Hollie**, **Hannah**, and **Robin** for joining the group. It was and is great seeing where all your paths are leading you, and I also enjoyed all the drinks together. **Floortje**, **Mieke**, and **Esther**, thanks for handling all the admin for the group.

Finally I also want to thank all the others that I met during my PhD journey at AMOLF. **Benjamin**, your supervision while I was a Master student was great: You were positively critical and always encouraging, which I am grateful for. Similarly, it was great to share the office with you too, **Christian**, I hope you are enjoying Sweden. I'd also like to thank my fellow current and former colleagues: **Jumin**, **Tianyi**, **Moritz F.**, **Lucie**, **Loreta**, **Silvia**, **Koen**, **Eline**, **Moritz S.**, **Imme**, **Jeroen**, **Marc**, **Gianluca**, **Maria**, **Thomas**, **Julia**, **Harshal**, **Jenny**, **Sarah**, **Susan**, **Eitan**, **Sven**, **Hongyu**, **Rohit**, **Mark**, **Nasim**, **Alex** (Si-bro), **Yorick** (HF-bro), **Daphne A.**, **Melanie**, **Marco**, **Patrick S.**, **Francesca**, **Mees**, **Ethan**, **Jente**, **Roel**, **Rene**, **Jesse**, **Falco**, **Deba**, and **Zhou**.

During my PhD I also learned how important good technical support is. For that I would like to thank everyone in the various **support departments** at AMOLF. You really provide all of us researchers at AMOLF with an advantage over others who cannot rely on such solid and efficient facilities. While I cannot mention everyone, some deserve special mention. **Wouter**, thanks for helping me with my secondment to Australia, enjoy your retirement. **Bob**, **Dimitry**, **Hans**, **Johan**, **Igor**, and **Dylan**, your management of the cleanroom and also your quick and creative support with cleanroom problems is truly exceptional, we are lucky to have you. Also thanks to **Henk-Jan** for designing such a beautiful IV-stage for our IBC cells. A special shout-out goes to the **precision manu-**

facturing department managed by **Jan**. Your capabilities really make the PhD life easier. **Clyde**, thanks for always being a joyful presence around the building.

I was lucky enough to work at another inspiring institute during my PhD: UNSW. **Ned**, **Jeana**, **Michael N.**, and **Michael P.**, your willingness to provide advice and support during my time at UNSW was important, and your research inspiring. Thanks to **Anastasia**, **Udo**, **Andreas**, **Chuqi**, for being a fun team of postdocs, and my office mates **Guojun** and **Nursultan** for interesting discussions. Thanks to **Kaiwen**, **Chang**, and **Shujie** for always being helpful and working together on CZTS.

I also want to thank all my other collaborators. **Anja**, **Rajrupa**, **Mira**, and **Anna F.**, thanks for welcoming me to EPFL and for a fruitful collaboration. **Yong**, **Yin**, and **Martina**, I wish you good fortune with further work on your exciting solar cell architectures. I would also like to thank the team at Macquarie University, **Matthias J.** and **David P**.

My gratitude is not limited to people: **Wikipedia**, **sci-hub.se**, and **libgen.li** have been valuable sources for my research. I commend them for their service to the public and hope they will continue to successfully undermine the greedy elements of the academic publishing industry. The **upper campus laksa stall** and the **Maze coffee corner** at UNSW have also been integral to my PhD life, so thanks!

Apart from my direct research environment, I would like to thank my friends who have joined me during my journey in Amsterdam. **Jorge** and **Albert T.**, you represent some of KB's greatest and are true friends. **Bas**, thanks for all the great Weesper flat parties. **Ben & Jaqui & Evelin Aura**, it is so great to witness the beginnings of your beautiful family. **Kyriakos**, already looking forward to see you returning for another ADE. **Anna P.**, it's so great to see how happy you are with your career and new home. Thanks for all the coffee walks, **Fleur**! **Flora**, you have such a comforting, special personality, it is always a blast meeting you, even if that means going to Berlin. **Rebekka K.**, thanks for always being open-minded and understanding, and for being a great bouldering partner. Towards yellow! **Ilya**, we have started our journey's at the same time, and it so great to see us finishing together as well, even if it is in different places. Towards many more great memories (hopefully surfing)!

Thanks to my friends who made my time in Australia outside of uni a great period of my life: **Barb**, **Abhinav**, **David S.**, **Alejandra**, **Shukla**, **Komal & Sankalp & Arjun**, **Eve**, **Patrick F.**, **the wine tour team**, and **the boot camp team**. I am really missing our days and nights around the eastern suburb beaches.

During my whole PhD, I was also lucky enough to visit and be visited by many friends from Austria. Thanks **Unta**, great we still get along after knowing each other for 18 years already. **Lukas**, it is always fun to meet up in Amsterdam or Vienna, creating new stories every time. **Hermann**, we have always been a great team, if it's doing physics together or participating in a mountain duathlon. **Gjin**, I really admire how you manage to keep up your lifestyle together with **Jeta**, taking great care of **Luan**, but still living the life. **Gramos**: Kopenhagen, Amsterdam, Venice, (Linz), Milan, looking forward to what's next, I am counting on a kajak or hiking trip! **Nahal**, thanks for being a great replacement for me after I left the WG in Austria. **Tina**, it's so great to know you, I really appreciate the cheerfulness that you bring to our conversations, trips, or parties. **Finch** and **Gote**, we have been best friends for a very long time now and whether it is bouldering, scuba diving, drinking beers, knitting, or travelling to random cities, we are always having a

blast together. **Gote**, enjoy the last bits of your PhD, looking forward to visiting you in Spain soon. **Finch**, enjoy the last few years before you replace your boss, and buy yourself a house with a vineyard then!

Finally, my family. **Oma**, bedankt dat ik altijd langs mag komen bij jou en **Jan** in Hippolythushoef. Ik geniet echt van de fietsrondjes, de rustige dagen en het inmiddels vegetarische eten bij jullie. **Andi**, immer wieder nice wenn ma uns sehen und random topics diskutieren, oder wenn du mi mal wieder bei einer kurzen Bergrunde pushesch. Bleib so fit und gsund und geh deinen ehrgeizigen Weg weiter. **Ronny**, immer wieder geil zusammen was auf da Switch zu zocken, oder sich über #antiwork zu unterhalten. I hoff dass die Pläne von dir und da **Ines** als Geoinformatiker und Microbiologin a bisl rumzuziehen aufgehn.

Bis jetzt hab I schon viele Dankesworte ausgsprochen, aber die einzigen zwei ohne de I wirklich nie hier gewesen wär seids ihr, **Mama** und **Papa**. **Mama**, du hasch mir als Kind immer richtig gut am Küchentisch mit den Hausaufgaben gholfen, sodass i a gute Basis legen hab können. **Papa**, die PM Zeitschriften de du früher glesen und mir gezeigt hasch warn wirklich der Anfang meines Interesses für die Wissenschaft. Und ihr habts natürlich noch so viel mehr für mi gmacht. Sorry, dass i so oft irgendwo bin, aber I hoff, dass ihr wissts wie dankbar I euch bin, und, dass I es ohne euch nie gschafft hätt.

Danke.

About the author

Stefan Wil Tabernig was born on April 1st 1994 in Lienz (Austria). He grew up in Gwabl (Ainet), a mountain village in the Austrian alps. He completed the science track at the local Gymnasium (high school) in 2012 and joined the Austrian Armed Forces for one year after that. Right after the army, he started studying physics at the Graz University of Technology and the University of Graz. He completed his Bachelor's degree in 2016, and moved to Amsterdam. There he obtained a Master's degree in Advanced Matter and Energy Physics from the University of Amsterdam and the Vrije Universiteit Amsterdam in 2018. During the work on his thesis, titled "Förster resonance energy transfer from PbS quantum dots to silicon: The missing link towards singlet fission solar cells", he got interested in the field of photovoltaics. This led him to pursue a PhD in the same field, at the research institute AMOLF in Amsterdam. His research, which culminated in a PhD thesis titled "Charge Carrier Generation Management in Photovoltaics", focused on the interplay between optical charge generation and electronic charge extraction in solar cells that utilize nanostructures. During his research, Stefan was a long-term visiting student at the University of New South Wales (Sydney, Australia), and attended many international conferences, at which he was awarded two "best presentation" awards.

He enjoyed the relative diversity of his research projects the most, appreciating the interdisciplinarity that solar research requires and enables. Stefan further likes learning languages and fluently (B2+) speaks German, English, and Dutch, as well as intermediate Spanish, high school level Latin, and beginner level Chinese. In his free time, Stefan enjoys sunny weather, sports (specifically bouldering, hiking, scuba diving, and team sports), and travelling the not so well-known parts of the world.